Semiconductors, Vol. 35, No. 2, 2001, pp. 125–131. Translated from Fizika i Tekhnika Poluprovodnikov, Vol. 35, No. 2, 2001, pp. 129–135.
Original Russian Text Copyright © 2001 by Tyschenko, Zhuravlev, Vandyshev, Misiuk, Yankov, Rebohle, Skorupa.

ELECTRONIC AND OPTICAL PROPERTIES OF SEMICONDUCTORS

Study of Photoluminescence of SiO_xN_y Films Implanted with Ge^+ Ions and Annealed under the Conditions of Hydrostatic Pressure

I. E. Tyschenko*, K. S. Zhuravlev*, E. N. Vandyshev*, A. Misiuk, R. A. Yankov***, L. Rebohle****, and W. Skorupa******

** Institute of Semiconductor Physics, Siberian Division, Russian Academy of Sciences, pr. Akademika Lavrent'eva 13, Novosibirsk, 630090 Russia*

e-mail: tys@isp.nac.ru

*** Institute of Electron Technology, Al. Lotnikow 46, 02-668 Warsaw, Poland*

**** CCR GmbH, Beschichtigungstechnologie, TZO Rheinbreitbach, Germany*

***** Institute of Ion Beam Physics and Materials Research, Research Center Rossendorf, Inc. POB 510119, D-01314 Dresden, Germany*

Submitted June 16, 2000; accepted for publication June 20, 2000

Abstract—The influence of hydrostatic pressure on photoluminescence of SiO_xN_y ($x = 0.25$ and $y = 1$) films grown on the Si substrates and implanted with Ge^+ ions, with pressure applied during annealing of the films, was studied for the first time. It is shown that hydrostatic compression leads to a tenfold increase in the photoluminescence intensity of the implanted SiO_xN_y films compared to that obtained as a result of postimplantation annealings at atmospheric pressure. The observed increase in the photoluminescence intensity is attributed to accelerated formation of radiative-recombination centers in the metastable-phase zones in the implanted silicon oxynitride. These centers are tentatively related to ≡Si–Si≡ centers and to complexes involving Ge atoms (of ≡Si–Ge≡ and ≡Ge–Ge≡ types). © *2001 MAIK "Nauka/Interperiodica".*

INTRODUCTION

In recent years, beginning with the discovery of visible photoluminescence (PL) in porous Si [1], study of properties of structures with low-dimensional Si-based objects has attracted great interest. One of the most promising methods for producing such structures is the ion-beam synthesis of Si and Ge clusters and nanocrystals in SiO_2 films grown thermally on Si [2–5]; these films represent the materials most widely used in Si technology. The silicon oxynitride (SiO_xN_y) layers are also widely used in the production of silicon-based devices and possess a number of remarkable properties that make it possible to use these devices as components of optical integrated circuits. When compared to SiO_2, the silicon oxynitride films feature a larger refractive index and are more suitable for the production of optoelectronic devices. Thus, the SiO_xN_y-based waveguides feature low optical losses [6]. The silicon-oxynitride films are more stable chemically compared to SiO_2 and possess good masking properties. Recently, it has been inferred that thermal SiO_2 as a gate insulator in nanometer-sized metal–insulator–semiconductor (MIS) devices is going to be replaced by amorphous SiO_xN_y films. This is due to the fact that silicon oxynitride contains a lesser amount of Si–Si bonds at the silicon–insulator interface (these bonds act as hole traps) and also possesses blocking properties for the dopant redistribution [7]. Until recently, there have been no published data on PL of silicon oxynitride at room temperature. It is only if the temperature is lowered to 90 K that the PL band, peaked at about $\hbar\omega = 2.8$ eV (the wavelength of $\lambda \approx 440$ nm), could be observed; the origin of this band has not been clarified [8]. Recently, the PL spectra of amorphous SiO_xN_y films with various compositions have been measured at room temperature [9]. In the visible region of the spectrum, a band peaked at about $\hbar\omega = 3.1$ eV ($\lambda \approx 400$ nm) was observed. The intensity of this PL band was at a maximum for the excitation-radiation energy of ~6.3 eV (the corresponding wavelength is ~200 nm). The intensity and width of this band depended on stoichiometric composition of the films. As the oxygen content in the film increased, a broadening of the PL band was observed, along with a decrease in its intensity. The origin of this band was related to recombination at the $N_3Si–SiN_3$ bond [9]. It has been also shown [10] that implantation of C^+ ions into SiO_xN_y films at room temperature results in excitation of a green PL band peaked at about $\lambda = 550$ nm ($\hbar\omega \approx 2.25$ eV). This band was related to recombination in complexes of Si, N, O, and C atoms, and its intensity was highest after an annealing at $T_a = 600$°C.

In spite of an ever increasing interest in the properties of silicon oxynitride, its photoluminescent properties and also the origin of the PL peaks observed are still not clearly understood. The possibilities of using oxynitride as a material for efficient sources of radiation have not been adequately investigated, either. We have found previously [11] that annealing of ion-implanted SiO_2 films under the conditions of uniform compression enhances the PL in the visible region of the spectrum at room temperature. The objective of this study was to gain insight into the influence of postimplantation annealing under conditions of hydrostatic pressure on PL of SiO_xN_y films implanted with Ge^+ ions.

EXPERIMENTAL

For initial substrates, we used single-crystal wafers of *n*-Si{100} with a resistivity of 3–10 Ω cm. A buffer SiO_2 layer 2 nm thick was then grown on silicon wafers. The SiO_xN_y films ($x = 0.25$ and $y = 1$) with the refractive index of ~1.882 and thickness of ~75 nm were deposited onto the substrate using a mixture of the gases SiH_2C_{12} (50 s cm^3), N_2O (150 s cm^3), and NH_3 (150 s cm^3) at a temperature of 780°C under a pressure of 200 mTorr. The siliconoxynitride films were implanted with Ge^+ ions with an energy of 55 keV and doses of 2.1×10^{15} cm^{-2} (a low dose, LD), 5.8×10^{15} cm^{-2} (a medium dose, MD), and 1.7×10^{16} cm^{-2} (a high dose, HD). The ion energy was chosen so that the ion projected range coincided with the midthickness of SiO_xN_y film. The substrate temperature during implantation was maintained at –(145–155)°C due to cooling with liquid-nitrogen vapors. The ion-current density was 0.5–1.0 μA/cm^2. The postimplantation annealings were performed for 5 h at temperatures of T_a = 450–1000°C in an Ar atmosphere under conditions of both atmospheric pressure and uniform compression under a pressure of P = 12 kbar. In the wavelength range of λ = 340–850 nm, the steady-state PL was excited by an N_2-laser radiation with a wavelength of λ_{ex} = 337 nm and a power of 10 mW. For measuring the time-resolved PL, we also used an N_2 laser with a pulse duration of 7 ns and a power of 16 mW. In order to vary the excitation power, we used neutral filters. All the measurements were performed at T = 300 K. The obtained spectra were normalized, with allowance made for the spectral sensitivity of the photomultiplier.

THE RESULTS

In our experiments, the unimplanted SiO_xN_y films luminesced in the violet region of the spectrum with the intensity peak at about λ = 400 nm (Fig. 1). An annealing of unimplanted siliconoxynitride layers both under atmospheric pressure and under P = 12 kbar did not lead to changes in the PL spectrum. Implantation of Ge^+ ions caused a disappearance of PL in the entire spectral region. The subsequent annealing gave rise to an increase in the PL intensity. The positions of the PL peaks and their intensities I_{PL} depended heavily on the temperature and pressure during annealing. For the sake of comparison, Fig. 1 shows the PL spectra of SiO_xN_y films implanted with LD Ge^+ ions after annealing at T_a = 800 and 1100°C under pressures of P = 1 bar and 12 kbar. An annealing under atmospheric pressure resulted in the formation of a peak in the vicinity of λ = 520 nm. Its intensity increased with an increase in the annealing temperature and, for $T_a \approx$ 800–1000°C, became comparable to the intensity of violet PL in unimplanted films. As a result of annealing under a pressure of P = 12 kbar, the intensity of the green PL band ($\lambda \approx$ 520 nm) also increased and exceeded about tenfold that obtained after annealing of the same layers under atmospheric pressure (see Fig. 1). Along with formation of an intense green PL peak, annealing under pressure also resulted in an increase in the PL intensity in the violet region of the spectrum ($\lambda \approx$ 400 nm). After annealing at T_a = 1000°C, the intensity of this PL was almost twice as high as that in unimplanted samples. The intensities of observed PL bands also increased as the annealing temperature was raised.

In the ion-dose and annealing-temperature ranges we used, the higher PL intensities corresponded to lower doses of Ge^+ ions. A decrease in the PL intensity with increasing ion dose was observed for the samples annealed both under atmospheric pressure and under uniform compression. Figure 2 shows the PL spectra of SiO_xN_y films implanted with three different doses of Ge^+ ions and then annealed at T_a = 1000°C and P = 12 kbar.

The steady-state PL spectra are shown in Fig. 3 for various excitation intensities. It can be seen that an increase in the excitation-radiation power (W) causes the intensities of both the violet and green PL peaks to increase, with positions of the peaks remaining unchanged. The squares and shaded circles in the inset in Fig. 3 correspond to the intensities of the 400- and 520-nm peaks in relation to W; these intensities were obtained by decomposing the experimental spectra into Lorentzian components. The dash-and-dot and dashed lines represent theoretical approximations for the experimental dependences $I_{PL}(W)$. An analysis shows that these dependences are virtually linear: $I_{PL} \propto W^\gamma$, where $\gamma = 1$ for the green PL band and $\gamma = 0.97$ for the violet PL band.

Figure 4 illustrates the decay kinetics for PL intensity in unimplanted siliconoxynitride films and the films implanted with LD Ge^+ ions and annealed at T_a = 1000°C under atmospheric pressure or under uniform compression with P = 12 kbar. The inset in Fig. 4 shows the spectra of nonsteady PL for SiO_xN_y films implanted with LD Ge^+ ions and annealed at T_a = 1000°C and P = 12 kbar. It can be seen that the shape of the spectra is time-independent; only the PL intensity decreases with time. The behavior of the nonsteady PL spectra for

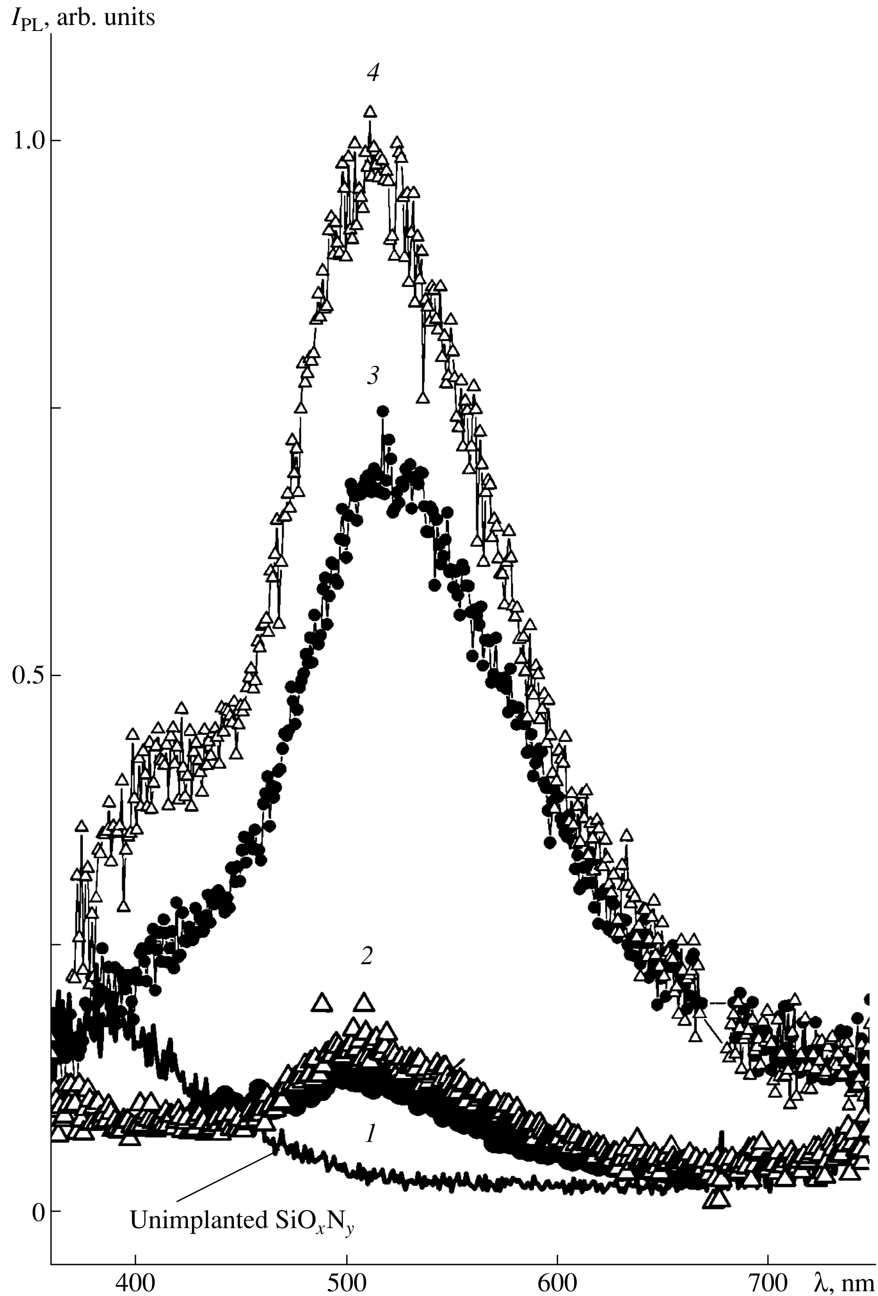

Fig. 1. The PL spectra of unimplanted silicon oxynitride (unimplanted SiO_xN_y) and also of SiO_xN_y films implanted with LD Ge^+ ions and then annealed for 5 h at T_a = (*1*, *3*) 800 and (*2*, *4*) 1000°C under the pressures of (*1*, *2*) 1 bar and (*3*, *4*) 12 kbar. The power of excitation radiation was W = 10 mW/cm^2, and the excitation-radiation wavelength was λ_{ex} = 337 nm.

unimplanted SiO_xN_y layers and the films implanted with Ge^+ ions and annealed at T_a = 1000°C and P = 1 bar is similar. For unimplanted siliconoxynitride layers, the decay of PL intensity can be described by an exponential function with characteristic relaxation time of τ = 17 μs. For the films implanted with Ge^+ ions and then annealed at T_a = 1000°C under a pressure of P = 1 bar or 12 kbar, the PL decay does not obey the exponential law. In these cases, the decay curves can be described by a power-law function $I_{PL} \sim \tau^{\beta}$, where β = 4.22 and 4.29 for the films annealed under atmospheric and high pressures, respectively. Characteristic times corresponding to a decrease in the PL intensity by *e* times are τ = 45 and 48 μs, respectively. It is important to emphasize that the values of β and τ are virtually independent of pressure during annealing.

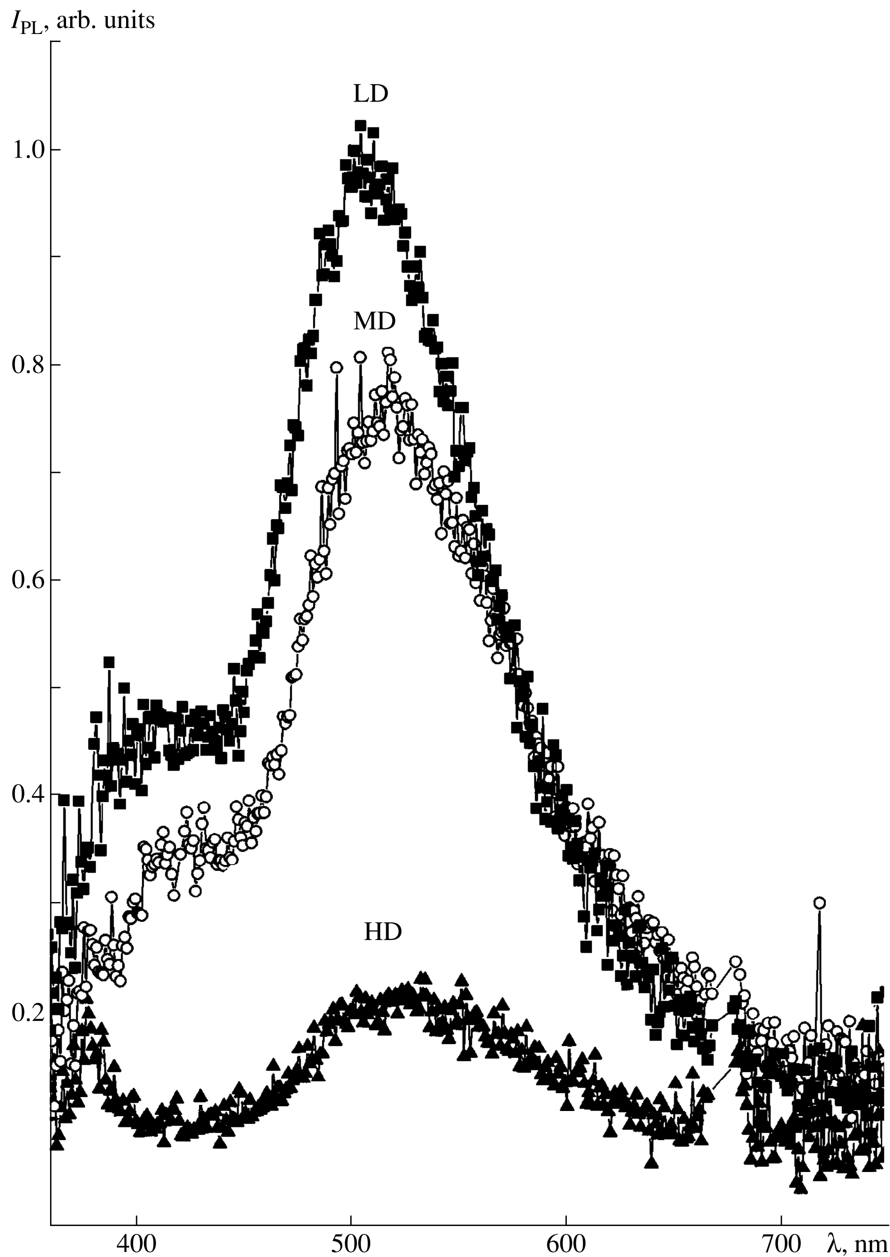

Fig. 2. The PL spectra of SiO_xN_y films implanted with Ge^+ ions with the doses of (LD) 2.1×10^{15}, (MD) 5.8×10^{15}, and (HD) 1.7×10^{16} cm^{-2} and then annealed for 5 h at T_a = 1000°C under a pressure of 12 kbar. The power of excitation radiation was W = 10 mW/cm^2, with the wavelength being λ_{ex} = 337 nm.

DISCUSSION

Before proceeding to an analysis of the influence of annealing under pressure on emission of light in SiO_xN_y films implanted with Ge^+ ions, we discuss the plausible mechanisms and origin of PL in these films. A linear dependence of PL intensity on the excitation intensity demonstrates that recombination in siliconoxynitride films occurs via recombination centers, rather than by direct recombination of electrons and holes (e.g., inside the Ge nanocrystals and nanoclusters formed as a result of ion implantation and subsequent annealing). In addition, the features of the dose dependence of the PL spectra (Fig. 2) indicate that recombination is most probably related to the centers composed of a small number of atoms, rather than to large Ge-atom agglomerates, whose formation is preferential when large doses of Ge^+ ions are used in implantation. We note that similar PL bands (peaked at 400 and 520 nm) have been recently observed by us in silicon nitride films [12], both in unimplanted Si_3N_4 and in the films implanted

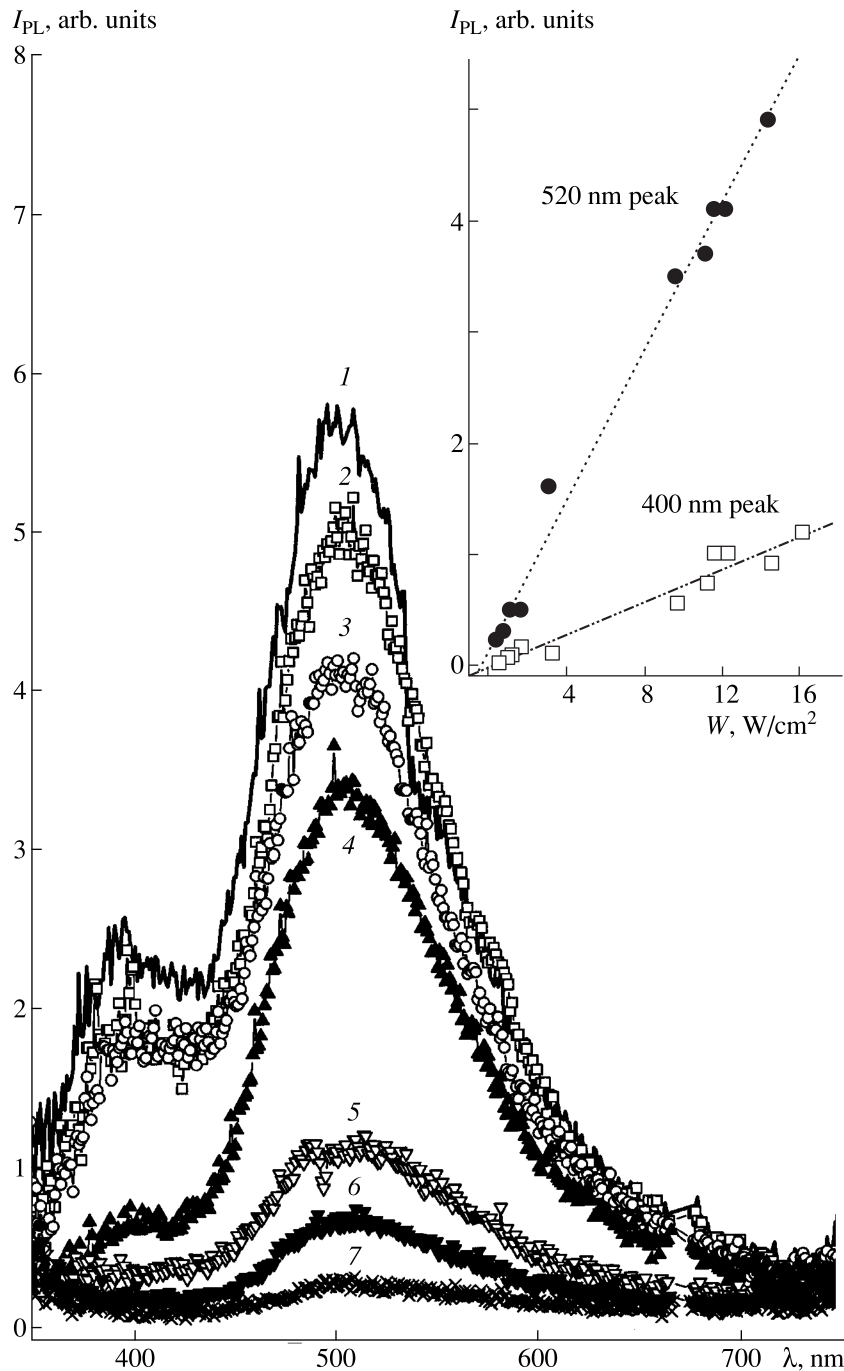

Fig. 3. The PL spectra of SiO_xN_y films implanted with LD Ge^+ ions and then annealed for 5 h at T_a = 1000°C under a pressure of 12 kbar for the excitation radiation with a wavelength of λ_{ex} = 337 nm and a power of W = (*1*) 16, (*2*) 14.4, (*3*) 12.2, (*4*) 9.6, (*5*) 3.2, (*6*) 1.6, and (*7*) 0.48 mW/cm^2. The inset shows the excitation-power dependences of the 400- and 520-nm PL peaks intensities obtained by decomposing the experimental spectra into Lorentzian components (squares and shaded circles) and theoretical approximations of theoretical dependences (the dash-and-dot and dotted straight lines).

with Ge^+ ions. These two PL bands have been previously attributed to recombination at the ≡Si–Si≡ centers [13]. The results of this study show that, in SiO_xN_y, the intensity of these bands increases only after Ge atoms have been introduced into the matrix. Furthermore, the role of Ge atoms in the recombination processes may be dual. These atoms can be involved in formation of both the centers absorbing radiation and the radiative-recombination centers (for example, the ≡Si–Ge≡ or ≡Ge–Ge≡ complexes). It is the latter centers

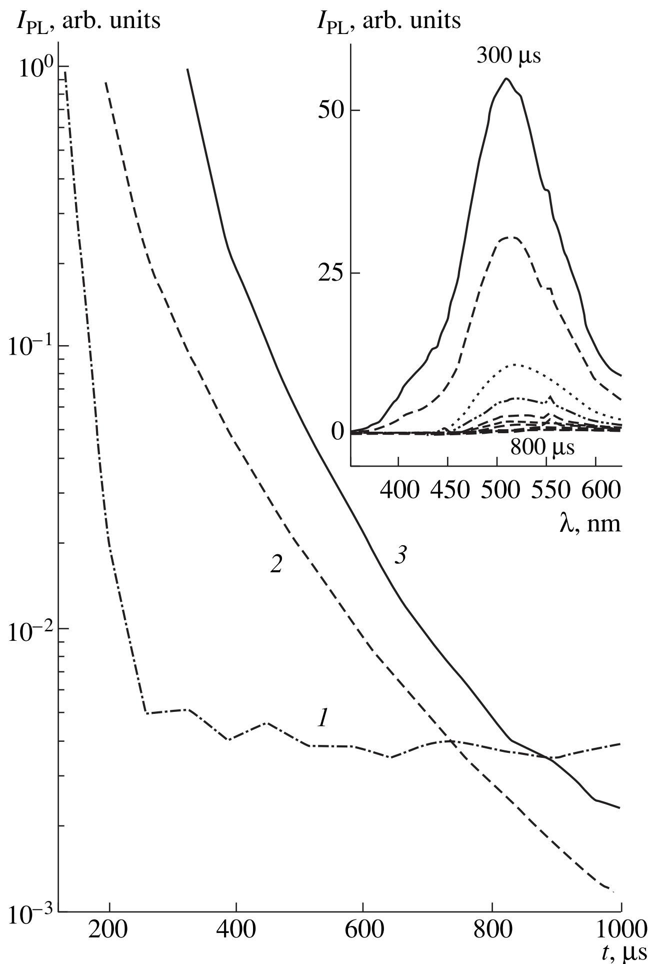

Fig. 4. The decay curves of PL intensity for (*1*) unimplanted SiO_xN_y and implanted with LD Ge^+ ions and then annealed for 5 h at T_a = 1000°C under the pressures of (*2*) 1 bar and (*3*) 12 kbar. The inset shows the nonsteady PL spectra of SiO_xN_y implanted with LD Ge^+ ions and then annealed for 5 h at T_a = 1000°C under a pressure of 12 kbar within a time interval of 300–800 μs.

that are apparently responsible for the green PL band. The violet PL band is present in the spectra of both unimplanted films and the films implanted with Ge^+ ions and then annealed under a pressure. Estimations of the decay time for the above band yield, in both cases, nearly the same values: $\tau \approx 17$ and 26 μs, respectively. On the basis of these findings, we may infer that the PL band peaked at 400 nm is related to recombination at the ≡Si–Si≡ centers. It is worth noting that the PL decay times obtained here differ from the published values [14, 15] of characteristic times for the transition between the excited (T_1) and ground (S_0) states of the ≡Si–Si≡ and ≡Ge–Ge≡ centers. This discrepancy may be caused by the fact that, in our experiments, the PL spectra were excited using photon energy which was insufficient for initiating the direct $(S_0) \longrightarrow (T_1)$ transitions. In the case under consideration, a charge-carrier transition to the excited-state level can be effected only via additional levels. The above-reported power-law dependence of the PL intensity on time for implanted films indicates that the generation and recombination of charge carriers are more complex than those in unimplanted films. It is also worth noting that the previously published data on the relaxation times of the ≡Si–Si≡ and ≡Ge–Ge≡ PL centers have been obtained, as a rule, for SiO_2 (rather than SiO_xN_y) films.

The results show that uniform compression during annealing of SiO_xN_y films implanted with Ge^+ ions does not give rise to new recombination centers in the annealing temperature T_a range used; rather, it is only conducive to an increase in the concentration of these centers compared to that obtained as a result of annealing under atmospheric pressure. This hypothesis is corroborated by the following facts. First, an annealing under compression does not give rise to new peaks in the PL spectra compared to the spectra of unimplanted SiO_xN_y films or the films annealed at P = 1 bar (Fig. 1). Only an increase in the intensity of the previously observed PL bands (peaked at ~400 and ~520 nm) is observed. Second, an analysis of the PL decay curves shows that the PL relaxation times for implanted SiO_xN_y layers are the same, irrespective of whether they have been annealed under atmospheric pressure or under P = 12 kbar. It is important that compression during postimplantation annealing stimulates the formation of complexes responsible for both violet and green PL bands. The origin and mechanism of this phenomenon are still not fully understood. One of the causes of promoted formation of the radiative-recombination centers may be a decrease in the interatomic distance as a result of uniform compression during annealing. The values of P used in our experiments are approximately an order of magnitude smaller than those initiating the structural phase transitions in the bulk material [16]. Our experiments also show that the compression does not give rise to additional PL-active centers in unimplanted silicon oxynitride. New centers emerge only if we are dealing with ion-implanted films that contain high concentrations of excess Ge atoms and defects. It is possible that such structural rearrangements occur under lower pressures in the regions of ion-implanted SiO_xN_y. Another explanation for promoted formation of radiative-recombination PL centers in the course of annealing under pressure was offered by us [11] in terms of promoted structural transitions within individual zones of metastable phases [17]; in the case under consideration, these phases are represented by nonstoichiometric regions of silicon oxynitrides enriched with silicon and germanium atoms. This means that the activation energy corresponding to the changes in the short-range order can be appreciably decreased if the matrix atoms are far from the equilibrium. This decrease in the local activation energy may be caused by the fact that one or several vibration frequencies of lattice atoms cease to exist in the vicinity of the insta-

bility threshold. In the case under consideration, this may result in the formation of a large number of small Si or Si–Ge clusters whose structure is most favorable energetically. The question as to which of these two mechanisms is responsible for accelerated formation of radiative-recombination centers during annealing of ion-implanted SiO_xN_y under compression requires further investigation. One way or the other, the accelerated formation of radiative-recombination centers in the case under consideration occurs only in the metastable-phase regions formed in the course of Ge^+-ion implantation.

CONCLUSION

We showed for the first time that the use of hydrostatic pressure in the course of the annealing of SiO_xN_y films implanted with Ge^+ ions results in about a tenfold increase in the intensity of PL in the visible region of the spectrum compared to the corresponding annealings at atmospheric pressure. Studies of the PL decay kinetics and the dependence of the PL intensity on the excitation-radiation power suggest that an increase in the PL intensity as a result of annealing under compression is caused by accelerated formation of radiative-recombination centers in the regions of metastable phases in silicon oxynitride implanted with Ge. These centers are presumably related to the ≡Si–Si≡ center and the complexes of Ge atoms (e.g., the ≡Si–Ge≡ and ≡Ge–Ge≡ centers).

ACKNOWLEDGMENTS

We thank Dr. V.A. Gritsenko for his helpful participation in discussion of the results. I.E. Tyschenko thanks the Ministry of Sciences and Arts of Saxony (Federal Republic of Germany) for support in conducting these studies.

This study was supported in part by the Polish Committee for Scientific Studies, grant no. 7T08F05717.

REFERENCES

1. L. T. Canham, Appl. Phys. Lett. **57**, 1046 (1990).
2. T. Shimizu-Iwayama, K. Fujita, S. Nakao, *et al.*, J. Appl. Phys. **75**, 7779 (1994).
3. H. A. Atwater, K. V. Shcheglow, S. S. Wong, *et al.*, Mater. Res. Soc. Symp. Proc. **321**, 363 (1994).
4. W. Skorupa, R. A. Yankov, I. E. Tyschenko, *et al.*, Appl. Phys. Lett. **68**, 2410 (1996).
5. L.-S. Liao, X.-M. Bao, N.-Sh. Li, *et al.*, J. Lumin. **68**, 199 (1996).
6. *Silicon Nitride in Electronics*, Ed. by A. V. Rzhanov (Nauka, Novosibirsk, 1982), p. 198.
7. M. L. Green, D. Brasen, L. C. Feldman, E. Garfunkel, E. P. Gusev, T. Gustafsson, W. N. Lennard, H. C. Lu, and T. Sorbsch, in *NATO Advanced Research Workshop* (Kluwer, Dordrecht, 1997), p. 335.
8. P. A. Pundur and Yu. G. Shavalgin, Izv. Akad. Nauk Latv. SSR, Ser. Fiz. Tekh. Nauk **26**, 58 (1985).
9. V. A. Gritsenko, Yu. G. Shavalgin, P. A. Pundur, *et al.*, Microelectron. Reliab. **39**, 715 (1999).
10. L. S. Liao, Z. H. Xiong, X. Zhou, *et al.*, Appl. Phys. Lett. **71**, 2193 (1997).
11. I. E. Tyschenko, L. Rebohle, R. A. Yankov, *et al.*, Appl. Phys. Lett. **73**, 1418 (1998).
12. I. E. Tyschenko, V. A. Volodin, L. Rebohle, *et al.*, Fiz. Tekh. Poluprovodn. (St. Petersburg) **33**, 559 (1999) [Semiconductors **33**, 523 (1999)].
13. V. A. Gritsenko, in *Structure and Electronic Properties of Amorphous Insulators in Silicon MIS Devices* (Nauka, Novosibirsk, 1993), p. 280.
14. L. Skuja, J. Non-Cryst. Solids **239**, 16 (1998).
15. R. Thomon, Y. Shimogaichi, H. Mizuno, *et al.*, Phys. Rev. Lett. **62**, 1388 (1989).
16. O. B. Tsiok, V. V. Brazhkin, A. G. Lyapin, and L. G. Khvostantsev, Phys. Rev. Lett. **80**, 999 (1998).
17. V. V. Brazhkin, J. Non-Cryst. Solids **124**, 34 (1990).

Translated by A. Spitsyn

Semiconductors, Vol. 35, No. 2, 2001, pp. 132–134. Translated from Fizika i Tekhnika Poluprovodnikov, Vol. 35, No. 2, 2001, pp. 136–138.
Original Russian Text Copyright © 2001 by Abramov, Tulupenko, Firsov.

ELECTRONIC AND OPTICAL PROPERTIES OF SEMICONDUCTORS

Quasi-Local Impurity States in Uniaxially Compressed *p*-Type Ge

A. A. Abramov*, V. N. Tulupenko*, and D. A. Firsov**

** Donbass State Engineering Academy, Kramatorsk, 84913 Ukraine*
e-mail: tvn@laser.donetsk.ua
*** St. Petersburg State Technical University, ul. Politekhnicheskaya 29, St. Petersburg, 195251 Russia*
Submitted April 28, 2000; accepted for publication June 21, 2000

Abstract—The main characteristics of quasi-local levels produced by shallow-level impurity centers (with a screened Coulomb potential) in uniaxially compressed *p*-Ge were studied theoretically. Stress dependences of positions and widths of the quasi-local impurity states were calculated. Results of the numerical computations for the Ga impurity are presented. © *2001 MAIK "Nauka/Interperiodica".*

INTRODUCTION

Interest in uniaxially compressed *p*-Ge has been aroused mainly due to the discovery of an emission stimulated by the electric field and uniaxial pressure applied in the parallel [1] or crossed [2] directions. An analogous effect was observed in *p*-Si/GeSi nanostructures [3], which can be considered as being uniaxially compressed in the growth direction owing to the lattice mismatch between Ge and Si. Altukhov *et al.* [4] demonstrated experimentally that this stimulated emission is related to the inversion of a hole population between two impurity levels, which occurs due to the removal of degeneracy of the shallow-level acceptor state by uniaxial stress (see also [2, 5]). As the stress X changes, one of these levels remains in the band gap, and another merges with the continuum at a certain X, and becomes a quasi-local state. This level becomes partially filled with holes owing to resonance scattering [6], whereas the level lying in the band gap becomes empty as a result of a breakdown in the electric field. This can lead to the intracenter inversion of a hole population and, as a consequence, to the generation of emission. Thus, for a theoretical description of the inversion mechanism, the stress dependences of the main characteristics of the quasi-local impurity states (positions, broadenings, wave functions) should be known. However, this problem still remains to be solved. For example, the positions and wave functions of levels induced by Coulomb impurity centers can be calculated in the limit of high or low stress [6, 7] by a procedure that requires no explicit stress dependences of these quantities. Analytic stress dependences of the characteristics of the quasi-local impurity states were obtained within a zero-range potential approximation [8, 9]. However, Odnoblyudov *et al.* [9] demonstrated that this approximation can be used for the description of Coulomb impurity centers at relatively low stresses corresponding to a valence-band splitting $\Delta \le 20$ meV at point $p = 0$ in the momentum space. At the same time, a great body of experimental data for uniaxially stressed *p*-Ge was obtained for the stress range corresponding to the values of Δ of up to 60 meV. As mentioned above, these results cannot be theoretically described, because the analytic stress dependences of the main characteristics of quasi-local levels produced by Coulomb impurity centers are unknown. In this paper, we present one of the first attempts to solve this problem.

CALCULATION OF THE MAIN CHARACTERISTICS OF COULOMB IMPURITY STATES

Let us consider the Schrödinger equation for holes at an impurity center

$$(H_{\mathbf{p}} - E)\Psi^i_{\mathbf{p}} = -\sum_{\mathbf{p}'} U_{\mathbf{pp}'}\Psi^i_{\mathbf{p}'}. \qquad (1)$$

Here, $H_{\mathbf{p}}$ is the Luttinger Hamiltonian, E is the binding energy of quasi-local impurity states, the one-by-four column matrix $\Psi^i_{\mathbf{p}}$ describes the impurity states, and $U_{\mathbf{pp}'}$ is the matrix element of the impurity potential in the momentum representation. For a screened Coulomb potential

$$U_{\mathbf{pp}'} = \frac{\gamma}{V}\frac{1}{|\mathbf{p}-\mathbf{p}'|^2 + p_0^2},$$

$\gamma = e^2\hbar^2/(\chi\chi_0)$, V is the normalization volume, $p_0 = \hbar/r_0$, e is the elementary charge, χ is the relative permittivity, χ_0 is the permittivity of free space, and r_0 is the Debye

1063-7826/01/3502-0132$21.00 © 2001 MAIK "Nauka/Interperiodica"

screening distance. Using the Green function $g_\varepsilon(p)$ for free holes ($U_{\mathbf{pp}'} \equiv 0$) [9, 10], we can rewrite Eq. (1) as

$$\Psi_{\mathbf{p}} = -\frac{\gamma}{V} g_\varepsilon(\mathbf{p}) \sum_{\mathbf{p}} \frac{\Psi_{\mathbf{p}'}}{|\mathbf{p}-\mathbf{p}'|^2 + p_0^2}, \tag{2}$$

where $\varepsilon = E + i0$. In the zero-range potential approximation, $p_0 = p_a \approx h/r_a$ (r_a is the lattice constant), which virtually coincides with the largest possible values of p and p'. Taking into account that $\Psi_p \propto g_\varepsilon(p) \propto p^{-2}$, we can consider the denominator under the summation sign as being independent of p and p' and replace it by a constant. In this case, Eq. (2) takes the form of $\Psi_{\mathbf{p}} = g_\varepsilon(\mathbf{p})N$ [9, 10], where N is a constant represented by a one-by-four column matrix. For the screened Coulomb potential $p_0 \ll p_a$, it is rather difficult to find solutions to (2) in a general form. However, taking into account that the positions of the quasi-local states calculated within the zero-range potential approximation agree satisfactorily with the solutions obtained for a Coulomb potential (for $\Delta < 20$ meV), we select a wave function for the model based on a zero-range potential as a zero-order approximation to Eq. (2). For further summation, let us assume that

$$g_\varepsilon(p) \approx 1/(\varepsilon_{-p} - E) + 1/(\varepsilon_{+p} - E)$$

and

$$\varepsilon_{\pm p} = \pm\Delta/2 + p^2/(2m_\pm^*),$$

where ε_{+p} and ε_{-p} are the energies of valence bands split by stress, and $m_\pm^*$ is the direction-averaged effective mass of holes in the ε_+ and ε_- bands. Let us denote $(p^*)^2 = 2(\Delta/2 + E)m_-$. Analyzing the expressions obtained as a result of substitution of the above-mentioned approximations into Eq. (2), we find that the sum appearing in Eq. (2) is independent of p for $p > 2|p^*|$ and is a nonmonotonic function of p in the range of $0 < p < 2|p^*|$. The maximum values of this function are about twice the value obtained for $p = 2|p^*|$ (see the inset in Fig. 1). Thus, we may neglect the dependence of the sum appearing in Eq. (2) on p for $p > 2|p^*|$ and replace p under the summation sign by a certain constant. As a result, the denominator will be a quadratic function of p'. Approximating this function by the relation $[\alpha(p')^2 + 1]\beta$, where α and β are the variables of the problem, we rewrite Eq. (2) for $p > 2|p^*|$ as

$$\Psi_{\mathbf{p}} = -\frac{\gamma\beta}{V} g_\varepsilon(\mathbf{p}) \sum_{\mathbf{p}} \frac{\Psi_{\mathbf{p}'}}{\alpha(p')^2 + 1}. \tag{3}$$

Assuming that Eq. (3) adequately describes the quasi-local states in the entire range of p, we obtain

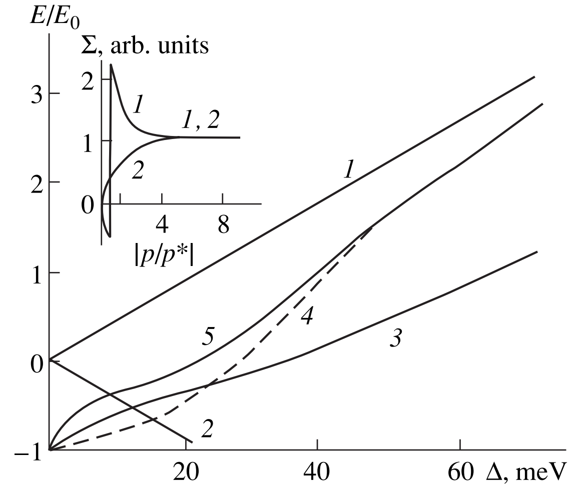

Fig. 1. Positions of extrema of (*1*) ε_{+p} and (*2*) ε_{-p} valence bands and the impurity level E (*3*) calculated in the zero-range potential approximation, (*4*) computed for a Coulomb potential, and (*5*) calculated by Eqs. (5) and (6) in relation to the splitting of the valence-band top Δ. The inset shows the dependence of the sum appearing in Eq. (2) on the value of $|p/p^*|$ for the cases where the level E is located (*1*) in the continuum and (*2*) in the band gap.

$$[1 + \lambda(E)] \sum_{\mathbf{p}'} \frac{\Psi_{\mathbf{p}}}{\alpha p^2 + 1} = 0,$$
$$\lambda(E) = \frac{\gamma\beta}{V} \sum_{\mathbf{p}} \frac{g_\varepsilon(\mathbf{p})}{\alpha p^2 + 1}. \tag{4}$$

The matrix λ given by Eq. (4) is diagonal, and the energy E and the broadening Γ of the spin-degenerate quasi-local states can be found from the equation

$$1 + \lambda_+(E) = 0, \tag{5}$$

where the diagonal elements $\lambda_\pm(\varepsilon)$ of the matrix $\lambda(\varepsilon)$ have the form

$$\lambda_\pm(\varepsilon) = \frac{\gamma\beta}{V} \times \sum_{\mathbf{p}} \frac{\gamma_1 p^2/2m \pm P_2(p_z/p)\gamma p^2/m \pm \Delta/2 - \varepsilon}{(\varepsilon_{+p} - \varepsilon)(\varepsilon_{-p} - \varepsilon)(\alpha p^2 + 1)}. \tag{6}$$

Here, γ_1 and $\gamma \cong \gamma_{2,3}$ are the Luttinger parameters, m is the free-electron mass, and $P_2(p_z/p) = P_2(x) = (3x^2 - 1)/2$. For $p = 0$, the splitting of the valence-band top $\Delta = \mu X$, where $\mu = 4$ and 6 meV/kbar for the stress applied in [111] and [001] directions, respectively. The z-axis coincides with the direction of the applied stress. The dispersion relations for the $\varepsilon_{\pm p}$ valence bands split

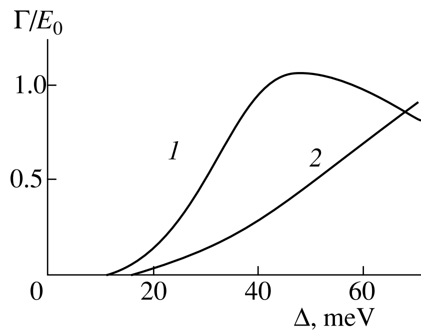

Fig. 2. Broadening Γ of the level E versus valence-band splitting Δ calculated by Eqs. (5) and (6) for (*1*) $\alpha = 0.25\gamma/m_0E_0$ and (*2*) $\alpha = 0$ (zero-range potential approximation).

by the stress have the form

$$\varepsilon_{\pm p} = \frac{\gamma_1 p^2}{2m} \pm \sqrt{\left(\frac{\gamma p^2}{m}\right)^2 - \frac{\gamma p^2}{m}\Delta P_2\left(\frac{p_z}{p}\right) + \left(\frac{\Delta}{2}\right)^2}. \quad (7)$$

The procedure for solving Eq. (5) was reported elsewhere [9]. The equation $1 + \lambda_-(\varepsilon) = 0$ determines the energy position of the lowest localized impurity level and will be omitted in the present discussion.

With the known positions of the quasi-local states of Ga in Ge ($E_0 = -11.5$ meV for $\Delta = 0$ and $E_1 \simeq 4.8$ meV for $\Delta \approx 50$ meV [6]), the parameters α and β can be calculated. We obtain $\alpha = 0.25\ \gamma/m_0E_0$. We did not calculate β, because this parameter did not appear in the final equations. For $\alpha = 0$, Eq. (5) corresponds to the zero-range potential approximation.

RESULTS AND DISCUSSION

Figure 1 shows the calculated positions of the quasi-local impurity state in relation to Δ. Also shown are the dependences calculated by Eq. (5) within the zero-range potential approximation for $\alpha = 0$ (curve *3*) and the dependence for a Coulomb impurity center (curve *4*), which was obtained by a smooth connection of three points corresponding to (1) the depth of the level at $\Delta = 0$, (2) the position of the level when it joins the continuum ($\Delta \approx 16$ meV [9]), and (3) the position of the quasi-local level at $\Delta \approx 50$ meV [6]. The position of the second point was estimated rather roughly, since the splitting of the impurity level by deformation was determined for $\Delta \ll E$ [7], and, even in this case, the accuracy of the obtained estimates is difficult to evaluate because of their strong dependence on the form of chosen test wave functions. It should be noted that our result (Fig. 1, curve *5*) is in a good qualitative agreement with the result obtained for a Coulomb impurity center (Fig. 1, curve *4*) in the limit of high stress (splitting Δ): the energy difference between the quasi-local impurity state and the bottom of the ε_{+p} band flattens out [6]. In the range of $0 \le \Delta \le 50$ meV, curve *5* deviates from curve *4*, since curve *4* was drawn rather roughly (see also the above remark concerning the second point), and the solution to Eq. (3) obtained for $p > 2|p^*|$ was extended to the range of p from 0 to $2|p^*|$. Nevertheless, the calculated curve qualitatively and semi-quantitatively represents the dependence of the energy position of the quasi-local impurity state on Δ. The computed dependence of the broadening of the quasi-local impurity state on Δ differs fundamentally from that calculated in the zero-range potential approximation: as Δ rises, the broadening passes through a maximum and then decreases (see Fig. 2). This suggests that the quasi-local impurity state tends to localize as the stress increases. This is physically clear, because, as the level splitting (stress) increases, the energy difference between the quasi-local impurity state and the lower valence band ε_{-p} increases, and the contribution of this band to the formation of the quasi-local impurity state decreases as $1/(\varepsilon_{+p} - E)$.

The wave function of the quasi-local impurity state described by Eq. (3) can be used in theoretical studies of various transient and optical phenomena in uniaxially stressed materials.

ACKNOWLEDGMENTS

This study was supported by the Ministry of Education and Science and by the Foundation for Basic Research of Ukraine, project no. 2.4/970.

REFERENCES

1. I. V. Altukhov, M. S. Kagan, and V. P. Sinis, Pis'ma Zh. Éksp. Teor. Fiz. **47**, 136 (1988) [JETP Lett. **47**, 164 (1988)].
2. V. M. Bondar', L. E. Vorob'ev, A. T. Dalakyan, *et al.*, Pis'ma Zh. Éksp. Teor. Fiz. **70**, 257 (1999) [JETP Lett. **70**, 265 (1999)].
3. I. V. Altukhov, M. S. Kagan, K. A. Korolev, *et al.*, in *Proceedings of the Conference "Nanophotonica"* (IFM Ross. Akad. Nauk, Nizhni Novgorod, 1999), p. 56.
4. I. V. Altukhov, M. S. Kagan, K. A. Korolev, and V. P. Sinis, Pis'ma Zh. Éksp. Teor. Fiz. **59**, 455 (1994) [JETP Lett. **59**, 476 (1994)].
5. A. T. Dalakyan, V. N. Tulupenko, D. A. Firsov, and V. M. Bondar', Pis'ma Zh. Éksp. Teor. Fiz. **69**, 638 (1999) [JETP Lett. **69**, 676 (1999)].
6. I. V. Altukhov, M. S. Kagan, K. A. Korolev, *et al.*, Zh. Éksp. Teor. Fiz. **115**, 89 (1999) [JETP **88**, 51 (1999)].
7. G. L. Bir and G. E. Pikus, *Symmetry and Strain-Induced Effects in Semiconductors* (Nauka, Moscow, 1972; Wiley, New York, 1975).
8. E. V. Bakhanova and F. T. Vas'ko, Fiz. Tverd. Tela (Leningrad) **32**, 86 (1990) [Sov. Phys. Solid State **32**, 47 (1990)].
9. M. A. Odnoblyudov, A. A. Pakhomov, V. M. Chistyakov, and I. N. Yassievich, Fiz. Tekh. Poluprovodn. (St. Petersburg) **31**, 1180 (1997) [Semiconductors **31**, 1014 (1997)].
10. A. A. Abramov, F. T. Vas'ko, V. N. Tulupenko, and D. A. Firsov, Fiz. Tekh. Poluprovodn. (St. Petersburg) **33**, 691 (1999) [Semiconductors **33**, 640 (1999)].

Translated by N. Izyumskaya

Semiconductors, Vol. 35, No. 2, 2001, pp. 135–137. Translated from Fizika i Tekhnika Poluprovodnikov, Vol. 35, No. 2, 2001, pp. 139–142.
Original Russian Text Copyright © 2001 by Klimenko, Komar', Migal', Nalivaĭko.

ELECTRONIC AND OPTICAL PROPERTIES OF SEMICONDUCTORS

The Effect of Stress Fields Produced by Growth Defects on the Dielectric Photoresponse of $Cd_{1-x}Zn_xTe$ Crystals

I. A. Klimenko*, V. K. Komar', V. P. Migal'*, and D. P. Nalivaĭko****

** KhAI State Aerospace University, Kharkov, 61070 Ukraine*

*** Institute of Single Crystals, National Academy of Sciences of Ukraine, pr. Lenina 60, Kharkov, 61001 Ukraine*

Submitted June 13, 2000; accepted for publication June 23, 2000

Abstract—It was demonstrated that plots of the imaginary part vs. the real part of the complex dielectric constant $\varepsilon^*(\lambda)$ in relation to a wavelength for $Cd_{1-x}Zn_xTe$ crystals grown from the melt show a series of special features that were not observed in the plots for other II–VI compounds. These features were found to be related to a variety of growth defects and to the considerable influence of electric and elastic-stress fields produced by these defects on the dielectric properties of the crystals. © *2001 MAIK "Nauka/Interperiodica".*

The influence of elastic-stress fields produced by two-dimensional (2D) structural defects on the photodielectric properties of ZnSe crystals is best reflected in the spectral dependences of the real part of the dielectric constant ε' and in the dielectric-loss factor ε'' represented in a complex plane as ε''–ε' plots in relation to a wavelength λ [1]. It was found that one band in the photosensitivity spectrum may correspond to several arc-shaped portions of the ε''–ε' plot in relation to λ, which reflect contributions from different groups of relaxators with close relaxation times τ to the dielectric photoresponse [2]. $Cd_{1-x}Zn_xTe$ crystals grown from the melt are promising high-resistivity semiconductor materials for gamma-ray spectroscopy. These crystals usually contain growth defects of various types, which strongly affect their transport properties (the mobility and lifetime of charge carriers) [3]. However, because of the high resistivity of the materials, it is difficult to reveal and identify such defects as well as to determine their influence on the generation, recombination, and transport of nonequilibrium charge carriers by methods commonly used in semiconductor research. In this study, we applied dielectric methods to reveal and study growth defects in $Cd_{1-x}Zn_xTe$ crystals.

$Cd_{1-x}Zn_xTe$ (x = 0.05–0.2) crystals were grown from the melt at a high pressure of an inert gas (up to 100 atm) by a vertical-solidification technique under various conditions. The shape of the solid/liquid interface was determined from the shape of a curve of equal Zn concentration. Inhomogeneities and growth defects were studied by infrared microscopy and the shadow method. Residual stresses produced by the growth defects in the samples were determined by the photoelasticity method. Samples for study were $11 \times 11 \times 2$ mm and $5 \times 5 \times 2$ mm in dimensions. In–Ga or Au contacts were formed at the opposite faces of the samples. Resistivity was measured by the four-point-probe technique. The dielectric constant ε' and the dielectric-loss factor ε'' were measured in the frequency range $f = 10^2$–10^7 Hz by the capacitance method.

It was found that the growth conditions have a strong impact on the shape of the solid/liquid interface and are responsible for a variety of types of growth defects. Therefore, we divided all the samples into two groups. The first group included the crystals that were grown under conditions providing the smallest curvature of the solid/liquid interface and contain only comparatively small voids and inclusions as well as few 2D structural defects (twins, etc.). Investigations by the shadow and photoelasticity methods revealed that these crystals are optically homogeneous. In the crystals grown under conditions providing a larger curvature of the solid/liquid interface, we observed Te and C precipitates and tubular and spherical pores as well as a variety of 2D defects (intercrystallite boundaries decorated with impurities, twins, slip bands) and composition fluctuations. The growth defects producing nonuniform electric and elastic-stress fields in piezoelectric crystals are characteristic of group II samples. Their resistivity $\rho < 10^{10}$ Ω cm.

The frequency dependences of ε' and ε'' measured under irradiation with light in the photosensitivity range showed a dispersion region of a relaxation type. Analysis of these dependences represented in the complex plane (with the use of the Cole–Cole plots) shows that the dispersion region is most pronounced in the dependences of group II samples. This region is characterized by a continuous distribution of relaxation times; the decrease in most probable relaxation time with increasing photoexcitation intensity is inherent in this distribution. Such frequency dependences of ε' and ε'' are also characteristic of $ZnS_{1-x}Se_x$ crystals [4].

1063-7826/01/3502-0135$21.00 © 2001 MAIK "Nauka/Interperiodica"

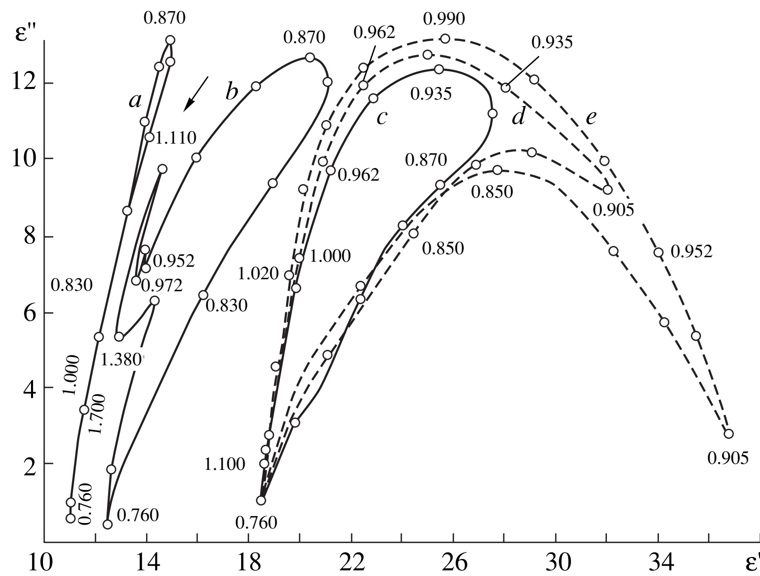

Fig. 1. ε" versus ε' in relation to λ for (*a*) group I and (*b*–*e*) group II samples; $f = 10^3$ Hz, $T = 293$ K. Numbers on the plots represent the wavelengths expressed in μm.

As compared with previously studied ZnSe crystals, the dielectric photoresponses of the $Cd_{1-x}Zn_xTe$ samples exhibit a series of special features. First of all, the $Cd_{1-x}Zn_xTe$ crystals show a wider variety of types of ε"–ε' plots in relation to λ (see Fig. 1). For example, the plots having the shape of a straight-line segment are characteristic of group I samples having the highest resistivity. As the intensity increases, a loop appears at one end of the straight-line segment (Fig. 1, curve *a*), which indicates that the ε' and ε" spectra become different. The plots for group II samples consist of arclike portions. Similar plots were observed previously for ZnSe crystals [1]. The number of arcs, the extent to which the arcs are pronounced, and the plot area were found to correlate with the concentration of the growth defects that produce residual stresses. It should be noted that the ε"–ε' plots in relation to λ for different crystals are dissimilar. Group II samples that are most optically homogeneous are characterized by fewer arcs and smaller plot areas.

The ε"–ε' plots in relation to λ for other group II samples are more complex. First, the plots for several crystals seem to be composed of separate plots, which obviously reflect the contributions from isolated complex centers of photosensitivity (see Fig. 1, an arrow near curve *b*). Well reproducible plots consisting of several such separate plots were observed. As a rule, the bands in the ε'(λ) and ε"(λ) spectra corresponding to these separate portions of the plots are virtually identical. Second, for the most photosensitive $Cd_{1-x}Zn_xTe$ samples, the increase in illumination intensity not only affects the increments of ε' and ε" under illumination, which is characteristic of ZnSe, as an example, but also considerably changes the plot shape (see Fig. 1, curves *c*–*e*). As the illumination intensity increases, ε' rises, and ε" passes through a maximum.

It is should also be noted that the shape of the plot (number of arcs, area, ranges of increments of ε' and ε", presence of separate plots, etc.) depends on the size and coordinates of the optical probe. This suggests that the revealed special features of the ε"–ε' plots are related to an intricate nonuniform distribution of the growth defects producing overlapping elastic-stress fields. To verify this presumption, we measured ε' and ε" under irradiation at a wavelength close to the intrinsic maximum in a scanning mode using an optical probe 100 μm in width. In fact, the obtained dependences of ε' and ε" on coordinate x show a series of local extrema. The number and the distribution of these extrema are characteristic features of each crystal (Fig. 2, curves *1*, *2*). We also found that, as the illumination intensity increases, the ε'(x) and ε"(x) dependences change in a complicated way: some extrema rise, others decrease, and some maxima even become minima and vice versa (Fig. 2, curves *3*, *4*). It is worth noting that the level of residual stress in group II samples is higher, which is attributable to the higher density of growth defects and the overlapping of their elastic-stress fields.

All the above-listed peculiarities of the dielectric photoresponse of the $Cd_{1-x}Zn_xTe$ crystals point to an intimate relationship between the distribution of relaxators and electric and elastic-stress fields produced by the growth defects. On this assumption, we can explain the variation in the ε"–ε' plot in relation to λ from sample to sample as well as the characteristic features of the ε'(x) and ε"(x) dependences. It is reasonable to associate the extrema in the ε'(x) and ε"(x) curves with a zonal distribution of the growth defects. This is confirmed by

the results of measurements using the photoelasticity and shadow methods. The nature of the complex centers responsible for the separate plots observed for some samples (Fig. 1, curve *b*) calls for further investigations. The $\varepsilon'(x)$ and $\varepsilon''(x)$ dependences of these samples are indicative of the uniform distribution of these complex centers over the sample.

The change in the shape of the $\varepsilon''(\lambda)$ plots for group II samples with increasing illumination intensity can apparently be attributed to the fact that contributions from nonequilibrium carriers to through conductance and polarization are redistributed as the photoexcitation intensity changes. Obviously, the filling of a large-scale potential relief with nonequilibrium charge carriers in these crystals is accompanied by a self-consistent change in the distributions of electric and elastic-stress fields. The character of the changes in the $\varepsilon'(x)$ and $\varepsilon''(x)$ dependences with increasing intensity confirms this conclusion. The redistribution of the above-mentioned contributions is responsible for the revealed special features of the $\varepsilon^*(x)$ plots, whose character is determined by the predominant type and concentration of the growth defects. We may presume that, at high concentrations of nonequilibrium charge carriers, it is elastic-stress fields that are induced by the growth defects, which produce large-scale potential fluctuations in piezoelectric crystals, which have the primary effect on the transport properties and make possible the preparation of crystals that are of sufficiently high quality for the fabrication of gamma-ray detectors.

Thus, the correlation between the electric and elastic-stress fields produced by growth defects and composition fluctuations is responsible for the special features of the dielectric relaxation in the $Cd_{1-x}Zn_xTe$ crystals. Each crystal has a unique and intricate distribution of these defects over the volume. As a result, the ε''–ε' plots in relation to λ for different samples are dissimilar, which allows us to identify the crystals on the basis of these plots. The character of the growth-defect distribution manifests itself in the $\varepsilon'(x)$ and $\varepsilon''(x)$ dependences, which is of particular importance for crystals opaque to visible light. In addition, by analyzing the changes in the $\varepsilon'(x)$ and $\varepsilon''(x)$ plots with increasing photoexcitation intensity, we can identify some of the growth-defect types. Based on the results obtained, we developed a method for identifying growth defects and diagnosing the crystal quality.

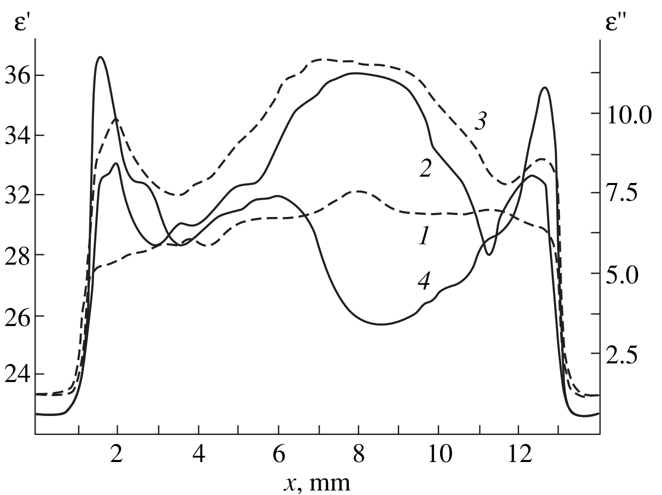

Fig. 2. Dependences of (*1*, *3*) ε' and (*2*, *4*) ε'' on *x* for group II samples; $f = 10^3$ Hz and $T = 293$ K.

REFERENCES

1. Yu. A. Zagoruĭko, V. K. Komar', V. P. Migal', and O. N. Chugaĭ, Fiz. Tekh. Poluprovodn. (St. Petersburg) **29** (6), 1065 (1995) [Semiconductors **29**, 552 (1995)].
2. Yu. A. Zagoruĭko, V. K. Komar', V. P. Migal', and O. N. Chugaĭ, Funkts. Mater. **1** (2), 135 (1994).
3. V. Komar, A. Gektin, D. Nalivaiko, *et al.*, in *Proceedings of the 11th International Workshop on Room Temperature Semiconductor X- and Gamma-ray Detectors and Associated Electronics, Vienna, 1999*, p. 8.
4. V. P. Migal', A. L. Rvachev, and O. N. Chugaĭ, Fiz. Tekh. Poluprovodn. (Leningrad) **19** (8), 1517 (1985) [Sov. Phys. Semicond. **19**, 935 (1985)].

Translated by N. Izyumskaya

Semiconductors, Vol. 35, No. 2, 2001, pp. 138–143. Translated from Fizika i Tekhnika Poluprovodnikov, Vol. 35, No. 2, 2001, pp. 143–148.
Original Russian Text Copyright © 2001 by Sokolov, Starovoĭtova.

Nickel Impurity Excitons and Photoinduced Lattice Distortion in $ZnSe_{1-y}S_y$:Ni and $Zn_{1-x}Cd_xSe$:Ni Solid Solutions

V. I. Sokolov* and V. N. Starovoĭtova

Institute of Metal Physics, Ural Division, Russian Academy of Sciences, ul. S. Kovalevskoĭ 18, Yekaterinburg, 620219 Russia

** e-mail: visokolov@imp.uran.ru*

Submitted June 20, 2000; accepted for publication June 23, 2000

Abstract—A heavy dependence of the zero-phonon line of the donor Ni excitons and of a series of its phonon replicas on the composition of $ZnSe_{1-y}S_y$:Ni and $Zn_{1-x}Cd_xSe$:Ni solid solutions was studied. A model of nonradiative recombination of impurity excitons with allowance made for an intermediate virtual state $\{d^8\}$ is discussed in detail. It is shown that this state depends on the lattice distortion induced by the Ni^{3+} impurity center whose charge is positive in reference to the lattice. © *2001 MAIK "Nauka/Interperiodica".*

1. INTRODUCTION

The Ni impurity excitons of the donor and acceptor types in II–VI semiconductors have been studied for a long time [1]. A heavy dependence on various factors is a characteristic property of the hydrogen-like excitations of the Ni impurity. The impurity excitons are reasonably easy to observe at the liquid-helium temperature and are almost not observed at all at the liquid-nitrogen temperature [2, 3]. For the ZnS_ySe_{1-y}:Ni solid solutions with $y \le 0.01$, the donor Ni $[d^7e]$ excitons are detected with ease, whereas, for $y \ge 0.1$, they are not detected at all [4]. Such behavior of impurity excitons is in harsh contrast with the properties of free excitons that are observed in ZnS_ySe_{1-y}:Ni solid solutions within a wide range of compositions at the liquid-nitrogen temperature. This property of Ni impurity excitons has not yet been described in detail theoretically. Solid solutions are ideal for further experimental study of the impurity excitons. Large-scale potential fluctuations affecting the hydrogen-like states of impurity excitons are characteristic of these solid solutions. The influence of large-scale fluctuations on free excitons has been widely studied [5]. However, local perturbations (clusters involving the impurity center and a variation in the lattice constant according to the Verdet law, which influences the d electrons in the impurity center) are characteristic of solid solutions. In our opinion, a comparative combined study of two types of hydrogen-like excitations (of free excitons and Ni impurity excitons in solid solutions doped with Ni) constitutes a productive approach to studying the properties of impurity excitons that are extremely difficult to study both theoretically and experimentally.

A model of nonradiative recombination $[d^7e] \longrightarrow (d^8)$ as a result of tunneling transition has been suggested previously [2]. A similar idea was discussed in [6]. In [4], a model of nonradiative recombination $[d^7e] \longrightarrow (d^8)$ was supplemented with the idea of the intermediate state $\{d^8\}$, although the meaning of this state remained not quite clear. In general, the tunneling model [2] is not quite consistent with adiabatic approximation, because we have to assume that the ions nearest to the impurity center (i.e., the heavy particles) are involved in tunneling. It is important for a correct understanding of the nonradiative-recombination model to take into account that the illumination-induced formation of impurity excitons is accompanied with the lattice distortion in the vicinity of the impurity center because of changes in the charge state. The lattice relaxation in the vicinity of the Ni^+ or Ni^{3+} impurity centers charged with respect to the lattice has been evaluated recently [7, 8]. These calculations show that, in the vicinity of a charged impurity, there occurs a substantial change in the positions of equilibrium for the ions in the first and second coordination shells. These results give a better insight into the meaning of intermediate state $\{d^8\}$; thus, the model of nonradiative recombination becomes clearer and consistent in terms of adiabatic approximation.

The objective of this study was to describe in more detail the intermediate state $\{d^8\}$ with allowance made for both new experimental data on the impurity excitons in solid solutions and for the results of simulations.

2. EXPERIMENTAL

We studied the samples cut from the single-crystal ZnS_ySe_{1-y}:Ni and $Zn_{1-x}Cd_xSe$:Ni ingots with different compositions (ZnSe, $ZnS_{0.26}Se_{0.74}$:Ni, $ZnS_{0.13}Se_{0.87}$:Ni, $ZnS_{0.0005}Se_{0.9995}$:Ni, $ZnS_{0.026}Se_{0.974}$:Ni, and $Zn_{0.99}Cd_{0.01}Se$:Ni) grown from the melt under a pres-

sure of inert gas. In order to determine x and y in the solid solutions, we detected the free-exciton line in the reflection spectra of all the above compounds at the liquid-helium and liquid-nitrogen temperatures. The composition was determined from the dependence of E_g on x (or, similarly, on y) as

$$E_g(x) = E_g(0) + ax - bx(1-x). \quad (1)$$

The constant b characterizing the degree of perfection of the solid solution [9] was taken equal to 0.6 for $Zn_{1-x}Cd_xSe$:Ni [9] and 0.67 for ZnS_ySe_{1-y}:Ni [10] at the temperatures $T = 4.2$ and 77 K. Free excitons were observed in the reflection spectra for all compositions of the compounds. The electroreflection spectra were measured at $T = 4.2$ K in the photon-energy range of $\hbar\omega = 2.60$–2.90 eV. The prepared samples had the resistivity of $\rho \approx 10^9$–10^{11} Ω cm. The applied fields were as high as ~25 kV/cm. In order to optimize the transmission in the vicinity of the zero-phonon line of the donor exciton Ni $[d^7e]$ and its phonon replicas, we chose the thickness of the samples to be ~500 μm.

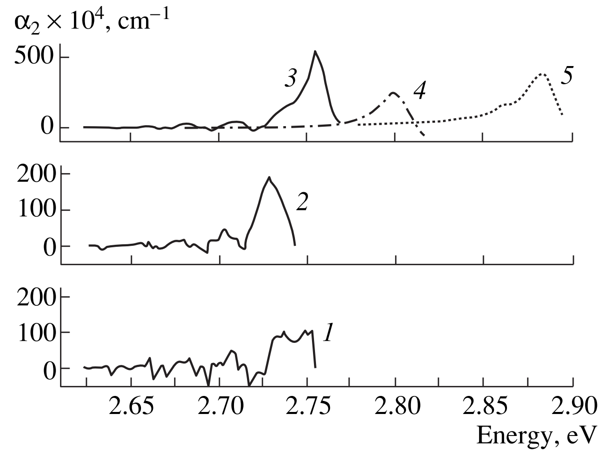

Fig. 1. Amplitude spectrum of the electroabsorption second harmonic α_2 measured at $T = 4.2$ K. The solid-solution compositions and the amplitudes of an ac electric field were (*1*) ZnSe:Ni and 16.6 kV/cm; (*2*) $Zn_{0.99}Cd_{0.01}Se$:Ni and 18.5 kV/cm; (*3*) $ZnS_{0.0005}Se_{0.9995}$:Ni and 15 kV/cm; (*4*) $ZnS_{0.133}Se_{0.867}$:Ni and 21.4 kV/cm; and (*5*) $ZnS_{0.26}Se_{0.74}$:Ni and 15 kV/cm.

3. RESULTS AND DISCUSSION

3.1. A Model of Nonradiative Recombination via Impurity Excitons

A decrease in the intensity of the peak due to the influence of an electric field on the Ni donor exciton constitutes the most important change in the electroabsorption spectrum. This can be clearly seen in Fig. 1, where the spectra of electroabsorption α_2 for ZnSe, ZnS_ySe_{1-y}:Ni (y = 0.26, 0.13, and 0.005), and $Zn_{1-x}Cd_xSe$:Ni (x = 0.01) samples at T = 4.2 K are shown. We explain this in the following way. A Ni $[d^7e]$ donor exciton is thought of as a structure that consists of an impurity center (charged positively in reference to the lattice) and an electron circulating along a hydrogen-like orbit; it is important, that the impurity charge changes at the instant the exciton is formed. Thus, it is necessary that the impurity atom is charged in reference to the lattice for an impurity exciton to exist. The impurity-center Coulomb field causes a displacement of the nearest ions and thus distorts the lattice. The Se^{2-} ions are attracted to the positively charged Ni^{3+} center, whereas the Zn^{2+} ions are repulsed from this center. This circumstance has not been properly taken into account in analyzing the impurity-exciton properties. The lattice distortion has been simulated previously for ZnSe:Ni [7]. These calculations demonstrate that the ions in the first coordination sphere (Se^{2-}) are displaced by 0.24 Å and the ions in the second coordination shell (Zn^{2+}) are displaced by 0.017 Å. Figure 2 shows the section of an $NiSe_4Zn_{12}$ cluster by the (110) plane in order to better conceive the distortion structure.

Figure 3 shows the adiabatic potential $E(q)$ for the ground state $^3T_1$ of the Ni impurity that is neutral in reference to the lattice (Ni^{2-}, the d^8 configuration). For the sake of simplicity, the excited states of the d^8 configuration [1, 2, 4] are not shown. Adiabatic potential for the $[d^7e]$ state of the donor exciton is also shown. The adiabatic potential specifies the dependence of the energy of electrons in the d shell on the displacement of the nearest neighbors of the impurity atom. For the $[d^7e]$ state, the adiabatic-potential parameters (the steepness of the parabola branches and the coordinate q_A of the parabola's minimum) characterize only the d^7 configuration, because the charge carrier located in a hydrogen-like orbit barely responds to the displacements of its nearest Ni neighbors (i.e., the ions in the first and second coordination shells shown in Fig. 2), because this orbit has a large radius. Thus, the adiabatic potential for the donor exciton $[d^7e]$ specifies the d^7 configuration of the Ni^{3+} ion that is charged in reference to the lattice.

In terms of adiabatic approximation, the generally accepted conventional description of nonradiative recombination amounts to the fact that the configuration curves for the ground and excited states intersect at the point C. The system in the excited state ascends along the configuration curve to the point C as the temperature increases. At the point C, a transition to the ground-state configuration curve occurs without changes in the configurational coordinate q_C in accordance with adiabatic approximation. After that, a descent along the configuration curve of the ground state occurs accompanied by phonon emission. Basically, a tunneling transition is possible from the excitation-state curve to the ground-state curve without reaching the point C; therefore, nonradiative transition

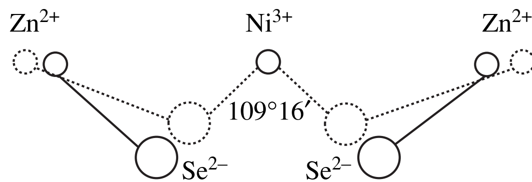

Fig. 2. Schematic representation of the (110) plane of a $NiSe_4Zn_{12}$ cluster in a ZnSe:Ni crystal. Positions of displaced atoms and the Ni^{3+}–Se^{2-} and Zn^{2+}–Se^{2-} bonds after the charge state of the Ni impurity atoms has been changed as $Ni^{2+} \longrightarrow Ni^{3+}$ are shown by the dashed lines.

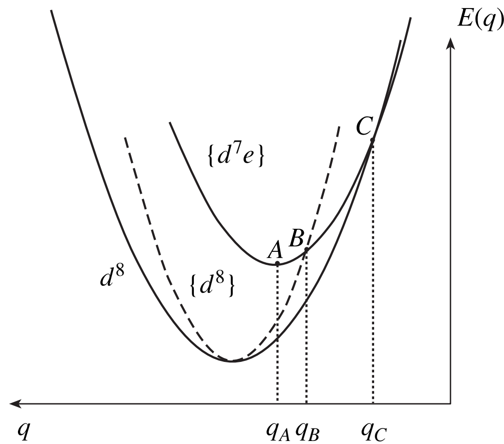

Fig. 3. Adiabatic potentials for the ground state of the d^8 configuration, the intermediate virtual state $\{d^8\}$, and the $[d^7e]$ state of Ni impurity exciton.

may occur at a lower temperature [11]. This idea has been used to describe the tunneling annihilation of the impurity excitons with the aim of gaining insight into the basic possibility of intense nonradiative recombination of the impurity excitons at temperatures of 30–40 K as was first observed in CdS:Ni [2] and then in ZnS:Ni [3].

However, the situation under consideration is more complicated. A system in the excited state consists of a localized portion (the d^7 configuration of a Ni^{3+} ion charged relative to the lattice) and a delocalized portion (an electron at the hydrogen-like orbit). The system in the ground state is represented by the d^8 configuration of the same impurity center in the state of Ni^{2+}, which is neutral in reference to the lattice. The tunneling $[d^7e] \longrightarrow d^8$ transition does not make sense because $[d^7e]$ and d^8 represent different charge states of the same center. We should consider a situation when an electron can return to the d shell without changing the configurational coordinate q, but to do so the lattice should rearrange itself in a certain manner, similar to that occurring at point C. Thus, the return of an electron to the d shell should not be accompanied with a change in the configurational coordinate q. After the return of the electron, the d shell happens to be in one of the d^8-configuration states. Furthermore, the Se^{2-} and Zn^{2+} lattice ions remain displaced; their positions correspond to those of charged impurities, as is shown by the dashed lines in Fig. 2. Therefore, it is clear that the adiabatic potentials for the energy terms of the d^8 configuration differ from those for a neutral center before ionization. Such an adiabatic potential $\{d^8\}$ for the ground state is shown by the dashed line in Fig. 3.

We can now interpret in the following way the high efficiency of nonradiative recombination of impurity excitons and its increase as the temperature is raised or the solid-solution composition is varied (with an increase in x and y). The origination of an impurity exciton is accompanied with a change in the d-shell configuration as $d^8 \longrightarrow [d^7e]$ for a donor exciton ($d^8 \longrightarrow [d^9h]$ for an acceptor exciton) and with a displacement of the ions in the nearest surroundings in accordance with the change in the impurity-center charge. The configuration curves $\{d^8\}$ exist virtually and depend on the extent of lattice distortion governed by a number of factors that are different for dissimilar II–VI compounds; these factors are the ionicity of the crystal, hybridization of the d states with the band states, the elastic lattice constants, and so on. Thus, all the $\{d^8\}$ curves for the ground and excited states will differ from the corresponding curves for the d^8 configuration. Therefore, we may assume that one or several virtual curves intersect the $[d^7e]$ curve in the vicinity of the minimum (for example, at the point B for the curve corresponding to the $[d^7e]$ in Fig. 3). As a result of fluctuations existing even at the liquid-helium temperature, the $[d^7e]$ system may ascend along the configuration curve to the vicinity of the intersection point. It is at this instant of complete readiness of the lattice in the region of the nearest surroundings of the impurity center that the electron in the hydrogen-like state (or hole for an acceptor center) returns to the d shell in accordance with adiabatic approximation. The Ni impurity atoms become neutral, the lattice distortion gradually relax, and the $\{d^8\}$ curves transform into the conventional adiabatic potential curves for the d^8 configuration. Simultaneously, a descent along the adiabatic-potential curve for the d^8 configuration occurs owing to emission of phonons to the lattice. If the time needed for the transformation of the intermediate state ($\{d^8\} \longrightarrow d^8$) is shorter than the characteristic time of the descent, then this transformation occurs without changes in the energy and may be represented by a horizontal arrow in an adiabatic-potential plot (as has been done previously [4]), which may be formally perceived as tunneling. As the temperature is raised, the $[d^7e]$ system ascends along the configuration curve until the point of intersection with the $\{d^8\}$ curve is reached. As a result, the nonadiabatic terms that induce an electron transition (hole) from the hydrogen-like state to the d shell become more important, the probability of the $[d^7e] \longrightarrow \{d^8\}$ transition increases, the impurity-exciton lifetime decreases,

and the impurity-exciton line becomes unobservable. It is such a situation that takes place for the donor and acceptor Ni excitons at the liquid-nitrogen temperature in the spectra of ZnO:Ni, ZnS:Ni, ZnSe:Ni, and CdS:Ni.

The electroabsorption spectrum in ZnS_ySe_{1-y}:Ni solid solutions are observed at a temperature of 4.2 K; therefore, the $[d^7e]$ system cannot ascend along the configuration curve. As y increases, the lattice constant varies according to the Verdet law as $a = a_0 - ky$. This leads to a relative shift of the $\{d^8\}$ and $[d^7e]$ curves, so that their intersection point descends progressively closer to the minimum q_A of the configuration curve $[d^7e]$. As a result, the probability of a charge carrier returning from the hydrogen-like state to the d shell increases drastically. Thus, the model of nonradiative recombination is completely consistent with adiabatic approximation and accounts qualitatively well for the effects of temperature and disorder in the ZnS_ySe_{1-y}:Ni and $Zn_{1-x}Cd_xSe$:Ni solid solutions on the impurity-exciton line. If a d impurity features numerous intracenter states of the d^n configuration (for example, Fe^{2+}), there is a high probability that one or several adiabatic-potential curves of the $\{d^n\}$ configuration intersect the configuration curve d^{n-1} (for Fe, this is the d^5 curve); as a result, the nonradiative donor-exciton annihilation $[d^5e] \longrightarrow d^6$ occurs with high probability even at a temperature of 4.2 K [12, 13]. As far as we know, the attempts to observe the $[d^5e]$ Fe donor excitons and the $[d^5h]$ Cr acceptor excitons in ZnSe and ZnS doped with these impurities have failed, although the photoionization bands corresponding to $Fe^{2+} \longrightarrow Fe^{3+} + e$ and $Cr^{2+} \longrightarrow Cr^{1+} + h$ in ZnSe and ZnS have been observed quite clearly.

3.2. Dependence of the Shift of the Donor-Exciton Line in Solid Solutions on Their Composition

The shifts of the Ni donor-exciton lines in relation to the composition of the ZnS_ySe_{1-y}:Ni and $Zn_{1-x}Cd_xSe$:Ni solid solutions make it basically possible to observe with spectroscopic accuracy the absolute shift of the conduction-band bottom in a solid solution as a function of composition. This reasoning has been used previously [14]. In the experimental spectra for the $Zn_{1-x}Cd_xSe$:Ni ($x = 0.01$) and ZnS_ySe_{1-y}:Ni ($y = 0.026$) solid solutions, a distinct shift of the leading line of the Ni donor exciton to the lower and higher energies is observed and amounts approximately to 6 and 5 meV, respectively (Fig. 4). This corroborates the idea [14] concerning the high accuracy inherent in the determination of absolute shifts of the band edges on the basis of observations of impurity excitons. It is very important to extend the ranges of x and y in the solid solutions. Unfortunately, at present we do not have crystals at our disposal with x and y in the range of 0.03–0.1, where the impurity-exciton leading line and its phonon replicas can be still observed. For the above composition range, the leading-line shift is expected to be larger, which will make it possible to analyze quantitatively the absolute shift of the conduction-band bottom as a function of the solid-solution composition. It is of interest to determine the parameter b_c which is similar to b in formula (1) and defines a nonlinear dependence of only the conduction-band bottom E_c on the composition.

3.3. Influence of an Electric Field on the Free-Exciton Line

In solid solutions, the allowed-band tails and the tails of the density of localized states are formed owing to a random distribution of substitutional atoms over the lattice sites. The density of states decreases exponentially with distance from an allowed-band edge. The fundamental-absorption edge formed by the band-to-band transitions is also described by an exponential dependence for the photon energies smaller than the band gap E_g (the Urbach rule); i.e., we have

$$\alpha \approx \exp\{-(E_g - \hbar\omega)/\varepsilon_0\}. \quad (2)$$

If an external uniform electric field is applied to the crystal, electrons tunnel from the valence band to the band gap, so that transitions to the conduction band become possible under the influence of a photon with an energy $\hbar\omega$ smaller than E_g (the Franz–Keldysh effect). For an exponential edge of the fundamental absorption, the influence of the electric field amounts to a shift of the exponential absorption curve to lower energies by the value E dependent on an electric field and the parameter that specifies the steepness of the exponential edge. The influence of the solid-solution composition on the free-exciton line makes itself evident primarily in the absorption-line shift to the lower or higher energies (depending on the solid-solution type). For the solid solutions with small x and y [$(x, y) \approx$ 0.01–0.02], a distinct contribution caused by the influence of the electric field on the free-exciton line is observed; for solid solutions with anionic substitution, this influence is much more pronounced, which agrees qualitatively with the results of luminescence studies [5]. As x (or y) increases, the absorption line shifts to the lower energies (for ZnCdSe:Ni) or to the higher energies (for ZnSSe:Ni). This can be easily deduced from Fig. 1, where the electroabsorption spectra of the ZnSe, ZnS_ySe_{1-y}:Ni, and $Zn_{1-x}Cd_xSe$:Ni samples are shown. It is evident that, for ZnS_ySe_{1-y}:Ni, the peaks of the zero-phonon Ni donor-exciton line (2.64 eV) smooth out with increasing y; however, a large positive peak related to the influence of the electric field on the free-exciton line is retained and, what is more, becomes more pronounced. For the samples with a relatively high content of S ($ZnS_{0.13}Se_{0.87}$ and $ZnS_{0.26}Se_{0.74}$), the spectra change quite radically: only a large-magnitude positive peak shift to higher energies in accordance

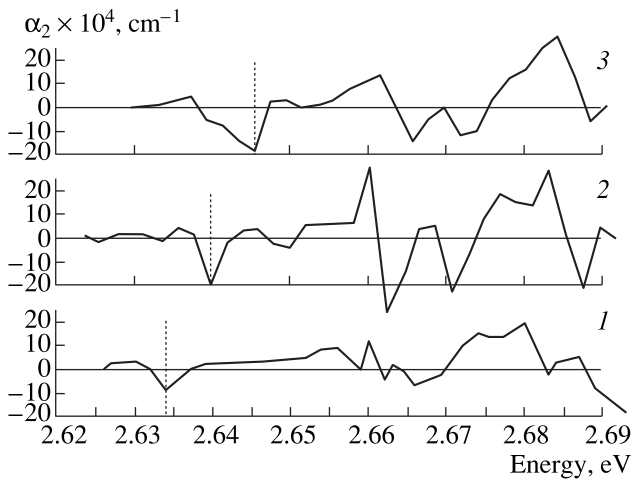

Fig. 4. Amplitude spectra of the electroabsorption second harmonic α_2 measured at $T = 4.2$ K. The solid-solution compositions and the amplitudes of an ac electric field were (*1*) $Zn_{0.99}Cd_{0.01}Se$:Ni and 15 kV/cm; (*2*) ZnSe:Ni and 16.6 kV/cm; and (*3*) $ZnS_{0.026}Se_{0.974}$:Ni and 16.6 kV/cm.

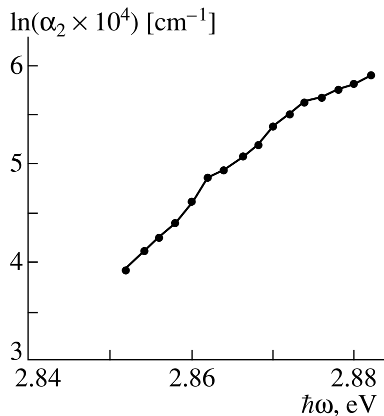

Fig. 5. Amplitude spectrum of the electroabsorption second harmonic α_2 for a $ZnS_{0.26}Se_{0.74}$ sample measured at T = 4.2 K. The amplitude of the ac electric field was 15 kV/cm.

with an increase in E_g is observed. Figure 5 shows the electroabsorption spectrum measured at $T = 4.2$ K for a sample with $y = 0.26$. This spectrum is plotted on the logarithmic scale in order to make the absorption-edge exponential shape more clear. It can be seen that the dependences of $\ln\alpha_2$ on $\hbar\omega$ fall nicely on a straight line. We can use the slope of this straight line and the Franz–Keldysh formula to approximately determine the value of ε_0 that specifies the fundamental-absorption edge. We calculated the parameter ε_0 for various solid solutions. For the solutions with $y = 0.13$ and 0.26, this parameter is about 12–15 meV at $T = 4.2$ K. At $T = 77$ K, the parameter ε_0 is larger. It should be noted that determination of the parameter ε_0 from the electroabsorption spectrum of doped crystals is difficult because, in such crystals, a significant contribution of impurity absorption exists in the tail region of the exciton line in addition to the free-exciton absorption (2). This distorts both the dc and ac components measured in the electroabsorption method [1], and, ultimately, can alter the value of the parameter ε_0 that specifies only the absorption in the region of the free-exciton exponential edge. Nevertheless, the methodical possibility of determining the value of ε_0 from the electroabsorption spectrum appears to be useful when applied to II–VI solid solutions.

4. CONCLUSION

The traditional approach to studies of the lattice distortion in the vicinity of an impurity center consists in the observation of the infrared-absorption and Raman spectra. Basically, the lattice distortion may also manifest itself in the nuclear magnetic resonance, scattering of phonons, and so on; however, as far as we know, no results of such studies have been reported. We use a new approach to studying the lattice distortion in the vicinity of a charged center. The lattice distortion occurring can be studied by observing the impurity excitons, for example, by analyzing the interaction of an impurity exciton with localized modes that emerge as a result of the lattice distortion in the vicinity of a charged center [7, 8]. Another approach suggested in this paper consists in studying the nonradiative recombination of impurity excitons. The intensities of the zero-phonon line and its vibrational replicas in the electroabsorption spectra decrease drastically as the temperature is raised or the solid-solution composition is varied both in the anionic and cationic sublattices. The lattice distortion plays an important role in the model we suggested for nonradiative recombination of Ni impurity excitons, because it is this distortion that gives rise to the $\{d^8\}$ intermediate virtual state of the Ni impurity. We note in conclusion that the photoinduced variation of the lattice distortion makes it basically possible to study the dynamics of the lattice rearrangement immediately after the impurity atom has been ionized.

REFERENCES

1. V. I. Sokolov, Fiz. Tekh. Poluprovodn. (St. Petersburg) **28**, 545 (1994) [Semiconductors **28**, 329 (1994)].
2. V. I. Sokolov and A. N. Mamedov, Pis'ma Zh. Éksp. Teor. Fiz. **43**, 187 (1986) [JETP Lett. **43**, 237 (1986)].
3. R. Heitz, A. Hoffmann, and I. Broser, Phys. Rev. B **48**, 8672 (1993).
4. V. I. Sokolov and O. V. Dolzhenkov, Fiz. Tekh. Poluprovodn. (St. Petersburg) **32**, 455 (1998) [Semiconductors **32**, 406 (1998)].
5. S. Permogorov and A. Reznitsky, J. Lumin. **52**, 201 (1992).
6. V. S. Vikhnin, Fiz. Tverd. Tela (Leningrad) **31**, 149 (1989) [Sov. Phys. Solid State **31**, 82 (1989)].

7. A. N. Kislov, V. G. Mazurenko, V. I. Sokolov, and A. N. Varaksin, Fiz. Tverd. Tela (St. Petersburg) **39**, 2147 (1997) [Phys. Solid State **39**, 1921 (1997)].
8. A. N. Kislov, V. G. Mazurenko, V. I. Sokolov, and A. N. Varaksin, Fiz. Tverd. Tela (St. Petersburg) **41**, 986 (1999) [Phys. Solid State **41**, 897 (1999)].
9. N. N. Berchenko, V. E. Krevs, and V. G. Sredin, in *Semiconductor II–VI Solid Solutions and Their Applications: Reference Book* (Voenizdat, Moscow, 1982), p. 208.
10. P. N. Newbury, K. Shahzad, J. Pertuzzello, and D. A. Cammack, J. Appl. Phys. **66**, 4950 (1989).
11. V. N. Abakumov, I. A. Merkulov, V. I. Perel', and I. N. Yassievich, Zh. Éksp. Teor. Fiz. **89**, 1472 (1985) [Sov. Phys. JETP **62**, 853 (1985)].
12. V. I. Sokolov, Acta Phys. Pol. A **90**, 245 (1996).
13. V. I. Sokolov, Proc. SPIE **2706**, 278 (1996).
14. V. I. Sokolov, Author's Abstract of Doctoral Dissertation (Sverdlovsk, 1988).

Translated by A. Spitsyn

Semiconductors, Vol. 35, No. 2, 2001, pp. 144–148. Translated from Fizika i Tekhnika Poluprovodnikov, Vol. 35, No. 2, 2001, pp. 149–154.
Original Russian Text Copyright © 2001 by Georgobiani, Gruzintsev, Aminov, Vorob'ev, Khodos.

ELECTRONIC AND OPTICAL PROPERTIES OF SEMICONDUCTORS

The Edge Ultraviolet Luminescence of GaN:Zn Films Activated in a Nitrogen Plasma

A. N. Georgobiani*, A. N. Gruzintsev, U. A. Aminov*, M. O. Vorob'ev*, and I. I. Khodos****

** Lebedev Physics Institute, Russian Academy of Sciences, Leninskiĭ pr. 53, Moscow, 117924 Russia*

*** Institute of Microelectronic Technology and Ultrahigh-Purity Materials, Russian Academy of Sciences, Chernogolovka, Moscow oblast, 142432 Russia*

e-mail: gran@ipmt-hpm.ac.ru

Submitted June 26, 2000; accepted for publication June 30, 2000

Abstract—The effect of annealing in nitrogen plasma on the photoluminescence and photoconductivity spectra, conduction type, and the surface morphology of gallium nitride films doped with zinc was studied. Emergence of intense ultraviolet edge emission peaking at a wavelength of 376 nm was observed after a high-temperature annealing in nitrogen plasma was detected. An appreciable suppression of blue donor–acceptor and excitonic photoluminescence in annealed GaN:Zn samples was observed. *© 2001 MAIK "Nauka/Interperiodica".*

INTRODUCTION

Production of high-quality *n*- and *p*-GaN films has made it possible to develop efficient light-emitting diodes and semiconductor lasers for the blue region of the spectrum [1–3]. It should be noted that, in this case, radiative recombination mainly proceeds via GaN native point defects that form deep energy levels in the band gap of the material [4, 5]. An improvement in stoichiometry and the crystallographic quality of GaN films would make it possible not only to shift the emission peak to the region of GaN ultraviolet excitonic luminescence but also to significantly increase the efficiency of electroluminescent structures. Our recent studies [6] indicated that blue emission with the peak at an energy of $\hbar\omega = 2.8$ eV has a donor–acceptor origin, with a nitrogen vacancy in one of its charge states acting as a donor. Consequently, annealing in nitrogen is required to improve the stoichiometry of gallium nitride. It can be noted that short-term high-temperature annealing in a nitrogen atmosphere does not yield the desired result owing to damage to the film surface and the evaporation of nitrogen from gallium nitride [7, 8]. Thus, it is necessary to increase the effective atomic-nitrogen pressure above the GaN film while simultaneously decreasing the annealing temperature in order to reduce the nitrogen evaporation rate. This is possible when the films are annealed in a nitrogen plasma where the fraction of atomic nitrogen is significantly larger.

Such an annealing would make it possible not only to reduce the concentration of native donor effects that are responsible for blue emission but would also affect the electrical conductivity of the film. This occurs since doping of gallium nitride with acceptor impurities (Mg or Zn) during growth results in the formation of high-resistivity material owing to the compensation phenomenon. It is only the use of electron-beam irradiation after the GaN:Mg films had been grown that made it possible [5] to obtain low-resistivity *p*-type samples. It was found [5] that annealing initially insulating GaN:Mg films at 700°C in a nitrogen ambient also results in the conversion to hole conduction. This effect was attributed [5] to the decomposition of electrically inactive Mg–H complexes formed during the film growth by the MOCVD; this decomposition leads to the formation of isolated acceptor Mg centers that give rise to effective hole conduction, which is necessary for the production of semiconductor structures.

It is of interest to study the influence of the acceptor-impurity activation on the luminescent properties of the films. Due to a lower hole mobility, radiative recombination of charge carriers in the light-emitting structure occurs in the *p*-type region. Therefore, it is the emission from the acceptor-doped film that governs the spectral characteristics of the devices. Thus, an increase in the intensity of the blue emission band of GaN:Mg films after rapid high-temperature annealing was reported previously [9]. On the other hand, a similar annealing of undoped films in a nitrogen atmosphere was shown [7] to result in a decrease in the intensity of impurity luminescence and in an increase in that of exciton luminescence. This appeared to indicate [7] that the crystallinity and morphology of the films improved in the course of annealing with a simultaneous change of their stoichiometry. In contrast, annealing under the same conditions was reported [8] to impair the morphology of the films and to result in an increase in the intensities of all emission bands.

In this study, we are interested in the effect of annealing at various temperatures in a nitrogen plasma on the activation of *p*-type conduction and on the photoluminescence (PL) and photoconductivity spectra of

doped GaN:Zn films. The use of nitrogen plasma makes it possible to change maximally the film's stoichiometry in the direction of an excess of nitrogen and to improve its crystal structure at comparatively low annealing temperatures.

EXPERIMENTAL

We used *n*-GaN:Zn films with an electron concentration of 5×10^{14} cm^{-3}, resistivity of 10^6 Ω cm, and thickness of 1 μm. The Hall effect measurements showed that the charge-carrier mobility was 100–150 cm^2/(V s) in unannealed films. The films were grown by molecular-beam epitaxy on sapphire substrates with (0001) orientation. The films were annealed for 2 h at temperatures T_a = 300–700°C in a nitrogen plasma; a setup for radical-beam epitaxy described in detail elsewhere [10] was used. The nitrogen plasma obtained in a high-frequency field was passed through a high-strength constant magnetic field in order to get rid of the ionic component of the plasma. Thus, the annealing was performed in an atmosphere of nitrogen neutral atoms (radicals).

In order to excite the PL, we used an ILGI-503 pulsed nitrogen laser with a radiation wavelength of 337.1 nm and a pulse duration of 10 ns. The spectra were analyzed using an MDR-6 double monochromator; the latter was computer controlled, which ensured a spectral resolution no worse than 1 meV for the slits used. The planar Au contacts were formed on the films before the photoconductivity measurements. We checked whether the contacts were nonrectifying by measuring the forward and reverse portions of the current–voltage characteristic. The photoconductivity was excited by the light emitted by a 100-W halogen lamp, modulated with a chopper, and passed through an MDR-12 monochromator with a large aperture ratio. During measurements, the samples were in an optical cryostat at liquid-nitrogen temperature.

We used a Jeol-2000 electron transmission microscope to study the effect of annealing on the surface crystallinity and morphology of the GaN:Zn films.

RESULTS

Figure 1 illustrates the effect of annealing in a nitrogen plasma on the PL spectra of the films. It can be seen that annealing at comparatively low temperatures (Fig. 1a) does not cause any significant changes in the emission spectrum. The blue emission band peaked at an energy of $\hbar\omega = 2.88$ eV and the exciton band peaked at $\hbar\omega = 3.48$ eV remain dominant. It is pertinent to note that we observe an insignificant increase in the intensity of the blue band and a decrease in its width up to the annealing temperature of $T_a = 600$°C. A further increase in the annealing temperature causes a drastic decrease in the intensities of both the blue and exciton emission of gallium nitride. In addition, a new ultraviolet PL

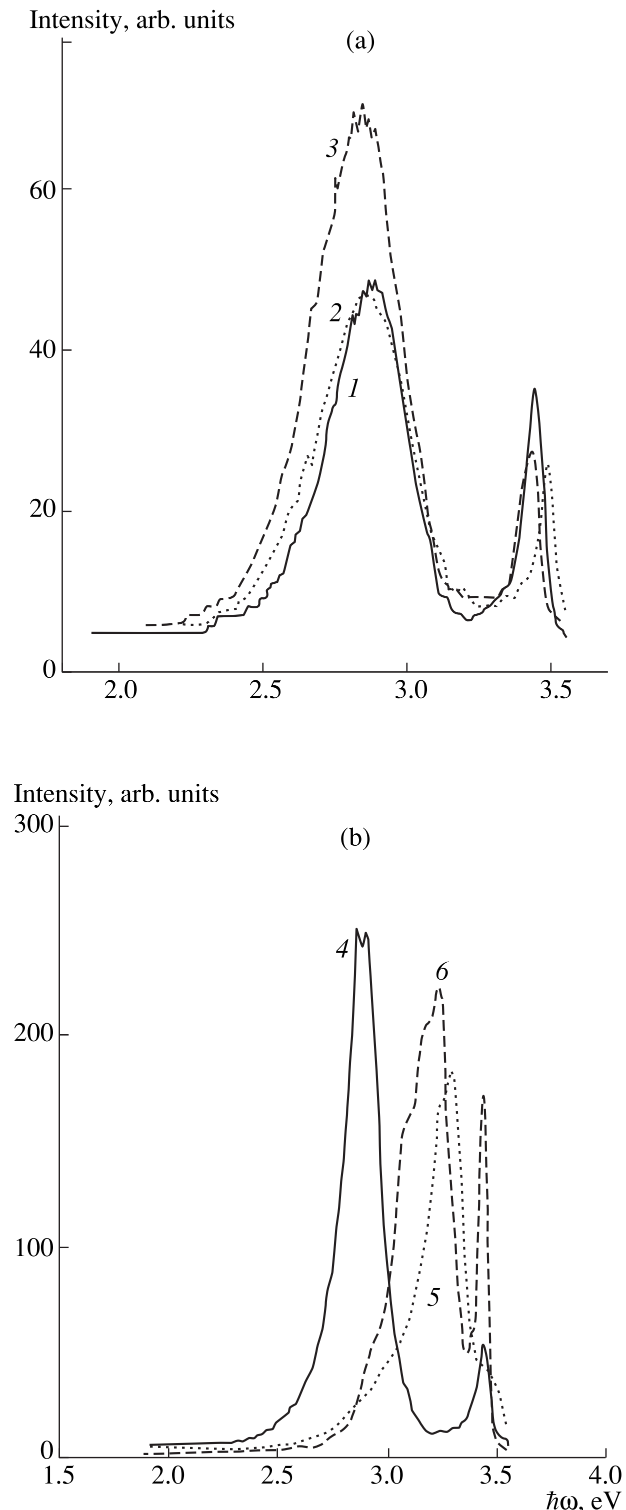

Fig. 1. Photoluminescence spectra of GaN:Zn and GaN:Mg films. (a) The spectra of (*1*) initial GaN:Zn films and the films annealed in nitrogen plasma at temperatures of (*2*) 400 and (*3*) 500°C. (b) The spectra of the GaN:Zn films annealed in the nitrogen plasma at temperatures of (*4*) 600 and (*5*) 700°C; curve *6* represents the spectrum for a GaN:Mg film. The spectra were measured at $T = 80$ K.

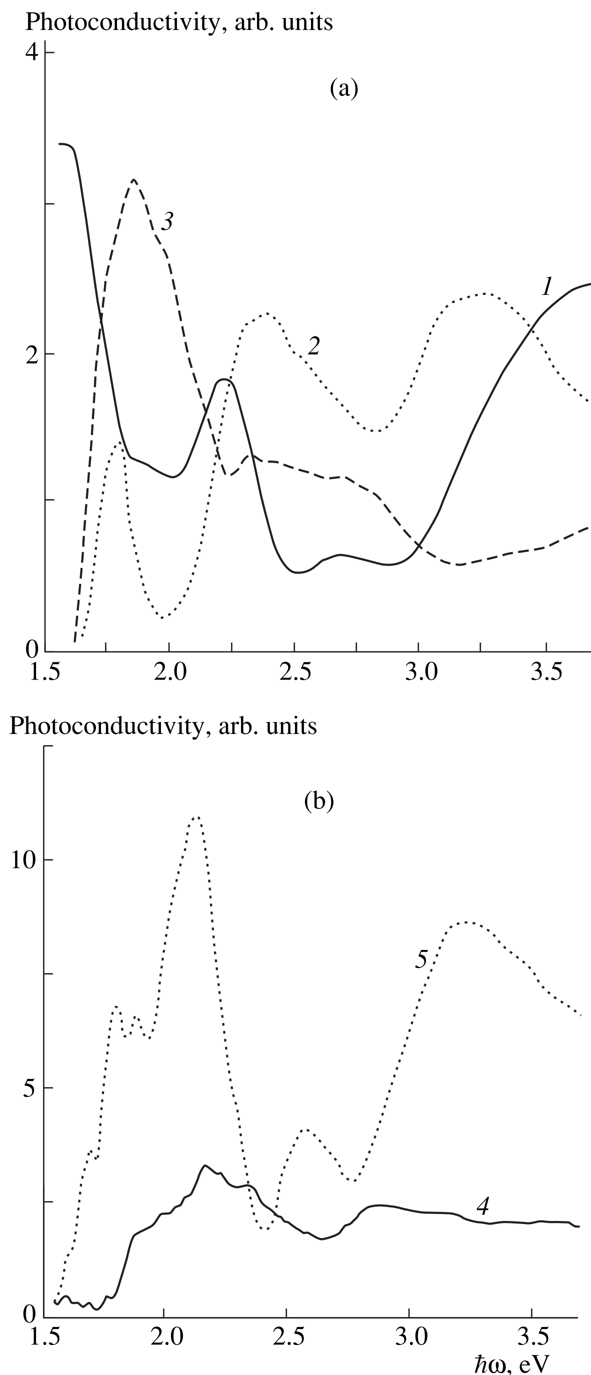

Fig. 2. Photoconductivity spectra of GaN:Zn films. (a) The spectra of (*1*) initial films and the films annealed in nitrogen plasma at (*2*) 400 and (*3*) 500°C. (b) The spectra of GaN:Zn films annealed in nitrogen plasma at (*4*) 600 and (*5*) 700°C. The spectra were measured at $T = 300$ K.

band peaking at $\hbar\omega = 3.27$ eV becomes pronounced (Fig. 1b, curve *5*). The PL spectrum of the films annealed at 700°C feature a shoulder at about $\hbar\omega = 3.45$ eV in the region of exciton emission.

Our studies indicate that annealing in nitrogen plasma significantly affects not only the luminescent but also the electrical and photoelectric properties of the films. The table lists the results of measuring the resistivity (ρ) of the films after annealing. As the annealing temperature is raised, an increase in resistivity is observed. Measurements of thermal emf showed that, in all cases, the films retained the *n*-type conduction. Consequently, acceptor centers are activated during annealing. However, in the case under consideration, we are not dealing with conventional splitting of the bonds between zinc and hydrogen [5] that would inevitably be present in the material if the films were deposited using organometallic compounds. The films we studied were obtained by molecular-beam epitaxy and did not contain excess hydrogen. Studies of impurity photoconductivity indicate that the types and concentrations of native and impurity defects in gallium nitride are affected by annealing. Even annealing at relatively low temperatures (Fig. 2a) significantly changes the photoconductivity curves. It is noteworthy that an intense impurity-photoconductivity band peaked at $\hbar\omega = 2.0$ eV emerges as a result of annealing at 400°C. Annealing at the highest temperature (700°C) induces, in addition, an increase in the photosensitivity of the films in the ultraviolet region of the spectrum at $\hbar\omega = 3.26$ eV by almost an order of magnitude (Fig. 2b, curve *5*).

The obtained spectral dependences of the PL and the photoconductivity indicate that the types and concentrations of point defects in the films change in the course of annealing in nitrogen plasma. However, annealing can also affect the surface morphology of the films. In order to clarify this phenomenon, we examined the image of the film surface obtained by scanning electron microscopy (SEM) (Fig. 3) before and after annealing. It can be seen that, before annealing, the GaN:Zn films had a smooth surface with protruding smooth grains 10–20 μm in size. Roughness of the surface amounted to ~1 nm. After high-temperature annealing in nitrogen plasma at 700°C, the film surface starts to deteriorate owing to reevaporation of the material (Fig. 3b). By examining Fig. 3b, we can deduce that the lateral sizes of the forming GaN islands range from 100 to 500 nm. Using the modulation mode and scanning the surface at various angles, we were able to find that the roughness of the annealed films amounted to 5–10 nm. Thus, annealing at a high temperature leads to the formation of a fine-grained island structure at the film surface. However, because of the relatively low annealing temperature (700°C), the increase in the roughness is significantly smaller than for a rapid high-temperature annealing [8]. In our experiments, the film surface remains optically smooth and does not lead to a decrease in the external PL efficiency, which is especially important for the development of waveguide resonator structures for semiconductor lasers.

DISCUSSION

The results we obtained indicate that annealing GaN:Zn films in nitrogen plasma exerts a much more profound effect on the type and concentration of point defects than annealing in vacuum or in nitrogen vapors does. Previously [11], only a blue-luminescence band peaked at $\hbar\omega = 2.88$ eV has been observed; the intensity of this band increased after a short-term high-temperature annealing. This emission was caused by the recombination of charge carriers within a donor–acceptor pair, in which the nitrogen vacancy acts as a donor. As for the acceptor in this pair, it can be either the zinc impurity or a native defect. It is due to the diversity of the types of acceptors and various distances between the donor and acceptor in a pair that the blue emission of gallium nitride has the shape of an inhomogeneously broadened band [5]. The width of this line and the position of the corresponding peak depend, as a rule, on the conditions of the film growth and, in our studies (Fig. 1), on the annealing temperature which affects the type and concentration of the point defects.

As the annealing temperature is raised, the donor–acceptor pairs (DAPs) decompose with the involvement of nitrogen vacancies, and their diffusion coefficient increases. Taking into account that nitrogen plasma yields the highest possible partial nitrogen pressure at the film surface, we may assume that nitrogen vacancies are filled by nitrogen atoms when these vacancies reach the surface. It is virtually only under annealing in these conditions that the gallium nitride stoichiometry can be shifted to an excess of nitrogen. The number of nitrogen vacancies starts to decrease; simultaneously, both the number of DAPs and the intensity of the blue-emission band peaking at $\hbar\omega = 2.88$ eV decrease. At the same time, a new ultraviolet band peaking at $\hbar\omega = 3.27$ eV emerges (Fig. 1b, curve *5*). Obviously, the zinc-impurity atom released after decomposition of the Zn–H and zinc–(nitrogen vacancy) DAPs (the centers responsible for blue emission) complex may be involved in formation of the corresponding emission centers.

An isolated defect (a zinc atom replacing a gallium atom) yields an acceptor level located in the vicinity of the valence-band top. Because of this, the ultraviolet edge PL band peaked at $\hbar\omega = 3.27$ eV may be caused by transitions of electrons from the conduction band to the zinc-atom acceptor level. By analogy with the wide-gap CdS compound that also had a hexagonal crystal structure, we may assume that the near-band edge PL can be caused not only by isolated acceptors but also by their complexes with native defects if the latter reside at the neighboring lattice sites [12]. Taking into account that the above level defines the emission peak and in order to exactly prove the involvement of zinc impurities in the ultraviolet emission of GaN:Zn films, we performed similar annealing in nitrogen plasma of GaN films doped with another acceptor impurity, i.e., Mg. It is clearly seen from Fig. 1b (curve *6*) that, in the latter case, the ultraviolet edge emission is prevalent in the PL spectrum as well. However, in this case, the ultraviolet-band peak has a different position (3.24 eV) and its half-width is significantly larger.

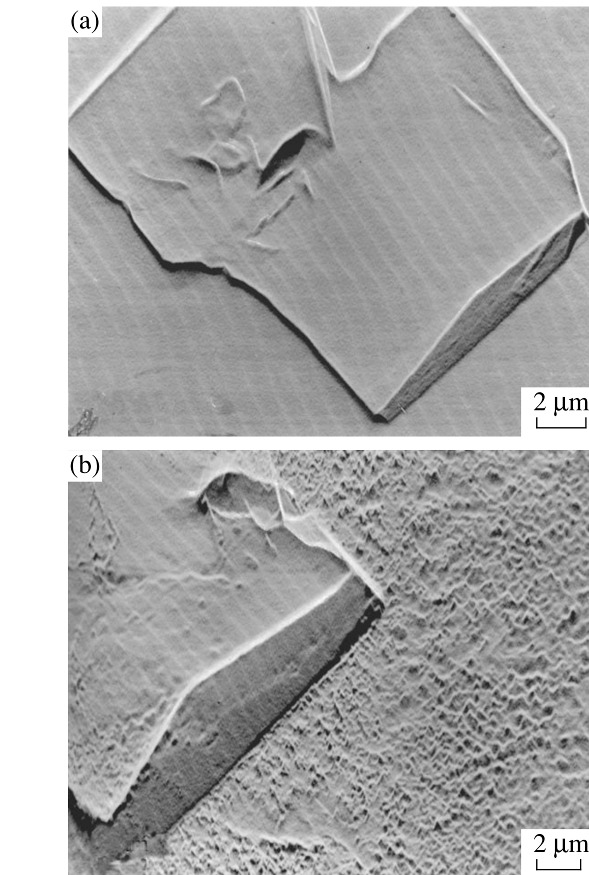

Fig. 3. A SEM image of the surface of (a) unannealed GaN:Zn films and (b) the films annealed at 700°C in nitrogen plasma. The image was obtained in the mode of detecting the secondary electrons.

Consequently, the position of the edge-ultraviolet-emission band depends on the type of introduced impurity; i.e., the acceptor level is directly involved in the electron recombination. We may note here [9] that the ultraviolet peak at 3.285 eV (at $T = 5$ K) in the edge

Dependence of resistivity of GaN:Zn films on the temperature of annealing in nitrogen plasma

Sample no.	1	2	3	4	5	6
T_a, °C	Unannealed	300	400	500	600	700
ρ, Ω cm	10^6	1.3×10^6	2×10^6	2.3×10^6	4.3×10^6	17.8×10^6

luminescence of the GaN films doped heavily with Mg to the concentration of 6×10^{19} cm^{-3} has been previously assigned to a radiative transition of electrons from the conduction band to the level of isolated Mg atom. In the case under consideration, the recombination mechanism is similar; however, the acceptor level is introduced by the zinc impurity. An interesting situation arises when the GaN films are doped with Group II acceptors. Both an increase in the doping level and activating annealing in the presence of an excess (plasma) of nitrogen suppress the blue emission at 2.88 eV and give rise to ultraviolet edge luminescence. Consequently, the optimal light-emitting diode structures based on gallium nitride should produce ultraviolet (peaked at about $\hbar\omega \approx 3.27$ eV) rather than blue emission. This ultraviolet emission is not related to the recombination of bound excitons, because the lifetime of these excitons is very short in heavily doped *p*-GaN. Thus, the intensity of the bound-exciton line at $\hbar\omega$ = 3.49 eV decreases drastically when the edge-emission intensity increases (Fig. 1b, curve *5*).

An increase in the concentration of the levels of isolated Zn acceptors in the GaN band gap as a result of high-temperature annealing in nitrogen plasma leads to the prevalence of the ultraviolet band peaked at 3.26 eV in the PL spectra (Fig. 2). This band may be related to electron transitions from acceptor levels to the conduction band. Photosensitivity in the impurity region increases as a result of annealing almost by an order of magnitude compared to that in unannealed films. It is known that GaN is used at present in detectors of ultraviolet radiation with a wavelength shorter than 350 nm. However, our studies showed that semi-insulating and insulating GaN:Zn films feature the photoconductivity bands in the visible region of the spectrum as well. Positions of the peaks for these bands correspond to the energy spacing between the relevant levels of the intrinsic and impurity defects and the conduction-band bottom. By controlling the GaN stoichiometry in the course of annealing, one can adjust the GaN photosensitivity in the impurity-related spectral region.

CONCLUSION

Thus, we showed that annealing GaN:Zn films in nitrogen plasma results not only in the acceptor activation due to dissociation of Zn–H complexes formed in the material during its growth but also in a deviation from the stoichiometry in the direction of an excess of nitrogen. Simultaneously, the number of donor–acceptor pairs that contain a nitrogen vacancy as a donor and are responsible for the blue emission band peaking at 2.88 eV in GaN:Zn decreases. The recombination of electrons directly from the conduction band to the Zn_{Ga} acceptor levels becomes prevalent; this recombination is responsible for the ultraviolet edge-luminescence band peaked at $\hbar\omega$ = 3.27 eV. It is the edge emission that governs the minimal emission wavelength of diode structures based on gallium nitride doped heavily with acceptor impurities.

It is shown that, due to the activation of acceptors as a result of annealing in nitrogen plasma, the films become more insulating and retain the *n*-type conduction (see table). At the same time, the photosensitivity of the films in the impurity-related region of the spectrum increases. It is demonstrated for the first time that GaN is photosensitive not only in the ultraviolet but also in the visible regions of the spectrum owing to transitions of electrons from local levels to the conduction band.

We found that activating annealing in the nitrogen plasma even at a temperature of 700°C impairs the surface morphology to a much lesser extent than does a short-term high-temperature annealing [8]. The emerging microirregularities with sizes of 1–10 nm leave the film surface optically smooth, which is important for the development of a number of light-emitting structures.

REFERENCES

1. S. Nakamura, S. Nagahama, N. Iwasa, *et al.*, Appl. Phys. Lett. **68**, 2105 (1996).
2. S. Nakamura, S. Nagahama, N. Iwasa, *et al.*, Appl. Phys. Lett. **68**, 3269 (1996).
3. S. Nakamura, S. Nagahama, N. Iwasa, *et al.*, Appl. Phys. Lett. **69**, 1477 (1996).
4. S. Nakamura, N. Iwasa, M. Senoh, and T. Mukai, Jpn. J. Appl. Phys. **31**, L1258 (1992).
5. S. Nakamura, M. Senoh, and T. Mukai, Jpn. J. Appl. Phys. **31**, L139 (1992).
6. U. Kaiser, A. N. Gruzintsev, I. I. Khodos, and W. Richter, Neorg. Mater. **36** (6), 458 (2000).
7. J. C. Zolper, M. Hagerott Crawford, A. J. Howard, *et al.*, Appl. Phys. Lett. **68**, 200 (1996).
8. N. I. Katsavets, G. M. Laws, I. Harrison, *et al.*, Fiz. Tekh. Poluprovodn. (St. Petersburg) **32**, 1175 (1998) [Semiconductors **32**, 1048 (1998)].
9. Y. Li, Y. Lu, H. Shen, *et al.*, Mater. Res. Soc. Symp. Proc. **395**, 369 (1996).
10. T. V. Butkhuzi, A. N. Georgobiani, E. Zade-Uly, *et al.*, Tr. Fiz. Inst. Akad. Nauk SSSR **182**, 140 (1987).
11. H. Amano, I. Akasaki, T. Kozawa, *et al.*, J. Lumin. **4**, 121 (1988).
12. A. N. Georgobiani, A. N. Gruzintsev, A. V. Zayats, and I. M. Tiginyanu, Semicond. Sci. Technol. **6**, 165 (1991).

Translated by A. Spitsyn

Semiconductors, Vol. 35, No. 2, 2001, pp. 149–152. Translated from Fizika i Tekhnika Poluprovodnikov, Vol. 35, No. 2, 2001, pp. 155–158.
Original Russian Text Copyright © 2001 by Grabov, Stepanov.

Reflection Spectra of Doped Bismuth–Antimony Crystals in the Far-Infrared Region of the Spectrum

V. M. Grabov* and N. P. Stepanov**

** Hertzen State Pedagogical University, St. Petersburg, 191186 Russia*

*** Chernyshevsky State Pedagogical University, Chita, 672000 Russia*

Submitted June 27, 2000; accepted for publication June 30, 2000

Abstract—The plasma reflection spectra of the doped bismuth and bismuth–antimony alloyed crystals were studied experimentally at liquid-nitrogen temperature within a range of 30–600 cm^{-1}. Specificities in the optical functions of the samples are revealed within the infrared range that lies on the low-frequency side of the plasma edge and coincides with the optical-phonon frequencies in bismuth. When the plasma frequency is approached, the character of the interaction of radiation with anisotropic electron–hole plasma changes considerably. *© 2001 MAIK "Nauka/Interperiodica".*

Study of the plasma reflection spectra [1, 2] has shown that optical functions deviate from those predicted by the Drude model; a considerable difference (from 1 to 2 orders of magnitude) between the optical and static values of conductivity was also observed. Measuring the optical transmission of bismuth within the range λ = 10–100 μm at the temperature T = 2 K, an interband absorption edge associated with direct interband transitions was determined in the neighborhood of λ = 17 μm (photon energy $\hbar\omega$ = 70 meV) [3]. The influence of interband transition on Bi–Sb crystal permittivity and plasma oscillation damping was considered in [4, 5]. More recent research on the optical transmission of the Bi–Sb crystals [6] has shown that, for an antimony content of 11.5–12.5 at. %, the samples are opaque within the considered range $\hbar\omega$ = 9–20 meV, and the predicted optical band gap for these samples is close to the longitudinal optical-phonon energy (~12–13 meV in bismuth [7]).

In this paper, we report the results of studying the reflection spectra of the doped Bi–Sb crystals in the neighborhood of frequencies typical of the lattice optical modes. From a practical point of view, it is important to clarify the cause of a pronounced decrease in photocarrier lifetime in a number of Bi–Sb semiconducting crystals that are used in the photodetectors operating in the long-wavelength infrared range [8].

We studied Bi single-crystals doped with donor impurity (Te) and acceptor impurity (Sn), undoped Bi single crystals, and also Bi–Sb solid solutions obtained by zone-melting recrystallization. Antimony concentration was determined using a CAMEBAX electron probe microanalyser; the Sb distribution over the sample was found to be uniform within 0.5 at. %. For all the samples, resistivity components and Hall coefficients were determined. The reflection (R) spectra were measured using an IFS-113V BRUKER Fourier spectrometer within the wave number range ν = 30–1000 cm^{-1} with a resolution of 2 cm^{-1} at temperature T = 78 K both in unpolarized and polarized radiation for the incident wave electrical field (**E**) orientations $\mathbf{E} \parallel \mathbf{C}_3$ and $\mathbf{E} \perp \mathbf{C}_3$, where $\mathbf{C}_3$ is the optical axis of the crystal. The polarization degree of radiation amounted to up to 98%. The angle of incidence of radiation was no larger than 8°. The necessity of using polarized radiation stems from the bismuth-crystal high anisotropy, which causes anisotropy of plasma reflection [3]. In general, the reflection spectra combine the additive contributions of the plasma independent interaction with the radiation of two mutually perpendicular polarizations and have two plasma-associated minima with relative intensities depending on the mutual orientation of **E** and $\mathbf{C}_3$ [9]. In line with this, when $\mathbf{E} \parallel \mathbf{C}_3$ or $\mathbf{E} \perp \mathbf{C}_3$, only one plasma-associated minimum is observed.

The reflection spectra of Bi and Bi–Sb crystals doped with donor and acceptor impurities were measured in the optical-phonon frequency range and are shown in Fig. 1. All the curves have a shape typical of plasma reflection. The spectrum calculated in terms of the Drude model is also shown for comparison. As can be seen from Fig. 1, the position and depth of the reflection (R) minimum essentially depends on the temperature, radiation polarization, the component ratio in solid solution $Bi_{1-x}Sb_x$, and the dopant (Sn or Te).

The long-wavelength portion of the spectra shown in Fig. 1 covers the optical-phonon frequency range, while the plasma edge lies in the higher frequency range $\nu > 200$ cm^{-1}.

For all of the reflection spectra depicted in Fig. 1, another minimum in addition to that associated with plasma is observed in the vicinity of the wave number with ν = 110 cm^{-1}. The results of temperature measurements, performed using an AFS-01 Fourier spectrometer at the Institute of Metal Physics (Yekaterinburg),

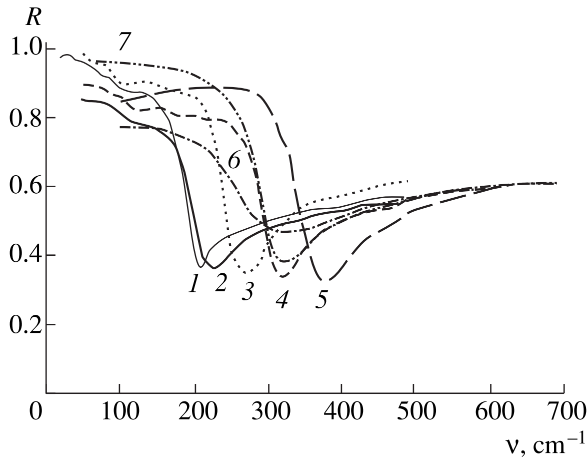

Fig. 1. Reflection spectra: (*1*) $Bi_{0.97}Sb_{0.03}$ ⟨0.02 at. % Zn⟩, nonpolarized radiation; (*2*) Bi ⟨0.16 at. % Sn⟩, **E** ∥ $\mathbf{C}_3$; (*3*) $Bi_{0.97}Sb_{0.03}$ ⟨0.07 at. % Sn⟩, **E** ∥ $\mathbf{C}_3$; (*4*) Bi ⟨0.16 at. % Sn⟩, **E** ⊥ $\mathbf{C}_3$; (*5*, *6*) $Bi_{0.97}Sb_{0.03}$ ⟨0.001 at. % Te⟩, **E** ⊥ $\mathbf{C}_3$; (*7*) calculation following the Drude model. T = (*1*–*4*) 80, (*5*) 20, and (*6*) 100 K.

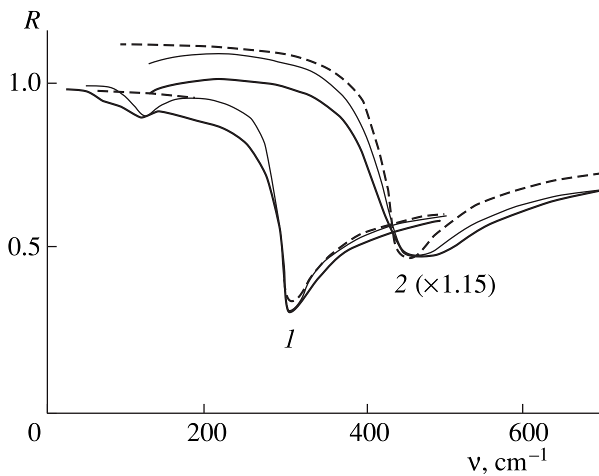

Fig. 2. The bold curve represents the experimental reflection spectra of (*1*) $Bi_{0.97}Sb_{0.03}$ ⟨0.1 at. % Sn⟩ and (*2*) $Bi_{0.93}Sb_{0.07}$⟨0.15 at. % Sn⟩ at T = 80 K, **E** ⊥ $\mathbf{C}_3$; the dashed curve is derived within the Drude model in accordance with (2); and the thin solid curve is derived on the basis of the Drude–Lorentz model in accordance with (1).

indicate (Fig. 1) that the discovered minimum is temperature-dependent, and the reflection coefficient deviates from the Drude model prediction in the long-wavelength region.

On the basis of the presented spectra, we argue that, in the spectral range ν = 90–120 cm^{-1}, along with the plasma interaction, an additional effect of radiation on the crystal manifests itself. The spectral position of the revealed feature is found to be independent of radiation polarization, carrier density, the position of the chemical potential within the energy bands, and the Sb content, up to a concentration of at least 7 at. %. However, the additional interaction was shown to be temperature-dependent. The body of data on the additional radiation–crystal interaction suggests that, in the wave number range ν = 90–120 cm^{-1}, the most probable mechanism of this effect is the absorption of radiation by lattice vibrations. The frequency of longitudinal optical phonons at the Γ point of the Brillouin zone (100 cm^{-1}, 12.4 meV [7]) is closest to the observed minimum.

For a more sophisticated qualitative and quantitative analysis of the experimental spectra, we employed the Kramers–Kronig dispersion relations linking the phase θ and the amplitude R of the reflected wave. Proceeding from the given frequency dependence of the reflection coefficient, Kramers–Kronig relations enable one to obtain spectral dependences of the real ε' and imaginary ε'' parts of permittivity and also the spectral dependence of the energy loss $-\mathrm{Im}(\varepsilon^{-1}) = \varepsilon''/[(\varepsilon')^2 - (\varepsilon'')^2]$. Further analysis of optical functions thus derived permits the determination of plasma frequencies ω_p, plasma-oscillation damping time τ_p, and of high-frequency permittivity ε_∞ without sticking to any particular model for radiation–crystal interaction. The obtained parameters were considered as initial for the permittivity calculation within the context of a model accounting (in adiabatic approximation) for the contribution of free carriers $\varepsilon(\omega)_{fc}$ and lattice vibrations $\varepsilon(\omega)_{\mathrm{ph}}$:

$$\varepsilon(\omega) = \varepsilon_\infty + \varepsilon(\omega)_{fc} + \varepsilon(\omega)_{\mathrm{ph}}. \quad (1)$$

Free carrier contribution was taken into account according to the Drude model, where, for $\omega_p\tau \gg 1$, the real and imaginary parts of permittivity are expressed as

$$\varepsilon'(\omega)_{fc} = \varepsilon_\infty\left(1 - \frac{\omega_p^2}{\omega^2 - \tau^{-2}}\right);$$
$$\varepsilon''(\omega)_{fc} = \varepsilon_\infty \frac{\omega_p^2}{\omega^3 \tau_p}. \quad (2)$$

To describe the contribution of the lattice long-wavelength optical vibrations to the real and imaginary permittivity parts, we used the model of a damped oscillator (the Lorentz model):

$$\varepsilon'_{\mathrm{ph}} = \varepsilon_\infty + \frac{(\varepsilon_0 - \varepsilon_\infty)[1 - (\omega/\omega_0)^2]}{[1 - (\omega/\omega_0)^2]^2 + (\omega/\omega_0)^2(\tau_{\mathrm{ph}}^{-1}/\omega_0)^2},$$
$$\varepsilon''_{\mathrm{ph}} = \varepsilon_\infty + \frac{(\varepsilon_0 - \varepsilon_\infty)(\omega/\omega_0)^2(\tau_{\mathrm{ph}}^{-1}/\omega_0)}{[1 - (\omega/\omega_0)^2]^2 + (\omega/\omega_0)^2(\tau_{\mathrm{ph}}^{-1}/\omega_0)^2}, \quad (3)$$

where τ_{ph}^{-1} is the phonon-oscillator damping parameter, ε_0 is the static or low-frequency permittivity at frequencies that are considerably lower than the transverse

optical-phonon cutoff frequency ω_0. The parameters ε_0 and ω_0 are related to the ε_∞ and the transverse optical phonon cutoff frequency ω_0 by the Lyddane–Sachs–Teller relation:

$$\frac{\omega_1}{\omega_0} = \frac{\varepsilon_0}{\varepsilon_\infty}. \quad (4)$$

The reflection coefficient calculated according to the presented model is shown in Fig. 2 together with the experimental data obtained for two different samples. As can be seen from the plot, the calculated spectral dependence of the reflection coefficient agrees satisfactorily with the experiment for most of the studied frequency range. The parameters ensuring the closest fit of the simulated spectra to the experimental curves have been calculated using an autofitting procedure and are listed in the table. The table also presents the Drude model parameters ensuring the best fit of calculated spectra to the experiment and the static relaxation time τ_c obtained from the measurements of electrical conductivity.

As is evident from the table, the consideration of not only the plasma but also of the lattice contribution to permittivity changes the plasma frequencies by a factor of 1.3 compared to those calculated by the Drude model, reduces the discrepancy between the optical and static relaxation times, and improves the agreement between the calculated and experimental spectra (Fig. 2). The above results confirm our conclusion that the role of interaction of radiation with optical phonons is significant.

The spectra shown in Fig. 2 indicate that the interaction mechanism considered above is most pronounced in Bi crystals and Bi–Sb alloys doped with a donor Sn impurity. The enhanced interaction of radiation with optical phonons in this case may be due to the ionized impurity present in the lattice and the approach of the plasma frequencies toward the optical-phonon frequency range.

The most complex behavior of the reflection spectra takes place for the geometry $\mathbf{k} \perp \mathbf{C}_3$ ($\mathbf{k}$ is the wave propagation vector) when the frequency of one or both plasma-associated minima is close to the optical-phonon frequency range. The spectra obtained in this geometry essentially differ in shape from those predicted by the Drude model (Fig. 3, curves *1*, *2*). Moreover, a noticeable difference is observed in the schemes for the spectra obtained using either a polarizer or an analyzer (the polarizer being installed between the radiation source and the detector and the analyzer, between the sample and the detector). Figure 3 shows (curves *1–4*) that in passing from the scheme involving a polarizer to that with an analyzer, the plasma frequency changes and the reflection spectrum acquires an additional minimum. It is readily seen that the additional minimum is associated with plasma oscillations, much like the minimum observed in the reflection spectrum of nonpolarized radiation (Fig. 1, curve *1*). Apparently, spectra *3* and *4* in Fig. 3 should be interpreted as a manifestation of the two modes $\omega_p^\perp$ and $\omega_p^\parallel$ of anisotropic plasma, rather than as a result of plasmon–phonon mode mixing. For the interaction of nonpolarized radiation with anisotropic plasma of charge carriers, the mutually perpendicular plasma modes are likely to be linked via the interaction with optical phonons. We note that the difference between the spectra obtained using a polarizer

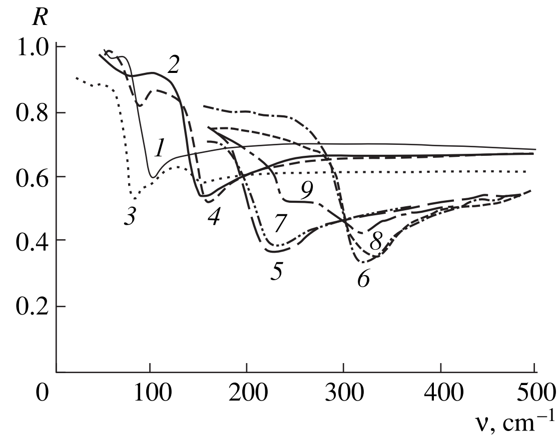

Fig. 3. Reflection spectra at T = 80 K. (*1–4*) $Bi_{0.97}Sb_{0.03}$ ⟨0.1 at. % Sn⟩ sample; (*1*, *2*) in the polarizer setup, (*3*, *4*) in the analyzer setup; (*1*, *3*) $\mathbf{E} \parallel \mathbf{C}_3$, (*2*, *4*) $\mathbf{E} \perp \mathbf{C}_3$. (*5–9*) The $Bi_{0.97}Sb_{0.03}$ ⟨0.15 at. % Sn⟩ sample; (*7*, *8*) in the polarizer setup, (*5*, *6*) in the analyzer setup, and (*9*) with nonpolarized radiation; (*5*, *7*) $\mathbf{E} \parallel \mathbf{C}_3$, (*6*, *8*) $\mathbf{E} \perp \mathbf{C}_3$.

The parameters of the simulated reflection spectra at T = 80 K

Sample, polarization	Drude model			Drude–Lorentz model					τ_c
	ε_∞	ω_p	τ_p	ω_1	ω_0	τ_{ph}	ω_p	τ_p	
Bi⟨0.16 at. % Sn⟩, $\mathbf{E} \parallel \mathbf{C}_3$	70	3.9	1.35	2.5	2.1	1.15	3.1	75	33
$Bi_{0.97}Sb_{0.03}$⟨0.1 at. % Sn⟩, $\mathbf{E} \perp \mathbf{C}_3$	120	5.63	1.85	2.45	2.1	1.95	4.3	8	7
$Bi_{0.93}Sb_{0.07}$⟨0.05 at. % Sn⟩, $\mathbf{E} \perp \mathbf{C}_3$	105	6.3	1.22	2.4	2.0	2.05	4.1	6	4

Note: Frequencies are expressed in units of [10^{13} s^{-1}]; times, in units of [10^{-13} s]; and τ_c is the static relaxation time derived from the electrical conductivity measurements.

and those obtained using an analyzer completely vanishes if the plasma frequencies shift from the optical-phonon frequency range to the higher frequency region (Fig. 3, curves *5–8*).

REFERENCES

1. V. D. Kulakovskiĭ and V. D. Egorov, Fiz. Tverd. Tela (Leningrad) **15**, 2053 (1973) [Sov. Phys. Solid State **15**, 1368 (1973)].
2. M. I. Belovolov, V. S. Vavilov, V. E. Egorov, and V. D. Kulakovskiĭ, Izv. Vyssh. Uchebn. Zaved., Fiz. **2**, 5 (1976).
3. W. S. Boyle and A. D. Brailsford, Phys. Rev. **120**, 1943 (1960).
4. V. M. Grabov, N. P. Stepanov, B. E. Vol'f, and A. S. Mal'tsev, Opt. Spektrosk. **69**, 134 (1990) [Opt. Spectrosc. **69**, 82 (1990)].
5. N. P. Stepanov, V. M. Grabov, and B. E. Vol'f, Fiz. Tekh. Poluprovodn. (Leningrad) **23**, 1312 (1989) [Sov. Phys. Semicond. **23**, 817 (1989)].
6. T. M. Lifshits, A. B. Ormont, E. G. Chirkova, and A. Ya. Shul'man, Zh. Éksp. Teor. Fiz. **72**, 1130 (1977) [Sov. Phys. JETP **45**, 591 (1977)].
7. R. Macfarlane, Phys. Chem. Solids **32**, 289 (1971).
8. V. A. Martyakhin, A. Ya. Oleĭnikov, A. Ya. Smirnova, *et al.*, Fiz. Tekh. Poluprovodn. (Leningrad) **14**, 1716 (1980) [Sov. Phys. Semicond. **14**, 1021 (1980)].
9. A. S. Mal'tsev, V. M. Grabov, and A. A. Kukharskiĭ, Opt. Spektrosk. **58**, 927 (1985) [Opt. Spectrosc. **58**, 567 (1985)].

Translated by A. Sidorova-Biryukova

Semiconductors, Vol. 35, No. 2, 2001, pp. 153–157. Translated from Fizika i Tekhnika Poluprovodnikov, Vol. 35, No. 2, 2001, pp. 159–163.
Original Russian Text Copyright © 2001 by Savkina, Ratnikov, Shuman.

ELECTRONIC AND OPTICAL PROPERTIES OF SEMICONDUCTORS

The Effect of High-Temperature Epitaxial SiC Layer Growth on the Structure of Porous Silicon Carbide

N. S. Savkina*, V. V. Ratnikov, and V. B. Shuman

Ioffe Physicotechnical Institute, Russian Academy of Sciences, Politekhnicheskaya ul. 26, St. Petersburg, 194021 Russia

**e-mail: nata.sav@pop.ioffe.rssi.ru*

Submitted July 4, 2000; accepted for publication July 4, 2000

Abstract—Porous silicon carbide layers obtained by electrochemical etching of 6*H*-SiC at three anode current densities were investigated. X-ray double- and triple-crystal diffractometry and scanning electron microscopy were used to study the structure of porous SiC layers before and after high-temperature sublimation growth of 6*H*-SiC epilayers. The density of pores in the structure is found to be independent of the current density in electrochemical etching. The effective diameter of pores increases with increasing current density, resulting in higher porosity of the structure. High-temperature annealing modifies the structure without changing the sample porosity. The structural rearrangement is accompanied by coalescence of single pores and an increase in their diameter. *© 2001 MAIK "Nauka/Interperiodica".*

1. INTRODUCTION

Persisting interest in porous-silicon properties and its industrial application inevitably stimulates studies of porous layers of other semiconductor materials. Among these, silicon carbide attracts special attention due to its thermal, electrical, and mechanical characteristics. Although porous silicon carbide (*por*-SiC) has long been known, mainly its photoluminescent properties have been studied [1–3]. Only a few studies have been devoted to the structural properties of *por*-SiC itself [4, 5]. Previously, we have demonstrated the possibility of obtaining high-quality 6*H*-SiC films on porous SiC, up to 10 μm thick, by vacuum sublimation epitaxy [6].

The objective of this study was to compare the characteristics of porous SiC before and after high-temperature growth of thin (0.5–3 μm) epitaxial 6*H*-SiC films using X-ray diffractometry and scanning electron microscopy (SEM).

2. EXPERIMENTAL

Like porous silicon, porous SiC is obtained by electrochemical anodizition [1, 7]. Parts of a commercial 6*H*-SiC wafer (produced by CREE with the carrier concentration of 3×10^{18} cm^{-3}) misoriented by 3.5° with respect to the *c* axis were used in the experiments. The opposite faces of the wafer were treated differently. The working (0001)Si face was polished, and the opposite face, lapped. The samples were anodized under UV illumination of the sample surface in HF : H_2O : C_2H_5OH = 1 : 1 : 2 electrolyte at three current densities: 20, 60, and 100 mA/cm^2. The etching duration was chosen so that the same charge passed through the substrate for 15, 5, and 3 min, respectively.

Thin (several μm) epitaxial 6*H*-SiC films were grown on porous SiC in a vertical water-cooled quartz reactor by vacuum sublimation at 2000°C. The growth technology is described elsewhere [8].

The thickness and morphology of porous SiC were determined from cross-sectional SEM images of the samples.

X-ray studies were performed using double- and triple-crystal diffractometry (DCD and TCD) with Cu$K_{\alpha1}$ radiation. The sample porosity was evaluated using X-ray absorption porometry [9] (with ±5% accuracy) and gravimetry. Macrostresses were evaluated from the DCD-measured sample bending radii *R* using the Stoney relation [10]. The bending radius was measured by recording the angular shift of the reflection peak for a sample in its linear X-ray scanning [11]. The structural perfection of layers was monitored by the behavior of the angular full width at half-maximum (FWHM) of a diffraction peak for the symmetric Bragg (0006) reflection. In TCD measurements, θ- and (θ–2θ) scanning modes were used.

3. RESULTS AND DISCUSSION

3.1. Scanning Electron Microscopy

The thickness of porous SiC before and after high-temperature growth of epilayers was measured on freshly cleaved samples. Figure 1a shows a cross-sectional SEM image of porous SiC immediately after the anodic etching of the substrate. As can be seen, not all pores reach the sample surface, as in the case described in [4, 5]. Near the surface, pores are nearly parallel to it. Deeper inside the substrate, pores are aligned perpendicular to the surface (Fig. 1b), forming "herringbone" structures in cross section. The well-defined

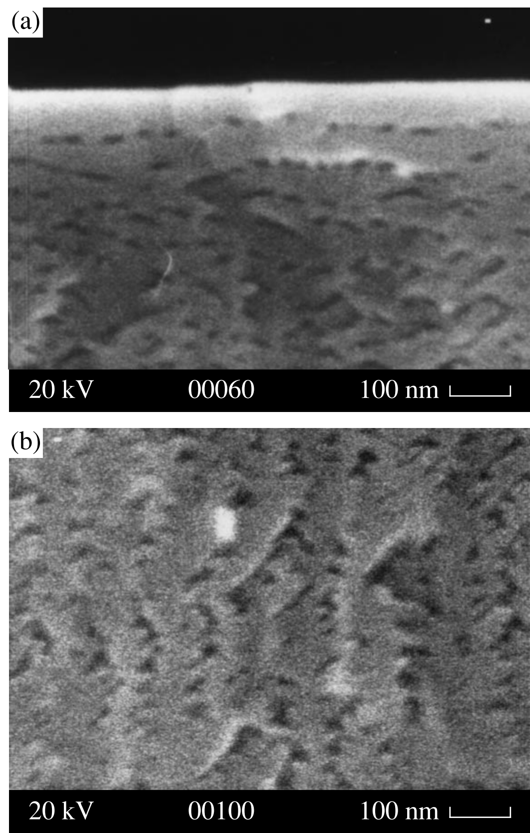

Fig. 1. Cross-sectional SEM image of porous SiC: (a) near the substrate surface and (b) inside the layer.

boundary between the substrate and the porous layer allows a relatively precise determination of the porous layer thickness. Initial porous SiC thicknesses in our samples were 26, 18, and 16 μm for anodic etching current densities of 20, 60, and 100 mA/cm^2, respectively. That is, the rate of the porous SiC layer growth increased nonlinearly with current density, being, respectively, 1.73, 3.6, and 5.33 μm/min.

Heating to 2000°C in vacuum modifies the porous SiC structure for all the three samples, especially at the porous SiC–substrate interface (Fig. 2). Pores not only become larger, but their cross section changes as well. Porous SiC prepared at 100 mA/cm^2 suffers the greatest changes near its lower interface, while the upper interface *por*-SiC–epilayer looks nearly the same in all the samples.

It is necessary to note that the present technology includes epitaxial polishing etching of a sample immediately before the epilayer growth. Comparison of porous-layer thicknesses before and after high-temperature growth implies that 4 μm of the porous layer has been removed during the sublimation etching. Therefore, the epilayer was grown on the portion of porous SiC where pores are aligned perpendicular to the sample surface.

3.2. X-ray Diffractometry

3.2.1. Bending and macrostresses in the samples. Table 1 lists the curvature radii R, biaxial stresses σ_a, calculated from these radii, macrostrains ε_z normal to the sample surface, and half-widths of the reflection curves obtained by DCD and TCD.

The curvature radii R in Table 1 were calculated from the experimental radii, taking into account the initial substrate curvature before the growth process, resulting from different types of treatment of the substrate surfaces (polishing of the working silicon surface and lapping of the back carbon surface).

During *por*-SiC layer fabrication on an SiC substrate, the sign of the substrate curvature is reversed (the initially concave sample becomes convex). However, sample curvature radii remain practically unchanged under the anodic etching with increasing current density. The biaxial tangential stresses in porous SiC, calculated by the Stoney relation, are compressive, and the strain normal to the sample surface

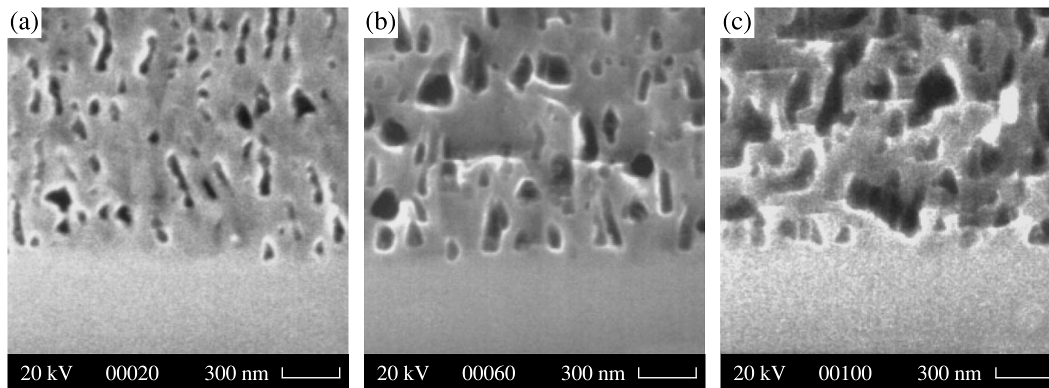

Fig. 2. Cross-sectional SEM image of *por*-SiC–substrate interfaces after high-temperature epilayer growth at anode current densities j = (a) 20, (b) 60, and (c) 100 mA/cm^2.

$\varepsilon_z = \delta d/d$, calculated from these stresses, has a positive sign.

When an epitaxial SiC layer is grown on the initial substrate, the sample curvature sign also changes, and biaxial compressive stresses in such a layer are as high as $\sigma_a = -1.34$ GPa.

Growth of 0.5–3-μm-thick epitaxial SiC layers on porous SiC does not change the sign of the sample curvature, but its absolute value slightly increases compared with porous SiC on a substrate before layer growth. Calculations show that biaxial stresses in epilayers on porous SiC are lower compared with porous SiC on a substrate for current densities of 20 and 60 mA/cm^2. However, for a current density of 100 mA/cm^2, stresses in the epilayer exceed those in porous SiC.

This behavior of sample macrobending in growth of thin epitaxial SiC layers on porous SiC may be due to a structural transformation of the initially grown porous SiC. The increase in biaxial stresses in the epilayer grown on porous SiC of the highest porosity (100 mA/cm^2) may have the same origin. As mentioned above, the SEM data for this sample were indicative of the most significant modification of the porous-layer structure upon vacuum annealing. It should also be noted that in this case the epilayer is considerably thinner (0.5 μm).

On the whole, biaxial compressive stresses in epilayers on porous SiC are 4–6 times lower than those in the layer grown on the initial SiC substrate.

3.2.2. Diffraction curves. Table 1 presents FWHM values for DCD and TCD schemes of diffracted intensity recording. The correction for sample curvature is included in the FWHM values listed.

The parameters of DCD rocking curves obtained from the initial substrate and from the SiC epilayer deposited on it coincide. At the same time, the more sensitive TCD method shows a minor decrease in half-width for both θ and (θ–2θ) curves taken from the epilayer, related, respectively, to micro-misorientation of diffracting planes and to the level of microstrain in the direction normal to the surface. In this case the structural uniformity over the sample area is substantially higher for the epilayer compared with the substrate.

DCD rocking curves for all the porous SiC samples on SiC substrate have the same shape, consisting of a narrow peak on a wide diffuse "pedestal" (Fig. 3). The FWHM values of the narrow (dynamic) peak ω_θ for porous SiC, exceeding by more than a factor of 1.5 those for the initial substrate, grow insignificantly with increasing current density. This is not surprising, since the anodic etching is a mild process of material removal in fabrication of porous samples without substantial damage to the crystal matrix of the initial substrate. At the same time, (θ–2θ) curves have the form of a narrow symmetric peak, indicating the matching of porous SiC and substrate lattice parameters for all the current densities.

The wide low-intensity portion of the DCD rocking curve is associated with diffuse scattering on the porous structure [12]. DCD measurements with a narrow slit in front of the counter demonstrated that the diffuse scattering is anisotropic and extends along the θ-scanning direction, thus reflecting the shape anisotropy of pores oriented normal to the surface. The diffuse peak width ω_{ds} yields the effective pore diameter. The decrease in ω_{ds} with increasing current density reflects the fact that this diameter grows (from 0.022 μm for 20 mA/cm^2 to 0.028 μm for 100 mA/cm^2). The diffuse peak shape with a flat top is due to the interference between X-rays scattered by neighboring pores [12].

Further growth of the epilayer on porous SiC leads to a decrease in the half-width for both the narrow and the diffuse peaks. Since the epilayers are thin (0.5–3 μm), the diffraction curve is mainly determined by the underlying porous SiC. Therefore, we ascribe the modification of the diffraction curve parameters to

Table 1. X-ray data for porous SiC layers before and after high-temperature epilayer growth

Sample	R, m	σ_a, GPa	ε_z, 10^{-3}	DCD	TCD	
				ω/ω_{ds},	ω_θ,	$\omega_{\theta-2\theta}$,
				seconds of arc		
Initial substrate	–3.40			22/–	20	6.8
Substrate + SiC epilayer	+4.07	–1.34	+2.70	22/–	18	5.5
PSC (20 mA/cm^2)	+2.03	–0.21	+0.41	35/2144	34	7.9
PSC + SiC epilayer	+2.28	–0.20	+0.40	28/1010	25	7.6
PSC (60 mA/cm^2)	+1.82	–0.33	+0.66	37/2059	34	7.5
PSC + SiC epilayer	+2.14	–0.30	+0.60	30/811	24	6.5
PSC (100 mA/cm^2)	+1.90	–0.36	+0.72	38/1856	37	7.4
PSC + SiC epilayer	+2.28	–0.42	+0.84	46/683	40	5.9

Note: PSC stands for porous SiC (anodizing current density is given in parentheses), DCD and TCD are double- and triple-crystal diffractometry.

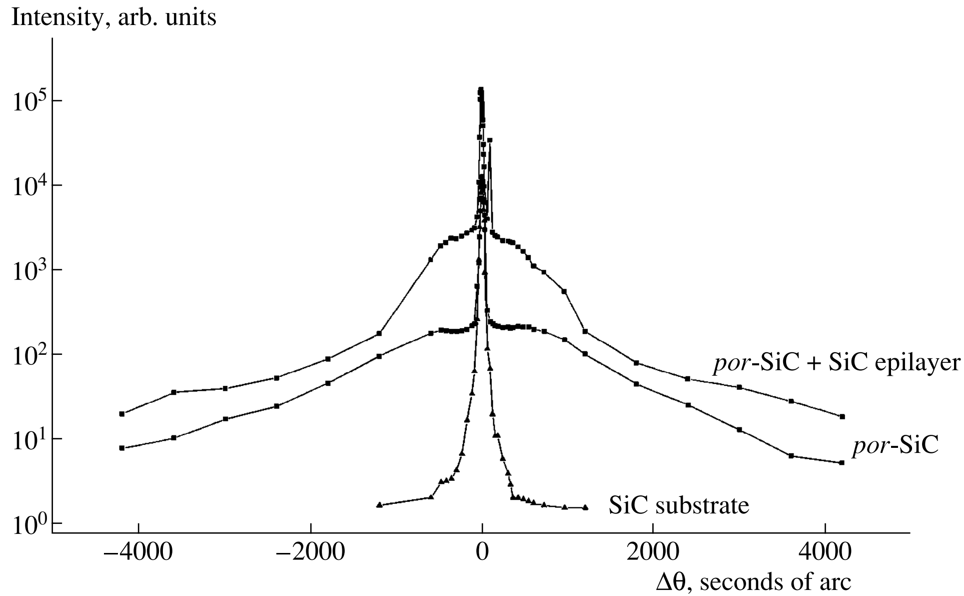

Fig. 3. CuK_α (0006) rocking curves measured using a double-crystal diffractometer. For clarity, the curves are shifted along the ordinate.

the annealing of porous SiC at 2000°C prior to epitaxial growth. The pronounced (by a factor of 2–3) decrease in ω_{ds} indicates a structural rearrangement in porous SiC. The evaluated pore diameter increases to 0.052 μm for 20 mA/cm^2 and 0.077 μm for 100 mA/cm^2.

The modification of the diffuse peak shape is related not only to the structural rearrangement in porous SiC, but also to the contribution of the thin epilayer to the obtained rocking curve. The X-ray diffraction characterization of the epilayer is hindered by the fact that it is 10–20 times thinner than porous SiC and by the coincidence of their peak positions in the diffraction curve. Nevertheless, the half-width of the dynamic peak suggests that the structural characteristics of the layer are not inferior to those of the initial substrate. However, unlike the latter, the epilayer is uniform over the sample area.

The use of asymmetrical reflections allows one to reduce the depth of X-ray penetration into the sample, thus increasing the contribution of the thin epilayer to the recorded signal. Measurements for the $10\bar{1}.10$ reflection (the angle of incidence was 9°) demonstrated that its half-width decreases for epilayers grown both on the initial substrate and on porous SiC (e.g., the reflection half-width falls from 50″ to 40″ for an epilayer on the initial substrate), thus indicating the improvement of the crystal quality of epitaxial SiC.

Table 2. Porous SiC layer characteristics before and after high-temperature epilayer growth

	j = 20 mA/cm^2		j = 100 mA/cm^2	
	before annealing	after annealing	before annealing	after annealing
h, μm	26	22	16	12
P, %	11.3		20	
Ph, % μm	294		330	
d, μm	22×10^{-3}	52×10^{-3}	28×10^{-3}	77×10^{-3}
V, μm^3	0.986×10^{-2}	4.67×10^{-2}	0.986×10^{-2}	5.6×10^{-2}
N, cm^{-2}	3×10^{10}	0.53×10^{10}	3.25×10^{10}	0.43×10^{10}
S, μm^2	1.8	3.59	1.41	2.9

Note: h stands for the porous SiC thickness; P, the gravimetric porosity; d, the pore diameter; V, the pore volume; N, the surface density of pores; and S, the pore surface area.

3.2.3. Sample porosity. X-ray studies yield porosity characteristics close to those obtained by gravimetry and effective pore diameters d obtained under the same assumptions as in [12]: (1) the pore is cylindrical and (2) pore openings on the surface form a square lattice. From these data, the volume and the surface area of a single pore can be obtained, along with the surface density of pores, N (Table 2). In the calculation, we have taken into account that the removed SiC volume for all the three samples coincides, because the charge passed through the substrates in anodic etching was the same. This conclusion is supported by the fact that $Ph \approx$ const, where P is the layer porosity and h is its thickness. Evidently, $Ph = NV$, where N is the number of pores per 1 cm^2 of the sample surface, and V is the volume of a single pore. It can be seen from Table 2 that the pore volume does not grow with increasing current density in anodic etching, and, therefore, the number of pores remains constant in this current density range, $N \approx 3 \times 10^{10}$ cm^{-2}. Hence, the increase in the porosity with

current density is due to the growing effective pore diameter, rather than to an increasing number of pores. At the same time, the pore surface area becomes smaller with increasing current density, owing to the decrease in the porous layer thickness with the simultaneously growing pore diameter.

X-ray data show that, within the experimental error, the porosity remains unchanged upon annealing of the porous sample prior to SiC epilayer deposition. At the same time, the number of pores decreases, and the surface area and the volume of a single pore increase (Table 2). This fact can be attributed to a structural rearrangement of porous SiC during high-temperature annealing, resulting in coalescence of individual pores, with their diameter increasing, as seen in Fig. 2. We may assume that the structural reconstruction is associated with material sublimation inside the pores, and also with the stresses existing in porous SiC.

4. CONCLUSION

Heating of porous silicon carbide to 2000°C and further epilayer growth on it cause a structural transformation in porous SiC, followed by the coalescence of individual pores and a decrease in their number. At the same time, the 4- to 6-fold reduction of biaxial compressive stresses in the epilayer on the porous SiC surface, improved uniformity of the diffraction characteristics of the epilayer over the entire sample area, and the previously observed order-of-magnitude decrease in the dislocation density in a thick layer [6] open up prospects for application of these layers as buffers. However, further investigations are necessary to determine the optimal conditions of formation and subsequent annealing of porous SiC.

REFERENCES

1. T. Matsumoto, J. Takahashi, T. Tamaki, *et al.*, Appl. Phys. Lett. **64**, 226 (1994).
2. A. O. Konstantinov, A. Henry, C. I. Harris, and E. Jansén, Appl. Phys. Lett. **66** (17), 2250 (1995).
3. A. M. Danishevskiĭ, V. B. Shuman, E. G. Guk, and A. Yu. Rogachev, Fiz. Tekh. Poluprovodn. (St. Petersburg) **31** (4), 420 (1997) [Semiconductors **31** (4), 354 (1997)].
4. A. M. Danishevskii, M. V. Zamoryanskaya, A. A. Sitnikova, *et al.*, Semicond. Sci. Technol. **3**, 1111 (1998).
5. S. Zangooie and H. Arwin, in *Abstracts of the 2nd International Conference, Madrid, 2000*, p. 117.
6. M. Mynbaeva, N. Savkina, A. Zubrilov, *et al.*, Mater. Res. Soc. Symp. Proc. **587** (2000).
7. J. S. Shor, I. Grimberg, B.-Z. Weiss, and A. D. Kurtz, Appl. Phys. Lett. **62**, 2836 (1993).
8. N. S. Savkina, A. A. Lebedev, D. V. Davydov, *et al.*, Mater. Sci. Eng. B **61-62**, 165 (1999).
9. V. V. Ratnikov, Fiz. Tverd. Tela (St. Petersburg) **39** (5), 956 (1997) [Phys. Solid State **39**, 856 (1997)].
10. G. Stoney, Proc. R. Soc. London, Ser. A **82**, 172 (1925).
11. G. Rozgonyi, P. Petroff, and M. Panish, J. Cryst. Growth **27**, 106 (1974).
12. D. Bellet, G. Dolino, M. Ligeon, *et al.*, J. Appl. Phys. **71**, 145 (1992).

Translated by D. Mashovets

Semiconductors, Vol. 35, No. 2, 2001, pp. 158–163. Translated from Fizika i Tekhnika Poluprovodnikov, Vol. 35, No. 2, 2001, pp. 164–170.
Original Russian Text Copyright © 2001 by Ravich, Nemov.

ELECTRONIC AND OPTICAL PROPERTIES OF SEMICONDUCTORS

Hopping Transport in Doped $(Pb_{0.78}Sn_{0.22})_{1-x}In_xTe$ Solid Solutions

Yu. I. Ravich and S. A. Nemov

St. Petersburg State Technical University, Politekhnicheskaya ul. 29, St. Petersburg, 195251 Russia

Submitted July 4, 2000; accepted for publication July 4, 2000

Abstract—Transport coefficients in $(Pb_{0.78}Sn_{0.22})_{1-x}In_xTe$ solid solutions with indium content $x = 0.03$ and 0.05 additionally doped with acceptors (Tl) or donors (Cl) have been measured and analyzed. The Seebeck coefficient S is positive for $x = 0.05$ in the low temperature range 77–200 K; its sign changes to negative when the Tl acceptor is added. This unusual behavior of the thermoelectric power can be attributed to hopping conduction at a nonmonotonic energy dependence of the density of localized states. The density-of-states function has been determined at $x = 0.03$ and 0.05 from experimental data on the thermopower. Theoretical estimates of the Nernst–Ettingshausen coefficient are made for $x = 0.03$ additionally doped with Cl. The estimates are based on taking into account, along with the hopping conduction, the contribution from electrons with energies above the mobility edge and on using the critical electrical conductivity exponent obtained in the percolation theory. The activation energies characterizing the temperature dependences of conductivity and Hall and Nernst–Ettingshausen coefficients are discussed and compared. © *2001 MAIK "Nauka/Interperiodica".*

The hopping conduction via localized states related to In impurities has been observed and studied in PbTe semiconductor compound and in solid solutions on its basis [1–6]. A characteristic feature of the In impurity states in IV–VI semiconductors is strong localization [7] characterized by an effective wave function radius one order of magnitude smaller than the effective Bohr radius in the semiconductors most widely studied [8]. That is why hopping conduction via In states was observed at unusually high impurity concentrations ($x \simeq 2$–22 at. %).

The In impurity energy levels decrease owing to the partial substitution of tin atoms for lead in PbTe, passing into the energy gap when the tin content in the solid solution is about 20 at. %. This circumstance enables us to study the hopping conduction via In-related localized states in the $Pb_{0.78}Sn_{0.22}Te$ solid solution under more favorable conditions compared with PbTe. For this reason, the hopping transport phenomena (electrical conductivity σ, thermopower S, and Hall R and Nernst-Ettingshausen Q coefficients) were studied in detail only in the solid solution of the composition mentioned above [2–6].

Analysis of the temperature dependence of electrical conductivity $\sigma(T)$ has shown that the electronic transport at temperatures within the range 100–400 K is due to electron hopping between neighboring impurity sites [3]. The temperature dependence of the Seebeck coefficient S is rather complicated. In particular, for an In content $x = 0.05$ and higher, the thermopower changes its sign at a temperature of about 200 K, with positive thermopower being observed at $T < 200$ K. A model of the energy spectrum of localized electrons was proposed to explain these experimental observations. The density of states $g(\varepsilon)$ was assumed to be a nonmonotonic function of energy $dg/d\varepsilon$, having a peak near the chemical potential μ. With changing temperature, the chemical potential passes through the peak, which leads to a change in the sign of the derivative $dg/d\varepsilon$, accompanied by a change in the thermopower sign.

In order to check our supposition concerning the nonmonotonic shape of the density of states $g(\varepsilon)$ we used additional doping with electrically active impurities that create no localized states in the energy range studied but shift the chemical potential, thereby changing the sign of the derivative $dg/d\varepsilon$ near μ. The additional doping with donors (Cl) and acceptors (Tl) at $x = 0.03$ [5] did not change the thermopower sign; i.e., the $g(\varepsilon)$ function was monotonic at this In content.

In this study, the thermopower was measured at the indium content $x = 0.05$ and with additional doping with thallium. The thermopower sign change obtained confirms our hypothesis on the nonmonotonic behavior of the density of states. The density of states as a function of energy is calculated at $x = 0.05$ and 0.03, using the experimental results on electrical conductivity and thermopower, obtained in this study and in [5]. Also, theoretical estimates of the Nernst–Ettingshausen coefficient in the case of additional doping with chlorine are carried out and compared with the earlier obtained experimental data [6]. The temperature dependence of the reciprocal Nernst–Ettingshausen coefficient is characterized by the activation energy, which is compared with the corresponding parameters determined from the temperature dependences of the electrical conductivity and the Hall coefficient.

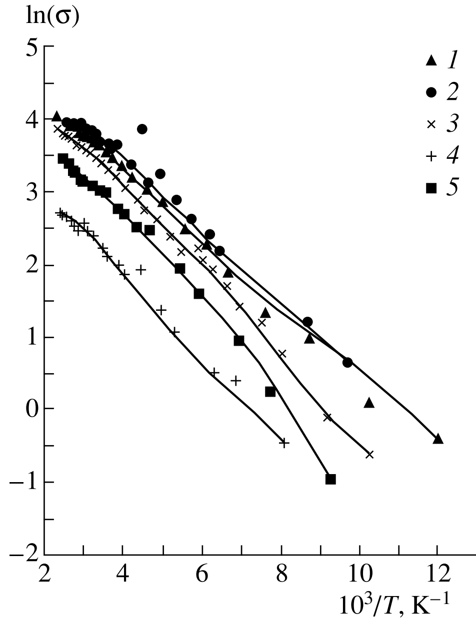

Fig. 1. Electrical conductivity in $(Pb_{0.78}Sn_{0.22})_{0.95-y}In_{0.05}Tl_yTe$ samples vs. reciprocal temperature. Thallium content y: (*1*) 0, (*2*) 0.5, (*3*) 1, (*4*) 1.5, and (*5*) 2 at. %.

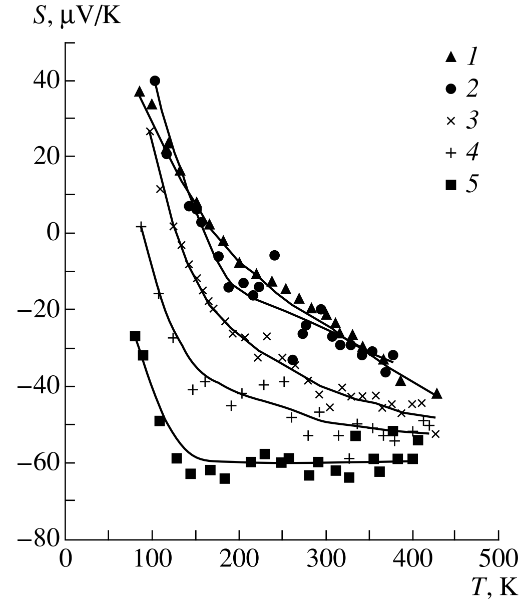

Fig. 2. Thermopower in $(Pb_{0.78}Sn_{0.22})_{0.95-y}In_{0.05}Tl_yTe$ samples vs. temperature. Thallium content y: (*1*) 0, (*2*) 0.5, (*3*) 1, (*4*) 1.5, and (*5*) 2 at. %.

1. THERMOPOWER AND ELECTRICAL CONDUCTIVITY IN THE CASE OF ADDITIONAL DOPING WITH THALLIUM

The temperature dependence of thermopower in the $(Pb_{0.78}Sn_{0.22})_{1-x}In_xTe$ solid solution at $x = 0.03$ [2, 4] in the nearest-neighbor hopping transport regime can be described by the expression obtained in [9] using the effective medium technique:

$$S = -\frac{5}{6}\frac{k}{e}\left(\frac{\varepsilon_h^2}{2kT} + \frac{2}{3}\pi^2 kT\right)\left(\frac{d\ln g}{d\varepsilon}\right)_{\varepsilon=\mu}, \qquad (1)$$

where ε_h is the activation energy of hopping conductivity, e is the absolute value of the electron charge, and k is the Boltzmann constant. The agreement between theoretical and experimental values at $x = 0.03$ is achieved under the assumption that the last multiplier in (1) is positive and weakly dependent on temperature; then the thermopower is negative and the sum in the parentheses gives the minimum value of the function $|S| = -S(T)$ at $T \approx 200$ K [4]. With the indium content increasing to $x \geq 0.05$, we have, instead of the minimum of $|S|$, a change in the thermopower sign at about 200 K, indicating a change in the sign of the derivative $(dg/d\varepsilon)_{\varepsilon=\mu}$. If the chemical potential μ is close to the density-of-states $g(\varepsilon)$ peak, its relatively small shift can lead to a pronounced change in thermopower. The positive sign of the thermopower at low temperatures, $T <$ 200 K, can be explained by a shift of the chemical potential from the peak of $g(\varepsilon)$ to the energy range where the derivative $dg/d\varepsilon$ is negative, i.e. toward the soft gap in the electronic spectrum [2]. With increasing temperature, the chemical potential passes from the gap to lower energies, where $dg/d\varepsilon > 0$ and the sign of the thermopower in the solid solution doped with indium becomes conventional, i.e., negative.

To verify this hypothesis, we lowered the chemical potential in samples with a fixed indium content x = 0.05 by introducing an additional acceptor impurity Tl (from 0 to 2 at. %). Both thallium and indium substitute cations in the crystal lattice. Although Tl impurities are known to create resonance states in PbTe and its solid solutions [7, 10], the related energy levels are located in the valence band far away from the chemical potential, and their filling with electrons ensures an acceptor-like compensation effect. In this case every Tl atom accepts a single electron.

Samples were fabricated using the metal-ceramic technique and subjected to homogenizing annealing at 650°C for 100 h.

The temperature dependence of conductivity $\sigma(T)$ was exponential within the range 100–400 K. The activation energies ε_h of hopping conductivity were obtained from the slope of the straight line depicting $\ln\sigma$ as a function of T^{-1} (Fig. 1). The dependence of the parameter ε_h on the thallium content was weak, within the experimental error $\varepsilon_h = (45 \pm 5)$ meV in all solid solution samples at indium content $x = 0.05$.

The thermopower S steadily decreased at all temperatures with increasing thallium content (Fig. 2). At low temperatures this decrease lead to a change in the thermopower sign from positive to negative, which confirms the above assumption that the density of localized

Table 1. Experimental Seebeck coefficients S at T=100 K and the function $f(n)$ for $(Pb_{0.78}Sn_{0.22})_{0.95}In_{0.05}Te$ additionally doped with thallium

Sample no.	N_{Tl}, at. %	S, μV/K	n, 10^{20} cm^{-3}	f, eV^{-1}
1	0	40	7.5	–3.2
2	0.5	40	6.8	–3.2
3	1.0	25	6.0	–2.0
4	1.5	–9	5.3	+0.7
5	2.0	–40	4.5	+3.2

states has a peak as a function of energy. In samples with the maximum thallium content of 2 at. %, the thermopower has the conventional negative sign at all temperatures.

We note that the observed pattern of the thermopower dependence on the concentration of the electrically active impurities is absolutely uncommon for semiconductors with wide allowed bands, to which IV–VI semiconductors belong. Doping with large amounts of a donor (indium) leads to an anomalous positive thermopower at relatively low temperatures $T < 200$ K. By contrast, addition of an acceptor (thallium) changes the thermopower sign to the conventional negative one. Such a result of doping, however, can be properly explained taking into consideration the hopping character of conduction at a complicated spectrum of localized states, containing a density-of-states peak and a soft gap.

2. FINDING THE DENSITY OF LOCALIZED STATES

The quantity

$$f = \left(\frac{d\ln g}{d\varepsilon}\right)_{\varepsilon = \mu} \quad (2)$$

can be found using (1) for any composition and fixed temperature at known thermopower S and activation energy ε_h of hopping conductivity. The quantity f is a function of electron density n in localized states. The predominance of the hopping conduction mechanism means that only a small proportion of electrons introduced by impurities are in extended states of the conduction band, and, therefore, we can assume with sufficient accuracy that the electron density n is equal to the difference of the donor and acceptor concentrations:

$$n = N_{In} - N_{Tl}. \quad (3)$$

Having a set of samples with varied thallium content, we obtain the function $f(n)$. The fixed content of indium producing localized states ensures an invariable density-of-states function $g(\varepsilon)$. Varying the chemical potential μ, we probe the function g at different energies and can reconstruct the density of states $g(\varepsilon)$ from the experimentally determined function $f(n)$.

Transforming the expression for f with the use of the equality

$$\frac{dn}{d\mu} = g(\mu) \quad (4)$$

gives

$$f = \frac{1}{g(\mu)}\frac{dg(\mu)}{d\mu} = \frac{1}{g(\mu)}\frac{dg(n)}{dn}\frac{dn}{d\mu} = \frac{dg}{dn}. \quad (5)$$

Obviously, at the edge of the impurity band $g \longrightarrow 0$, and, with the chemical potential approaching the edge, $n \longrightarrow 0$. This allows us to integrate (5):

$$g(n) = \int_0^n f(n')dn'. \quad (6)$$

Integration of (4) gives:

$$\mu - \mu_0 = \int_{n_0}^{n} \frac{dn'}{g(n')}, \quad (7)$$

where n_0 is the minimum of the available electron concentrations in samples with the maximum thallium content Tl, and μ_0 is the corresponding chemical potential. Numerical calculation of the integrals (6) and (7) gives the functions $\mu(n)$ and $g(n)$; i.e., the function $g(\mu)$ in the parametric form. Because of the limited solubility of thallium, it is impossible to reach the value $n_0 = 0$, which forces us to extrapolate the experimentally obtained function $f(n)$ to $n = 0$, but the result of calculation by formula (6) is qualitatively independent of the extrapolation method. As regards the constant μ_0 in formula (7), it remains unknown; i.e., the energy origin is undetermined.

The experimental data obtained at $N_{In} = 5$ at. % are presented in Table 1 for the temperature $T = 100$ K. After numerical integration using (6) and (7) we get a curve with a peak depicting the densities of localized states (Fig. 3).

Similar calculations were carried out for samples with indium content of 3 at. %, using the experimental data published in part earlier [5]. The sign of the thermopower was negative in these samples at any temperature. Additional doping was done both with donors (chlorine) and acceptors (thallium). An analysis of the temperature dependence of conductivity also demonstrated that the activation energy ε_h weakly depends on the concentration of additional impurities and can be taken to be (35 ± 5) meV in all samples. The data obtained from the thermopower S at room temperature $T = 300$ K are presented in Table 2. Calculation of the density-of-states function (Fig. 4) shows that this function is monotonic but has an inflection point instead of a maximum, which is, presumably, a weak manifestation of the indium-related impurity band.

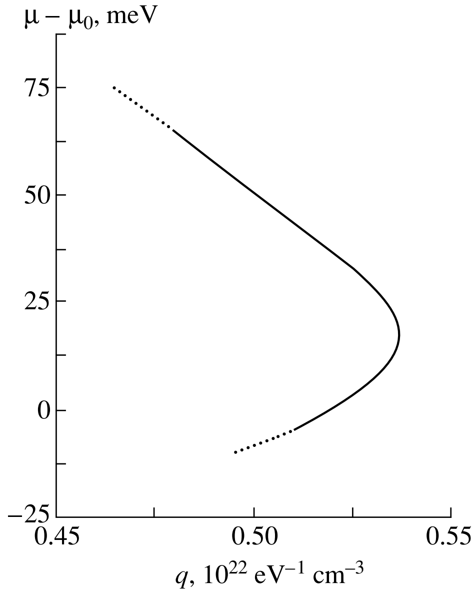

Fig. 3. Density of localized states g as a function of energy $\varepsilon = \mu$ in $(Pb_{0.78}Sn_{0.22})_{1-x}In_xTe$ sample at $x = 0.05$, $T = 100$ K.

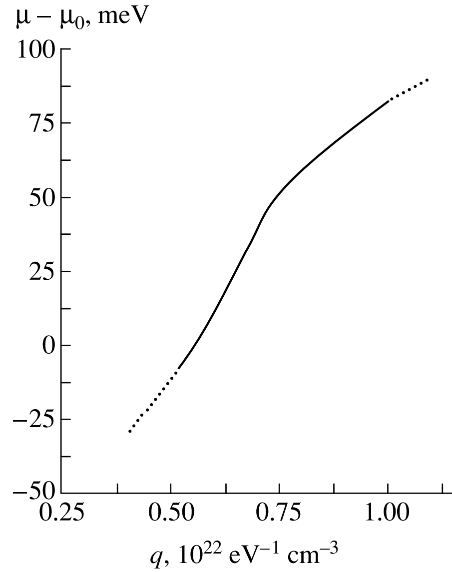

Fig. 4. Density of localized states g as a function of energy $\varepsilon = \mu$ in $(Pb_{0.78}Sn_{0.22})_{1-x}In_xTe$ sample at $x = 0.03$, $T = 100$ K.

3. NERNST–ETTINGSHAUSEN COEFFICIENT AT $x = 0.03$ AND ADDITIONAL DOPING WITH CHLORINE

Experimental data on the Nernst–Ettingshausen effect Q in $(Pb_{0.78}Sn_{0.22})_{0.97}In_{0.03}Te$ additionally doped with chlorine were presented in [6]. The data were discussed in terms of the model taking into account both the hopping conductivity via localized states, σ_h, and the band conductivity σ_b of electrons with energies above the mobility edge ε_C. The model employed explained the sign, the order of magnitude, and the type of the temperature dependence of the Nernst–Ettingshausen coefficient. At the same time, there are inaccuracies in the theoretical estimates made in [6] for a sample without additional doping. Firstly, the effective scattering parameter r was erroneously identified with the critical exponent obtained in the percolation theory. Secondly, the formulas used for estimation were derived for the case when the electron density of extended states is proportional to $\varepsilon^{1/2}$, whereas it would be more correct to assume it constant near the mobility edge in the narrow band having a width on the order of kT. Therefore, it is worthwhile to return to theoretical estimates of Q in order to refine and supplement the previous calculations by including into consideration the data for samples with additional doping. Moreover, the activation energy ε_h of hopping conductivity is

Table 2. Experimental Seebeck coefficients S at $T = 300$ K and the function $f(n)$ for $(Pb_{0.78}Sn_{0.22})_{0.97}In_{0.03}Te$ additionally doped with chlorine (samples C1–C7) and with thallium (samples T1–T4)

Sample no.	N_{Tl}, at. %	N_{Cl}, at. %	S, μV/K	n, 10^{20} cm^{-3}	f, eV^{-1}
C7		3.0	–190	9.0	13.6
C6		2.5	–140	8.3	9.9
C5		2.0	–95	7.5	6.8
C4		1.5	–88	6.8	6.5
C3		1.0	–80	6.0	5.8
C2		0.5	–55	5.3	3.9
C1		0	–38	4.5	2.5
T1	0		–38	4.5	2.5
T2	0.5		–100	3.8	6.8
T3	1.0		–150	3.0	10.6
T4	1.5		–140	2.3	9.0

obtained in the present study from the temperature dependence of the Nernst–Ettingshausen coefficient $Q(T)$ and compared with similar values obtained from the temperature dependences of conductivity $\sigma(T)$ and Hall coefficient $R(T)$.

The model taking into account two kinds of conduction gives, after some transformations, the following expression for the Nernst–Ettingshausen coefficient [6]:

$$Q = Q_b\frac{\sigma_b}{\sigma} + S_bR\sigma - SR\sigma, \quad (8)$$

where the measured quantities taking account of both conductivity mechanisms are written without subscripts, and the symbols with the subscript b stand for partial quantities that could be observed with only the band conduction mechanism. Three terms in (8) are respectively labeled as Q_1, Q_2 and Q_3,

$$Q = Q_1 + Q_2 + Q_3.$$

The quantity Q_3 is negative, its calculation by (8) creates no difficulties since the expression for Q_3, contains only directly measurable quantities: conductivity and Hall and Seebeck coefficients.

In estimating Q_2, we use the following expression for the thermopower S_b due to extended electronic states lying above the mobility edge:

$$S_b = -\frac{k}{e}\frac{\int_{\varepsilon_C}^{\infty}\left(-\frac{df_0}{d\varepsilon}\right)\left(\frac{\varepsilon-\mu}{kT}\right)\sigma(\varepsilon)d\varepsilon}{\int_{\varepsilon_C}^{\infty}\left(-\frac{df_0}{d\varepsilon}\right)\sigma(\varepsilon)d\varepsilon}, \quad (9)$$

where f_0 is the Fermi–Dirac distribution $\sigma(\varepsilon)d\varepsilon$ is the conductivity of electrons within the energy range $d\varepsilon$. As previously [6], we assume that the current flows via percolation channels above the mobility edge, and the function $\sigma(\varepsilon)$ is proportional to $(\varepsilon - \varepsilon_C)^t$, where t is the critical conductivity exponent equal to 1.6 [8]. Further, assuming $\mu < \varepsilon_C$, we replace f_0 by the Boltzmann distribution at $\varepsilon > \varepsilon_C$ and, using the integral representation for the gamma-function, we get

$$S_b = -\frac{k}{e}\left(t + 1 + \frac{\varepsilon_C - \mu}{kT}\right). \quad (10)$$

The quantity $\varepsilon_C - \mu$, equal to the activation energy ε_b of band conductivity, is relatively small [6] and cannot be found. (In the concluding part of this paper, discussing the activation energies obtained from various kinetic coefficients, we give one more proof of the small value of ε_b.) Therefore, we neglect, as before, the second term in (10) to obtain

$$Q_2 \approx 2.6\frac{k}{e}|R\sigma|. \quad (11)$$

The first term Q_1 in (8) is proportional to the partial Nernst–Ettingshausen coefficient Q_b for delocalized electrons. To estimate it, we must know the scattering parameter r characterizing the energy dependence of the relaxation time τ:

$$\tau \propto (\varepsilon - \varepsilon_C)^r. \quad (12)$$

The mobility edge acts here as the edge of an allowed band in the conventional theory of kinetic phenomena in semiconductors. It is known from this theory that the quantity $\sigma(\varepsilon)$ appearing in the integrand for the band conductivity is proportional to $G(\varepsilon)\tau(\varepsilon)$, where the function $G(\varepsilon)$ is determined by the energy dependence of the density of states $g(\varepsilon)$:

$$G(\varepsilon) = \int_{\varepsilon_C}^{\varepsilon} g(\varepsilon')d\varepsilon'. \quad (13)$$

Assuming that the density of states weakly varies within the layer of width kT near the mobility edge, $g(\varepsilon) \approx \text{const}$, we obtain $G(\varepsilon) \propto (\varepsilon - \varepsilon_C)$ and

$$\sigma(\varepsilon) \propto (\varepsilon - \varepsilon_C)\tau(\varepsilon) \propto (\varepsilon - \varepsilon_C)^{1+r}. \quad (14)$$

On the other hand, $\sigma(\varepsilon) \propto (\varepsilon - \varepsilon_C)^t$; therefore, $r = t - 1 = 0.6$.

Calculation of Q_b yields the same formula as that furnished by the theory of kinetic phenomena in nondegenerate semiconductors, regardless of the type of the density-of-states function $g(\varepsilon)$:

$$Q_b = -r\frac{k}{e}R_b\sigma_b. \quad (15)$$

Using the expression for the Hall coefficient, taking into account the hopping and band conduction mechanisms, we obtain [6]

$$R\sigma = R_b\sigma_b\frac{\sigma_b}{\sigma}, \quad (16)$$

which gives, with account of (8) and (15),

$$Q_1 = r\frac{k}{e}|R\sigma|. \quad (17)$$

Making use of formulas (8), (11), and (17), we can estimate all the three terms in the expression for the Nernst–Ettingshausen coefficient Q. The experimental data on kinetic coefficients of the samples studied at various temperatures are presented in Table 3. These values are used for theoretical estimates of the three terms in (8). As is evident from Table 4, the positive term Q_2 is the largest in absolute value. Only the term Q_3 is negative, and the sum of all three terms is positive in all cases, in accordance with the experimental data. The theoretical estimates also yield a correct order of magnitude for Q and a temperature dependence pattern consistent with the experiment.

Table 3. Experimental data for four kinetic coefficients for $(Pb_{0.78}Sn_{0.22})_{1-x}In_xTe$ at $x = 0.03$

N_{Cl}, at. %	T, K	σ, Ω^{-1} cm^{-1}	S, μV/K	R, cm^3/C	$Q/(k/e)$, cm^2/(V s)
0	150	5	–80	–17	300
	200	12	–41	–2.1	150
	300	28	–45	–0.35	80
1	150	9	–127	–35	700
	200	17	–80	–4.5	350
	300	30	–80	–0.7	150
2	150	11	–180	–70	800
	200	20	–120	–11	350
	300	30	–125	–1.6	150

Table 4. Results of the theoretical estimates for the Nernst–Ettingshausen coefficient $Q/(k/e)$ and for three components of it in the formula (8), cm^2/(V s)

N_{Cl}, at. %	T, K	$Q_1/(k/e)$	$Q_2/(k/e)$	$Q_3/(k/e)$	$(Q_1 + Q_2 + Q_3)/(k/e)$
0	150	50	220	–80	190
	200	15	65	–12	68
	300	6	25	–5	26
1	150	188	820	–465	543
	200	46	199	–20	225
	300	13	55	–5	63
2	150	460	2000	–1610	850
	200	132	570	–307	395
	300	29	125	–70	84

4. ACTIVATION ENERGIES OF THE HOPPING AND BAND CONDUCTIVITIES

Let us compare, considering only the exponential factors in the expressions for temperature dependence of the kinetic coefficients at predominating hopping conduction, the activation energies of the quantities:

$$\sigma \propto \exp\left(-\frac{\varepsilon_h}{kT}\right), \tag{18}$$

$$R^{-1} \propto \exp\left(-\frac{\varepsilon_R}{kT}\right), \quad \varepsilon_R = 2\varepsilon_h - \varepsilon_b, \tag{19}$$

$$Q^{-1} \propto \exp\left(-\frac{\varepsilon_Q}{kT}\right), \quad \varepsilon_Q = \varepsilon_h - \varepsilon_b, \tag{20}$$

where ε_h and ε_b are, respectively, the activation energies of hopping and band conductivity. The first two expressions are well known [8]; the third follows from the fact that all the three terms in the expression for the Nernst–Ettingshausen coefficient (8) are proportional to $R\sigma$.

The values of ε_h and ε_R for samples not subjected to additional doping have been compared earlier [3] (at $x = 0.03$, $\varepsilon_h = 44$ meV and $\varepsilon_R = 84$ meV), and it has been concluded that the parameter ε_b is relatively small and that the activation energy ε_R is approximately $2\varepsilon_h$. The ε_Q value, determined from the experimental data [6], is 37 meV, i.e., close to ε_h, which is the second independent proof of the smallness of ε_b. We determined all the three activation energies (18)–(20) from experimental data for samples additionally doped with chlorine. Taking into consideration the significant scatter of the obtained parameters, we compare the values averaged over five samples with a chlorine content Cl from 0 to 2 at. % (with 0.5 at. % increments): $\varepsilon_h = 35$ meV, $\varepsilon_R = 93$ meV, $\varepsilon_Q = 32$ meV. The relative values of these three parameters are also in agreement with the concept that the band conductivity is characterized by small activation energy ε_b and that the temperature dependence of the Hall and Nernst–Ettingshausen coefficients is governed mainly by the activation energy ε_h of hopping conductivity.

REFERENCES

1. S. N. Lykov, Yu. I. Ravich, and I. A. Chernik, Fiz. Tekh. Poluprovodn. (Leningrad) **11**, 1731 (1977) [Sov. Phys. Semicond. **11**, 1016 (1977)].
2. S. A. Nemov, Yu. I. Ravich, A. V. Berezin, *et al.*, Fiz. Tekh. Poluprovodn. (St. Petersburg) **27**, 299 (1993) [Semiconductors **27**, 165 (1993)].
3. Yu. I. Ravich, S. A. Nemov, and V. I. Proshin, Fiz. Tekh. Poluprovodn. (St. Petersburg) **29**, 1448 (1995) [Semiconductors **29**, 754 (1995)].
4. S. A. Nemov, V. I. Proshin, and Yu. I. Ravich, Fiz. Tekh. Poluprovodn. (St. Petersburg) **30**, 2164 (1996) [Semiconductors **30**, 1128 (1996)].
5. T. G. Abaĭdulina, S. A. Nemov, V. I. Proshin, and Yu. I. Ravich, Fiz. Tekh. Poluprovodn. (St. Petersburg) **30**, 2173 (1996) [Semiconductors **30**, 1133 (1996)].
6. S. A. Nemov, Yu. I. Ravich, V. I. Proshin, and T. G. Abaĭdulina, Fiz. Tekh. Poluprovodn. (St. Petersburg) **32**, 311 (1998) [Semiconductors **32**, 280 (1998)].
7. V. I. Kaĭdanov and Yu. I. Ravich, Usp. Fiz. Nauk **145**, 51 (1985) [Sov. Phys. Usp. **28**, 31 (1985)].
8. B. I. Shklovskiĭ and A. L. Éfros, *Electronic Properties of Doped Semiconductors* (Nauka, Moscow, 1979; Springer-Verlag, New York, 1984).
9. T. E. Whall, J. Phys. C **14**, L887 (1981).
10. S. A. Nemov and Yu. I. Ravich, Usp. Fiz. Nauk **168**, 817 (1998) [Phys. Usp. **41**, 735 (1998)].

Translated by S. Ktitorov

Semiconductors, Vol. 35, No. 2, 2001, pp. 164–169. Translated from Fizika i Tekhnika Poluprovodnikov, Vol. 35, No. 2, 2001, pp. 171–176.
Original Russian Text Copyright © 2001 by Zobov, Rizakhanov.

ELECTRONIC AND OPTICAL PROPERTIES OF SEMICONDUCTORS

The Spread of Cross Section for Electron Capture by a Trap with a Discrete Energy Level in γ-La_2S_3 Crystals

E. M. Zobov* and M. A. Rizakhanov

Institute of Physics, Dagestan Scientific Center, Russian Academy of Sciences, ul. 26 Bakinskikh komissarov 94, Makhachkala, 367003 Dagestan, Russia

**e-mail: kamilov@datacom.ru*

Submitted April 28, 2000; accepted for publication July 26, 2000

Abstract—The data on a new phenomenon (a formation of the range of values for an electron-capture cross section) are reported by the example of an electron trap with a discrete level of $E_c - 0.2$ eV in γ-La_2S_3 crystals; the data were obtained by employing the thermally stimulated luminescence. The range of variations in the cross section is as large as four orders of magnitude (10^{-23}–10^{-19} cm^2). A model, according to which the electron trap at $E_c - 0.2$ eV is a donor involved in the donor–acceptor pairs distributed in interatomic distances and localized in the vicinity of a negatively charged dislocation, is suggested. It is shown that the formation of a range of electron-capture cross sections is a result of a spread of the cross-section modulation factor at points with different values of potential of the dislocation electric field. *© 2001 MAIK "Nauka/Interperiodica".*

1. INTRODUCTION

Impurity-photoconductivity studies of fast electron traps related to donor–acceptor pairs (DAPs) and to single-, double-, and multiple-donor particles in II–VI compounds [2–9] have shown that these traps possess large electron capture cross sections ($S_t \geq 10^{-15}$ cm^2) characteristic of point defects with an attractive potential; in addition, it has been shown that the cross sections S_t decrease with increasing ionization energy (E_t) of the center in accordance with the theory of the charge-carrier nonradiative capture [10].[1]

An analysis of the known data on the kinetic properties of slow electron traps ($R \ll 1$) makes it possible to state that there are two groups of electron traps of this type. Slow electron traps of the first group are characterized by theoretically predictable kinetic properties, whereas the electron traps of the second group possess anomalous kinetic properties and are photoelectrically inactive [9, 11]. As the results of studying the thermally stimulated phenomena showed, these slow traps may feature the cross sections S_t that (irrespective of the electron-trap origin) decrease exponentially to very small values on the order of 10^{-25} cm^2 as the energy released during electron localization decreases (see, for example, [6, 9, 11–16]). If we hold to the conventional concepts of individual properties of both kinetic parameters and slow electron traps belonging to the second group, then their interpretation meets serious difficulties from the standpoint of both the statistical aspect of the center's charge state and the dynamic aspect of the mechanism of capturing the charge carriers by these centers.

Previously [6, 11], one of us suggested a model according to which the electron traps with anomalous kinetic properties are point defects located in the region of collective electric fields within large-scale imperfections in a crystal. If the cross sections S_t for both the fast and normal slow electron traps are intrinsic (unperturbed by other defects), then the cross sections of electron traps localized in the region of macroinhomogeneities become effective because of modulation by collective potential fields; to the first approximation, these cross sections may be represented as $S_t = S_{t0}\exp(-\varphi/kT)$. Here, S_{t0} is the intrinsic cross section, and φ is the recombination-macrobarrier height. This model not only accounts for the known anomalous properties of slow electron traps (for example, the exponential increase in the cross sections S_t with increasing E_t), but also leads to a number of other inferences [11]. In particular, a discrete cross section S_t of a separate electron trap may transform into a range of values without changing the energy spectrum. A necessary condition for this is the distribution of electron-trap atoms over the entire volume of the macroinhomogeneity, within which the field potential changes.

In this paper, we report for the first time the experimental evidence for the existence of cross section S_t expansion into the range of values; this evidence was obtained by the method of thermally stimulated luminescence (TSL) for an electron trap with a discrete level of $E_c - 0.2$ eV in γ-La_2S_3 crystals.

[1] According to the accepted concepts, the fast electron traps are the centers for which the ratio of the probability of electron capture to the probability of electron recombination is $R \gg 1$ [1].

1063-7826/01/3502-0164$21.00 © 2001 MAIK "Nauka/Interperiodica"

2. PHOTOELECTRIC AND THERMOLUMINESCENT PROPERTIES OF γ-La_2S_3

The photoconductivity spectrum of γ-La_2S_3 crystals at 295 K consists of two bands, the intrinsic and impurity-related (Fig. 1, curve *a*) bands. The photosensitivity to the light in the fundamental-absorption region increases with decreasing temperature, whereas the photosensitivity to impurity-absorption light first increases, attains a maximum in the vicinity of T = 190 K, and then decreases with a deactivation energy of 0.06 eV. At 90 K, only an intrinsic band is observed in the photoconductivity spectrum (Fig. 1, curve *b*).

The TSL of γ-La_2S_3 features a number of nontrivial properties. These properties manifest themselves most clearly in the measurements allowing for a variation in the photon energy of the preliminary excitation radiation. If integral light from the impurity-photoconductivity region ($h\nu \cong 2.0$–2.6 eV) is used for low-temperature preliminary excitation, a single broad band with a poorly resolved structure is observed in the TSL spectrum (Fig. 2, curve *a*). This band decomposes into a series of daughter bands if photons belonging to the impurity-photoconductivity region and having a certain energy are used for excitation. The daughter band located at the highest temperature corresponds to the photons with the lowest energy and shifts to lower temperatures as the energy $h\nu$ increases within the impurity-photoconductivity range (Fig. 2, curves *a*'–*e*'). The largest TSL-band shift amounts to 85 K. Preliminary excitation with light with a wavelength in the fundamental-absorption range gives rise to a TSL spectrum with a single discrete band at T_m = 110 K of another origin (Fig. 2, the dashed curve). Under the conditions of combined excitation with light corresponding to fundamental and impurity absorption, this band is adjacent to the broad TSL band on the low-temperature side.

The γ-La_2S_3 TSL possesses other properties as well. Dependence of the TSL intensity on the photon energy within the impurity-absorption range at the peaks of the amplitude-saturated daughter bands replicates the profile of the impurity-photoconductivity band (cf. curves *a* and *c* in Fig. 1). Preliminary excitation of γ-La_2S_3 with impurity-absorption light at 90 K, which is necessary for the observation of TSL, is not accompanied by photoconductivity and photoluminescence.

The thermally stimulated currents in γ-La_2S_3 possess similar properties. This is also evidenced by the results of pioneering studies of thermally stimulated currents in γ-La_2S_3 [17]; unfortunately, the kinetic parameters of electron traps were not estimated.

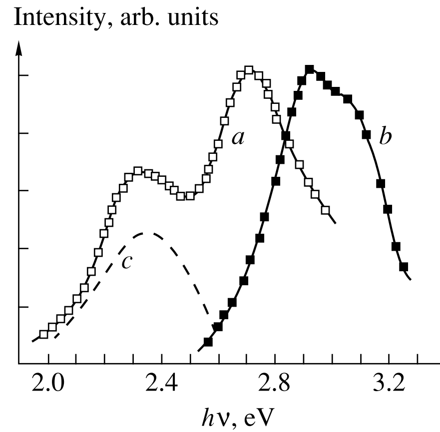

Fig. 1. Photoconductivity spectra of γ-La_2S_3 crystals at (*a*) 295 and (*b*) 90 K. Curve *c* represents the dependence of amplitude values of intensities of the daughter TSL bands on the photon energy of preliminary excitation.

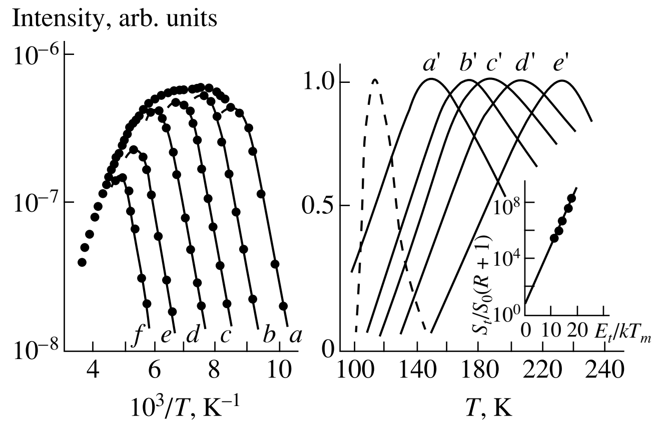

Fig. 2. (*a*) Integral TSL spectrum of the γ-La_2S_3 crystal measured with preliminary excitation with integral light belonging to the impurity band of photoconductivity ($h\nu \cong$ 2.0–2.6 eV). Curves (*b*–*f*) represent the calculated TSL spectra. The points correspond to experimental values of TSL intensities measured using thermal purification. Curves *a*'–*e*' represent a series of normalized daughter TSL bands for γ-La_2S_3. These bands are observed under preliminary irradiation with photons with energies $h\nu$ = (*a*') 2.58, (*b*') 2.48, (*c*') 2.3, (*d*') 2.13, and (*e*') 2.07 eV. The dashed line represents the TSL observed under preliminary exposure to the light corresponding to fundamental absorption ($h\nu \cong$ 3.0 eV). The recording rate for the TSL spectra was β = 0.16 K/s. The inset shows the straight line corresponding to the universal plot of $S_t/S_0(R + 1)$ vs. E_t/kT_m [24]; the points correspond to characteristic parameters of the electron trap with E_c – 0.2 eV and the daughter *a*'–*e*' bands.

3. EFFECT OF EXPANDING OF THE CROSS SECTION S_t TO A RANGE VALUES

As a rule, structurally complex thermally stimulated spectra are interpreted on the assumption that these spectra are related to an electron-trap set corresponding to the number of bands; each of the traps is characterized by the discrete parameters E_t and S_t. The γ-La_2S_3 TSL spectrum observed under excitation with integral light corresponding to the impurity absorption (Fig. 2, curve *a*) may be regarded as a structurally complex

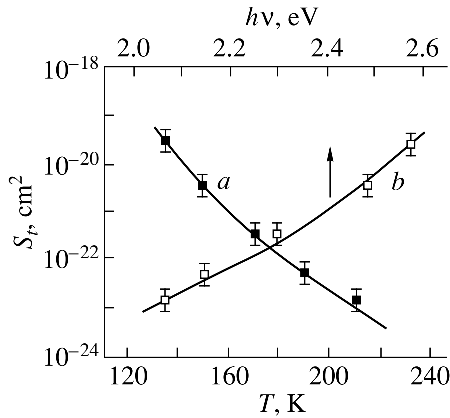

Fig. 3. Dependences of the cross section S_t of the electron trap with the level of $E_c - 0.2$ eV on (*a*) the temperature corresponding to the peaks of the daughter TSL bands in γ-La_2S_3 and (*b*) the energies of excitation photons.

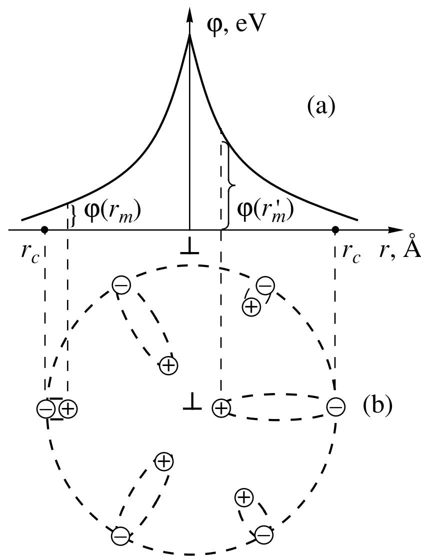

Fig. 4. (a) Hypothetical curves describing the variation in the electric-field potential of a negatively charged dislocation as the distance from its core increases; r_c is the distance from the dislocation core to the DAP acceptor centers; and $\varphi(r_m)$ and $\varphi(r'_m)$ are the heights of recombination barriers for electrons trapped by DAPs with r_m and r'_m. (b) A section of dislocation tube; for the sake of clarity, six arbitrary dipoles with different interatomic distances r_m are shown in the cross-section plane.

spectrum. However, analyzing it by "thermal purification" gives rise to the concept of a new type of electron trap with a single level $E_c - 0.2$ eV and a cross section S_t expanded to the range of 10^{-23}–10^{-19} cm^2.

The energy $E_t = 0.2$ eV is determined from the slope of the linear logarithmic dependence of the TSL intensity at the initial stage of its increase on the reciprocal temperature [18, 19]; i.e.,

$$\ln I = C - \frac{E_t}{kT}. \quad (1)$$

In accordance with the above statement that the electron-trap spectrum is monoenergetic ($E_t = E_c - 0.2$ eV), the slopes of the straight lines separated within the broad TSL band by thermal purification coincide (cf. curves *a*–*e* in Fig. 2) and are equal to 0.2 ± 0.01 eV. The cross sections were estimated with the formula [20, 21]

$$S_t = \frac{\beta I_{\text{ext}}}{v N_c \Delta T}, \quad (2)$$

however, formulas (1) and (2) may be used if the initial stage of an increase in TSL can be identified. In formula (2), β is the rate of sample heating in the course of recording the TSL spectra, N_c is the effective density of electron states in the conduction band, and v is the electron thermal velocity. The quantity I_{ext} is the extrapolated value of TSL intensity at the intersection point of the straight line given by (1) with the ordinate corresponding to $T^{-1} = 0$ under the condition that the amplitude value of TSL intensity is normalized and is equal to unity (in arbitrary units). In the case of complex spectra, the half-width ΔT may be determined to a reasonable accuracy as the doubled value of the half-width of the low-temperature component of the discrete band extracted by thermal purification. Under the same condition of amplitude value normalization, formula (2) can be used to estimate the S_t cross section using not only the TSL method but also other thermal stimulation methods.

The dependences of the cross section S_t on the photon energy in the preliminary excitation of the daughter TSL bands and on the temperature positions T_m of the peaks of these bands are shown in Fig. 3.

The reliability of the values of E_t and S_t measured using (1) and (2) is supported by good agreement between the contours of experimental TSL bands (they are represented by points in Fig. 2) and those of the TSL bands calculated with the formula [22, 23]

$$I(T) = \nu_t \exp\left(-\frac{E_t}{kT}\right) \times \exp\left[-\frac{\nu_t}{\beta}\left(\frac{kT^2}{E_t}\right)\exp\left(-\frac{E_t}{kT}\right)\left(1 + \frac{4kT}{E_t}\right)\right] \quad (3)$$

the results of calculations are shown by continuous lines *a*–*f* in Fig. 2. When calculating $I(T)$, we used experimental values E_t and the frequency factor $\nu_t = vN_cS_t = \frac{\beta I_{\text{ext}}}{\Delta T}$ [see formula (2)]. In order to prove that the parameters E_t and S_t are reliable and that the electron traps with $E_t = E_c - 0.2$ eV belong to the class of

slow electron traps, we demonstrated that these parameters along with the parameters of the daughter TSL bands (see the inset in Fig. 2, the points) fall on the previously [24] suggested universal plot $[S_t/S_0(R+1)$ vs. $E_t/kT_m]$ for the characteristic parameters of thermally stimulated spectra (T_m and β) and electron traps (E_t, S_t, and R) in semiconductors and insulators (see the inset in Fig. 2, the straight line) provided that the capture factor $R = 0$. The slope of this plot with respect to the horizontal axis E_t/kT_m is equal to 0.45. The coordinates of the origin point are (5, 0). The quantity S_0 is defined as $S_0 = \beta/nN_cT_m$.

4. A MODEL OF ELECTRON TRAP WITH $E_t = E_c - 0.2$ eV

As a rule, the electron-trap atoms and the TSL-excitation centers are spatially separated. Their wave functions do not overlap, which rules out the process of direct transfer of charge carriers between them. An attempt to interpret correctly the nontrivial special features of TSL in γ-La_2S_3 suggests that the corresponding thermoluminescence-active centers are structurally complex and that the nonequilibrium accumulation of electrons at these centers may be accomplished only by the extraband (interimpurity) mechanism.

According to the multiparameter model we suggest, the roles of the electron trap with $E_t = E_c - 0.2$ eV and the corresponding excitation center (the TSL-excitation center) are played by the donor and acceptor, respectively, of the same DAPs that possess a number of unusual properties. These DAPs are distributed in interatomic distances (r_m) and are located around a negatively charged dislocation in such a manner that the acceptor atoms in all the pairs occupy the quasi-equidistant positions relative to the dislocation core, whereas the donor atoms are randomly distributed in the space between this core and the acceptor atoms. The DAPs, together with the dislocation core, form the space charge of the dislocation tube (Fig. 4). Kinetic parameters of the donor incorporated into the DAP are modulated by an electric field of dislocation. The modulation factor depends on the spatial extent of the DAPs; therefore, the latter are distributed not only in r_m and in the energy of interimpurity electron transition $h\nu_m$ but also in the cross section S_t. The donor that acts directly as an electron trap has an excited state E_c – 0.06 eV in addition to the ground trap state $E_c - 0.2$ eV. The distribution of the DAPs in r_m is such that only the wave functions of the donor excited state ($E_c - 0.06$ eV) and the acceptor ground state ($E_V + 0.54$ eV) overlap in the DAPs.

It is also worth noting here that, in the polycrystalline sample, the role of sources of macroscopic electric fields may be played not only by dislocations but also by intercrystallite boundaries.

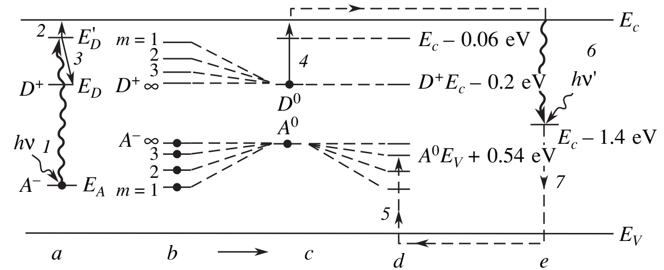

Fig. 5. (*a*) A scheme of energy levels of unexcited $(A^- - D^+)^0$ centers with a certain value of r_m. (*b*) The energy spectrum of the $(A^- - D^+)^0$ DAP ground states distributed in r_m. (*c*, *d*) The energy spectrum of a DAP in the excited state $(A^0 - D^0)^0*$ and in the semiexcited state $(A^0 - D^+)^+$. (*e*) The energy level of the recombination center. The electron transitions indicated by the arrows are described in the text.

5. INTERPRETATION OF PHOTOELECTRIC AND THERMOLUMINESCENT PROPERTIES

In terms of the model we suggest, the impurity photoconductivity of γ-La_2S_3 crystals is a result of two-stage ionization of DAPs. The first (optical) stage involves an intracenter transition of electrons from the acceptor's ground state to the donor's excited state (Fig. 5, scheme *a*, transition *1*). In the second stage, a thermal emission from the donor's excited state to the conduction band occurs (transition *2*).

Thermooptical processes "freeze" as the temperature is lowered. Simultaneously, the rate of transition of electrons (transferred optically to the donor's excited state) to the donor's ground state (transition *3*) increases. According to experimental data, the impurity photoconductivity of γ-La_2S_3 is thermally quenched with a rate governed by the thermal ionization energy of the donor's excited state ($E_c - 0.06$ eV).

The spectrum of DAPs distributed in r_m and $h\nu_m$ is polyenergetic (Fig. 5, scheme *b*). The absence of the relevant structure in the impurity-photoconductivity spectra (Fig. 1, curve *a*) indicates that the half-width of individual photoconductivity bands is much larger than the energy spacing between the neighboring levels of DAP.

As a result of the quantum-mechanical condition for the overlap of the wave functions of the acceptor's ground state only with those of the donor's excited state, the electrons transferred via an intracenter transition to the donor's ground state ($E_c - 0.2$ eV) at fairly low temperatures (Fig. 5, scheme *a*, transitions *1*, *3*) remain linked to the above states. These electrons can be neither involved in the transitions from the donor's ground state to the conduction band nor involved in the interimpurity donor ⟶ acceptor transitions. Since, in this temperature region, not only electrons but also holes appearing simultaneously at the acceptor atoms with their deeper state ($E_V + 0.54$ eV) remain bound, the lifetime of the excited (inversely populated) DAP

state may be infinitely long. Such three-level systems are of interest for the efficient "conservation" of optical energy.

The destruction of the inversely populated state by heating the γ-La_2S_3 crystals is accompanied by TSL, which is a result of the thermal emission of electrons from the DAP donor atoms to the conduction band and the subsequent radiative recombination of these electrons. Studies of spectral distribution of the TSL intensity suggest that the center with a level of E_c – 1.4 eV (presumably, the lanthanum vacancy), rather than the DAP directly responsible for the generation and accumulation of stored optical energy, acts as recombination center [25]. The charge carriers released from a DAP (Fig. 5, schemes *c*, *d*, transitions *4*, *5*) arrive at the center with E_c – 1.4 eV via the allowed bands (Fig. 5, scheme *e*, transitions *6*, *7*). The fact that DAPs are recombinationally inactive may be caused by the following two mechanisms. In the range of thermal ionization of the donor with the level of E_c – 0.2 eV, the probability of electron transitions from the excited donor state to the conduction band is higher than the probability of their interimpurity transition from this state to the acceptor's ground state. In addition, the thermal ionization and conversion of a donor to a charged state leads to a shift of the acceptor level towards the valence band and to a decrease in the lifetime of the holes localized at this level. The thermal ionization of an acceptor (Fig. 5, scheme *d*, transition *5*), made easier by interimpurity interaction [26], also rules out the electron transitions from the conduction band to the acceptor DAP. The short lifetimes of charge carriers captured separately by a DAP make it possible to understand why these carriers cannot be transferred to the excited (inversely populated) state under the conditions of γ-La_2S_3 irradiation with light corresponding to the fundamental-absorption region.

The suggested model, according to which TSL excitation is responsible for the low-temperature intracenter electron transitions in a DAP without generation of free charge carriers, can also be used to naturally interpret the "latent" mechanism of the TSL excitation.

A transition of a DAP to an excited state $(D^0 - A^0)^{0*}$ upon absorption of photons with energies corresponding to the impurity absorption results in the "condensation" of their *A* and *D* levels in the single-energy lines (Fig. 5, schemes *b*, *c*). Because of this, only a single unshifted (in depth) trap state E_c – 0.2 eV characteristic of an isolated donor is observed.

As we pass from compact to spatially extended pairs, the donor atoms become more and more involved in the electric field of dislocation with an ever increasing potential (Fig. 4). As a result, the height of the potential barrier for electrons passing to the DAP donor atoms increases, whereas the corresponding cross section S_t decreases. Obviously, the donor cross section S_t expands into a range of values. As r_m increases, it is not only the value of S_t, which governs the temperature position of the daughter TSL bands, that decreases. Simultaneously, the energy of interimpurity electron transition in a DAP decreases as well. Exposure of γ-La_2S_3 to photons with energies corresponding to the impurity absorption leads to the selective excitation of DAP with certain values of r_m, $h\nu_m$, and S_t. This circumstance explains the origin of the decomposition of integral TSL spectrum into daughter bands, the shape of the functional dependences $S_t = f(h\nu)$ and $S_t = f(T_m)$ (Fig. 3), and the consistency between spectral distribution of the impurity-photoconductivity intensity and the intensity amplitudes of the daughter TSL bands (Fig. 1, curves *a*, *c*).

The knowledge of cross sections limiting the range of the values of S_t (Fig. 3) makes it possible to assess the variation in the macrobarrier height $\Delta\varphi$ when passing from the most compact of the observable DAPs to the most extended (Fig. 4). The corresponding calculations based on the assumption that $S_t = S_{t0}\exp(-\varphi/kT_m)$ and that the intrinsic cross section S_{t0} is in the range of 10^{-15}–10^{-17} cm^{-2} (as in the case of neutral donors) yield the difference $\Delta\varphi = 0.21 \pm 0.02$ eV.

6. CONCLUSION

A number of implications follow from the suggested model of an electron trap with a level of E_c – 0.2 eV; when experimentally studied, these implications may additionally validate this model. In particular, we bear in mind the effect of the destruction of the DAP's inversely populated state by infrared illumination. New studies are also necessary to clarify the DAP origin and the cause of the quasi-equidistant arrangement of acceptor atoms around the dislocation core.

REFERENCES

1. S. M. Ryvkin, *Photoelectric Effects in Semiconductors* (Fizmatgiz, Moscow, 1962; Consultants Bureau, New York, 1964).
2. M. A. Rizakhanov and F. S. Gabibov, Fiz. Tekh. Poluprovodn. (Leningrad) **13**, 1324 (1979) [Sov. Phys. Semicond. **13**, 776 (1979)].
3. M. A. Rizakhanov, Yu. N. Émirov, and N. A. Abilova, Fiz. Tekh. Poluprovodn. (Leningrad) **14**, 1665 (1980) [Sov. Phys. Semicond. **14**, 991 (1980)].
4. M. A. Rizakhanov and E. M. Zobov, Fiz. Tekh. Poluprovodn. (Leningrad) **14**, 2407 (1980) [Sov. Phys. Semicond. **14**, 1429 (1980)].
5. M. A. Rizakhanov, Fiz. Tekh. Poluprovodn. (Leningrad) **16**, 699 (1982) [Sov. Phys. Semicond. **16**, 448 (1982)].
6. M. A. Rizakhanov, Author's Abstract of Doctoral Dissertation (Vilnius, 1982).
7. M. A. Rizakhanov and M. M. Khamidov, Pis'ma Zh. Tekh. Fiz. **11** (9), 561 (1985) [Sov. Tech. Phys. Lett. **11**, 234 (1985)].
8. E. M. Zobov, G. G. Garyagdyev, and M. A. Rizakhanov, Fiz. Tekh. Poluprovodn. (Leningrad) **21**, 1637 (1987) [Sov. Phys. Semicond. **21**, 991 (1987)].

9. F. S. Gabibov, E. M. Zobov, G. G. Garyagdyev, *et al.*, in *Photoelectronics* (Vishcha Shkola, Kiev, 1987), No. 1, p. 54.
10. G. Ascarelli and S. Rodrigues, Phys. Rev. **124**, 1321 (1961).
11. M. A. Rizakhanov and M. M. Khamidov, Fiz. Tekh. Poluprovodn. (St. Petersburg) **27**, 721 (1993) [Semiconductors **27**, 397 (1993)].
12. K. H. Nicholas and T. Woods, Br. J. Appl. Phys. **5**, 783 (1964).
13. A. G. Zhdan, V. B. Sandomirskij, and A. D. Ozheredov, Solid-State Electron. **11**, 783 (1968).
14. V. P. Mushinskiĭ and V. P. Ambros, Izv. Vyssh. Uchebn. Zaved., Fiz., No. 4, 135 (1972).
15. V. M. Lupin and P. E. Ramazanov, Izv. Vyssh. Uchebn. Zaved., Fiz., No. 6, 142 (1976).
16. V. Ya. Kunin, A. N. Tsikin, and N. L. Shturbina, Fiz. Tverd. Tela (Leningrad) **15**, 3417 (1973) [Sov. Phys. Solid State **15**, 2276 (1973)].
17. A. N. Georgobiani, V. I. Demin, and E. S. Logozinskaya, Tr. Fiz. Inst. im. P.N. Lebedeva, Akad. Nauk SSSR **182**, 69 (1987).
18. V. V. Antonov-Romanovskiĭ, Izv. Akad. Nauk SSSR, Ser. Fiz. **10**, 477 (1946).
19. G. F. T. Garlic and A. F. Gibson, Proc. Phys. Soc. London, Sect. A **60** (342), 574 (1948).
20. M. A. Rizakhanov, Izv. Vyssh. Uchebn. Zaved., Fiz., No. 1, 153 (1971).
21. M. A. Rizakhanov, *Electron-Oxygen Quasi-Particles in Proteins. Electronic–Atomic Theories of Elementary Photobiological Phenomena* (Bari, Makhachkala, 1998).
22. Ch. B. Lushchik, *Investigation of Trapping Centers in Alkali-Halide Phosphor Crystals* (Tartu, 1955).
23. S. V. Bulyarskiĭ and N. S. Grushko, *Generation–Recombination Effects in Semiconductor Structures* (Ul'yanovsk. Gos. Univ., Ul'yanovsk, 1997).
24. M. A. Rizakhanov, Fiz. Tverd. Tela (Leningrad) **31** (11), 193 (1989) [Sov. Phys. Solid State **31**, 1946 (1989)].
25. E. M. Zobov, V. V. Sokolov, A. Kh. Sharapudinova, and S. M. Luguev, Fiz. Tverd. Tela (St. Petersburg) **35**, 636 (1993) [Semiconductors **35**, 325 (1993)].
26. M. A. Rizakhanov, Fiz. Tekh. Poluprovodn. (Leningrad) **9**, 2002 (1975) [Sov. Phys. Semicond. **9**, 1310 (1975)].

Translated by A. Spitsyn

Semiconductors, Vol. 35, No. 2, 2001, pp. 170–174. Translated from Fizika i Tekhnika Poluprovodnikov, Vol. 35, No. 2, 2001, pp. 177–181.
Original Russian Text Copyright © 2001 by Averkiev, Gutkin, Sedov.

Photoluminescence of $Cu_{Ga}Te_{As}$ and $Cu_{Ga}Sn_{Ga}$ Complexes in *n*-GaAs under Resonance Polarized Excitation

N. S. Averkiev, A. A. Gutkin, and V. E. Sedov

Ioffe Physicotechnical Institute, Russian Academy of Sciences, Politekhnicheskaya ul. 26, St. Petersburg, 194021 Russia

Submitted July 17, 2000; accepted for publication July 26, 2000

Abstract—Photoluminescence (PL) of *n*-type GaAs:Te:Cu and GaAs:Sn:Cu with an electron density of about 10^{18} cm^{-3} was studied at 77 K. A broad band with a peak at the photon energy near 1.30 eV (GaAs:Te:Cu) or 1.27 eV (GaAs:Sn:Cu) was dominant in the PL spectrum under interband excitation. This band arose from the recombination of electrons with holes trapped by $Cu_{Ga}Te_{As}$ or $Cu_{Ga}Sn_{Ga}$ complexes. It has been found that the low-energy edge of the excitation spectrum of this PL band at photon energies below ~1.4 eV is controlled by the optical ejection of electrons from a complex into the conduction band or to a shallow excited state. The PL polarization factors upon excitation by polarized light from this spectral range suggest that the complexes have no additional distortions caused by an interaction of a hole bound at the center in the light-emitting state with local phonons of low symmetry. This feature makes $Cu_{Ga}Te_{As}$ and $Cu_{Ga}Sn_{Ga}$ complexes different from those with the Ga vacancy (V_{Ga}) instead of Cu_{Ga}. The dissimilarity arises from the difference in the intensity of interaction of a hole localized at the orbital of an isolated deep-level acceptor in the state corresponding to its pre-emission state in the complex (Cu_{Ga}^{-} and V_{Ga}^{2-}) with low-symmetry vibrations of atoms. The perturbation of the hole orbital induced by the donor in the complex practically does not affect this interaction. *© 2001 MAIK "Nauka/Interperiodica".*

1. INTRODUCTION

It is known that the optical properties of complexes containing a gallium vacancy (V_{Ga}) and a shallow donor (Te_{As} or Sn_{Ga}) in the neighboring lattice sites of GaAs are determined to a significant extent by additional distortions, which are induced by the interaction of carriers localized at the complex with noncompletely symmetric phonons [1–4]. A phenomenological model, which qualitatively describes the spatial structure and features of the optical properties of these defects, relates their distortion to the Yahn–Teller effect that exists in an isolated vacancy V_{Ga} [5, 6]. Studies of the transformations of these properties by the substitution of V_{Ga} by another deep acceptor is essential for understanding the effect of complex component characteristics on these properties. As the objects of such studies, $Cu_{Ga}Te_{As}$ and $Cu_{Ga}Sn_{Ga}$ complexes can be chosen; in *n*-GaAs:Te(Sn):Cu subjected to interband excitation, these complexes give rise to a photoluminescence (PL) band with a peak at the photon energy of ~1.3 eV [7–9]. This emission is related to the trapping of the conduction-band electron by the above complexes. The properties of PL under the polarized resonance excitation are studied and reported in this paper. The results are compared with the similar data for $V_{Ga}Te_{As}$ and $V_{Ga}Sn_{Ga}$ complexes.

2. EXPERIMENTAL

The properties of the PL band studied are controlled only by complexes resonantly excited by optical ejection to the conduction band, if all the complexes in the initial state are occupied by electrons. This condition is easily fulfilled if the semiconductor remains *n*-type after doping with Cu. At the same time, the Cu concentration should be sufficiently high to ensure intense luminescence. We introduced Cu by diffusion. This process is complicated by the fact that Cu forms eutectic and chemical compounds with As [10], which evaporates from the GaAs surface during diffusion or is introduced into the cell in order to prevent this evaporation. We failed to satisfy the above conditions, which concern the Cu concentration in GaAs, by diffusion from the sputtered layer. Therefore, we prepared the samples by gas-phase diffusion, for which purpose a piece of Cu was placed in the cell. As an initial material, the *n*-GaAs crystals grown by the Czochralski method and doped with Te or Sn up to an electron concentration of ~10^{18} cm^{-3} were used. A broad band peaked at the photon energy near 1.2 eV and associated with an emission of $V_{Ga}Te_{As}$ and $V_{Ga}Sn_{Ga}$ complexes was dominant in the PL spectra of these crystals. Six oriented samples in a rectangular-parallelepiped shape ~$3 \times 3 \times 20$ mm in size and a piece of Cu with a mass of ~100 mg were placed in a silica cell with a volume of ~6 cm^3. The diffusion parameters (a duration of

1063-7826/01/3502-0170$21.00 © 2001 MAIK "Nauka/Interperiodica"

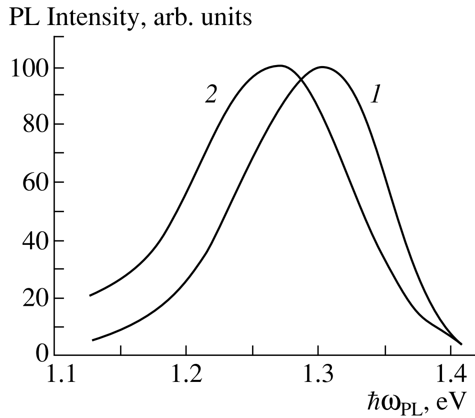

Fig. 1. Photoluminescence spectra of (*1*) *n*-GaAs:Te:Cu and (*2*) *n*-GaAs:Sn:Cu at 77 K for the interband excitation.

~80 h and a temperature of ~760°C) ensured a uniform distribution of complexes in the bulk of the samples and their concentration within the range required. The cell was furnace-cooled. After diffusion, a ~100 μm thick layer was ground off the sample surface, and the samples were polished in $H_2SO_4 : H_2O_2$ etchant. The PL spectra were measured under He–Ne laser excitation (the flux density was ~2 × 10^{19} s^{-1} cm^{-2}). PL was detected in the photon energy range $\hbar\omega_{PL}$ = 0.9–1.55 eV using a germanium photodiode. Under the resonance excitation, PL was detected by a photomultiplier cooled by liquid-nitrogen vapor with a high quantum efficiency up to the photon energy of ~1.2 eV. To eliminate the influence of the scattered exciting light, an InP filter was placed in front of the photomultiplier. The PL polarization was measured (similar to [2, 4, 11]) in an orthogonal scheme for two configurations of the experiment: (i) the direction of the exciting light was [110] and the direction of the radiation detected was [001] (configuration [110]–[001]), and (ii) the direction of the exciting light was [100] and the direction of the radiation detected was [001] (configuration [100]–[001]). Consistent with these configurations, the faces of the samples under study were the (110) and (001) or (100) and (001) planes. In order to determine the PL degree of polarization $\rho = (I_\parallel - I_\perp)/(I_\parallel + I_\perp)$, we measured the intensities of radiation $I_\parallel$ and $I_\perp$ with the electric vector parallel and perpendicular, respectively, to the sample plane. The electric vector of the polarized exciting light was perpendicular or parallel to the emission direction. All the measurements were carried out at 77 K.

3. RESULTS

As a result of diffusion, the electron concentration in the samples barely changed, and in the PL spectra of the crystals the 1.2 eV band disappeared, and, in its place, a band associated with $Cu_{Ga}Te_{As}$ and $Cu_{Ga}Sn_{Ga}$ appeared and prevailed. The peak of this band under the interband excitation for the samples doped with Te and

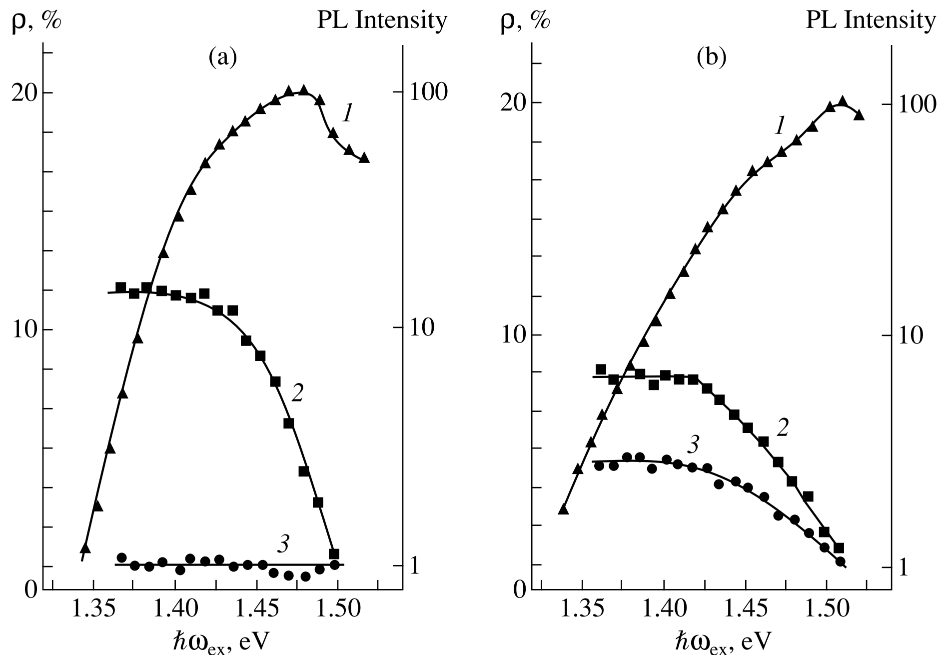

Fig. 2. (*1*) Excitation spectra of the 1.3 eV photoluminescence band and dependences of its degree of polarization (*2*) ρ_1 and (*3*) ρ_2 on the photon energy of the exciting light at 77 K. The photon energies of the emission detected correspond to the band peak. (a) For *n*-GaAs:Te:Cu; (b) for *n*-GaAs:Sn:Cu.

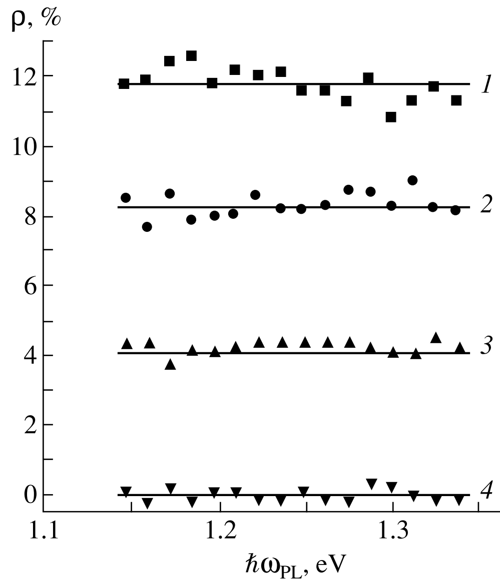

Fig. 3. Distributions of the degree of photoluminescence polarization (*1* and *2*) ρ_1 and (*3* and *4*) ρ_2 inside the 1.3 eV band. The exciting light photon energy is 1.385 eV. Lines *1* and *4* correspond to *n*-GaAs:Te:Cu; *2* and *3* are for *n*-GaAs:Sn:Cu.

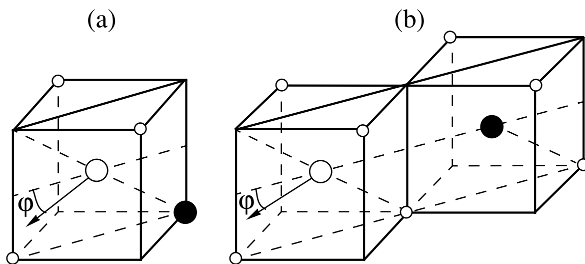

Fig. 4. Possible directions of dipole axes, which characterize the optical properties of (a) $Cu_{Ga}Te_{As}$ and (b) $Cu_{Ga}Sn_{Ga}$ complexes in GaAs. Small unshaded circles represent As atoms; large unshaded circles, Cu atoms; and shaded circles represent donor atom (Te or Sn).

Sn was near photon energies of 1.3 and 1.27 eV, respectively (Fig. 1). Studies have shown that this PL is also excited in *n*-GaAs by photons with an energy ($\hbar\omega_{ex}$) less than the band gap (E_g) (Figs. 2, 3). If the electric vector of the exciting light was perpendicular to the observation direction, then the PL was polarized for certain configurations of the experiment (Figs. 2, 3). For the electric vector of light parallel to the observation direction, the PL polarization was absent. These facts testify that the emitting centers are anisotropic and uniformly distributed over all the possible orientations in the crystal, and their excitation for $\hbar\omega_{ex} < E_g$ is at least partially caused by optical transitions of electrons bound at the centers to the conduction band rather than by a hole capture. The leveling off of the spectral dependence of the degree of polarization for fairly small $\hbar\omega_{ex}$ (Fig. 2) indicates that such resonance excitation in this photon energy region is unique. As shown in Fig. 3, the polarization degree of emission was nearly independent of $\hbar\omega_{PL}$ in the region of the band studied. This means that the contribution of centers noticeably differing from those of the complexes under study is insignificant in this emission. As follows from Figs. 2 and 3, the degree of polarization of the band under the resonance excitation by the light with the electric vector perpendicular to the observation direction ρ_1 (configuration [110]–[001]) and ρ_2 (configuration [100]–[001]) is ~12 and 0%, respectively, for complexes $Cu_{Ga}Te_{As}$ and is ~8 and ~4% for complexes $Cu_{Ga}Sn_{Ga}$.

4. DISCUSSION

The values of ρ_1 and ρ_2 presented in the previous section allow us to determine the parameters of optical dipoles, which describe the defects under study in single-dipole approximation. Since $\rho_1 \neq 0$ and $\rho_2 = 0$ for $Cu_{Ga}Te_{As}$ complexes, the axis of the optical dipole for these defects is directed along one of the $\langle 111\rangle$ axes of a crystal according to calculations [10, 12, 13]. This could be either the axis passing through the Cu and Te atoms, or one of the other three $\langle 111\rangle$ axes (Fig. 4). The first variant would mean that the Yahn–Teller effect is absent. The second variant would mean that, in contrast, the Yahn–Teller effect is sufficiently profound, and the combined impact of the displacement of the complex atoms and the donor field turns out to be sufficient to direct the optical dipole of a defect along the $\langle 111\rangle$ axis which does not coincide with an initial Cu_{Ga}–Te_{As} axis. This suggestion is implausible, and, therefore, the $Cu_{Ga}Te_{As}$ complex should be considered as having no Yahn–Teller distortions. As for the $Cu_{Ga}Sn_{Ga}$ complex, one would expect its symmetry to be monoclinic and it to have a symmetry plane (Fig. 4). In fact, even the interaction with phonons of low symmetry does not lower the symmetry of the center [2, 3], as the studies of the $V_{Ga}Sn_{Ga}$ complex show, this being similar in its initial structure to the $Cu_{Ga}Te_{As}$ complex. For such centers, $\rho_1 = 0$ and $\rho_2 \neq 0$, and the magnitude of the angle φ, which determines the optical dipole direction (Fig. 4), is related to ρ_1 and ρ_2 by the following formula [10]:

$$\tan\varphi = \pm\sqrt{\frac{1}{2} + \frac{\rho_2}{\rho_1}\left(1 \pm \sqrt{\frac{3\rho_1}{2\rho_2} + 1}\right)}. \qquad (1)$$

For the $Cu_{Ga}Sn_{Ga}$ complex, $\rho_2/\rho_1 \simeq 0.5$ and, among the possible values of the angle φ determined by (1) ($\varphi_1 = 0$ and $\varphi_{2,3} = \pm 54.8°$), a value exists that corresponds to the absence of additional distortions of a complex ($\varphi = 0$). Given the similarity to $Cu_{Ga}Te_{As}$ complexes, this value can be assumed to be φ, which also corresponds to reality for the $Cu_{Ga}Sn_{Ga}$ complex. The coincidence of

the optical dipole axis with the initial axis of $Cu_{Ga}Te_{As}$ and $Cu_{Ga}Sn_{Ga}$ complexes distinguishes these complexes from the corresponding complexes containing V_{Ga} instead of Cu_{Ga}, in which the directions of the axes indicated markedly differ due to displacements of the defect atoms [2, 4].

We now determine the relative fraction (μ) of the rotator in the emission and absorption of light by the optical dipoles of the complexes under study. According to [2, 10], we have

$$\mu = \frac{1}{2} + \frac{\frac{1}{2}(3\rho_1 + 2\rho_2) \pm \sqrt{(3\rho_1 + 2\rho_2)(3 - \rho_2)}}{4 - \rho_1 - 2\rho_2}. \quad (2)$$

Substituting into (2) the experimental values of ρ_1 and ρ_2, we obtain two values of $\mu \sim 0.28$ and ~ 0.82, which are approximately equal for $Cu_{Ga}Te_{As}$ and $Cu_{Ga}Sn_{Ga}$ complexes and are markedly larger than the values of ~ 0.18 for $V_{Ga}Te_{As}$ and $V_{Ga}Sn_{Ga}$ complexes [2]. Such an enhancement of the rotator fraction may be due, at least partially, to the absence of distortions and the related mixing of the wave functions of the complex states, which are split owing to the spin–orbit interaction. This enhances the relative role of the spin–orbit interaction, which reduces the component of the emission electric vector, which is parallel to the axis of each center [14, 15]. In the classic dipole approximation under consideration, such a decrease in the degree of polarization is described by the enhancement of the rotator fraction μ.

However, it is worth noting that, within the trigonal acceptor–donor complex model, where a state with symmetry Γ_8 becomes the ground one as a result of the spin–orbit splitting of the initial t_2-level of the acceptor that is similar in symmetry to the GaAs valence band, a minimal value of ρ_1 is shown to be equal to 25%. This value is twice as large as the experimental value. Such a discrepancy between the theoretical and experimental data may be associated with the simplification of the model, in which the effect of random deformation and electric fields is disregarded, as well as the mixing of the complex ground state with states that do not arise from the initial t_2-level.

CONCLUSION

Thus, the optical properties of $Cu_{Ga}Te_{As}$ and $Cu_{Ga}Sn_{Ga}$ complexes in *n*-GaAs are described by a model which implies the absence of additional distortions induced by the interaction of carriers bound at the complexes with the vibrations of low symmetry. This reveals a substantial difference of these defects from $V_{Ga}Te_{As}$ and $V_{Ga}Sn_{Ga}$ complexes with similar structures; such distortions exist in the latter and strongly affect the emission polarization and the light absorption by the centers. Qualitatively, such a difference can be explained as follows. We may assume that a hole appearing at the complex in an emitting state is localized at the orbitals of a deep acceptor. It is known that, in the state Cu_{Ga}^- (which corresponds to the acceptor state in the complexes under study prior to the emission), a center formed by an isolated Cu atom binds the hole, whose interaction with a noncompletely symmetric vibration is minimal and does not result in the static distortions of the center [16]. As, in the complex (Cu_{Ga}—donor), the hole state is one of the acceptor states split under the donor influence, one can expect that, in this case also, the situation indicated is retained. On the other hand, the isolated V_{Ga} in the state V_{Ga}^{2-} and probably also in the V_{Ga}^- state, which can correspond to the state of a deep acceptor in the (V_{Ga}–shallow donor) complexes prior to emission, is subjected to additional trigonal distortions [17]. These distortions themselves split the initial V_{Ga} state, which binds a hole. The donor effect in V_{Ga}–donor complexes is not too profound in comparison with the influence of these distortions [2, 4, 16], and the interaction of the hole localized at such a complex with low-symmetry vibrations is retained. Therefore, the additional distortions are present also in the (V_{Ga}–donor) complexes.

ACKNOWLEDGMENTS

This study was supported by the Russian Foundation for Basic Research, project no. 98-02-18327.

REFERENCES

1. N. S. Averkiev, A. A. Gutkin, E. B. Osipov, *et al.*, Fiz. Tekh. Poluprovodn. (St. Petersburg) **26**, 1269 (1992) [Sov. Phys. Semicond. **26**, 708 (1992)].
2. A. A. Gutkin, T. Piotrowski, J. Pultorak, *et al.*, Fiz. Tekh. Poluprovodn. (St. Petersburg) **32**, 40 (1998) [Semiconductors **32**, 33 (1998)].
3. A. A. Gutkin, M. A. Reshchikov, and V. E. Sedov, Fiz. Tekh. Poluprovodn. (St. Petersburg) **33**, 42 (1999) [Semiconductors **33**, 37 (1999)].
4. A. A. Gutkin, M. A. Reshchikov, and V. E. Sedov, Fiz. Tekh. Poluprovodn. (St. Petersburg) **34** (10), 1201 (2000) [Semiconductors **34**, 1151 (2000)].
5. A. A. Gutkin, N. S. Averkiev, M. A. Reshchikov, and V. E. Sedov, in *Defects in Semiconductors 18*, Ed. by M. Suezawa and H. Katayama-Yoshida; Mater. Sci. Forum **196–201** (1), 231 (1995).
6. N. S. Averkiev, A. A. Gutkin, M. A. Reshchikov, and V. E. Sedov, Fiz. Tekh. Poluprovodn. (St. Petersburg) **30**, 1123 (1996) [Semiconductors **30**, 595 (1996)].
7. H. J. Queisser and C. S. Fuller, J. Appl. Phys. **37**, 4895 (1966).
8. K. D. Glinchuk, A. V. Prokhorovich, and V. E. Rodionov, Fiz. Tekh. Poluprovodn. (Leningrad) **11**, 35 (1977) [Sov. Phys. Semicond. **11**, 18 (1977)].

9. N. S. Averkiev, A. A. Gutkin, A. A. Isakov, *et al.*, Fiz. Tekh. Poluprovodn. (Leningrad) **19**, 893 (1985) [Sov. Phys. Semicond. **19**, 549 (1985)].

10. M. Hansen and K. Anderko, *Constitution of Binary Alloys* (McGraw-Hill, New York, 1958; Metallurgizdat, Moscow, 1962).

11. A. A. Gutkin, M. A. Reshchikov, and V. E. Sedov, Fiz. Tekh. Poluprovodn. (St. Petersburg) **31**, 1062 (1997) [Semiconductors **31**, 908 (1997)].

12. I. Ya. Buyanova, S. S. Ostapenko, and M. K. Sheĭnkman, Fiz. Tverd. Tela (Leningrad) **27**, 748 (1985) [Sov. Phys. Solid State **27**, 461 (1985)].

13. N. S. Averkiev, A. A. Gutkin, E. B. Osipov, *et al.*, Fiz. Tekh. Poluprovodn. (Leningrad) **25**, 50 (1991) [Sov. Phys. Semicond. **25**, 28 (1991)].

14. N. S. Averkiev, A. A. Gutkin, E. B. Osipov, *et al.*, Fiz. Tekh. Poluprovodn. (Leningrad) **25**, 58 (1991) [Sov. Phys. Semicond. **25**, 33 (1991)].

15. N. S. Averkiev, A. A. Gutkin, E. B. Osipov, *et al.*, Fiz. Tekh. Poluprovodn. (Leningrad) **25**, 1976 (1991) [Sov. Phys. Semicond. **25**, 1190 (1991)].

16. T. K. Ashirov and A. A. Gutkin, Fiz. Tekh. Poluprovodn. (Leningrad) **17**, 418 (1983) [Sov. Phys. Semicond. **17**, 258 (1983)].

17. Y. Q. Jia, H. J. von Bardeleben, D. Stievenard, and C. Delerue, Phys. Rev. B **45**, 1645 (1992).

18. N. S. Averkiev, A. A. Gutkin, and M. A. Reshchikov, Fiz. Tekh. Poluprovodn. (St. Petersburg) **33**, 1323 (1999) [Semiconductors **33**, 1196 (1999)].

Translated by T. Galkina

Semiconductors, Vol. 35, No. 2, 2001, pp. 175–176. Translated from Fizika i Tekhnika Poluprovodnikov, Vol. 35, No. 2, 2001, pp. 182–183.
Original Russian Text Copyright © 2001 by Nikol'skiĭ, Zyuzin.

Electrical Conductivity of *n*-InSb Films in Strong Electric Fields

Yu. A. Nikol'skiĭ* and S. E. Zyuzin

Borisoglebsk State Pedagogical Institute, Borisoglebsk, 397160 Russia

** e-mail: bgpi@minas.rosmail.com*

Submitted July 10, 2000; accepted for publication August 2, 2000

Abstract—The effect of a strong electric field on the electrical conductivity of *n*-InSb films grown on oxidized silicon substrates was considered. It is established that the electrical conductivity increases with increasing charge-carrier density. The activation energy of charge carriers is estimated from experimental data. © *2001 MAIK "Nauka/Interperiodica".*

The electric conduction of the *n*-InSb films in strong electric fields is poorly understood. Ling *et al.* [1] dealt mainly with the scattering of charge carriers by intercrystallite barriers. It is also reported that the recrystallized *n*-InSb films grown on mica substrates can be employed as an electric-field sensor [2]. In this study, we estimated for the first time the activation energy of the charge carriers in such structures by measuring the electrical conductivity in strong electric fields.

The *n*-InSb films were grown by discrete evaporation on oxidized silicon substrates with a subsequent thermal recrystallization. The recrystallized layers consisted of a single-crystal matrix with low-resistivity inclusions of the two-phase InSb + In system with *p*-type conduction [3]. The thickness of the layers was 0.5–1.0 μm, the concentration of the charge carriers at room temperature was (2–9) $\times 10^{17}$ cm^{-3}, and the mobility was (2–4) $\times 10^3$ cm^2/(V s) (300 K). The temperature of the substrate during the deposition was $T \approx$ 300°C, which gave rise to compensated layers with the compensation factor of about 0.7–0.8 for polycrystalline samples and 0.5–0.6 for recrystallized ones.

In Figs. 1 and 2, the current–voltage (*I*–*V*) characteristics for polycrystalline and recrystallized samples in the range of intrinsic conductivity of InSb are shown. In this temperature range, the voltage at which Ohm's law no longer holds decreases with increasing temperature (Fig. 3). Such behavior can be explained by the limiting level of occupancy of traps, since our structures are the compensated ones (the compensation factor was given above). Similar arguments were considered in [4].

From the *I*–*V* characteristics measured at various temperatures, one can determine the depth of monoenergy levels E_t, which is related to the voltage V_0 of the transition from the ohmic portion to a "trapped" portion of $I(V)$ curves by the formula [5]

$$V_0^{-1} \propto \exp\left(\frac{(E_t - E_c)}{kT}\right),$$

where E_c is the energy of the conduction band bottom. The activation energy determined from the temperature dependence of V_0 (Fig. 3) is equal to 0.11 and 0.12 eV for recrystallized and polycrystalline layers, respectively.

It is known that in the majority of semiconductors, the conductivity obeys the Frenkel law

$$\sigma = \sigma_0 \exp\beta\sqrt{E},$$

where

$$\sigma_0 = A\exp\left(\frac{-\Delta E_0}{2kT}\right)$$

is the conductivity in weak fields, β is the Frenkel coefficient, E is the electric field intensity, and ΔE_0 is the activation energy of conductivity. In our samples, the increase in conductivity with increasing electric field sets in at $E \gtrsim$ 10–15 V/cm at 300 K.

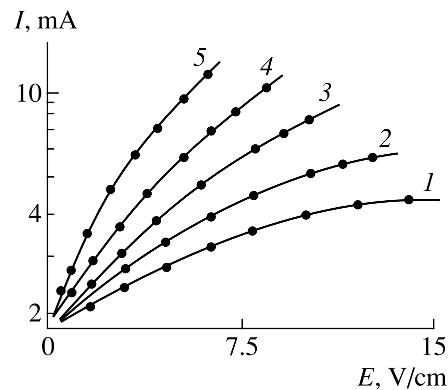

Fig. 1. Typical *I*–*V* characteristics of a polycrystalline *n*-InSb film grown on the oxidized silicon substrate at various temperatures of (*1*) 290, (*2*) 300, (*3*) 330, (*4*) 350, and (*5*) 370 K.

1063-7826/01/3502-0175$21.00 © 2001 MAIK "Nauka/Interperiodica"

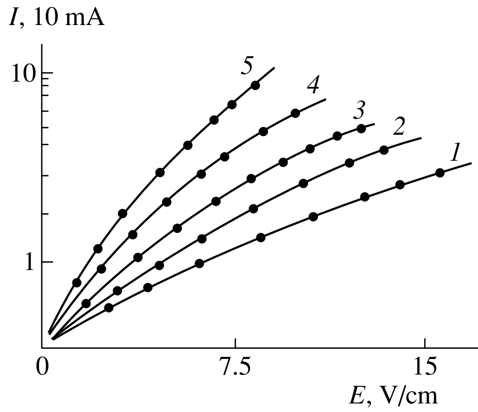

Fig. 2. Typical *I–V* characteristics of a recrystallized *n*-InSb film grown on the oxidized silicon substrate by the thermal recrystallization at temperatures of (*1*) 290, (*2*) 300, (*3*) 330, (*4*) 350, and (*5*) 370 K.

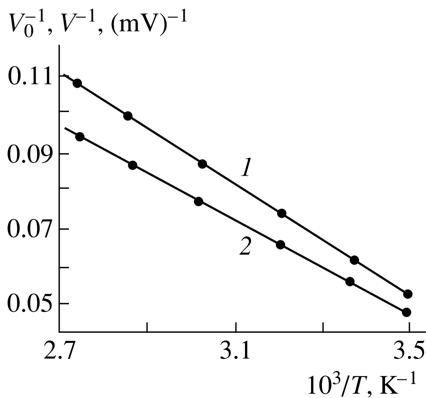

Fig. 3. Temperature dependences of the voltage corresponding to transition from the ohmic portion to a "trapped" portion of *I–V* characteristics for (*1*) polycrystalline and (*2*) recrystallized InSb films.

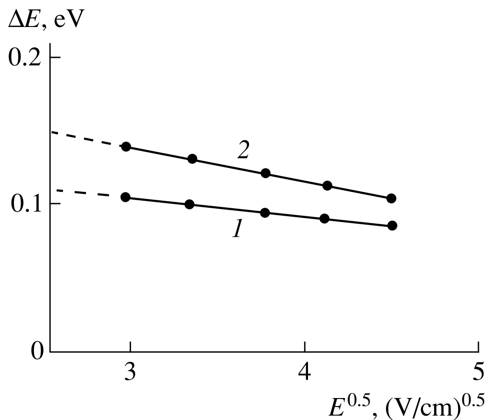

Fig. 4. Activation energy of electrical conductivity ΔE of (*1*) the polycrystalline and (*2*) recrystallized *n*-InSb films grown on the oxidized silicon substrate as a function of electric-field intensity.

Substituting the expression for σ_0 into the Frenkel formula, we obtain [4]

$$\sigma = A\exp\left(\frac{-\Delta E_0}{2kT}\right)\exp\beta\sqrt{E}$$

$$= A\exp\left[-\frac{1}{kT}\left(\Delta E_0 - 2e\sqrt{\frac{eE}{\varepsilon_0}}\right)\right].$$

Introducing

$$\Delta E(E) = \Delta E_0 - 2e\sqrt{\frac{eE}{\varepsilon_0}},$$

we obtain

$$\sigma = A\exp(-\Delta E/2kT),$$

where $\Delta E(E)$ is the field dependence of activation energy ΔE.

The activation energy ΔE as a function of $\sqrt{E}$ is shown in Fig. 4. It can be seen that ΔE decreases linearly with increasing $\sqrt{E}$. Extrapolation of the straight line $\Delta E = f(\sqrt{E})$ to $\sqrt{E} \longrightarrow 0$ yields the activation energy ΔE_0 in a weak electric field. The activation energy is found to be equal to ~0.12 and ~0.14 eV for polycrystalline and recrystallized samples, respectively.

Thus, our data confirm that electrical conductivity increases in strong electric fields in accordance with the Frenkel law. Consequently, we may state that the electrical conductivity increases owing to increasing concentration of the charge carriers with increasing electric field. The magnitudes of activation energy correlate with the Hall effect data.

REFERENCES

1. C. H. Ling, J. H. Fisher, and I. C. Anderson, Thin Solid Films **14**, 267 (1972).
2. S. E. Zyuzin and Yu. A. Nikol'skiĭ, RF Patent No. 2148791.
3. V. A. Kas'yan, P. I. Ketrush, Yu. A. Nikol'skiĭ, and F. I. Pasechnik, in *Thin Films of Indium Antimonide* (Shtiintsa, Kishinev, 1992), p. 162.
4. O. B. Tagiev, T. Sh. Gashimova, and I. M. Askerov, Fiz. Tekh. Poluprovodn. (St. Petersburg) **32** (6), 701 (1998) [Semiconductors **32**, 629 (1998)].
5. N. S. Grushko, L. A. Gerasimenko, and T. I. Goglidze, in *Physics of Semiconductors and Dielectrics* (Shtiintsa, Kishinev, 1992), p. 83.

Translated by A. Zalesskiĭ

Semiconductors, Vol. 35, No. 2, 2001, pp. 177–180. Translated from Fizika i Tekhnika Poluprovodnikov, Vol. 35, No. 2, 2001, pp. 184–187.
Original Russian Text Copyright © 2001 by Vlasenko, Gorelenok, Emtsev, Kamanin, Poloskin, Shmidt.

ELECTRONIC AND OPTICAL PROPERTIES OF SEMICONDUCTORS

Surface Gettering of Background Impurities and Defects in GaAs Wafers

L. S. Vlasenko, A. T. Gorelenok, V. V. Emtsev, A. V. Kamanin*, D. S. Poloskin, and N. M. Shmidt

Ioffe Physicotechnical Institute, Russian Academy of Sciences, Politekhnicheskaya ul. 26, St. Petersburg, 194021 Russia

**e-mail: kamanin@ffm.ioffe.rssi.ru*

Submitted August 3, 2000; accepted for publication August 3, 2000

Abstract—The first data on surface gettering of background impurities and defects from the bulk of single-crystal undoped GaAs(111) wafers are reported. The wafers were 1.6 mm thick, with an initial electron density of (1–3) × 10^{15} cm^{-3} and a mobility of 1500–2000 cm^2/(V s) at room temperature. The wafers were cut from single crystals grown by the Czochralski method from a nonstoichiometric As-enriched Ga–As melt. Gettering was carried out during thermal treatment of the wafers in hydrogen at 400–850°C, with the preliminary deposited layer of Y or SiO_2 1000 Å thick. As a result of gettering, the charge carrier density decreased to 10^8–10^{10} cm^{-3}, while the mobility increased to 7000 cm^2/(V s). © *2001 MAIK "Nauka/Interperiodica".*

1. INTRODUCTION

To improve the characteristics of power devices and detectors of X-ray and γ-radiation, as well as of the elementary particles (particularly the neutrino), it is necessary to obtain specific GaAs wafers with thickness from 0.5 mm to several millimeters. The charge carrier density must be below 10^{10} cm^{-3} and be uniformly distributed over the wafer thickness, the width of the space charge region must be larger than 100 μm, and charge carrier mobility should be high.

The conventional way to solve this problem consists of decreasing the concentration of the background impurities by using ultraclean equipment and ultrapure starting materials, namely, Ga and As of purity grade 99.99999. This makes the process considerably more expensive and, additionally, gives no guarantees that the charge carrier distribution across the ingot will be uniform or that the concentrations in sequential processes will be reproducible. It was demonstrated [1] that the carrier density along the wafer thickness is irreproducible and nonuniform at the shallow-level background-impurity concentration below 10^{15} cm^{-3}. This is caused by the effect of intrinsic defects on the carrier determination from the electrical and optical properties of the semiconductor. Monitoring the generation, recombination, and annihilation of intrinsic defects allows one to improve the reproducibility of results. It is possible to thereby decrease the carrier density to (2–6) × 10^7 cm^{-3} at mobility of 6500–7000 cm^2/(V s) [2].

In this paper, we consider another method for obtaining the pure material, which is based on surface gettering [3–5], for preparing the bulk materials with given properties. The advantage of this method is the low cost of both the materials used and the method itself.

In this paper, the first successful results related to the surface gettering of the background impurities from the GaAs wafers by Y are discussed.

2. EXPERIMENTAL

Starting undoped GaAs(111) single crystals were grown by the Czochralski method from a nonstoichiometric As-enriched Ga–As solution–melt. The ingot was cut into wafers, whose thickness subsequent to polishing was 1.6 mm. The carrier density and mobility measured by the van der Pauw method were (1–3) × 10^{15} cm^{-3} and 1500–2000 cm^2/(V s) at room temperature.

Both sides of the wafers were covered either by pyrolithic SiO_2 or by Y film thermally deposited in a vacuum. The films deposited were 1000 Å thick. The wafers were further thermally treated in hydrogen at 400–850°C for 0–5 h. Subsequent to treatment, the SiO_2 and Y films were removed in HF and HNO_3 etchants, respectively.

The charge carrier distribution over the depth was determined by the capacitance–voltage (*C*–*V*) method using a Schottky Hg probe in combination with layer-by-layer chemical etching. The temperature dependences of the concentration, carrier mobility, and electrical conductivity were determined from the Hall effect measurements in the van der Pauw geometry. In addition, measurements of microwave photoconductivity were carried out. This method was found to be well suited for the investigation of pure silicon crystals. Specifically, the spectra of the electron spin resonance (ESR) for recombination centers with a low concentration 10^{10}–10^{12} cm^{-3} were determined using this method [6–8].

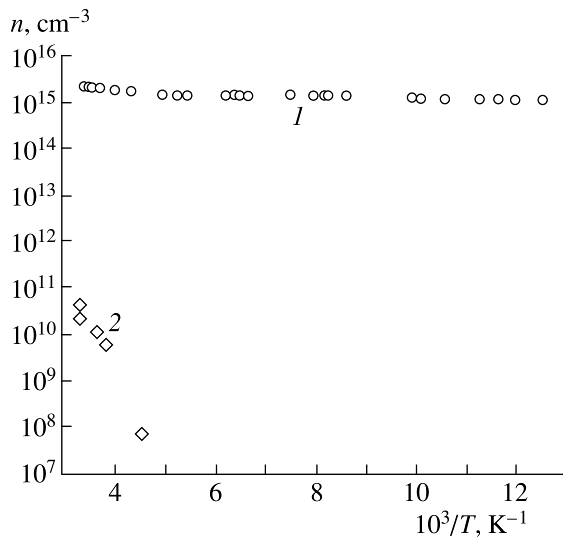

Fig. 1. Temperature dependences of the electron density for GaAs wafers: (*1*) initial wafer and (*2*) Y-covered wafer thermally treated at 800°C for 5 h.

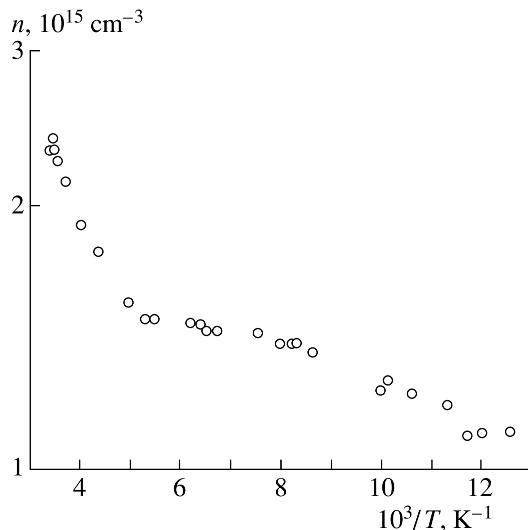

Fig. 2. Temperature dependence of the electron density for initial GaAs wafer.

The sensitivity of the method was four orders of magnitude higher than the conventional ESR method.

A microwave photoconductivity of the samples was measured using an ESR spectrometer operating at a frequency of 9 GHz. The temperature range was 3–150 K. The samples placed into the resonator of the spectrometer were irradiated using a halogen incandescent lamp (100 W power). The Q-factor of the ESR spectrometer resonator depended on the sample conductivity. In the course of the experiments, voltage variation on the microwave detector was measured. The voltage was proportional to the Q-factor of the resonator at a frequency of 80 Hz at 100% modulation of the light. Signals of the microwave photoconductivity were measured at various temperatures, as well as by sweeping a magnetic field.

3. RESULTS

The first stage of the study was devoted to determining the thermal–temporal mode, which permitted both the reduction of the carrier density and the uniform distribution of carriers. When choosing the mode, we started from the known published data on thermal treatment of GaAs [9–12]. The published data on the behavior and parameters of electrically active centers are often contradictory. However, all authors observed the variation in the parameters and density of the electrically active centers in GaAs, specifically, the *EL*2 center at 800–850°C.

A comparative study of the GaAs wafers covered with SiO_2 and Y and annealed demonstrated that the onset of variation in the carrier density for structures of both types was at 700°C. The p-type surface region 50–100 μm thick was formed with the hole density $p \simeq 10^{17}$ cm^{-3}. The edge photoluminescence peaked at $h\nu$ = 1.48–1.49 eV (77 K).

For SiO_2-covered wafers, a higher degree of compensation was observed at a depth more than 100 μm. An increase in the duration and temperature of thermal treatment introduced no crucial changes in the pattern observed. The carrier distribution over the depth was nonuniform, and both n- and p-type conduction regions with the carrier density 10^{14}–10^{15} cm^{-3} were observed.

For Y-covered GaAs wafers, the charge carrier density subsequent to thermal treatment at 800°C at a depth more than 100 μm was 10^{10}–10^{11} cm^{-3}. If the thermal treatment duration was increased to 30 min and more, the carrier density significantly decreased (to 10^8 cm^{-3}), and the n-type conduction was observed. The conduction type and carrier density remained unchanged over the wafer thickness ~1500 μm.

The samples with an electron density lower than 10^{11} cm^{-3} were tested for uniformity of the density distribution over the thickness of wafers by the methods of van der Pauw and microwave photoconductivity. The temperature dependences of the electron density for starting GaAs and Y-covered GaAs, which were thermally treated for 5 h, are shown in Fig. 1, curves *1* and *2*, respectively. The former dependence is shown in Fig. 2 using another scale. The carrier mobility for starting GaAs was 1500 cm^2/(V s) at room temperature.

The analysis of the temperature dependence for starting GaAs demonstrated that the carrier density of 2.5×10^{15} cm^{-3} at room temperature was determined by the shallow-level and deep-level donors. The activation energies for these levels were 10–12 meV and ~150 meV, respectively. The degree of compensation was 40%, and the acceptor concentration was 10^{15} cm^{-3}. Subsequent to thermal treatment at 800°C for 5 h, the degree

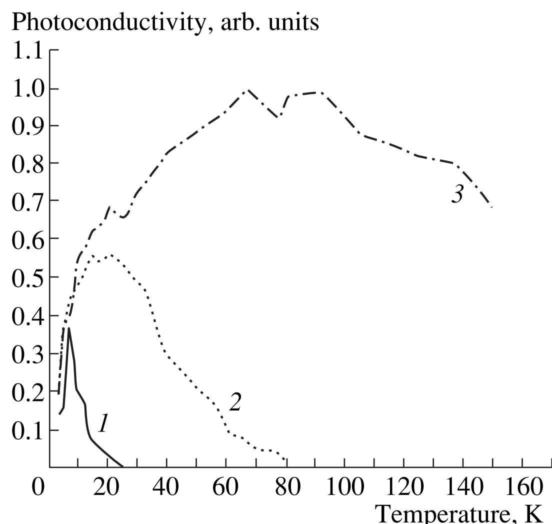

Fig. 3. Temperature dependences of the microwave photoconductivity for GaAs crystals: (*1*) prior to the thermal treatment, (*2*) thermally treated for 0.5 h (ShGA-6), and (*3*) thermally treated for 3 h (ShGA-4).

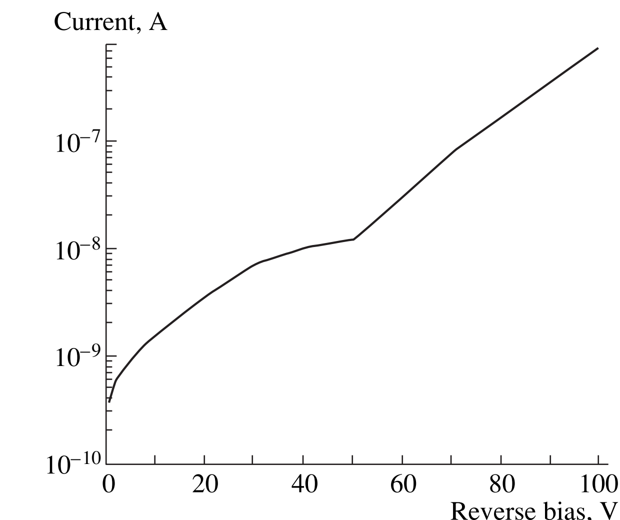

Fig. 4. Reverse portion of the current-voltage characteristic for the gettered GaAs-based Schottky barrier.

of compensation for these wafers covered with Y decreased to 30%. The carrier mobility increased to 7000 $cm^2/(V\ s)$. For this material, the temperature dependence of carrier density was governed only by the donor level with the activation energy of 430 meV.

The effect of gettering was also confirmed by the data obtained from the measurements of microwave photoconductivity. The latter was measured for GaAs wafers before and after gettering; a method similar to that developed for investigation of the spin-dependent recombination in silicon was used [6–8].

The temperature dependences of the microwave photoconductivity for pure GaAs crystals before and after annealing are shown in Fig. 3. Prior to annealing, the crystals had a low resistivity, which considerably lowered the Q-factor. The photoresponse was only observed for these samples in the temperature range 3–25 K, and it peaked at ~5–7 K (see Fig. 3, curve *1*). Thermal treatment for 0.5 h increased the resistivity of the crystal, while the photoresponse appeared at higher temperatures, i.e., below 70 K (Fig. 3, curve *2*). The samples thermally treated for 3 h had an increased resistivity even at room temperature, and the photoresponse was clearly observed over the entire temperature range (Fig. 3, curve *3*).

An increase in the dark photoconductivity for the annealed samples could not be explained by a straightforward compensation of shallow-level donors with deep-level centers. In fact, an increase in the recombination rate for photoinduced carriers was observed, and, consequently, the photoconductivity decreased. Specifically, this effect was observed for the Fe-doped GaAs. For the annealed GaAs, photoconductivity increased, and the spectra of spin-dependent recombination and ESR were absent. This could be explained by passivation of shallow-level donors and formation of electrically and paramagnetically inactive centers.

Schottky barriers with a diameter of 2 mm were fabricated from the material obtained. The reverse portion of the current–voltage characteristic for this barrier is shown in Fig. 4. The current values were identical to those reported elsewhere [2] for GaAs-based radiation detectors, where GaAs was obtained under ultraclean conditions.

4. CONCLUSION

Surface gettering was used for GaAs wafers 1.6 mm thick. The initial charge carrier density and mobility were 2.0×10^{15} cm^{-3} and 1500–2000 $cm^2/(V\ s)$, respectively. Gettering allowed us to attain the carrier density of 10^8–10^{10} cm^{-3} and mobility of 7000 $cm^2/(V\ s)$. Thus, the first successful results were encouraging, and the gettering method suggested here looks like a promising method.

ACKNOWLEDGMENTS

This study was supported by the Russian Foundation for Basic Research, project no. 00-02-17026.

REFERENCES

1. H. J. von Bardeleben and J. C. Bougoin, *Defect Control in Semiconductors*, Ed. by K. Sumino (Elsevier, Amsterdam, 1990).
2. C. M. Buttar, Nucl. Instrum. Methods Phys. Rev. A **395**, 1 (1997).

3. E. I. Ivanov, L. V. Lopatina, V. L. Sukhanov, *et al.*, Fiz. Tekh. Poluprovodn. (Leningrad) **16**, 207 (1982) [Sov. Phys. Semicond. **16**, 129 (1982)].

4. L. F. Zakharenkov, V. V. Kozlovskii, A. T. Gorelenok, and N. M. Shmidt, in *Semiconductor Technology: Processing and Novel Fabrication Techniques*, Ed. by M. E. Levinstein and M. S. Shur (Wiley, New York, 1997), p. 91.

5. A. T. Gorelenok, V. L. Kryukov, and G. P. Furmanov, Pis'ma Zh. Tekh. Fiz. **20** (13), 60 (1994) [Tech. Phys. Lett. **20**, 546 (1994)].

6. L. S. Vlasenko, M. P. Vlasenko, V. N. Lomasov, and V. A. Khramtsov, Zh. Éksp. Teor. Fiz. **91**, 1037 (1986) [Sov. Phys. JETP **64**, 612 (1986)].

7. L. S. Vlasenko, in *Semiconductors and Insulators: Optical and Spectroscopic Research*, Ed. by Yu. Koptev (Nova Sciences, 1992), p. 217.

8. L. S. Vlasenko, Yu. V. Martynov, T. Gregorkievicz, and C. A. J. Ammerlaan, Phys. Rev. B **52**, 1144 (1995).

9. C. H. Kang, J. Lagowski, and H. C. Gatos, J. Appl. Phys. **62**, 3482 (1987).

10. P. N. Brunkov, S. Gaĭbullaev, S. G. Konnikov, *et al.*, Fiz. Tekh. Poluprovodn. (Leningrad) **25**, 338 (1991) [Sov. Phys. Semicond. **25**, 205 (1991)].

11. I. Ohbi, M. Takahama, and K. Hiruma, Appl. Phys. Lett. **61**, 1679 (1992).

12. N. Ohkobo, M. Shishikura, and S. Matsumoto, J. Appl. Phys. **73**, 615 (1993).

Translated by N. Korovin

Semiconductors, Vol. 35, No. 2, 2001, pp. 181–184. Translated from Fizika i Tekhnika Poluprovodnikov, Vol. 35, No. 2, 2001, pp. 188–191.
Original Russian Text Copyright © 2001 by Pipinys, Rimeika, Lapeika, Pipiniene.

SEMICONDUCTOR STRUCTURES, INTERFACES, AND SURFACES

Mechanism of Reverse Current in the Al/*p*-InP Schottky Diodes

P. A. Pipinys, A. K. Rimeika*, V. A. Lapeika, and A. V. Pipiniene

Vilnius Pedagogical University, LT-2034 Vilnius, Lithuania

**e-mail: fizdidkat@vpu.lt*

Submitted May 10, 2000; accepted for publication June 21, 2000

Abstract—Reverse current–voltage characteristics of the Al/*p*-InP Schottky diodes based on Zn-doped InP epilayers were measured in relation to bias and temperature. Temperature dependence of reverse current is characterized by the activation energies of 0.75 and 0.51 eV in the high-temperature region and at temperatures $T < 280$ K, respectively. Results are explained by the phonon-assisted tunneling generation of charge carriers from the surface states of a semiconductor with regard to the Frenkel emission mechanism. It is found that, in the low-temperature region, tunneling occurs via the centers with energy levels of 0.51 eV. Comparing experimental results with theory, we estimated electric-field strength in the barrier at $(5–13) \times 10^7$ V/m and the surface density of the hole charge in the boundary layer of the semiconductor. © *2001 MAIK "Nauka/Interperiodica".*

INTRODUCTION

Semiconductor compound InP is an attractive material for optoelectronic engineering. Metal–semiconductor and metal–insulator–semiconductor structures are widely used in various devices based on the InP compound.

Characteristics of rectifying contacts to InP of *n*- and *p*-type conductivity have been studied repeatedly [1–8]. However, it is difficult to explain some properties of the current–voltage characteristics, especially the temperature dependences of current, in terms of the conventional theory of current flow in the Schottky diodes based on thermionic emission (TE) or thermionic-field-assisted emission (TFE). For example, temperature dependences of reverse current I in the Al/*p*-InP diodes are not linear in coordinates $\ln(I/T^2)$ vs. $1/T$ in the low-temperature region [3, 6, 7], which contradicts the TE theory. It was shown [4–6] that the barrier height deduced from the capacitance–voltage characteristics significantly exceeds the barrier height obtained from the current–voltage ($I–V$) characteristics. In addition, it was found [7] that the barrier height determined from the $I–V$ characteristics decreases with increasing voltage more significantly than the theory would predict. According to [7], reduction of the barrier height causes the absence of the reverse current saturation. The reverse $I–V$ characteristics measured at different temperatures in the Au/*p*-InP diodes with thin oxide interlayer were explained in [7] on the basis of model [9] by the charge transport mechanism. This mechanism implies the existence of the interlayer, and the voltage drop on the interlayer and the factor of transit through it are considered in the modified TE theory. The reverse $I–V$ and current–temperature characteristics of the Schottky diodes fabricated on some *n*-type semiconductors [10–12] were described using a model of the phonon-assisted electron tunneling from a state at the metal–semiconductor interface through the barrier into the conduction band. It was shown [12] that this model consistently explains the dependence of the effective barrier height, deduced from the $I–V$ characteristics, on the reverse bias voltage. Using this model, reverse-biased $I–V$ characteristics of the Schottky diodes based on *n*-InP measured at various temperatures, as well as temperature dependences of current in diodes with the Schottky barrier on *p*-InP, were analyzed in this study.

The analysis indicates that the mechanism of the Frenkel emission, in addition to the tunneling mechanism, is important in the carrier generation process at higher temperatures. These diodes are also characterized by the fact that dopant centers are involved in the charge transport at temperatures below 300 K.

RESULTS OF MEASUREMENTS AND INTERPRETATION

Measurements were performed for the Al/*p*-InP diodes fabricated on epilayers of Zn-doped InP.[1] Carrier concentration at room temperature was of 2×10^{16} cm^{-3}; diameter of the barrier contact was 0.8 mm. Reverse current dependences I_r on the bias voltage at various temperatures and temperature dependences of current were measured in a vacuum cryostat.

$I–V$ characteristics are shown in logarithmic coordinates in Fig. 1. It can be seen that the $I–V$ characteristics depend strongly on temperature: slope of the curves

[1] Diodes were kindly provided by I.M. Tiginyanu, Institute of Semiconductors, Moldova.

1063-7826/01/3502-0181$21.00 © 2001 MAIK "Nauka/Interperiodica"

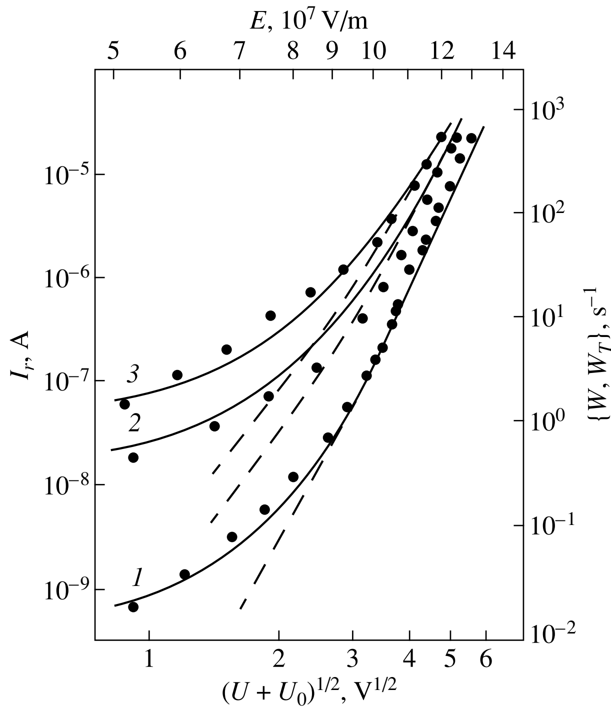

Fig. 1. Experimental reverse current (I_r) *I–V* characteristics for the Al/*p*-InP diode (dots), and results of calculation of total ionization probability W (solid lines) and tunneling ionization probability W_T (dashed lines) in relation to the electric field strength E at temperatures T = (*1*) 294, (*2*) 343, and (*3*) 364 K. Calculation were performed for the parameters: Δ = 0.75 eV, the electron–phonon coupling constant a = 6.0, effective mass $m_h^* = 0.50m_c$, the phonon energy $\hbar\omega$ = 0.042 eV, $\nu_0 = 3 \times 10^8$ s^{-1}, and ε = 12.5. Diffusion potential U_0 = 0.5 V.

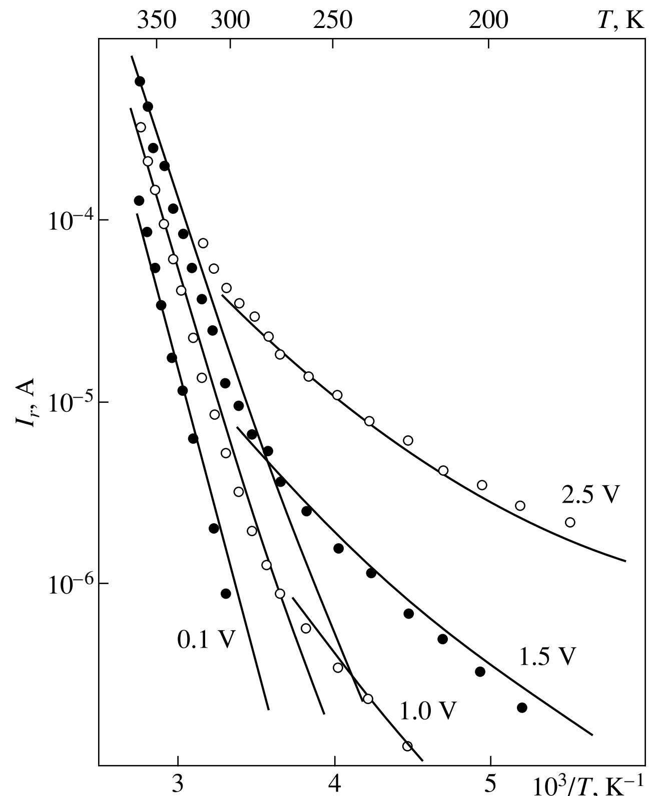

Fig. 2. Experimental (dots) and calculated from formula (2) (solid lines) dependences of reverse current I_r on $1/T$ at different voltages for the Al/*p*-InP diode for the hole surface-charge density $N_s = 5 \times 10^{13}$ cm^{-2} for Δ = 0.75 eV and for $N_s = 2 \times 10^9$ cm^{-2} for Δ = 0.51 eV. W is calculated for the same parameters as in Fig. 1.

decreases as temperature increases. Temperature dependences of current plotted as $\ln I_r$ vs. $1/T$ and obtained at several reverse bias voltages are shown in Fig. 2. There are two distinct portions in the curves: the high-temperature region that is characterized by the activation energy higher than 0.7 eV and the low-temperature region (T < 280 K) with lower activation energy. Therefore, the current is thermally activated. It does not level off in the high-voltage region. This type of current dependence for diodes on *n*-type semiconductors was explained [10–12] by the phonon-assisted electron tunneling from the electron states into the conduction band of the semiconductor. We will interpret experimental data obtained for the Al/*p*-InP diodes in terms of this model.

According to this model, in the case of *p*-type semiconductors, current is controlled by the hole tunneling from a state at the metal–semiconductor interface into the valence band of the semiconductor. Assuming that current across the barrier is proportional to the tunneling probability W_T, we compare the current dependences on the reverse bias voltage with the dependence of W_T on the electric field strength E calculated from formula (16) in [13]. These dependences calculated for the hole effective mass $m_h^* = 0.5m_e$ [7] are shown in Fig. 1 (dashed lines). Comparison of the reverse *I–V* characteristics with $W_T(E)$ shows that, in these diodes, *I–V* characteristics are less steep, and experimental data are in good agreement with the results of calculation only in the region of higher voltages (fields). Especially significant disagreement between theory and experiment is observed at high temperatures. This disagreement is apparently caused by the fact that, in addition to the mechanism of tunnel emission, which is dominant in the region of high voltages and low temperatures, there exists another mechanism for the hole emission, which manifests itself at lower voltages and higher temperatures. Such a mechanism may involve the Frenkel emission, which is characterized by strong temperature dependence and less pronounced dependence on the electric field strength than those of the tunneling mechanism. Ionization probability of center with consider-

ation for the Frenkel emission is $W = W_T + W_F$. W_F is calculated from the relation obtained by Frenkel [14],

$$W_F = \nu_0 \exp\left[-\frac{\mathscr{E}_T - e\sqrt{eE/(\pi\varepsilon_0\varepsilon)\mathscr{E}}}{kT}\right], \quad (1)$$

where $\mathscr{E}_T$ is the energy of thermal activation, and E is the electric field strength. Dependences of the total ionization probability of center W are shown in Fig. 1 (solid lines). It can be seen that these curves fit quite satisfactory the experimental data. If all released holes overcome the depletion region, then

$$I_r = eN_sWS, \quad (2)$$

where N_s is the surface charge density, and S is the barrier contact area equal to 0.5 mm^2. Substituting the current value and W from Fig. 1 into relation (2), we obtain $N_s = 5 \times 10^{13}$ cm^{-2}.

As it was mentioned above, we can distinguish two portions in the temperature dependences of current with different thermal activation energies. Activation energies for the high- and low-temperature regions are 0.75 and 0.51 eV, respectively. Assuming that in the low-temperature region the barrier current involves the centers with the above energy levels (such centers in Zn-doped InP were observed in [15]), we calculated $W(T)$ for the barrier height $\Delta = 0.51$ eV at $T < 260$ K and for $\Delta = 0.75$ eV in the high-temperature region.

Comparison of the experimental dependences $\ln I_r$ vs. $1/T$, obtained at different voltages, with calculations according to formula (2) is illustrated in Fig. 2. It can be seen that the charge transport is predominantly defined by the Frenkel emission. Contribution of the Frenkel emission, as can be seen from Fig. 1, is most significant in the low-field region and at higher temperatures.

It should be noted that temperature variations of the *I–V* characteristics obtained in this study are similar to the results obtained for the Au/*p*-InP diodes [7]. Reverse-biased *I–V* characteristics obtained in [7] in a wide temperature region and theoretical curves $W(E)$ calculated with consideration for the phonon-assisted tunneling and the Frenkel emission are shown in Fig. 3. In this case as well, the energy levels of centers were assumed in calculations to be equal to 0.51 eV at temperatures lower than 280 K. In the high-temperature region, this energy is assumed to be 0.76 eV, which is equal to the barrier height obtained in [7]. It can be seen that experimental and theoretical *I–V* characteristics are in satisfactory agreement.

Comparison of experimental data with theoretical calculations shows that, for diodes based on *p*-InP, it is necessary to take into account two competing mechanisms in analyzing the charge transport at reverse bias: tunneling and the Frenkel emission. The significant role of the Frenkel emission in these diodes is caused, in our opinion, by the fact that the effective mass of carriers is too large for the tunneling processes; as a result, the tunneling probability, which is relatively low, increases with the field strength more slowly than in materials with small effective mass (see, e.g., [16]). Due to this, the Frenkel emission can be dominant at higher temperatures. This fact explains the softness of the *I–V* characteristics. It should be noted that the apparent decrease of the barrier height, calculated from the *I–V* characteristics, with an increase in the reverse bias is caused by tunneling current through the barrier. As shown in [12], such a decrease completely agrees with prediction of the phonon-assisted tunneling. Absence of the current saturation expected at large reverse bias voltages is also the result of tunneling, because tunneling current through the barrier is dominant at higher voltages. The current should not be saturated, because the tunneling rate, as can be seen from Fig. 1, increases with the field strength in the investigated field region.

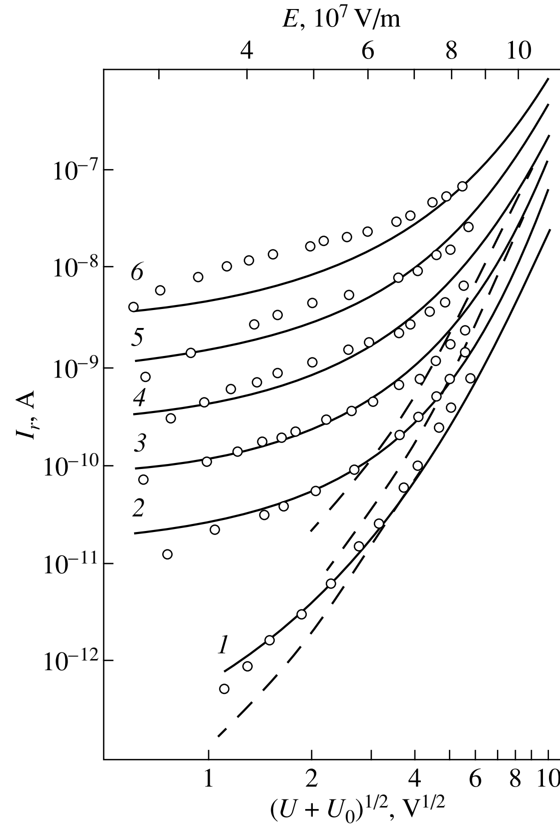

Fig. 3. Reverse *I–V* characteristics for the Au/*p*-InP diode obtained in [7] (dots); reverse current dependences on the electric field strength calculated from formula (2) with consideration for the Frenkel emission (solid lines) and only tunneling emission (dashed lines) at temperatures T = (*1*) 260, (*2*) 300, (*3*) 320, (*4*) 340, (*5*) 360, and (*6*) 380 K. Calculations of W were performed for the parameters: $N_s = 4 \times 10^{12}$ cm^{-2} for $\Delta = 0.76$ eV (T = 300–380 K) and $N_s = 2 \times 10^7$ cm^{-2} for $\Delta = 0.51$ eV (T = 260 K). The remaining fitting parameters are the same as in Fig. 1.

In conclusion, in the *p*-type semiconductors as well, the tunneling mechanism of the carrier generation is dominant for the charge transport in the reverse biased Schottky diodes. In this case, due to the large effective mass of holes, it is necessary to consider additionally the generation of carriers by the Frenkel mechanism that may dominate over tunnel mechanism at higher temperatures and low electric fields.

REFERENCES

1. G. S. Korochenkov and I. M. Molodyan, Mikroélektronika **2**, 168 (1978).
2. O. Wada, A. Majerfeld, and P. N. Robson, Solid-State Electron. **25**, 381 (1982).
3. B. Tuck, G. Eftekhari, and D. M. de Cogan, J. Phys. D **15**, 457 (1982).
4. E. Hokelek and G. Y. Robinson, J. Appl. Phys. **54**, 5199 (1983).
5. Y. P. Song, R. L. van Meirhaege, W. H. Laflére, and F. Cardon, Solid-State Electron. **29**, 663 (1986).
6. A. Singh, K. C. Reinhardt, and W. A. Anderson, J. Appl. Phys. **68**, 3475 (1990).
7. A. Singh, P. Cova, and R. A. Masut, J. Appl. Phys. **76**, 2336 (1994).
8. Z. Ouennoughi, K. Boulkroun, M. Remy, *et al.*, J. Phys. D **27**, 1014 (1994).
9. Ch.-Y. Wu, J. Appl. Phys. **51**, 3786 (1980).
10. R. Brazis, P. Pipinys, A. Rimeika, and L. Gėgžnaitė, Solid State Commun. **55**, 25 (1985).
11. P. A. Pipinys, A. K. Rimeika, and V. A. Lapeika, Fiz. Tekh. Poluprovodn. (St. Petersburg) **32**, 882 (1998) [Semiconductors **32**, 785 (1998)].
12. P. Pipinys, A. Pipiniene, and A. Rimeika, J. Appl. Phys. **86**, 6875 (1999).
13. F. I. Dalidchik, Zh. Éksp. Teor. Fiz. **74**, 472 (1978) [Sov. Phys. JETP **47**, 247 (1978)].
14. I. Ya. Frenkel', Zh. Éksp. Teor. Fiz. **8**, 1292 (1938).
15. A. N. Georgobiani and I. M. Tiginyanu, Fiz. Tekh. Poluprovodn. (Leningrad) **22**, 3 (1988) [Sov. Phys. Semicond. **22**, 1 (1988)].
16. P. A. Martin, B. T. Streetman, and K. Hess, J. Appl. Phys. **52**, 7409 (1981).

Translated by I. Kucherenko

Semiconductors, Vol. 35, No. 2, 2001, pp. 185–192. Translated from Fizika i Tekhnika Poluprovodnikov, Vol. 35, No. 2, 2001, pp. 192–199.
Original Russian Text Copyright © 2001 by Dmitriev, Markin.

SEMICONDUCTOR STRUCTURES, INTERFACES, AND SURFACES

Quasi-Static Ion Currents in Thin Insulating Films of Metal–Insulator–Semiconductor Structures and the Distribution of Ions in the Films

S. G. Dmitriev and Yu. V. Markin

Institute of Radio Engineering and Electronics, Russian Academy of Sciences (Fryazino Branch), pl. Vvedenskogo 1, Fryazino, Moscow oblast, 141120 Russia

Submitted April 28, 2000; accepted for publication June 21, 2000

Abstract—A method for calculating the quasi-static current–voltage characteristics for ion currents in a metal–insulator–semiconductor structure is suggested. Theoretical and experimental peaks of ion currents in the current–voltage characteristic were compared. The influence of a semiconductor on the characteristic current–voltage shape was considered. The distribution of ions in the insulator film was calculated. Formulas for determining both the background concentration of ions in the film and their concentration at the insulator–semiconductor interface are suggested. © *2001 MAIK "Nauka/Interperiodica".*

1. INTRODUCTION

The ions mobile at elevated temperatures ($T \approx$ 300–600 K) in thin ($d \approx$ 100–1000 Å) insulator films can accumulate at the interfaces of thin-film structures subjected to strong electric fields and then exert an appreciable influence on the properties of these structures. In Si–SiO_2 structures, these are typically the alkali-metal ions whose concentration (per unit area) may be as high as $N_S \approx 10^{12}$–10^{13} cm^{-2}; the fields generated by these ions may range up to $\mathscr{E} \approx 10^5$–10^6 V/cm. The processes of trapping the ions at the surface and of their subsequent emission, the interaction of electrons with ions in the vicinity of the interface, and other phenomena can be studied by various methods [1]. In addition, the mobile ions themselves can be used to probe the properties of interfaces by studying the special features introduced by these ions into the temperature and field dependences of various parameters of the metal–insulator–semiconductor (MIS) structures [1, 2].

In order to determine the concentration and type of ions in the film, the dynamic (with a linear scan of the voltage) current–voltage (*I*–*V*) characteristics that have the form of peaks [3, 4] are often used. The points in the quasi-static *I*–*V* characteristics (see Fig. 1) correspond to the equilibrium (for a given voltage) distributions of ions in the film, and the currents themselves are induced by redistribution of ions in the film as the voltage V_g applied to the structure is varied; i.e., the ion-current peaks (in the *I*–*V* characteristics of the structures) also provide information about the ion distribution itself. This information can be extracted by processing the results using a theoretical model. In this paper, we suggest a simple model and compare the theoretical and experimental peaks in the *I*–*V* characteristics of silicon-based MIS structures. We also calculate the distribution of ions in the insulator film and suggest formulas for the background ion concentration in the film and their concentration at the interface for various values of the parameters.

2. THEORY

It is convenient to determine the current density in a MIS structure using the formula $j = d\sigma/dt$, where $\sigma = \varepsilon_i\mathscr{E}_0/4\pi$ is the charge density at the metal, $\mathscr{E}_0$ is the field in the metal, and ε_i is the permittivity of the insulator. For a linear ($\partial V_g/\partial t = \beta_V$) voltage scan, the current density is given by

$$j = (\varepsilon_i\beta_V/4\pi)\partial\mathscr{E}_0/\partial V_g.$$

Using the relation (valid for the one-dimensional configuration)

$$\partial\mathscr{E}_0/\partial V_g = \alpha\partial\mathscr{E}_0/\partial(\Delta\varphi), \quad \alpha = 1 - \partial\varphi_S/\partial V_g, \quad (1)$$

where $\Delta\varphi = \varphi_0 - \varphi_S$ is the potential difference between the metal (subscript 0) and semiconductor (subscript S) and the potential is measured from its value in the semiconductor bulk, the expression for the current density may be written as

$$j = \alpha j^*, \quad (2)$$

$$j^* = j_0 d\partial\mathscr{E}_0/\partial(\Delta\varphi), \quad (3)$$

$$j_0 = C_0\beta_V, \quad C_0 = \varepsilon_i/(4\pi d). \quad (4)$$

Here, C_0 is the capacitance (per unit area) of the insulator film, j_0 is the capacitive current in the film ($j_0 \approx 7 \times 10^{-10}$ A/cm^2 for d = 1000 Å, β_V = 20 mV/s, and ε_i = 3.9 for a SiO_2 film [5]), and j^* is the current density in the film in the absence of a semiconductor [for exam-

1063-7826/01/3502-0185$21.00 © 2001 MAIK "Nauka/Interperiodica"

ple, in a metal–insulator–metal (MIM) structure, if the voltage $\Delta\varphi$ is applied to this structure]. The normalized currents j/j_0 (j^*/j_0) are independent of β_V and may be considered as functions of the voltages $V_g(\Delta\varphi)$ (quasi-static I–V characteristics), which facilitate a comparison with the experiment and are to be used in this study. It is worth noting that $j(V_g)$ represents the quasi-static I–V characteristic of a MIS structure, whereas the $j^*(\Delta\varphi)$ corresponds to the similar property of a MIM structure.

Thus, the effect of a semiconductor on the current is governed by the multiplier α in expression (2) and, in addition, by the voltage shift by $\varphi_S(V_g)$ and, under actual conditions, also by the contact potential difference $\varphi_C \sim 0.1$–1 V [5] between the metal and semiconductor. The multiplier α accounts for the effect of the capacitive sharing of the voltage V_g at the structure between the film and semiconductor. Indeed, $\alpha = C_{S0}/(C_{i0} + C_{S0})$ (where C_{i0} and C_{S0} are differential capacitances per unit area of the film with ions and of the semiconductor, respectively) and $\partial\mathcal{E}_0/\partial(\Delta\varphi) = (4\pi/\varepsilon_i)C_{i0}$.

When analyzing the ion distribution in the film, the dependence $j^*(\Delta\varphi)$ is of interest. As for the semiconductor, it exerts an obscuring effect and gives rise to appreciable discrepancies between $j^*(\Delta\varphi)$ and the actually measured dependence $j(V_g)$; these discrepancies will be considered in what follows.

In the quasi-static mode, the distribution of singly positively charged ions in the film $N(z)$ is at equilibrium at any point in time and is defined by the voltage V_g or the field $\mathcal{E}_0$ (the charge density σ) in a metal in accordance with the Poisson equation

$$\varepsilon_i d^2\varphi(z)/dz^2 = -4\pi q N(z), \quad (5)$$

where q is the elementary charge.

In the simplest case where ions in the insulator have only a single state with the energy E_i, the energy distribution of ions (in terms of the Boltzmann statistics) is given by

$$N(z) = N_{\mathrm{eff}}\exp[-u(z)], \quad (6)$$

$$u(z) = [E_i + q\varphi(z) - F_i]/kT, \quad (7)$$

where $u(z)$ is the normalized ion energy, F_i is the ion Fermi level, k is the Boltzmann constant, and N_{eff} is the effective density of ion states. For the diffusion via interstices, we have $N_{\mathrm{eff}} \propto a_0^{-3}$, where a_0 is the characteristic size of a unit cell; thus, $N_{\mathrm{eff}} \approx 10^{22}$–$10^{23}$ cm^{-3}. Obviously, the Boltzmann distribution is also valid for the band of states; in this case, the density of states will be temperature-dependent, as in the case of electrons [5].

We note that the hydrodynamic approximation that is often used to describe ions (see, for example, [6, 7]) is equivalent to the model under consideration if the degeneracy effects are insignificant and there are no additional states of the ions (for example, the states at the interface [8]). Otherwise, the more general formulas of the Gibbs statistics should be used [9]. In particular, the degeneracy effects may become significant in the vicinity of the interface for the ion concentrations of $N_S \approx 10^{13}$–10^{14} cm^{-2} [8]. In this paper, we consider the Boltzmann statistics.

The form of solutions to Eq. (5) depends on the sign of its first integral I [6, 7] written as

$$I = [\varepsilon_i\mathcal{E}^2(z)/(8\pi kT)] - N(z) = \text{const}. \quad (8)$$

In the region of the ion-current peak, $I < 0$ [8] and the solution is given by

$$u(z) - u_m = \ln\{\cos^2[(z - z_m)/2r_m]\}, \quad (9)$$

$$N(z) = N_{\mathrm{eff}}\exp(-u_m)\cos^{-2}[(z - z_m)/2r_m], \quad (10)$$

$$r_m^2 = \varepsilon_i kT/[8\pi q^2 N_{\mathrm{eff}}\exp(-u_m)]. \quad (11)$$

At the point $z = z_m$, the distribution $N(z)$ has a minimum, whereas $\varphi(z)$ and $u(z)$ have maxima (the z-axis is directed from the metal to the semiconductor, with $z = 0$ at the boundary with the metal); r_m is the Debye radius at the point z_m. In addition, we have [see (7)] $\varphi(z) - \varphi_m = kT[u(z) - u_m]/q$, although $\varphi(z) \neq kTu(z)/q$.

The boundary conditions for the fields $\mathcal{E}(0) = \mathcal{E}_0$ and $\mathcal{E}(d) = \mathcal{E}_0 + \mathcal{E}_i$ at the inner ($z = +0$ and $z = d - 0$) boundaries are given by

$$\begin{aligned} \mathcal{E}_0/\mathcal{E}_d &= -y\tan(yz_m/d), \\ (\mathcal{E}_0 + \mathcal{E}_i)/\mathcal{E}_d &= y\tan[y(1 - z_m/d)], \end{aligned} \quad (12)$$

$$\mathcal{E}_i = 4\pi q N_S/\varepsilon_i, \quad \mathcal{E}_d = 2kT/(qd), \quad y = d/2r_m, \quad (13)$$

where $\mathcal{E}_i$ is the ion field and $\mathcal{E}_d$ is the characteristic (thermal) field of the film. We can use (12) to derive the following equation for y:

$$\begin{aligned} &\arctan[(\mathcal{E}_0 + \mathcal{E}_i)/(\mathcal{E}_d y)] \\ &- \arctan[\mathcal{E}_0/(\mathcal{E}_d y)] = y, \end{aligned} \quad (14)$$

the solutions to Eq. (14) are independent of N_{eff} and depend on $\mathcal{E}_0$ (or σ) and N_S. The same parameters [see (12), (13)] define the quantities r_m and z_m, and also [see (9)] $\varphi_0 - \varphi(z)$ and $\varphi(z) - \varphi_S$, where $\varphi_0 = \varphi(0)$ and $\varphi_S = \varphi(d)$. In particular, the voltage drop across the film $\Delta\varphi = \varphi(0) - \varphi(d) = \varphi_0 - \varphi_S$ is given by

$$\begin{aligned} \Delta\varphi &= (kT/q)\ln \\ &\times\{\cos^2(z_m/2r_m)/\cos^2[(d - z_m)/2r_m]\}. \end{aligned} \quad (15)$$

The absolute values of potential in the films are determined from the formula $\varphi(z) = \varphi_S + [\varphi(z) - \varphi(d)]$ and expression (9) and depend on the potential φ_S at the boundary; the latter potential is equal to the magnitude of the band bending in the semiconductor.

The magnitude of the band bending $\varphi_S(\mathscr{E}_S)$ in the semiconductor depends on the field $\mathscr{E}_S = (\mathscr{E}_0 + \mathscr{E}_i)\varepsilon_i/\varepsilon_S$ at the interface with the semiconductor, where ε_S is the relative permittivity of semiconductor ($\varepsilon_S = 11.9$ for Si [5]). The quantity $\varphi_S(\mathscr{E}_S)$ was calculated by the conventional method [5] with allowance made for the charges of electrons in the conduction band and holes (at elevated temperatures, $T \simeq 500$ K) in the valence band. For large magnitudes of band bending, the degeneracy of electrons in the conduction band and the donor level (for more details, see [8]) was taken into account. Numerical values of the parameters corresponded to silicon [5]; in particular, the ionization energy of the donor level was assumed to be $E_d = 0.045$ eV (for phosphorus atoms) and the band gap was taken as E_g = 1.12 eV.

The quantities $\partial\mathscr{E}_0/\partial(\Delta\varphi)$, $V_g = \Delta\varphi + \varphi_S$, and $\partial\varphi_S/\partial V_g$ can be now calculated in relation to $\mathscr{E}_0$ using formula (15); the dependence $j(V_g)$ can be then determined from formulas (1)–(4).

We note that Eq. (14) has solutions only in the field range of $-(\mathscr{E}_i + \mathscr{E}_{\rm th}) \le \mathscr{E}_0 \le \mathscr{E}_{\rm th}$, where

$$\mathscr{E}_{\rm th} = -\mathscr{E}_i/2 + [(\mathscr{E}_i/2)^2 - \mathscr{E}_i\mathscr{E}_d]^{1/2}. \quad (16)$$

At the end of the range, we have $y(\mathscr{E}_{\rm th}) = y[-(\mathscr{E}_i + \mathscr{E}_{\rm th})] = 0$. The dependence $y(\mathscr{E}_0)$ has a maximum for $\mathscr{E}_0 = -\mathscr{E}_i/2$ ($y \in [0; y_{\max}]$); this maximum corresponds to the symmetric distribution of the potential and ions in the film. The inverse (two-valued) dependence $\mathscr{E}_0(y)$ is simpler and is given by

$$\mathscr{E}_0(y) = (-\mathscr{E}_i/2) \pm [(\mathscr{E}_i/2)^2 - (y\mathscr{E}_d)^2 + y\mathscr{E}_i\mathscr{E}_d\cot y]^{1/2}. \quad (17)$$

In the remaining range of the fields $\mathscr{E}_0$, the first integral (8) has the reversed sign ($I > 0$) and the solutions have a different form; i.e., the trigonometric functions are replaced by hyperbolic functions. In this case, the analysis is similar to that outlined above and has been reported previously [8].

A typical dependence $j(V_g)$ calculated using the above scheme is shown in Fig. 1 (the continuous line). For the sake of comparison, a plot of $j^*(V_g) \equiv j^*[\Delta\varphi(V_g)]$ is also shown (the dashed line); the quantity j^* represents the current for the same values of $\Delta\varphi(V_g)$ in the films but in the absence of a semiconductor [see (3)]. The values of the parameters are $N_S = 10^{12}$ cm^{-2}, $d = 1000$ Å, $T = 500$ K, and the donor concentration is $N_d = 10^{15}$ cm^{-3}. As can be seen from Fig. 1, the presence of a semiconductor affects the width and amplitude of the peak and results in its shift and in the emergence of a characteristic feature, i.e., a dip on the left-hand side of the peak; this dip is related to voltage sharing between the film and the semiconductor. Points *1* and *3* correspond to zero fields in the metal and the semiconductor, respectively; therefore, in the film, the potential has a maximum and the ion distribution has a minimum for any values of the voltage between the metal and the semiconductor. In the remaining voltage range, the maximum is either located outside the film ($I < 0$) or is not present at all ($I > 0$) [8]; i.e., the potential varies monotonically within the film. It is noteworthy that the area under the ion peak in the *I–V* characteristic between points *1* and *3* corresponds exactly to the concentration N_S.

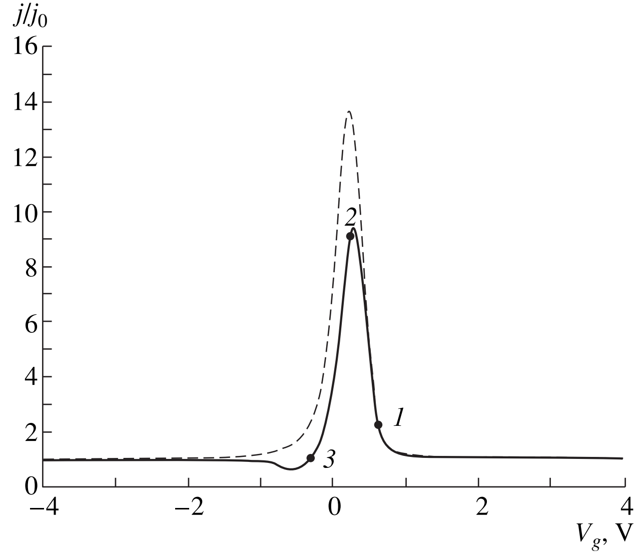

Fig. 1. Quasi-static current–voltage characteristic $j(V_g)$ for an ion current in a MIS structure. Points *1* and *3* correspond to zero fields in the metal and semiconductor, respectively; point *2* corresponds to symmetric distribution of ions in the film. The dashed line represents the $j^*(V_g)$ characteristic obtained disregarding the effect of a semiconductor on the current amplitude; j_0 is the capacitive current in the film, $N_S = 10^{12}$ cm^{-2}, $d = 1000$ Å, $T = 500$ K, and $N_d = 10^{15}$ cm^{-3}.

We now perform certain estimations. The amplitudes of voltages and currents depend appreciably on the parameter λ given by

$$\lambda = \mathscr{E}_d/\mathscr{E}_i, \quad \lambda \ll 1; \quad (18)$$

this parameter is usually small. Indeed, $\mathscr{E}_i \approx 4.6 \times 10^5$ V/cm (for $N_S = 10^{12}$ cm^{-2}) and $\mathscr{E}_d \approx 0.86 \times 10^4$ V/cm (for d = 1000 Å and $T = 500$ K); thus, $\lambda \approx 10^{-2}$. At points *1* and *3*, we have $y_1 = y_3$ and $j_1^* = j_3^*$ (subscripts 1 and 3 correspond to points *1* and *3*); furthermore, $y_1 = \pi/(2\xi_1)$, where $\xi_1 \approx 1 + \lambda$ in approximation (18). Then,

$$j_1^*/j_0 = (y_1)^2\gamma_1 \approx (\pi/2)^2, \quad \gamma_1 = [1 + \lambda + (\lambda y_1)^2]/(1 + \lambda y_1^2). \quad (19)$$

The approximate equalities in (19)–(22) correspond to condition (18). Voltages at points *1* and *3* are equal to

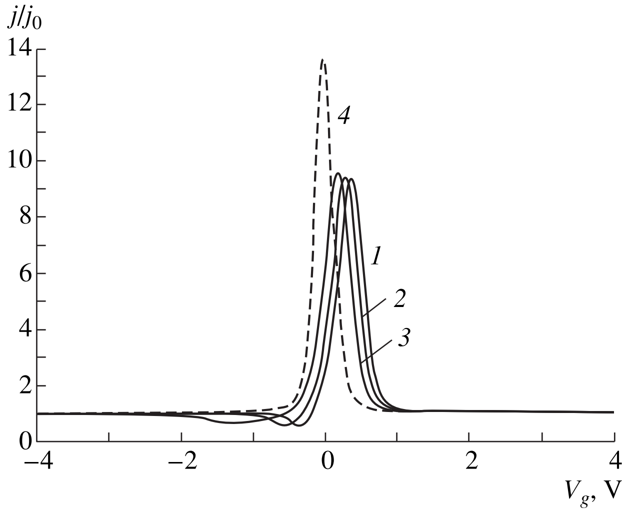

Fig. 2. The effect of a semiconductor on the current–voltage characteristics $j(V_g)$ for the ion current in a MIS structure. The quasi-static characteristics were calculated for the dopant concentrations of N_d = (*1*) 10^{14}, (*2*) 10^{15}, and (*3*) 10^{16} cm^{-3}; curve *4* is for a MIM structure; j_0 is the capacitive current in the film; $N_S = 10^{12}$ cm^{-2}, $d = 1000$ Å, and $T = 500$ K.

$V_{g1} \approx 0.628$ V and $V_{g3} \approx -0.306$ V, whereas the voltages at the film are $\Delta\varphi_1 = -\Delta\varphi_3$, with

$$\Delta\varphi_1 = (kT/q)\ln[1 + 1/(\lambda y_1)^2] \approx -(2kT/q)\ln(\lambda\pi/2); \quad (20)$$

furthermore, $V_{g3} = \Delta\varphi_3$ because $\varphi_{S3} = 0$.

In addition, at point *2* (the corresponding subscript is 2) in Fig. 1, we have $\mathcal{E}_{02} = -\mathcal{E}_i/2$; $[\mathcal{E}(d)]_2 = \mathcal{E}_i/2$; $\Delta\varphi_2 = 0$; $V_{g2} = \varphi_{S2} \approx 0.263$ V; the quantity y attains a maximum $y_{\max} = y_2 = \pi/\xi_2$, where $\xi_2 \approx 1 + 4\lambda$ under condition (18); and the current is given by

$$j_2^*/j_0 = \gamma_2/(4\lambda) \approx 1/(4\lambda), \quad \gamma_2 = [1 + (2\lambda y_2)^2]. \quad (21)$$

The height of the interior barrier in the film between the surface (φ_{02}) and the point corresponding to the maximum of potential (φ_{m2}) is equal to $\Delta\varphi_B = \varphi_{m2} - \varphi_{02}$, so that

$$\Delta\varphi_B = (kT/q)\ln[1 + 1/(2\lambda y_2)^2] \approx -(2kT/q)\ln(2\lambda\pi). \quad (22)$$

For the actual parameters of the structure, the barriers are not high: $\Delta\varphi_B \approx 0.1$–$0.5$ eV.

The impact of a semiconductor is illustrated in Fig. 2, where a series of *I–V* characteristics for several values of the dopant concentration N_d are shown; curve *4* corresponds to a MIM structure. The values of the parameters used were $N_S = 10^{12}$ cm^{-2}, $d = 1000$ Å, and $T = 500$ K. It is worth noting that the amplitudes of currents depend only slightly on N_d in the range of actual concentrations. The major changes are related to the shift of the peak and to the suppression of the dip on its left-hand slope, until this dip disappears completely in the range of high concentrations.

3. DISTRIBUTION OF IONS IN THE FILM

Figure 3 shows the ion distributions $N(z)$ plotted using formulas (10) and (11) for typical values of the parameters ($N_S = 5 \times 10^{11}$ cm^{-2}, $d = 1000$ Å, $T = 500$ K, and $N_d = 10^{15}$ cm^{-3}) and for the voltages at the structure V_g = (curve *1*, $\Delta\varphi = 0$) 0.205 V, (curve *2*) 0 V, and (curve *3*, $\mathcal{E}_0 = 0$) 0.511 V.

The distributions feature a wide "background" portion, and a sharp increase in concentration is observed in the vicinity of one or both (depending on the voltage) interfaces at a distance of about (0.1–0.2)d from these interfaces. It follows from formulas (10) and (12) that the concentration $N(d)$ at the interface with the semiconductor can be written as

$$N(d) = N^*[(\lambda y)^2 + (1 + \mathcal{E}_0/\mathcal{E}_i)^2];$$
$$N^* = 2\pi q^2 N_S^2/(\varepsilon_i kT), \quad (23)$$
$$N^*[\text{cm}^{-3}] \approx 4.64 \times 10^{18}(N_S[\text{cm}^{-2}]/10^{12})^2 \times (0.05/kT[\text{eV}])(3.9/\varepsilon_i),$$

where N^* is the characteristic (in the fields $\mathcal{E}(d) \sim \mathcal{E}_i$) concentration. Actually, we have $N(d) \approx N^*$ on the right-hand side of the peak (point *1* in Fig. 1, $\mathcal{E}_0 = 0$), whereas $N(d) \approx N^*/4$ at the peak center point (point *2* in Fig. 1, $\mathcal{E}_0 = -\mathcal{E}_i/2$). It is pertinent here to write out the following useful relation between $\mathcal{E}_0$ and the voltage at the film Δu:

$$(\lambda y)^2 + (1 + \mathcal{E}_0/\mathcal{E}_i)^2 = [(1 + \mathcal{E}_0/\mathcal{E}_i)^2 - (\mathcal{E}_0/\mathcal{E}_i)^2]/[1 - \exp(-\Delta u)].$$

This expression follows from formulas (12) and (15).

In the region between points *1* and *3*, the ion concentration in the film has a minimum at the point z_m, $N(z_m) = N_{\min}$. Using (10) and (12), we obtain

$$N_{\min} = N_{bg}(y/\pi)^2; \quad N_{bg} = (\pi\varepsilon_i kT)/(2q^2 d^2),$$
$$N_{bg}[\text{cm}^{-3}] \approx 2 \times 10^{16} \quad (24)$$
$$\times (kT[\text{eV}]/0.05)(0.1/d[\mu\text{m}])^2(\varepsilon_i/3.9),$$

where N_{bg} is a characteristic "background" concentration, with $N_{\min} \approx N_{bg}$ at point *2* [under condition (18)]. A plot of $N_{\min}$ as a function of voltage is shown in Fig. 4. The difference in concentrations is quite distinct: $N_{bg}/N^* = (\pi\lambda)^2 \ll 1$. It is this condition and also the form of the dependence $N(z)$ [see (10)] that govern

the presence of background portions in the distribution of concentration for small $V_g \approx 0.1$ V. Such portions disappear and the segregation effect becomes more pronounced in the region of high voltages, where the first integral (8) has the reverse sign ($I > 0$).

The so-called frozen-out distributions (when the ions that are mobile at the high-temperature technological stage lose their mobility after rapid cooling of the sample) may also be close to the equilibrium distributions. We note that, even in the absence of both the external voltage and the fields of the contact potential difference (for example, in a vacuum–insulator–semiconductor system), the ions by themselves are attracted very effectively to the semiconductor. This situation corresponds to a zero field at the outer boundary of the film ($\mathcal{E}_0 = 0$, point *1* in Fig. 1, curve *3* in Fig. 3). Thus, under actual conditions, the potential drop in an insulator–semiconductor system may be significant $|\Delta\Phi| \approx$ 0.1–1 V. In this situation the following three types of distributions may emerge. (i) Symmetric distributions with a background portion and an increase in concentration at the boundaries (Fig. 3, curve *1*). (ii) Asymmetric distributions with an accumulation of ions at one of the boundaries and with a background (with a slow variation in the concentration) portion (Fig. 3, curves *2*, *3*). These distributions emerge for small $|\Delta\Phi| \approx$ 0.1–1 V. (iii) Highly asymmetric distributions without background portions and with ion-localization regions of ~10–100 Å in size. These distributions exist if the values of $\Delta\Phi$ are sufficiently large [8]. The distributions of the discussed types have been observed experimentally [5, 10]. However, the distributions of more intricate types are also observed, which may be related to the presence of other ions, ion traps, and inhomogeneities in the interfaces.

It is noteworthy that negative (the minus sign at the outer interface) values of $\Delta\Phi$ are encountered rarely [5]. Thus, in many cases, the ions accumulate at exactly the inner boundary of the film. The ion distribution can be changed by annealing [5, 10]; however, in order to eliminate the ions from the interior boundary, we have to use negative polarizing voltages or coatings that induce negative contact potential differences (coatings with a large work function). For the ions that are mobile even at low temperatures (as is the case for Na), the most radical method for eliminating such ions may consist in introducing surface ion traps with sufficiently high concentrations. The role of such traps can be played by impurity atoms (for example, phosphorus) that can form high-bonding-energy complexes with sodium.

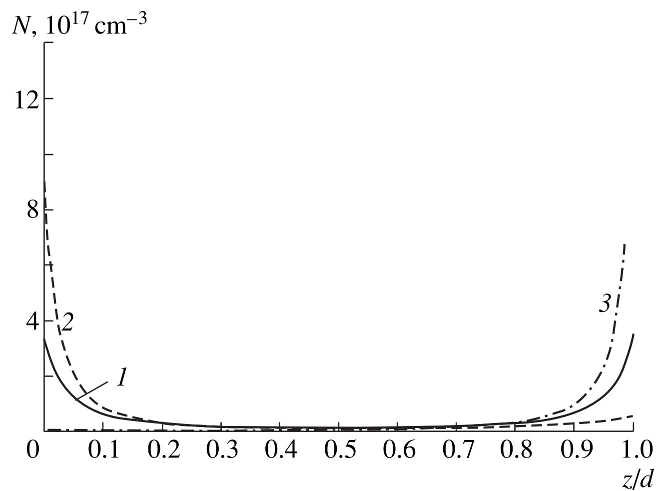

Fig. 3. Distribution $N(z)$ of ions in the film for the voltages at the structure V_g = (*1*) 0.205, (*2*) 0, and (*3*) 0.511 ($\mathcal{E}_0 = 0$) V. The values of the parameters are $N_S = 5 \times 10^{11}$ cm^{-2}, d = 1000 Å, T = 500 K, and $N_d = 10^{15}$ cm^{-3}; $\mathcal{E}_0$ is the field at the exterior surface of the film.

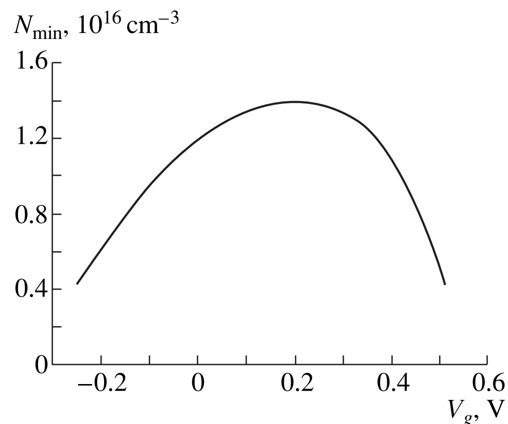

Fig. 4. Dependence of the minimal ion concentration in the film (N_{min}) on the voltage V_g at the structure. The parameters used were $N_S = 5 \times 10^{11}$ cm^{-2}, d = 1000 Å, T = 500 K, and $N_d = 10^{15}$ cm^{-3}.

4. EXPERIMENT

Dynamic I–V characteristics of ion currents and other experiments aimed at identifying the mobile ions and studying their properties in Si–SiO_2 are well known (see review [3]). Typically, these are sodium ($T >$ 300 K) or potassium ($T >$ 500 K) ions. However, at relatively low temperatures ($T <$ 500 K), the hysteresis phenomena are observed in the experiments with ions [4]. In addition, as the temperature increases, the obscuring effect of leakage currents (related, for example, to the hole injection into the film) becomes more and more pronounced. Therefore, the realization of the conditions for quasi-equilibrium deserves special attention.

For experiments, we used the metal–oxide–semiconductor (MOS) structures produced by oxidizing a silicon KÉF-20 (n-Si:P, $\rho = 20\ \Omega$ cm) substrate in a dry-oxygen atmosphere; the oxide thickness was d = 1000 Å. The measurements were performed at 200 ≤

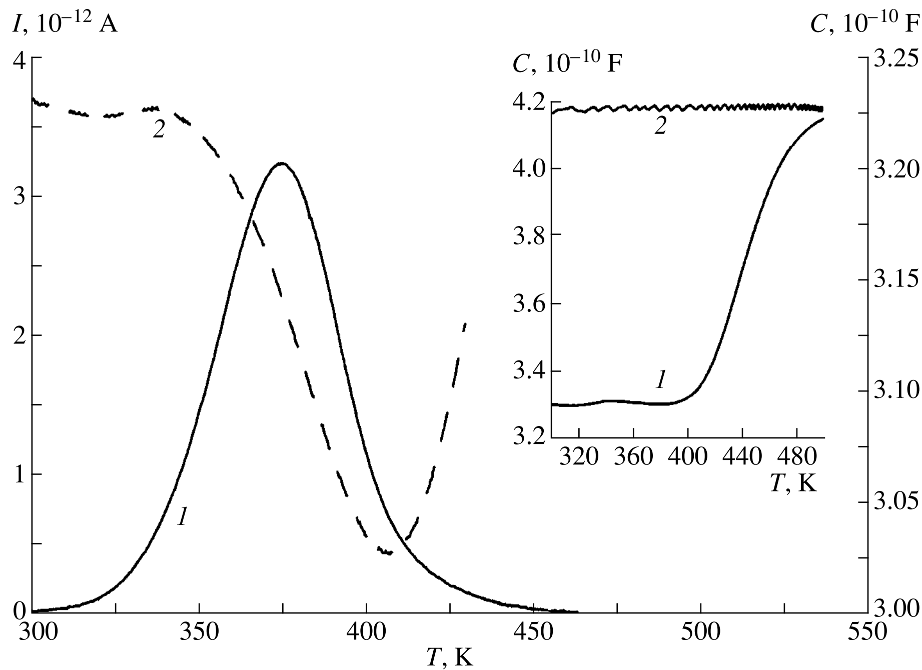

Fig. 5. Temperature dependences of (*1*) the depolarization current $I(T)$ and (*2*) the high-frequency capacitance $C(T)$ for a Si-based MOS structure. In the inset, we show the temperature dependences $C(T)$ of the (*1*) high-frequency and (*2*) low-frequency capacitances of the structure in the enhancement mode (the bias voltage is $V_g = 5$ V). The temperature-scan rate is 0.18 K/s.

$T \leq 500$ K using an automated setup that made it possible to record the isothermal (dynamic) and thermally stimulated ion currents while simultaneously measuring the structure capacitance C. The latter was measured using an E7-12 digital L, C, and R meter at a frequency of $f = 1$ MHz (high-frequency measurements of C) or using an E7-14 immitance meter at a frequency of $f = 100$ Hz (low-frequency measurements of C) for a series equivalent scheme connecting the active and reactive impedance components.

At first, the sample was polarized by a voltage of $V_g = 5$ V at $T = 500$ K. After the current had decreased to zero, the structure was cooled to $T = 200$ K under application of the above voltage V_g. At this temperature, the sample was heated with a rate of $\beta_T = 0.18$ K/s under the zero bias voltage. The temperature dependences of the current of thermally stimulated depolarization $I(T)$ and the high-frequency capacitance $C(T)$ were measured in the course of heating.

The dependences $I(T)$ (curve *1*) and $C(T)$ (curve *2*) are shown in Fig. 5. It is noteworthy that, at $T > 300$ K, the ions which were initially localized at the Si–SiO_2 interface become mobile; this temperature region of the mobility activation corresponds to sodium ions [3, 4]. At $T > 400$ K, an increase in the high-frequency capacitance is observed. The inset in Fig. 5 shows the temperature dependences of the high-frequency (curve *1*) and low-frequency (curve *2*) capacitances of the initially polarized sample (the polarization conditions were $T = 500$ K and $V_g = 5$ V); these dependences were measured under the voltage of $V_g = 5$ V.

It is noteworthy that, in the pronounced-enhancement mode, we typically have $C(T)$ = const to a high accuracy, because, in this case, the semiconductor capacitance C_S is large ($C_S \gg C_{ox}$, where C_{ox} is the oxide capacitance) [5] and is connected in series to the insulator capacitance. The temperature dependence (shown in the inset in Fig. 5) of the low-frequency capacitance ($C \approx 418$ pF) is quite consistent with the above reasoning. Relatively small (compared to the low-frequency C) values of the high-frequency capacitance at comparatively low temperatures and the subsequent increase in this capacitance count in favor of the activation (at $T > 400$ K) of additional electronic processes in the insulator and semiconductor; these processes have time to respond to the test-signal frequency (1 MHz). We discuss possible mechanisms of this phenomenon below.

Isothermal measurements at $T = 400$ K were performed in the following manner. The sample was polarized using a voltage of $V_g = 5$ V for a time during which the polarization current decayed to the zero value. When this process was terminated, the voltage V_g was varied linearly in the direction of depolarizing biases. The dependences $I(V_g)$ and $C(V_g)$ were recorded during variations in V_g.

In the inset in Fig. 6, we show the dynamic dependences $C(V_g)$ for the high-frequency (curves *1*, *2*) and low-frequency (curve *3*) capacitance; these depen-

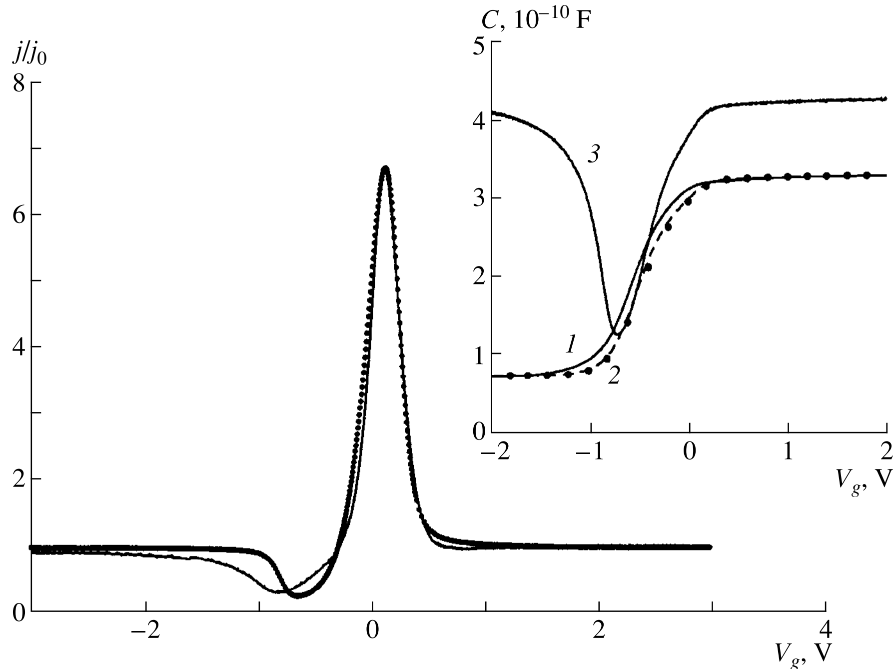

Fig. 6. Theoretical (points) and experimental (solid line) dynamic current–voltage characteristics $j(V_g)$ of a Si-based MOS structure; j_0 is capacitive current in the film; the rate of the bias-voltage scan was β_V = 1.7 mV/s; and T = 400 K. In the inset, we show the (*1*, *2*) high-frequency and (*3*) low-frequency dynamic capacitance–voltage characteristics $C(V_g)$ of the structure; the characteristics were measured for the β_V = (*1*) 16 and (*2* and *3*) 1.7 mV/s; T = 400 K; the points correspond to the steady-state values of the high-frequency capacitance.

dences were obtained for the voltage (V_g) scanning velocities β_V equal to (curve *1*) 16 mV/s and (curves *2*, *3*) 1.7 mV/s. The points correspond to steady-state values of the high-frequency capacitance measured under a constant bias voltage after the relaxation processes occurring as a result of steplike variation in the voltage V_g have been completed (the characteristic times of these processes may amount to several minutes). It can be seen that curve *2* is already close to the quasi-equilibrium characteristic. Therefore, the voltage scan with β_V = 1.7 mV/s was chosen when measuring the dynamic *I*–*V* characteristic.

Figure 6 shows an experimental dynamic *I*–*V* characteristic $I(V_g)/I_0$ (continuous line) normalized to $I_0 \approx 0.726 \times 10^{-12}$ A (the value of current in the range of $V_g \approx$ 2–5 V). It is worth noting that $I_0 \approx \beta_V C$ (for $C \approx 418$ pF); i.e., this value of current corresponds exactly to the low-frequency capacitance. In this situation, the effective metal-electrode area determined from the value of the capacitance ($C \approx 418$ pF) for d = 1000 Å is $S \approx 0.012$ cm^2; the latter value is consistent with the estimate of the area using a microscope. Since, for a one-dimensional configuration, we have $I(V_g)/I_0 = j/j_0$, we also show in Fig. 6, for the sake of comparison, the theoretical *I*–*V* characteristic $j(V_g)/j_0$ (the points) calculated for $N_S = 5.71 \times 10^{11}$ cm^{-2}, d = 1000 Å, T = 400 K, $N_d = 2 \times 10^{14}$ cm^{-3}, and φ_C = 0.138 V.

We now discuss the results obtained. Satisfactory agreement between the theory and experiment is observed for the main part of the peak. We may expect that, for this part of the peak, the actual distribution of ions in the film is consistent with theoretical predictions as well. Discrepancies between the theory and experiment are distinct at the peak sides, especially at its left-hand side in the region of the capacitance-related dip. Typically, such effects are related to the presence of traps in the film, the recharging of which leads to a shift and an "extension" of experimental dependences [5, 11]. In such a situation, longer relaxation times are caused by the tunneling character of the recharge process and the high barriers for electrons and holes in the insulator. Differences between curves *2* and *3* in Fig. 6 also count in favor of this mechanism.

However, another effect is also observed; this effect manifests itself in the difference between the values of the high- and low-frequency capacitances (see the inset in Fig. 6) in the enhancement region. The frequency dispersion of the voltage dependences of capacitance may be related to various factors. One of the popular models (the so-called two-dimensional model [11, 12]) attributes this dispersion to the presence of peripheral (outside the metal electrode) charges at the exterior or interior surfaces of the film. This phenomenon has been studied most thoroughly for the *p*-type samples. Its influence on the ion peaks has not been studied so far.

Thus, the shape of quasi-static *I–V* characteristics in actual samples may be affected by additional charges and traps in the film. This effect is most pronounced at the peak sides in which case the ions are localized at one of the interfaces. Further studies in this area will require additional experiments (for example, experiments with samples provided with guard rings) and the development of a theoretical model, in particular, with allowance made for the surface ion states.

5. CONCLUSION

The quasi-static current–voltage characteristics of the ion currents in thin insulating films of MIS structures (Figs. 1, 2) and the spatial distribution of ions in these films (Fig. 3) were calculated in terms of a model with a Boltzmann distribution of ions in energy. The points in the *I–V* characteristic (points *1* and *3* in Fig. 1) are identified such that the ion-peak area between these points corresponds exactly to the ion concentration in the film. For small potential drops across the structure ($\Delta\Phi \approx 0.1$–1 V), the ion distribution in the film is characterized by the presence of a "background" portion and by an increase in the concentration in the vicinity of the one or two film boundaries; depending on the magnitude and sign of $\Delta\Phi$, this distribution may be either symmetric (curve *1* in Fig. 3) or asymmetric (curves *2*, *3*). We suggested the formulas for the background concentration [see (24) and Fig. 4] and the ion concentration at the film boundary [see (23)]. For high voltages, the ions are localized within distances smaller than 100 Å from one of the interfaces, and there are no background portions.

We reported the experimental dynamic *I–V* characteristics of the silicon-based MOS structures and the simultaneously measured capacitance–voltage characteristics. Discrepancies between theoretical and experimental *I–V* characteristics (Fig. 6) are mainly observed at the ion-peak slopes and outside the peak; i.e., these discrepancies are observed in the regions where the ions are localized at one of the interfaces. We discussed some plausible reasons for these discrepancies.

REFERENCES

1. T. Ando, A. B. Fowler, and F. Stern, Rev. Mod. Phys. **54**, 437 (1982).
2. S. G. Dmitriev and Yu. V. Markin, Fiz. Tekh. Poluprovodn. (St. Petersburg) **32**, 1439 (1998) [Semiconductors **32**, 1284 (1998)].
3. J. F. Verwey, E. A. Amerasekara, and J. Bisschop, Rep. Prog. Phys. **53**, 1297 (1990).
4. G. F. Derbenwick, J. Appl. Phys. **48**, 1127 (1977).
5. S. Sze, *Physics of Semiconductor Devices* (Wiley, New York, 1981; Mir, Moscow, 1984).
6. A. G. Tangena, J. Middelhoek, and N. F. Rooij, J. Appl. Phys. **49**, 2976 (1978).
7. V. P. Romanov and Yu. A. Chaplygin, Phys. Status Solidi A **53**, 493 (1979).
8. S. G. Dmitriev and Yu. V. Markin, Fiz. Tekh. Poluprovodn. (St. Petersburg) **34** (8), 970 (2000) [Semiconductors **34**, 931 (2000)].
9. L. D. Landau and E. M. Lifshitz, in *Statistical Physics* (Nauka, Moscow, 1976; Pergamon, Oxford, 1980), Part 1.
10. A. G. Dutov and V. A. Komar, Élektron. Tekh., Ser. 2: Poluprovodn. Prib., No. 1 (204), 52 (1990).
11. K. H. Zaininger, in *Field-Effect Transistors: Physics, Technology and Applications*, Ed. by J. T. Wallmark and H. Johnson (Prentice-Hall, Englewood Cliffs, 1966; Sov. Radio, Moscow, 1971).
12. S. R. Hofstein and G. Warfield, Solid-State Electron. **8**, 321 (1965).

Translated by A. Spitsyn

Semiconductors, Vol. 35, No. 2, 2001, pp. 193–195. Translated from Fizika i Tekhnika Poluprovodnikov, Vol. 35, No. 2, 2001, pp. 200–202.
Original Russian Text Copyright © 2001 by Berman.

SEMICONDUCTOR STRUCTURES, INTERFACES, AND SURFACES

Simulation of Hysteresis in a Metal–Ferroelectric–Semiconductor Structure

L. S. Berman

Ioffe Physicotechnical Institute, Russian Academy of Sciences, Politekhnicheskaya ul. 26, St. Petersburg, 194021 Russia
Submitted June 16, 2000; accepted for publication June 21, 2000

Abstract—The hysteresis in the dependence of the polarization P on the electric field E was simulated for a metal–ferroelectric–semiconductor structure with a perovskite semiconductor. The simulation is based on the analysis of an experimental $P(E)$ hysteresis loop observed in a metal–ferroelectric–metal structure and approximated by hyperbolic tangent. Poisson's equation is numerically integrated with consideration for the dependence of the ferroelectric permittivity on electric field. The depolarizing action of the semiconductor reduces the remanent polarization several times, with the depolarization effect more pronounced for a semiconductor with lower impurity concentration. © *2001 MAIK "Nauka/Interperiodica".*

INTRODUCTION: PROBLEM FORMULATION

The use of field-effect transistors (FETs) based on metal–ferroelectric–semiconductor (MFES) structures was proposed as far back as in the 1960s [1–5]. At present, this line of investigation is developing rapidly because of technological achievements and the growing demand for memory elements [6–12].

One of fundamental difficulties encountered in creating MFES FETs is depolarization; i.e., weakening of polarization in thin layers of a ferroelectric (FE). In a semiconductor, the charge screening the FE polarization penetrates deep inside the material, which causes band bending and gives rise to a surface potential ψ_s and, consequently, to a depolarizing field E_f in FE [13–19]. Reduction of depolarization is a topical task whose solution could be aided by simulating the MFES structures, which enables prognostication of MFES FET properties. In [20], an MFES FET was simulated, with the operation of the FET based on the formation of an inversion layer in the semiconductor. However, the matching of FE to silicon entails severe technological difficulties (see, e.g., [11, 21]).

At present, mainly perovskite semiconductors technologically compatible with FE are used in developing the MFES FETs [9–11, 22, 23]. In these FETs, the channel conductance is modulated without formation of an inversion layer in the semiconductor [9, 10]. In [16–19], MFES and metal–ferroelectric–metal structures were simulated, and their stable equilibrium states were calculated from the minimum in the dependence $F(P)$, where F is the free energy and P is the polarization. However, the $F(P)$ dependences used in these works had been developed for a single-domain FE [24, 25], while actual FEs (both ceramics and films) are, as a rule, multidomain polycrystals.

In this study, the simulation is based on an analysis of the experimental $P(E)$ hysteresis loop (E is the electric field) of a metal–ferroelectric–metal (MFEM) structure, i.e., on reliable information. This loop is approximated by hyperbolic tangent. Then, Poisson's equation for the MFES structure is integrated to yield its basic characteristics: dependences of the quantities ψ_s, Q_s, E_s, V_f, and P on external voltage V (here ψ_s is the surface potential of the semiconductor, Q_s is the charge in the semiconductor, E_s is the electric field at the semiconductor surface, and V_f is the voltage drop across the ferroelectric). It is assumed that the contact to FE forms a Schottky barrier, the contact to the semiconductor is ohmic, and both the FE and the semiconductor are doped with shallow-level acceptors. It is also assumed that the current through the MFES structure is small and has no effect on the polarization.

BASIC EQUATIONS

For the semiconductor, the solution to Poisson's equation and also expressions for E_s, Q_s, and ψ_s are well-known (see, e.g., [26, 27]) and, therefore, are not presented here. We note that the concentrations of electrons and/or holes were calculated using the Boltzmann statistics for the case of depletion and the Fermi–Dirac statistics for accumulation.

For the FE, Poisson's equation takes the form (see, e.g., [28])

$$\frac{\partial^2\psi}{\partial x^2} = -\frac{\rho}{\left(\varepsilon_0 + \frac{\partial P}{\partial E}\right)}, \tag{1}$$

where ψ is the potential, ε_0 is the permittivity of free space, and ρ is the volume charge density.

At the FE–semiconductor interface, the following relation is observed

$$\varepsilon_0\varepsilon_s E_s + Q_{ss} = \varepsilon_0 E_f + P. \tag{2}$$

1063-7826/01/3502-0193$21.00 © 2001 MAIK "Nauka/Interperiodica"

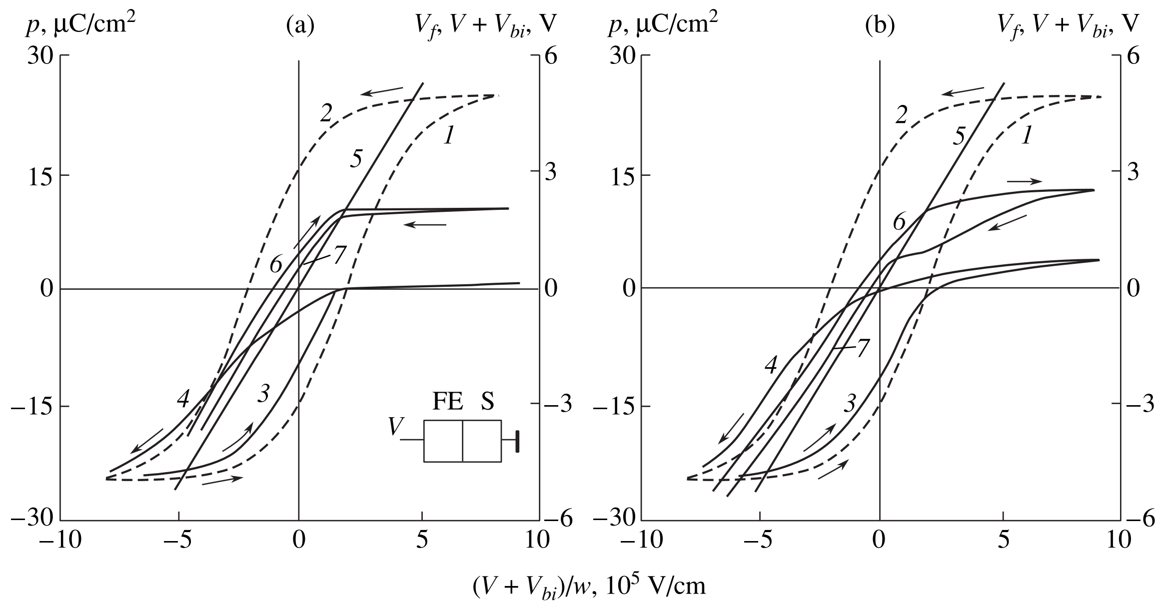

Hysteresis loops of metal–ferroelectric–metal (MFEM) and metal–ferroelectric–semiconductor (MFES) structures. Concentration of shallow-level acceptors in the semiconductor N_s = (a) 10^{15} and (b) 10^{19} cm^{-3}; other parameters are the same for (a) and (b); ferroelectric thickness $w = 0.1$ μm; concentration of shallow-level acceptors in the ferroelectric $N_f = 10^{18}$ cm^{-3}, $\varepsilon_s = 10$, $P_s = 25$ μC/cm^2, $P_r = 15$ μC/cm^2, and $E_c = 2 \times 10^5$ V/cm. (*1*, *2*) Ascending and descending portions of the hysteresis loop of an MFEM structure; (*3*, *4*) ascending and descending portions of the hysteresis loop of an MFES structure; (*5*) $V + V_{bi}$; (*6*, *7*) V_f for the ascending and descending portions, respectively. Inset: FE, ferroelectric; S, semiconductor; and *V*, voltage applied to the structure.

Here, ε_s is the dielectric constant of the semiconductor, Q_{ss} is the charge of surface states, and E_f is the electric field in the ferroelectric.

The electric-field dependence of the polarization $P(E)$ was approximated at various initial conditions by expressions (19)–(23) from [29] and (1)–(3) from [30]. The distribution of the electric field and potential in the FE was found by numerical integration of Poisson's equation. The calculations were performed for a metal–⟨*p*-type ferroelectric⟩–⟨*p*-type semiconductor⟩ structure, with voltage increasing from a value corresponding to $-P_s$ (carrier accumulation at the semiconductor surface, P_s is the spontaneous polarization) to values corresponding to the depletion of the semiconductor surface, and also for a reverse sweep of the voltage.

The following parameter values were adopted:

(a) For FE, spontaneous polarization $P_s = 25$ μC/cm^2, remanent polarization $P_r = 15$ μC/cm^2, coercive field $E_c = 2 \times 10^5$ V/cm, shallow-level acceptor concentration $N_f = 10^{18}$ cm^{-3}, and thickness 0.1 μm.

(b) For semiconductor, dielectric constant $\varepsilon_s = 10$, shallow-level acceptor concentration $N_s = 10^{15}$ and 10^{19} cm^{-3}, and surface-state charge $Q_{ss} = 0$.

RESULTS OF CALCULATION AND DISCUSSION

The main results of the calculations are shown in Figs. 1a and 1b; also shown for comparison is a saturated hysteresis loop (from $-P_s$ to P_s and back) of an MFES structure with the same FE, but without impurities in the FE ($N_f = 0$) (lines *1* and *2*). In the figure, V_{bi} is the contact potential difference between the contact to the ferroelectric and the semiconductor. The surface potential of the semiconductor ψ_s is calculated as the difference between dependences *5* ($V + V_{bi}$) and *6* (V_f for the ascending portion) or dependences *5* and *7* (V_f for the descending portion).

In the case of carrier accumulation at the semiconductor surface ($\psi_s < 0$), its properties approach the properties of a metal and, therefore, the ascending portions for the MFEM and MFES structures run close (lines *1* and *3*, respectively). The electric field strength at the semiconductor surface, E_s, may be as high as several times 10^7 V/cm; however, such strong electric fields exist only in a very thin layer (on the order of several angstroms), which rules out the possibility of avalanche breakdown. The carrier accumulation at the semiconductor surface is replaced by its depletion at $E \simeq E_c$ (the point of intersection of lines *5* and *6*), where E_c is the coercive field.

In the case of depletion of the semiconductor surface ($\psi_s > 0$), an increase in the voltage V leads to a

higher voltage drop across the semiconductor ψ_s (difference between lines *5* and *6*); the voltage V_f across the FE (and, consequently, its polarization) change only slightly. This feature is more pronounced for semiconductors with lower impurity concentration (cf. run of lines *6* in Figs. 1a and 1b). For $N_s = 10^{18}$–10^{19} cm^{-3} and voltages of several volts, the field strengths E_s at the semiconductor surface may be as high as several times 10^6 V/cm, i.e., exceed severalfold the breakdown electric field in silicon [27]. However, the carrier mobility in perovskite semiconductors is much lower than that in silicon. Therefore, there is good reason to assume that electrons (or holes) in perovskite semiconductors will not acquire an energy sufficient for impact ionization along the mean free path.

Comparison of the remanent polarizations $-P_r$ and P_r for the ascending and descending portions of the hysteresis loop of the MFEM structure with the corresponding values for the MFES structure shows that the depolarization under the impact of the semiconductor strongly reduces (from two to three times) the remanent polarization.

The hysteresis loop of the MFES structure in this study is qualitatively similar to the experimental dark hysteresis loop of the structure Au–⟨triglycine sulfate⟩–*p*-Si [17], which confirms the correctness of our simulation procedure. However, our results differ somewhat from the calculated dependence $P(E)$ from [16], which, in particular, shows stepwise changes in depolarization at certain fields. This discrepancy is due to the use of different simulation methods (see above).

CONCLUSION

The hysteresis in a metal–ferroelectric–semiconductor structure is simulated on the basis of an analysis of an experimental hysteresis loop of a metal–ferroelectric–metal structure. It is shown that the depolarizing effect of the semiconductor reduces the remanent polarization severalfold, with the depolarization effect being more pronounced for a semiconductor with lower impurity concentration.

ACKNOWLEDGMENTS

I am grateful to I.V. Grekhov for problem statement and for his helpful participation in discussions.

REFERENCES

1. J. Moll and Y. Tarui, IEEE Trans. Electron Devices **ED-10**, 338 (1963).
2. R. Zuleeg and H. H. Wider, Solid-State Electron. **9**, 657 (1966).
3. S. Y. Wu, IEEE Trans. Electron Devices **ED-21**, 499 (1974).
4. K. Sugibuchi, Y. Kurogi, and N. Endo, J. Appl. Phys. **46**, 2877 (1975).
5. S.Y. Wu, Ferroelectrics **11**, 379 (1976).
6. Y. Higuma, Y. Matsui, M. Okuyama, *et al.*, Jpn. J. Appl. Phys., Suppl. **17**, 209 (1978).
7. J. F. Scott and D. A. Araujo, Science **246**, 1400 (1989).
8. J. T. Evans and R. Womack, IEEE J. Solid-State Circuits **23**, 1171 (1988).
9. Y. Watanabe, Appl. Phys. Lett. **66**, 1770 (1995).
10. Y. Watanabe, M. Tanamura, and Y. Matsumoto, Jpn. J. Appl. Phys., Part 1 **35**, 1564 (1996).
11. Y. Watanabe, Phys. Rev. B **59**, 11257 (1999).
12. Y. Watanabe, M. Tanamura, Y. Matsumoto, and H. Asami, Appl. Phys. Lett. **66**, 299 (1995).
13. B. M. Vul, G. M. Guro, and I. I. Ivanchik, Fiz. Tekh. Poluprovodn. (Leningrad) **4**, 162 (1970) [Sov. Phys. Semicond. **4**, 128 (1970)].
14. B. V. Sandomirskiĭ, Sh. S. Khokhlov, and E. V. Chenskiĭ, Fiz. Tekh. Poluprovodn. (Leningrad) **16**, 440 (1982) [Sov. Phys. Semicond. **16**, 279 (1982)].
15. R. R. Mehta, B. D. Silverman, and J. T. Jacobs, J. Appl. Phys. **44**, 3379 (1973).
16. I. P. Batra and P. Wurfel, Phys. Rev. B **8**, 3257 (1973).
17. P. Wurfel and I. P. Batra, Phys. Rev. B **8**, 5126 (1973).
18. Y. Watanabe, J. Appl. Phys. **83**, 2179 (1998).
19. Y. Watanabe, Phys. Rev. B **57**, 789 (1998).
20. S. L. Miller and P. J. McWhorter, J. Appl. Phys. **72**, 5999 (1992).
21. E. Tokumitsu, K. Itani, B.-K. Moon, and H. Ishiwara, Jpn. J. Appl. Phys., Part 1 **34**, 5202 (1995).
22. Y. Watanabe, Y. Matsumoto, and M. Tanamura, Jpn. J. Appl. Phys., Part 1 **34**, 5254 (1995).
23. Y. Watanabe, Appl. Phys. Lett. **66**, 28 (1995).
24. L. D. Landau and E. M. Lifshitz, *Statistical Physics* (Nauka, Moscow, 1995; Pergamon, Oxford, 1980), Part 1.
25. V. M. Fridkin, *Photoferroelectrics* (Nauka, Moscow, 1976; Springer-Verlag, Berlin, 1979).
26. I. E. Tamm, *The Principles of the Electricity Theory* (Nauka, Moscow, 1989).
27. S. Sze, *Physics of Semiconductor Devices* (Wiley, New York, 1981; Mir, Moscow, 1984), Vol. 1.
28. P. W. M. Bloom, R. M. Wolf, J. F. M. Cilessen, and M. P. C. M. Krijn, Phys. Rev. Lett. **73**, 2107 (1994).
29. S. L. Miller, J. R. Schwank, R. D. Nasby, and M. S. Rodgers, J. Appl. Phys. **68**, 6463 (1990).
30. S. L. Miller, J. R. Schwank, R. D. Nasby, and M. S. Rodgers, J. Appl. Phys. **70**, 2849 (1991).

Translated by M. Tagirdzhanov

Semiconductors, Vol. 35, No. 2, 2001, pp. 196–198. Translated from Fizika i Tekhnika Poluprovodnikov, Vol. 35, No. 2, 2001, pp. 203–205.
Original Russian Text Copyright © 2001 by Vasil'ev, Zakhar'yash, Kesler, Parm, Solov'ev.

Investigation of a Change in the Chemical Composition of the Surface of $Cd_xHg_{1-x}Te$ Samples as a Result of Treatment by N_2O and H_2 Gases Activated in a High-Frequency Discharge

V. V. Vasil'ev, T. I. Zakhar'yash, V. G. Kesler*, I. O. Parm, and A. P. Solov'ev

Institute of Semiconductor Physics, Siberian Division, Russian Academy of Sciences, pr. Akademika Lavrent'eva 13, Novosibirsk, 630090 Russia

** e-mail: kesler@isp.nsc.ru*

Submitted June 16, 2000; accepted for publication July 4, 2000

Abstract—A change in the chemical composition of the $Cd_xHg_{1-x}Te$ surface as a result of its treatment by atomic beams of oxygen and hydrogen was investigated. The beams were obtained by the electron impact in a high-frequency plasma of N_2O and H_2 gases. The consecutive action of beams of atomic oxygen and hydrogen was shown to result in the removal of carbon-containing compounds, a layer of native oxide, and tellurium in its elemental state from the surface of samples. © *2001 MAIK "Nauka/Interperiodica".*

A large number of methods are used nowadays for passivating the surface of compounds based on cadmium, mercury, and tellurium (CMT), with the subsequent formation of insulating protective films. Of wide usage are the methods of vacuum deposition of zinc-sulfide layers, the molecular-beam epitaxy (MBE) and MOC-hydrate epitaxy of cadmium telluride, and the pyrolytic and plasma-chemical deposition of silicon-dioxide and silicon-nitride layers [1–3].

An actual surface of II–VI semiconductors is always covered by a layer of the native oxide 1–3 nm thick, formed as a result of the interaction of a substrate with oxidizing components of an etchant and atmospheric oxygen. The chemical composition of this oxide depends substantially on the method of chemical treatment of the semiconductor and the relationship between components of the etchant and the solutions used for rinsing the surface. In the process of the synthesis of an insulator, the chemical composition of the native oxide can also undergo considerable chemical transformations, which ultimately exerts an adverse effect on the parameters of photoelectronic devices.

The idea of obtaining structures on the II–VI semiconductors with an oxygenfree interface, i.e., with a complete removal of the native oxide, and the subsequent synthesis of the insulating layer, has been actively discussed [4]. Treatment of a semiconductor by atomic hydrogen obtained by the method of thermal decomposition of H_2 at a heated tungsten filament was suggested [4]. According to [4], under these conditions (a substrate temperature is T = 80°C), the following reducing reactions can proceed:

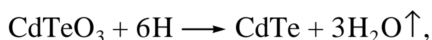

$$CdTeO_3 + 6H \longrightarrow CdTe + 3H_2O\uparrow,$$

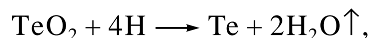

$$TeO_2 + 4H \longrightarrow Te + 2H_2O\uparrow,$$

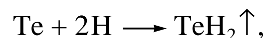

$$Te + 2H \longrightarrow TeH_2\uparrow,$$

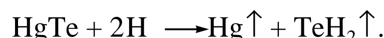

$$HgTe + 2H \longrightarrow Hg\uparrow + TeH_2\uparrow.$$

In this case, mercury in the elemental state is thermally desorbed from the surface of a semiconductor. According to the model suggested, the removal of oxide and elemental phases from a CMT surface is theoretically attainable. At the same time, cleaning the substrate surface of carbon-containing contaminations (residues of organic solvents after rinsing, etc.) is impossible by atomic hydrogen from the standpoint of the chemical thermodynamics [5]. The carbon-containing particles are removed from the surface by activated oxygen [for example, by means of a high-frequency (HF) discharge]. As a gas reactant in such processes, nitrogen oxide with a low dissociation energy of its molecules (E = 1.7 eV) can be used. In our opinion, the combination of treatments of a surface by atomic beams of oxygen (carbon-containing contaminations are removed) and hydrogen (the native-oxide layer is reduced and elemental phases are removed) is promising for the technology of improving the insulator–CMT interface.

In our study, we investigated the influence of atomic beams of hydrogen and oxygen on a CMT surface. The beams were obtained by electron impact in the high-frequency (f = 13.56 MHz) plasma. The usage of a two-chamber reactor in our technological setup with a special separation of the substrate and the HF-discharge zones precluded the impact of ions and electrons of the plasma upon the surface of CMT samples [6]. This

1063-7826/01/3502-0196$21.00 © 2001 MAIK "Nauka/Interperiodica"

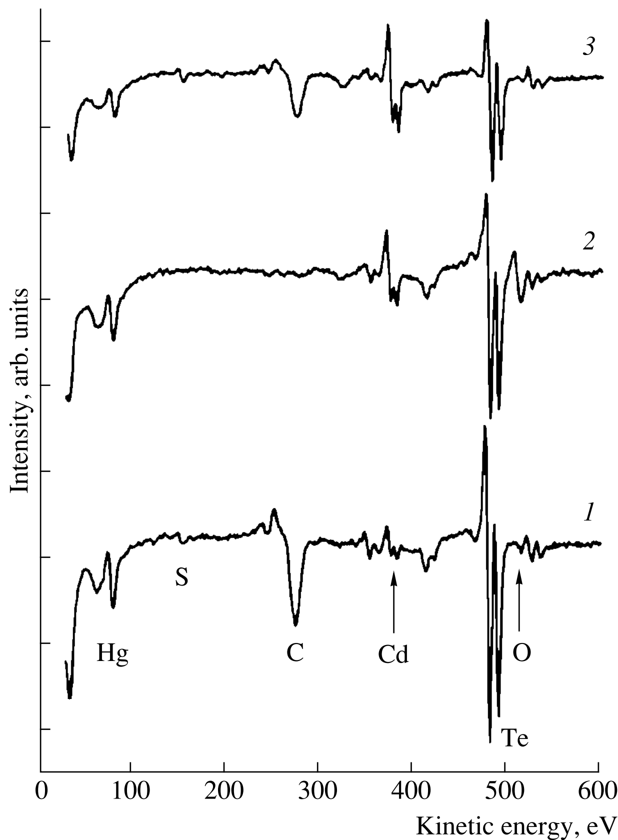

Fig. 1. The Auger spectra of the surface of a $Cd_{0.22}Hg_{0.78}Te$ sample: (*1*) initial surface; (*2*) surface after the treatment by a beam of atomic oxygen, and (*3*) surface after the treatment by a beam of atomic hydrogen.

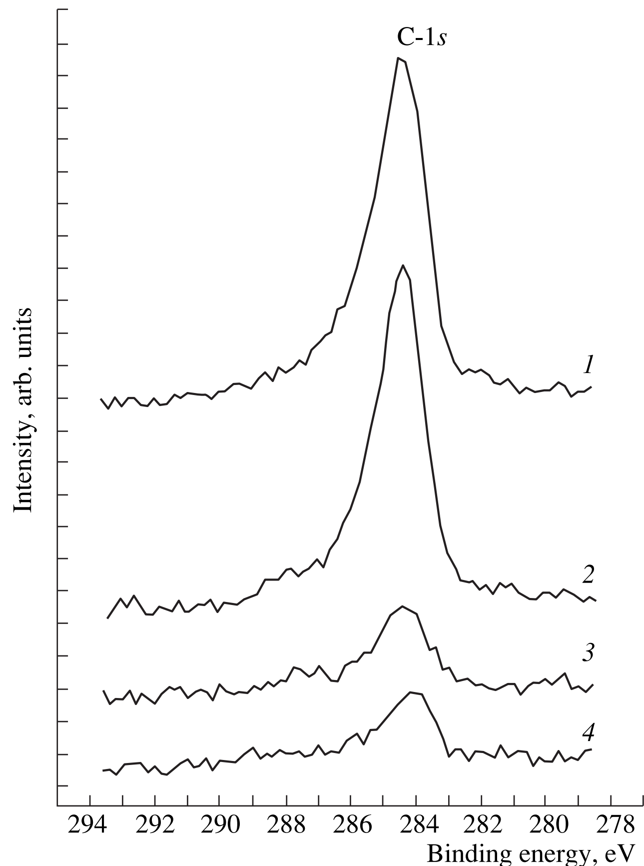

Fig. 2. X-ray photoelectron spectra C-1*s* of the surface of a $Cd_{0.22}Hg_{0.78}Te$ sample: (*1*) initial surface, (*2*) surface after the treatment by a beam of atomic hydrogen (sample 3), (*3*) surface after the treatment by a beam of atomic oxygen (sample 2), and (*4*) surface after the combined treatment.

setup also made it possible to deposit an insulating layer immediately after atomic-beam treatment, without removing the sample from the reactor.

Preliminary electrical investigations of the MIS structures manufactured on the basis of CMT show that electrical parameters depend strongly on the conditions existing during treatment of the semiconductor surface (the nature of a gas reactant, a substrate temperature, the duration of exposure to activated gas, etc.). With the purpose of clarifying the causes of significant modification of MIS-structure parameters, we investigated the chemical composition of the surface of substrates.

The analysis was carried out by Auger electron spectroscopy (AES) and X-ray photoelectron spectroscopy (XPS). These methods are exclusively sensitive to the upper monolayers of the sample and are mutually complementary; their combination makes it possible to determine both the elemental composition of the surface under investigation and the chemical state of atoms. The AES spectra of the sample surface were obtained using an OPC-2 Riber analyzer with a relative energy resolution $\Delta E/E = 0.2\%$. For obtaining the spectrum of secondary electrons, they were excited by an electron beam with an energy of 3 keV. The electron-beam diameter amounted to 5 μm, and the beam current was 100 nA. The XPS spectra were obtained using a MAC-2 Riber analyzer of the two-stage cylindrical-mirror type. For exciting the X-ray radiation, we used a Mg-anode source with a Mg-line energy of 1253.6 eV. The X-ray-beam diameter amounted to 5 mm, the source power was 300 W, and the energy resolution of the analyzer amounted to 0.5 eV and was constant within the entire energy range measured.

The objects of investigation were p-$Cd_xHg_{1-x}Te$ ($x = 0.22$) bulk samples subjected to the mechanochemical polishing (a damaged layer was removed up to a depth of 100 μm), the dynamic chemical polishing in a brom–ethanol etchant (a damaged layer of 10 μm was removed), and a rinsing in three portions of acetone and in deionized water. The treatment in gases activated by a high-frequency discharge was performed at a substrate temperature equal to 80°C. In this paper, we display the results of investigating a chemical composition for four CMT samples:

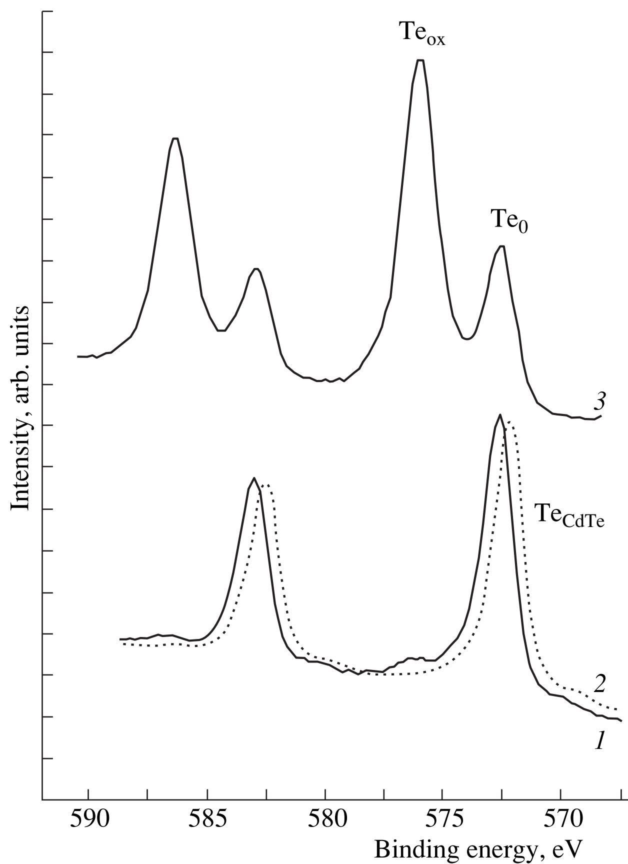

Fig. 3. X-ray photoelectron Te-3*d* spectra from the surface of a $Cd_{0.22}Hg_{0.78}Te$ sample: (*1*) initial surface, (*2*) surface after the treatment by a beam of atomic hydrogen (sample 3), and (*3*) surface after the treatment by a beam of atomic oxygen (sample 2).

sample 1 is the initial sample after the chemical preparation and rinsing;

sample 2 is the sample treated in nitrogen oxide activated by the HF discharge (t = 30 s);

sample 3 is the sample treated in hydrogen activated by the HF discharge (t = 30 s); and

sample 4 is the sample subjected consecutively to the same treatments as samples 2 and 3 for 60 s.

For investigating the chemical composition of the surface, all the samples were transported from the reactor to the setup through atmospheric air with an identical exposure to air for each sample. On the initial surfaces of the samples 1–4, the peaks of elements Te, Cd, Hg, O, and C were observed. No other elements were detected within several atomic percent. The carbon concentration on the surface of samples 2 and 4 is much lower than that on the surface of samples 1 and 3 (Figs. 1, 2), which substantiates the conclusions [5] that it is impossible to clean the substrate surface of carbon-containing contaminations exclusively by means of atomic hydrogen. It is necessary to emphasize that the use of combined treatment (sample 4) makes it possible to fix the effect of cleaning the surface of carbon-containing contaminations.

The energy position of the photoelectron peak of tellurium (Te-3$d_{5/2}$) (Fig. 3) observed in the XPS spectra of the samples under investigation bears important information. For example, for sample 2, we observe a pronounced splitting into two peaks, with binding energies of 576.1 and 572.8 eV corresponding to oxidized and elemental (metallic) states of tellurium [4]. Assuming that the peak with lower binding energy is the substrate signal weakened by a thin oxide film, it is possible to calculate a thickness of the oxide film, which amounts to ~1.6 nm in our case. A similar calculation for the initial sample 1 yields a value of ~0.2 nm, and tellurium under a thin oxide layer is also observed in the metallic state. On the surface of the sample 3, treated by atomic hydrogen, and sample 4, subjected to combined treatment, there is no oxide film, and tellurium resides in the CdHgTe compound with a binding energy of 572.3 eV.

Thus, the proposed combined treatment of the CMT-sample surface by atomic beams of O and H produced using the high-frequency discharge leads to an efficient removal of carbon atoms, the surface oxide film, and also of tellurium in the elemental state. The method proposed for treating the surface of CMT substrates can be efficiently used in the technology of fabrication of CMT-based structures.

REFERENCES

1. C. H. Lee, S. W. Paik, J. W. Park, *et al.*, J. Electron. Mater. **27** (6), 668 (1998).
2. Y. Nemirovsky, N. Amir, D. Goren, *et al.*, J. Electron. Mater. **24**, 1161 (1995).
3. V. M. Emerksuzyan, L. N. Romashko, G. Y. Saleeva, *et al.*, in *Extended Abstracts of the 1995 International Conference on Solid State Devices and Materials, Osaka, 1995*, p. 1061.
4. L. S. Hirsch, K. S. Ziemer, M. R. Richards-Babb, *et al.*, J. Electron. Mater. **27**, 651 (1998).
5. K. Asakawa and S. Sugata, J. Vac. Sci. Technol. A **4**, 677 (1986).
6. I. I. Marakhovka, I. O. Parm, L. S. Ronzhin, and A. P. Solov'ev, USSR Inventor's Certificate No. 1378767, MKI N05N 1/00/; No. 4038579/31–25.

Translated by V. Bukhanov

Semiconductors, Vol. 35, No. 2, 2001, pp. 199–203. Translated from Fizika i Tekhnika Poluprovodnikov, Vol. 35, No. 2, 2001, pp. 206–210.
Original Russian Text Copyright © 2001 by Khanin, Novoselov, Vdovin.

SEMICONDUCTOR STRUCTURES, INTERFACES, AND SURFACES

Tunneling via Impurity States Related to the *X* Valley in a Thin AlAs Barrier

Yu. N. Khanin*, K. S. Novoselov, and E. E. Vdovin***

* *Institute of Problems in Microelectronics Technology and Ultrahigh-Purity Materials, Russian Academy of Sciences, Chernogolovka, Moscow oblast, 142432 Russia*

e-mail: khanin@ipmt-hpm.ac.ru

** *Research Institute for Materials, High Field Magnet Laboratory, University of Nijmegen, 6525 ED Nijmegen, The Netherlands*

Submitted July 3, 2000; accepted for publication July 4, 2000

Abstract—Special features corresponding to resonance tunneling of electrons from the Γ valley of GaAs to the *X* valley of AlAs were observed in the current–voltage characteristics of single-barrier GaAs/AlAs/GaAs heterostructures. Tunneling both via the states related to the two-dimensional X_{xy} and X_z subbands and via the related impurity states was detected. It is shown that the energy position of such impurity states is largely controlled by two factors: (i) spatial confinement of the AlAs layer, which influences both the size-quantization energy levels of the X_{xy} and X_z subbands and the corresponding binding energies of impurity states, and (ii) the biaxial compression of the AlAs layer due to a mismatch of the AlAs and GaAs lattice parameters, which results in the splitting of the X_{xy} and X_z valleys. This made it possible to determine directly the binding energy of the impurity states; this energy was found to be ~50 meV for the X_z valley and ~70 meV for the X_{xy} valley. © *2001 MAIK "Nauka/Interperiodica".*

It is known that AlAs (unlike GaAs) is an indirect-gap semiconductor (the minimum of the conduction band is located in the vicinity of the *X* point of the Brillouin zone) and represents a quantum well (QW) for the *X*-valley electrons and a barrier for the Γ-valley electrons in AlAs/GaAs heterostructures (Fig. 1). The offset of the conduction-band bottom between the GaAs *X* valley and the AlAs Γ valley amounts to ~0.12 eV. Such a combination of properties has rendered the AlAs/GaAs-based heterosystems convenient objects for experimental studies of transitions between the states corresponding to the different symmetry points (Γ and *X*) of the Brillouin zone. It has been found experimentally that quantum states related to the *X* valley in AlAs exert a pronounced effect on the optical and transport properties of AlAs/GaAs-based heterosystems [1–4]. This has motivated interest in the mechanisms of transitions between the Γ and *X* states and in the spectra of states in the *X* valley of AlAs and the related impurity states.

Experimental studies of the optical [1, 2] and transport [3, 4] properties of AlAs/GaAs heterosystems have shown the following. The *X* valleys that are sixfold degenerate in the bulk AlAs are transformed into two types of two-dimensional (2D) *X* subbands with different energies if thin AlAs films are considered (i.e., under the conditions of size quantization in a single direction). This phenomenon is often referred to as the splitting of the *X* valleys and is caused by the following. First, for a thin AlAs layer (the *X* wells), the X_z and X_{xy} valleys (Fig. 1) are no longer equivalent owing to a difference in effective masses that govern the motion of electrons in the direction perpendicular to the heteroboundaries (the QW walls). The effective mass is $1.1m_0$ for the X_z valleys, whereas it is $0.19m_0$ for the X_{xy} valley. Therefore, the energy positions of 2D electron subbands belonging to the X_z and X_{xy} valley are different. Second, due to a 0.12% mismatch between the lattice constants of AlAs and GaAs, the lattice is compressed in the well plane in the AlAs layer and is extended in the perpendicular direction in accordance with the Poisson ratio. The compression leads to a descent of the X_{xy} valley, whereas the Poisson tension results in an ascent of the X_z valley. Thus, the X_z valley is located below the X_{xy} valley for AlAs layers less than 60 Å thick; the reverse situation is observed for an AlAs layer thicker than 60 Å [1].

The presence of donors in AlAs leads to the emergence of impurity states. The ground state of a silicon donor in bulk AlAs is triply degenerate [2]. The nature of these states is such that each of them may be independently related to a specific pair of *X* valleys. In the conditions of a thin AlAs layer, the triplet states are split into a doubly degenerate state (related to the X_{xy} valleys) and a singly degenerate state (related to the X_z valleys); this occurs in addition to the splitting of the *X* states. The binding energies of such impurity states have been calculated previously [5] with allowance made for the mass anisotropy and the size-quantization effect.

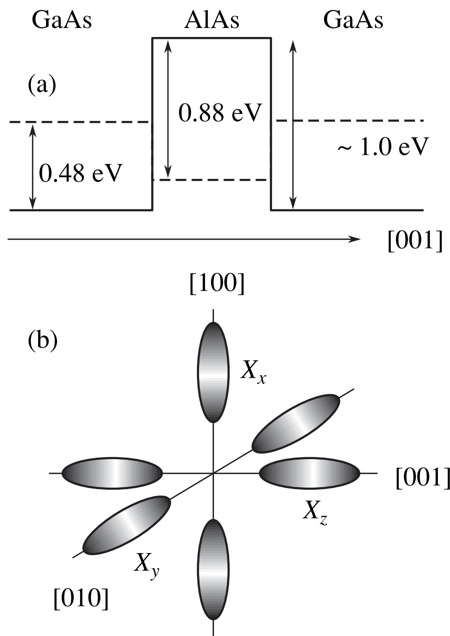

Fig. 1. (a) The profile of the conduction-band bottom of a GaAs/AlAs/GaAs heterostructure. (b) A schematic representation of the constant-energy ellipsoids in reference to the point X in the Brillouin zone in the k space for AlAs.

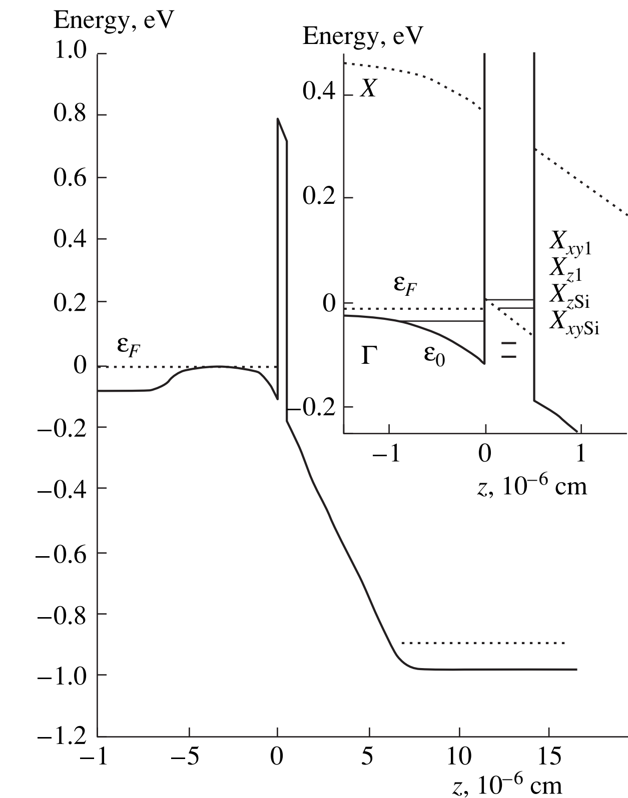

Fig. 2. Calculated profile of the conduction-band bottom (for the Γ point in the Brillouin zone) for a single-barrier GaAs/AlAs structure under a bias voltage of $V = 900$ mV. The profiles of the Γ- and X-band bottoms in the vicinity of the AlAs layer are shown in the inset. The positions of the Fermi level ε_F, the size-quantization level ε_0 in the 2D accumulation Γ layer in GaAs, and the size-quantization energy levels of the X_{xy} and X_z subbands in the AlAs barrier are shown. The energy positions of the X_{xySi} and X_{zSi} impurity states generated by the X_{xy} and X_z valleys in AlAs are also shown.

Tunneling spectroscopy makes it possible to directly measure the binding energy of the donor state if we observe the tunneling both via the ground state and via the impurity state and if we can convert the measured voltages to the energy values (i.e., if we know the potential distribution over the structure). Tunneling via the Si donor state in GaAs QWs in two-barrier resonance-tunneling $GaAs/Al_xGa_{1-x}As$-based diodes has been observed previously [6–8]; the experimentally determined value of binding energy [6–8] for such a donor state is in excellent agreement both with the calculated value for a QW with corresponding width and with the results of optical measurements. As far as we know, there have so far been only two publications [10, 11] (in addition to our preliminary study [9]) where the impurity states in the AlAs X valley have been reported. However, the results of the above studies do not give an accurate idea either of the impurity-state structure in the X valley or of the value of the corresponding binding energy.

In this study, we detected tunneling both via the states corresponding to the 2D X_{xy} and X_z subbands in the AlAs layer and via the related impurity states. This made it possible to directly determine the binding energies of the impurity states and to demonstrate that the energy positions of such impurity states is largely governed by the following two factors:

(i) The spatial confinement of the AlAs layer, which influences both the size-quantization levels in the X_{xy} and X_z subbands and the impurity-state binding energies.

(ii) The biaxial compression of AlAs layer due to the mismatch between the AlAs and GaAs lattice constants, which results in the splitting of the X_{xy} and X_z valleys by ~23 meV.

Heterostructures used in the fabrication of the samples were grown by molecular-beam epitaxy on the heavily doped n^+-GaAs(100) substrates at 570°C and had the following sequence of layers: an n^+-GaAs layer with $n = 2 \times 10^{18}$ cm^{-3} and a thickness of 400 nm; an n^--GaAs layer with $n = 2 \times 10^{16}$ cm^{-3} and a thickness of 50 nm; an undoped GaAs layer 10 nm thick; an undoped AlAs layer 5 nm thick; an undoped GaAs layer 10 nm thick; an n^--GaAs layer with a thickness of 50 nm and $n = 2 \times 10^{16}$ cm^{-3}; and an n^+-GaAs layer with a thickness of 400 nm and $n = 2 \times 10^{18}$ cm^{-3}. Silicon was used as a dopant. Nonrectifying contacts were formed by the consecutive deposition of AuGe, Ni, and Au layers with subsequent thermal annealing at 400°C. In order to form a mesa structure 100 μm in diameter,

we used the conventional technology of chemical etching. The calculated profile of the conduction-band bottom (for the Γ point in the Brillouin zone) in an experimental structure for a bias voltage of $V = 900$ mV is shown in Fig. 2. The profiles of the Γ and X bands in the vicinity of the AlAs layers are shown in the inset.

We measured the dependences of the current I, the differential conductance dI/dV, and the second derivative d^2I/dV^2 on the bias voltage in a magnetic field with an induction of up to 8 T at temperatures of T = 1.5–4.2 K. The dependences of differential conductance dI/dV and the second derivative d^2I/dV^2 on the bias voltage were measured using the modulation technique.

An experimental current–voltage (I–V) characteristic of the sample is shown in Fig. 3a. As the voltage increases, a drastic increase in the current is observed. Such a shape of I–V characteristic in single-barrier GaAs/AlAs heterostructures is unambiguously related to tunneling via the X states in the AlAs barrier [10, 12]. For individual AlAs barriers 5 nm thick, the magnitudes of the effect observed in this study (the current density increases from 10 to 100 A/cm^2 when the tunneling via the X valley becomes effective) and those reported in previous publications [10, 12] are the same. In addition, an excess current (indicated by an arrow in Fig. 3a) is distinct below the threshold corresponding to the onset of tunneling via the X valley in the AlAs barrier. A similar special feature has been observed in the I–V characteristics of single-barrier GaAs/AlAs heterostructures with a δ-doped barrier and has been attributed to resonance tunneling via the zero-dimensional impurity states belonging to the X valley in the AlAs barrier [10].

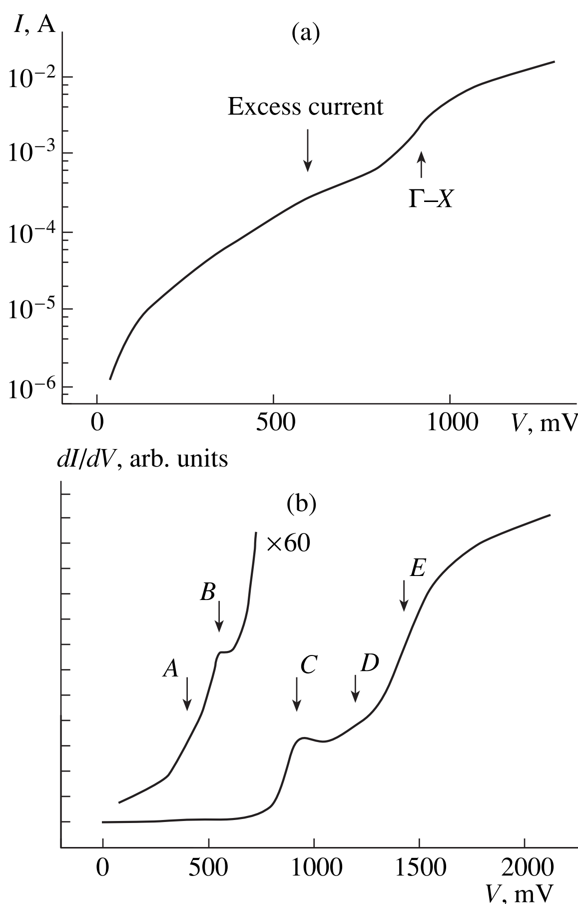

Fig. 3. (a) The I–V characteristic of GaAs/AlAs/GaAs heterostructure. (b) The dependence of differential conductance on the applied voltage.

Figure 3b shows the bias-voltage dependence of the differential conductance dI/dV. The special features corresponding to the transitions via the 2D X subbands are denoted by C, D, and E. As will be shown below, the resonance C corresponds to tunneling via the X_{z1} subband; we attribute the resonance D to tunneling via the subband X_{xy1} with the emission of a transverse acoustic (TA) phonon in AlAs, and the transition E is attributed to tunneling via the subband X_{z2}.

For the bias voltages below the threshold of tunneling via the ground state in the AlAs X valley, two low-intensity peaks (A and B) are observed in Fig. 3b. These special features are clearly distinguishable in Fig. 4, which shows the dependence of the second derivative of the current with respect to the voltage d^2I/dV^2 on the voltage V. We relate the peaks A and B to the resonance tunneling via the Si donor states belonging to the X_{xy} and X_z valleys, respectively, in the X-AlAs QW. It should be noted that, in our case, the barrier was not intentionally doped; however, the presence of impurities in the barrier was caused by the diffusion of Si from the heavily doped regions during heterostructure growth and also by residual (background) doping that amounted to 10^{15} cm^{-3} in the case under consideration. The existence of a large amount of impurities in the barrier in the structures used is verified both by the presence of the zero-voltage anomaly (a conductance peak) [13] and by the experimental voltage dependence of electron concentration in the accumulation layer (this dependence was obtained as a result of processing the tunneling-current Shubnikov–de Haas oscillations in a magnetic field perpendicular to the 2D electron layer). Extrapolation of concentration to the zero external bias indicates that a large density of built-in positive charge (~1×10^{11} cm^{-2}) is present in the barrier. However, the absolute value of concentration determined from the measured period of the tunneling-current oscillations yields only the upper bound of the built-in charge, because the true value of the Fermi energy in a 2D layer may be smaller than the measured value [14].

In Fig. 4, the arrows indicate the calculated values of voltages for which the Fermi level ε_F in the accumulation layer coincides with the impurity level ε_i in the AlAs-layer X well ($X_{xy\mathrm{Si}}$ or $X_{z\mathrm{Si}}$) or with the size-quantization level (X_{z1} and X_{xy1}); i.e., a new channel of tunneling becomes effective. The voltage corresponding to the condition $\varepsilon_F = \varepsilon_i$ is referred to as the threshold of

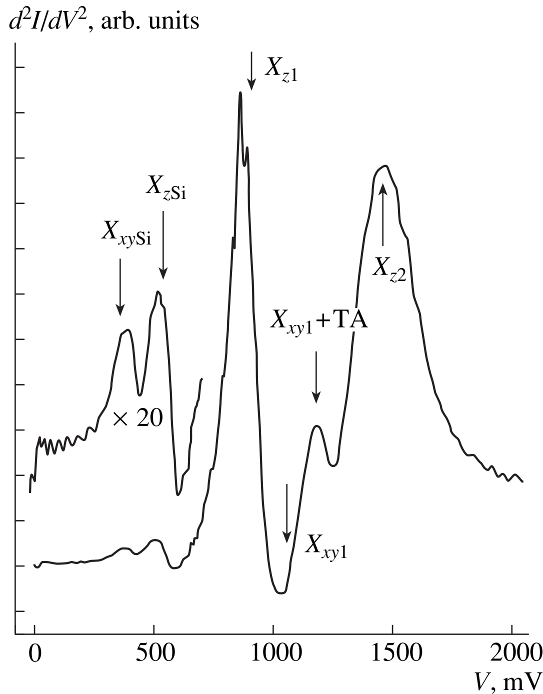

Fig. 4. Dependence of the second derivative d^2I/dV^2 on the applied voltage. The arrows indicate the calculated values of voltages for which the Fermi level in the accumulation layer coincides with the impurity level in the X well in the AlAs layer ($X_{xy\mathrm{Si}}$ or $X_{z\mathrm{Si}}$) or with the size-quantization level (X_{z1} or X_{xy1}) (i.e., when a new channel for tunneling becomes available).

tunneling via the ith level in the well [3]. The maximum of the second derivative d^2I/dV^2 corresponds to such a condition in the I–V characteristic [15]. As can be seen from Fig. 4, the positions of the peaks in the $d^2I/dV^2(V)$ curve coincide with the calculated values. When calculating the thresholds of tunneling via the size-quantization levels X_z and X_{xy}, the electron effective masses (the longitudinal m_l and the transverse m_t ones) in the AlAs X valley were assumed to be $m_l = 1.1m_0$ and $m_t = 0.19m_0$ and the energy difference between the GaAs Γ band and the AlAs X band was taken to be 120 meV in accordance with [3]. In addition, the influence of biaxial compression of AlAs as a result of the mismatch between the GaAs and AlAs lattice constants on the energy levels in the X well was taken into account. We note that the special features related to tunneling via the X_{xy1} level were not observed experimentally; however, the special feature corresponding to tunneling via this level with emission of a TA phonon with an energy of $\hbar\omega_{\mathrm{TA}} = 12$ meV was observed in AlAs. Such a relation between the magnitudes of experimental features corresponding to tunneling transitions $\Gamma \longrightarrow X_z$, $\Gamma \longrightarrow X_{xy}$, and $\Gamma \longrightarrow X_{xy} + \mathrm{TA}$ has been observed previously [3] and has been attributed to different probabilities of the processes $P_{\Gamma \to X_z} \gg P_{\Gamma \to X_{xy} + \mathrm{TA}} \gg P_{\Gamma \to X_{xy}}$. Such a relation between the probabilities is independently supported by the experiments concerned with studying the photoluminescence spectra for the GaAs/AlAs-based structures [1]. A low probability of elastic transition to the side X_{xy} valley is caused by the fact that, in this case, a large change in the transverse electron momentum (by a value of $q \approx 2\pi/a$, where a is the lattice constant) is required.

Voltages corresponding to tunneling via impurities belonging to the X_z and X_{xy} valleys were calculated using the results reported in [5], according to which the binding energy of the impurity located at the center of the 5-nm-thick AlAs barrier is 51 meV for the X_z valley and is 68 meV for the X_{xy} valley. The calculated values of the tunneling thresholds for such impurities are 551 mV for the X_z valley and 358 mV for the X_{xy} valley and agree closely with the positions of the peaks in the curve for the second derivative d^2I/dV^2. It should be noted that, in contrast to the structures with a δ-doped layer in the AlAs-barrier center [6–8, 10], the structures we used were randomly doped. Since the impurity energy depends on its position in the QW [5], the resonance should occur at somewhat different bias voltages for the impurities located at different distances from the heteroboundary. However, as has been shown previously [16], only tunneling via impurities located in the vicinity of the barrier center contributes significantly to the current. Thus, we may state that, in our heterostructures, the binding energy of a Si impurity is ~50 meV for the X_z valley and is ~70 meV for the X_{xy} valley.

Thus, in this study, we detected for the first time tunneling both via the states belonging to the 2D X_{xy} and X_z subbands in the AlAs layer and via the related impurity states, which made it possible to directly measure the binding energies of these donor states.

ACKNOWLEDGMENTS

We thank T.G. Andersson for placing the heterostructures at our disposal, and also Professor V.A. Tulin and Yu.V. Dubrovskiĭ for their helpful participation in discussions and for their interest in this study.

This study was supported in part by the Russian Foundation for Basic Research, project no. 00-02-17903.

REFERENCES

1. H. W. van Kesteren, E. C. Cosman, P. Dawson, *et al.*, Phys. Rev. B **39**, 13426 (1989).
2. E. R. Glaser, T. A. Kennedy, and B. Molnar, Phys. Rev. B **43**, 14540 (1991).
3. R. Teissier, J. J. Finley, M. S. Skolnick, *et al.*, Phys. Rev. B **54**, 8329 (1996).
4. J. J. Finley, R. J. Teissier, M. S. Skolnick, *et al.*, Phys. Rev. B **54**, 5251 (1996).
5. Gerald Weber, Appl. Phys. Lett. **67** (10), 1447 (1995).

6. M. W. Delow, P. H. Beton, C. J. M. Langerak, *et al.*, Phys. Rev. Lett. **68**, 1754 (1992).
7. J. W. Sakai, P. C. Main, P. H. Beton, *et al.*, Appl. Phys. Lett. **64**, 2563 (1994).
8. J. W. Sakai, T. M. Fromhold, P. H. Beton, *et al.*, Phys. Rev. B **48**, 5664 (1993).
9. Yu. Khanin, E. Vdovin, K. Novoselov, *et al.*, in *Proceedings of the 24th International Conference on Physics of Semiconductors, Jerusalem, 1998.*
10. H. Fukuyama and T. Waho, Jpn. J. Appl. Phys. **34**, L342 (1995).
11. I. E. Itskevich, L. Eaves, P. C. Main, *et al.*, in *Proceedings of the 23rd International Conference on Physics of Semiconductors, Berlin, 1996.*
12. Y. Carbonneau, J. Beerens, and H. C. Liu, Appl. Phys. Lett. **62** (16), 1955 (1993).
13. Yu. V. Dubrovskiĭ, Yu. N. Khanin, T. G. Andersson, *et al.*, Zh. Éksp. Teor. Fiz. **109**, 868 (1996) [JETP **82**, 467 (1996)].
14. T. G. Andersson, Yu. V. Dubrovskii, I. A. Larkin, *et al.*, Phys. Rev. B **50**, 4897 (1994).
15. M. Tsuchiya and H. Sakaki, Jpn. J. Appl. Phys. **30**, 1164 (1991).
16. I. P. Roche, G. P. Whittington, P. C. Main, *et al.*, J. Phys.: Condens. Matter **2**, 4439 (1990).

Translated by A. Spitsyn

Semiconductors, Vol. 35, No. 2, 2001, pp. 204–208. Translated from Fizika i Tekhnika Poluprovodnikov, Vol. 35, No. 2, 2001, pp. 211–215.
Original Russian Text Copyright © 2001 by Romanov, Romanova.

SEMICONDUCTOR STRUCTURES, INTERFACES, AND SURFACES

Spectra of the Field and Current Oscillations in Superlattices Exposed to Terahertz Laser Radiation

Yu. A. Romanov and Yu. Yu. Romanova*

Institute of Physics of Microstructures, Russian Academy of Sciences, Nizhni Novgorod, 603600 Russia

** e-mail: jul@ipm.sci-nnov.ru*

Submitted June 8, 2000; accepted for publication July 17, 2000

Abstract—Nonlinear oscillations of field and current excited by terahertz laser radiation in semiconductor superlattices were studied, taking into account the fact that the self-consistent internal field is multifrequncy. Oscillatory nonlinear susceptibilities, as well as dissipative and parametric instabilities in superlattices, lead to ambiguous and hysteresis dependences of the oscillation spectra on the external-field amplitude and frequency. The spectrum shape features are controlled by spontaneous generation of a static field and parametric amplification of external-field harmonics and subharmonics. The conventional approximation of single-frequency internal field was shown to be unsatisfactory, especially for superlattices with a high electron density. *© 2001 MAIK "Nauka/Interperiodica".*

When studying generation of current harmonics arising in semiconductor superlattices (SL) exposed to terahertz laser radiation, their internal field is, as a rule, considered to be predetermined and of a single-frequency [1–4]. This is allowed for SLs with a low electron density ($\omega_0 \ll \omega_1$, where ω_0 and ω_1 are plasma and laser field frequencies, respectively). A nonlinear current excited by an "initial" harmonic field in SLs with a high electron density induces strong fields at multiple frequencies, which in turn substantially change all the current harmonics. More important factors influencing the oscillation spectrum in SLs may be dissipative [5, 6] and parametric [7, 8] instabilities causing field harmonics with frequencies not only multiple to the external source frequency but also to those fractional and incommensurate to it [7–10]. In this case, a static (zero-harmonic) field often arises spontaneously in SLs [5, 6] (spontaneous generation of a corresponding static voltage was first observed in homogeneous gallium arsenide samples in [11]). These factors can substantially expand and complicate excited current and emission spectra. In particular, a static field spontaneously induced in SLs causes additional generation of even harmonics absent in the approximation of predetermined internal harmonic field. Hence, the SL electron plasma dynamics in the self-consistent multifrequency field calls for further investigation.

Taking the above factors into account, we construct the spectra of the field and current oscillations arising in SLs exposed to terahertz laser radiation injected via a microwave antenna. The electrodynamic system considered is similar to that proposed in [3]. Its equivalent electric circuit used in calculations includes an SL that has thickness Nd (where d is the period and N is the number of periods in a sample) and is shunted by resistance R; a voltage supply ($V(t) = V_0\cos(\omega_1 t)$) whose amplitude is controlled by the laser field; external capacitance C_1 including the antenna, substrate, and environment capacitances; and the load resistance r_i including the antenna radiation impedance and the contact and voltage supply resistances. All dimensions of the system are believed to be small compared to the emission wavelength.

A self-consistent set of equations for the electric current $j(t)$, longitudinal (relative to the SL axis) kinetic energy $n\langle\varepsilon_3\rangle$ of electrons, and electric field $E(t)$ inside the SL is written in dimensionless variables as

$$\omega_1\tau\frac{d\Phi(t)}{d\tilde{t}} + [1 + i\omega_1\tau g(t)]\Phi(t) = 1, \qquad (1)$$

$$\frac{dg(t)}{d\tilde{t}} = w[\mathrm{Im}\Phi(t) + \tilde{j}_e(t)] - \frac{g(t)}{\omega_1 RC_S}, \qquad (2)$$

where

$$\Phi(t) = \frac{\langle\varepsilon_3\rangle - \frac{\Delta}{2}}{\langle\varepsilon_3\rangle_0 - \frac{\Delta}{2}} - i\frac{j(t)}{j_0}, \qquad (3)$$

τ is the relaxation time of electron, $\langle\varepsilon_3\rangle_0$ is its average equilibrium longitudinal energy, Δ is the miniband width, $g(t) = edE(t)/\hbar\omega_1 = \Omega(t)/\omega_1$ is the dimensionless field in the SL, $\Omega(t) = eE(t)d/\hbar$ is the instantaneous "Bloch" frequency, $\tilde{t} = t\omega_1$, $C_S = \varepsilon_0 S/2\pi Nd$ is the SL linear capacitance, S and ε_0 are the SL cross section and the dielectric constant (neglecting electrons), $j_0 = \frac{\hbar\varepsilon_0\omega_0^2}{4\pi ed}$, $\omega_0^2 = \frac{4\pi ne^2d^2}{\varepsilon_0\hbar^2}\left(\frac{\Delta}{2} - \langle\varepsilon_3\rangle_0\right)$ is the squared plasma frequency, n is the concentration of electrons in

SL, $\tilde{j}_e = j_e/j_0$ is the dimensionless density of the external current dependent on the SL connection into the external circuit, and $w = (\omega_0/\omega_1)^2$. Equation (1) is a complex form of the balance equations derived in [1] for the electron current and energy with a harmonic dispersion, and (2) is the equation of the total current constancy.

The external current $j_e(t)$ in the above equivalent circuit is given by

$$Sj_e(t) = C_1 \frac{dV_1(r)}{dt}, \tag{4}$$

$$\left[1 + C_1 r_i \frac{d}{dt}\right] V_1(t) = V_0(t) - E(t)Nd, \tag{5}$$

where $V_1(t)$ is the voltage across the capacitor with capacitance C_1. We believe that the conditions $\omega_1 r_i C_1 \ll 1$ and $\omega_1 R C_S \gg 1$ implying a high Q-factor of the circuit are satisfied. In this case, Eq. (2) takes the form

$$\frac{dg(t)}{d\tilde{t}} = \tilde{w}\mathrm{Im}\Phi(t) - \tilde{V}_0 \sin\tilde{t}, \tag{6}$$

where $\tilde{V}_0 = \dfrac{eV_0}{N\hbar\omega_1(1 + C_S/C_1)}$ and $\tilde{w} = \dfrac{w}{1 + C_1/C_S}$. The power of sample emission at the frequency ω is determined from the approximate formula

$$P_\omega = \frac{V_\omega^2 R_r}{2[r_i^2 + (\omega C_1)^{-2}]}, \tag{7}$$

where V_ω is the amplitude of a harmonic of frequency ω of the nonlinear voltage induced in the SL and R_r is the antenna radiation resistance (r_i component). For the typical SL parameters (given in [3]): $d = 100$ Å, $N = 100$, $\Delta = 0.018$ eV, $r_i = 7\ \Omega$, $R_r = 5\ \Omega$, $C_S \sim C_1 = 10$ fF, $\omega_1 = 2\pi \times 0.7$ THz, and $V_\omega \approx 0.1$ V (corresponding to the numerical calculation considered below), we have $P_\omega \sim 5 \times 10^{-5}$ W.

It is readily shown that Eq. (6) also describes the SL behavior in the predetermined external electric field $E_e(t) = E_0\cos(\omega_1 t)$ with $\tilde{w} = w$, $\tilde{V}_0 = (\varepsilon_e/\varepsilon_0)(eE_0 d/\hbar\omega_1)$, where ε_e is the dielectric constant of external medium. Therefore, the results found below are also applicable to this case.

The general solution to Eq. (1) is written as

$$\Phi(t) = \psi(t)\Big[\Phi(0)\exp\left(-\frac{t}{\tau}\right) + \int_0^t \exp\left(-\frac{t - t_1}{\tau}\right)\psi^*(t_1)dt_1\Big], \tag{8}$$

where

$$\psi(t) = \exp\left(-i\int_0^t \Omega(t_1)dt_1\right), \tag{9}$$

and $t = 0$ is the time of turning the field on. Hence, according to (3), any field $E(t)$ excites in the SL the current

$$j(t) = j_0\left\{\exp\left(-\frac{t}{\tau}\right)\sin\left[\int_0^t \Omega(t_1)dt_1\right] + \int_0^t \exp\left(-\frac{t - t_1}{\tau}\right)\sin\left[\int_{t_1}^t \Omega(t_2)dt_2\right]\frac{dt_1}{\tau}\right\}. \tag{10}$$

If all the field harmonics except for the fundamental and zero (static field) ones inside the SL are negligible, i.e., $E(t) = E_c + E_1\cos(\omega_1 t)$, according to (10), there arises the electric current

$$j(t) = 2j_0\mathrm{Re}\, i\sum_{\mu=-\infty}^{\infty} J_\mu(g_1)\left[1 - \sum_{n=-\infty}^{\infty}\frac{J_n(g_1)}{1 + i(\Omega_c + n\omega_1)\tau}\right] \times \exp\{-[\tau^{-1} + i(\Omega_c + \mu\omega_1)]t\} + 2j_0\mathrm{Re}\, i \times \sum_{\mu, n=-\infty}^{\infty}\frac{J_n(g_1)J_{n+\mu}(g_1)}{1 + i(\Omega_c + n\omega_1)\tau}\exp(-\mu\omega_1 t), \tag{11}$$

where $\Omega_c = eE_c d/\hbar$ is the Stark frequency, $g_1 = eE_1 d/\hbar\omega_1$, and $J_n(g_1)$ is the nth order Bessel function. Formula (11) describes the transformation of the current spectrum in time after turning the field on. Initially, the spectrum coincides with that of Bloch oscillations of individual electrons (i.e., it contains only frequencies $\Omega_c + n\omega_1$, $n = 0, \pm 1, \ldots$). These harmonics decay in time τ, and a steady current spectrum containing only the field harmonics is established. A Block-oscillation aftereffect is a resonance property of the amplitude of current harmonics with frequencies of $\omega \approx \Omega_c/n$. Of experimental interest is the mode of alternate sharp turning on the static and harmonic fields, as well as fast interband generation of carriers in the presence of the static and harmonic fields.

If only a harmonic field exists in the SL, then (according to (11)) the steady-state current contains only odd harmonics with complex amplitudes

$$j_{\mu\omega_1} = 2ij_0\sum_{n=-\infty}^{\infty}\frac{J_n(g_1)J_{n+\mu}(g_1)}{1 + in\omega_1\tau} \xrightarrow[\omega\tau \to \infty]{} 2ij_0 J_0(g_1)J_\mu(g_1). \tag{12}$$

As it follows from (12) and the Bessel function properties, the current oscillation spectrum terminates at the harmonic $\mu \sim g$. The problem of cutoff frequency of current harmonic generation in the predetermined sin-

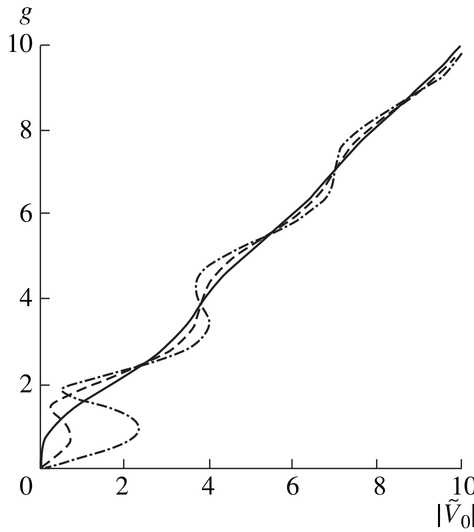

Fig. 1. Correlation between amplitudes of the first harmonic of field in the SL and the external field at $\omega_1\tau = 10$ and $\tilde{w} = 1$ (solid curve), 2.5 (dashed curve), and 5 (dash-and-dot curve).

gle-frequency internal field was studied in [4]. Radiation harmonic generation was studied in [3], with regard to the ambiguous correlation between amplitudes of the fundamental (and single!) harmonic in the nondissipative SL and the external-field amplitude. According to (6) and (12), such a correlation in the dissipative SL is given by

$$\tilde{V}_0 \exp(i\varphi) = g_1 - 2\tilde{w} \sum_{n=-\infty}^{\infty} \frac{J_n(g_1)J_{n+1}(g_1)}{1 + in\omega_1\tau}, \quad (13)$$

where φ is the phase shift of the field fundamental harmonic in the SL relative to the external field. For $\omega_1\tau \gg 1$, we use (13) to obtain

$$\tilde{V}\exp(i\varphi) \approx g_1 - 2\tilde{w}J_0(g_1)J_1(g_1) + i\frac{2\tilde{w}}{\omega\tau g_1}[1 - J_0^2(g_1)]. \quad (14)$$

Equation (14) differs from that used in [3] by the last dissipative term. Figure 1 displays dependences (13) for $\omega_1\tau = 10$ and various $\tilde{w}$. It is evident from (14) and Fig. 1 that the field fundamental harmonic in the SL can have multiple-values in relatively narrow ranges of $\tilde{V}_0$ for large values of $\omega_1\tau$ and $\tilde{w} > 1$. As $\tilde{w}$ increases, these ranges extend, and their number increases. The ambiguous correlation between amplitudes of the internal field fundamental harmonic and the external field is retained up to $\omega_1\tau \sim 1$ for $\tilde{w} \gg 1$. At $\omega_1\tau \gg 1$ and $\tilde{w} \gg 1$, this correlation begins from the value $\tilde{V}_0 \sim \tilde{w}/\omega_1\tau$, which can be great. The ambiguous fundamental-harmonic amplitude of the internal field, relationships (7) and (12), and the approximate equality

$$V_{\mu\omega_1} \approx \frac{N\hbar\omega_1}{e\mu j_0} j_{\mu\omega_1}, \quad \mu = 3, 5\ldots,$$

following from (6) all point to hysteresis and multivalued property of the dependences of the emission spectra intensities on the power of laser radiation incident on the lattice. The hysteresis generation pattern of the laser-field harmonics strongly depends on dissipation in the SL. Neglect of this factor leads to incorrect prediction of field and current harmonic generation, even in zero laser fields.

As an example, we consider nonlinear oscillations in the SL for $\omega_1\tau = 10$, $\tilde{w} = 2.5$, and $\tilde{V}_0 = 0.26$. According to Fig. 1, the numerical solution to the set of Eqs. (1) and (6) yields two stable steady oscillations with dimensionless amplitudes of the first harmonics of the field ($g_1^{(1)} = 0.18$ and $g_1^{(2)} = 1.5$) and current ($j_{\omega_1}^{(1)}/j_0 = 0.17$ and $j_{\omega_1}^{(2)}/j_0 = 0.58$). The second nonlinear oscillation contains the third appreciable (about 0.1) current harmonic, which is small in the first oscillation. In the above example, the current harmonic amplitudes calculated by formula (12) with $g_1^{(1)} = 0.18$ and $g_1^{(2)} = 1.5$ conform well to those found by the numerical solution of Eqs. (1) and (6).

As was indicated above, the approximation of single-frequency internal field is strictly valid only for SLs with low electron concentrations ($\tilde{w} < 1$) or in weak electric fields. However, hysteresis phenomena do not arise in these cases (see Fig. 1) when neglecting (as in [3]) spontaneous generation of the static field. If the multifrequency property of the self-consistent internal field is taken into account, new channels are revealed for the initiation of multiple-valued spectra of nonlinear oscillations. As this takes place, Eqs. (13) and (14) and the dependences in Fig. 1 lose their meaning; i.e., they yield unstable and not self-consistent solutions. It seems impossible to study nonlinear oscillations taking into account the multifrequency electric field by analytical methods. Therefore, we solve Eqs. (1) and (6) numerically for some values of the parameters $\omega_1\tau$, $\tilde{w}$, and $\tilde{V}_0$ (see Figs. 2, 3). For comparison, the current spectra also contain the results of approximate calculations (single-frequency field in the SL) by formulas (12) (asterisks) and (10) ($t \longrightarrow \infty$) taking into account the static field (closed circles). Corresponding field amplitudes (g_1 and g_c) are determined from the numerical-calculation results. For the comparison convenience, amplitudes of the first harmonics of current were normalized to the values found by solving Eqs. (1) and (6).

Figure 2 displays the voltage and current spectra of three steady states arising in the SL with $\omega_1\tau = 10$ and

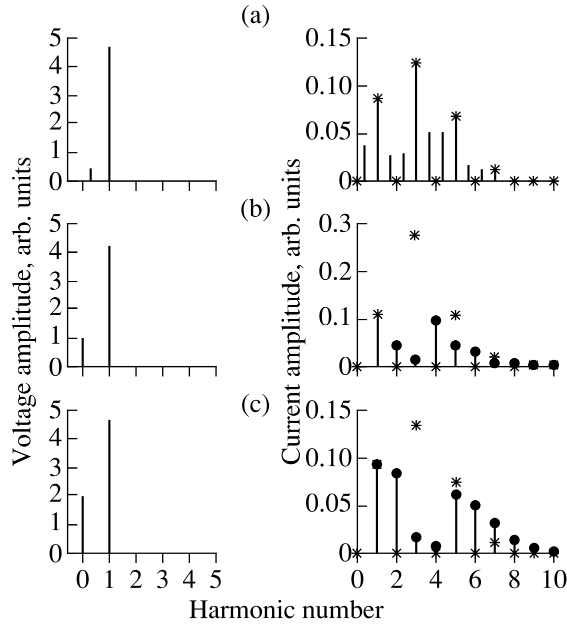

Fig. 2. The field and current spectra of three steady states in the SL with $\omega_1\tau = 10$ and $\tilde{w} = 2.5$ for $\tilde{V}_0 = 4.5$: nonlinear oscillations (a) with a tripled period and a zero static field and with the static field of g_c = (b) –0.99 and (c) –2.025; exact (solid lines) and approximate solutions by formula (11) with a zero field (asterisks) and with a nonzero static field (closed circles).

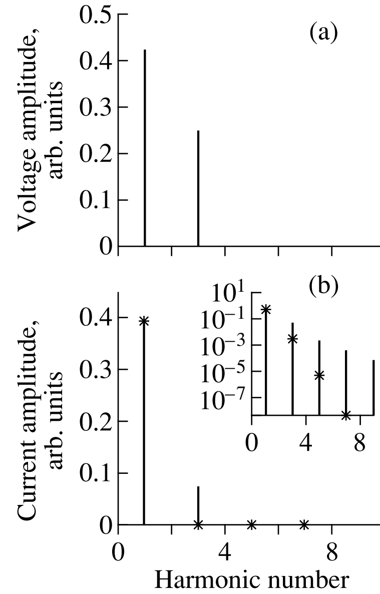

Fig. 3. Field (a) and current (b) spectra in the SL with a high electron concentration for $\omega_1\tau = 10$, $\tilde{w} = 10$, and $\tilde{V}_0 = 3.5$. The inset shows the current spectrum on the logarithmic scale.

$\tilde{w} = 2.5$ for the same $\tilde{V}_0 = 4.5$ but under different initial conditions. In the first state, the oscillation spectrum is enriched by harmonics with fractional frequencies $(2n + 1)\omega_1/3$, which virtually do not change amplitudes of odd current harmonics. Fractional harmonics arise due to parametrically coupled decays such as $(2n + 1)\omega_1 = 3\omega_2$ (n = 0, 1, 2, …, hard excitation mode), $2m\omega_1 = (m - 2/3)\omega_1 + (m + 2/3)\omega_1$ (m = 1, 3, …, soft mode) and corresponding merging of oscillations. The static field is absent in this state. (For other system parameters, nonlinear oscillation spectra can be complemented by other fractional harmonics, for example, by half-integer ones arising due to coupled parametric decays such as $2\omega_1 = 1/2\omega_1 + 3/2\omega_1$ and then by even harmonics arising due to merging processes such as $\omega_1 + 2(1/2\omega_1) = 2\omega_1$.)

The second and third states are characterized by static fields with $g_c = -0.99$ and –2.025, respectively, complementing the oscillation spectrum with even harmonics. Initiation of these three states is not related to the multiple-valued fundamental harmonic of the internal field, described by Eq. (13) (see Fig. 1). (This harmonic is almost identical in all the three oscillations.) This is caused by generation of the third subharmonic (parametric resonance) and spontaneous generation of the static field (dissipative instability). As is evident from Fig. 2, static fields significantly decrease the third harmonic amplitude in the spectrum of current oscillations, which should be taken into account in experimental studies.

Another example demonstrating the necessity of taking into account the multifrequency internal field is shown in Fig. 3. High SL electron concentrations ($n = 6 \times 10^{16}$ cm^{-3} for the typical SL parameters d = 100 Å and Δ = 0.018 eV and room temperature) cause parametric generation of the third field harmonic [9] with a significant amplitude and, hence, lead to substantially larger amplitudes of the higher field harmonics compared to the single-frequency approximation. The strong parametric coupling between harmonics in this oscillation also decreases the amplitude of the fundamental field harmonic in the SL. An analysis of phase relations between g_ω and $g_{3\omega}$ shows that their contributions to currents of the highest harmonics are not synchronous. Therefore, the spectra of SL nonlinear current can be both extended and narrowed due to the multifrequency internal field.

The results obtained show that dissipative and parametric instabilities play a significant role in formation of the oscillation spectra in SLs. The approximation of predetermined internal field cannot even yield qualitative results for relatively high electron concentrations. Generation of a static field and external source subharmonics represents the most important method for forming the multiple-valued spectra of nonlinear oscillations.

ACKNOWLEDGMENTS

The study was supported by the Interindustrial Scientific and Technical Program "Fundamental Technologies of Nanostructures," project no. 99-1129.

REFERENCES

1. A. A. Ignatov and Yu. A. Romanov, Phys. Status Solidi B **73**, 327 (1976).
2. M. C. Wanke, A. G. Markelz, K. Unterrainer, S. J. Allen, and R. Bhatt, in *Physics of Semiconductors*, Ed. by N. Scheffter and R. Zimmerman (World Scientific, Singapore, 1996), p. 1791.
3. A. W. Ghosh, M. C. Wanke, S. J. Allen, and J. W. Wilkins, Appl. Phys. Lett. **74**, 2164 (1999).
4. M. W. Feise and D. S. Citrin, Appl. Phys. Lett. **75**, 3536 (1999).
5. Yu. A. Romanov and L. K. Orlov, Fiz. Tverd. Tela (Leningrad) **19**, 726 (1977) [Sov. Phys. Solid State **19**, 421 (1977)]; Yu. A. Romanov, V. P. Bovin, and L. K. Orlov, Fiz. Tekh. Poluprovodn. (Leningrad) **12**, 1665 (1978) [Sov. Phys. Semicond. **12**, 987 (1978)]; Yu. A. Romanov, Fiz. Tverd. Tela (Leningrad) **21**, 877 (1979) [Sov. Phys. Solid State **21**, 513 (1979)].
6. Yu. A. Romanov, in *Multilayer Semiconductor Structures and Superlattices*, Ed. by A. M. Belyantsev and Yu. A. Romanov (Gor'kiĭ, 1984), p. 63.
7. Yu. A. Romanov, Izv. Vyssh. Uchebn. Zaved., Radiofiz. **23**, 617 (1980); L. K. Orlov and Yu. A. Romanov, Izv. Vyssh. Uchebn. Zaved., Radiofiz. **25**, 570 (1982); Izv. Vyssh. Uchebn. Zaved., Radiofiz. **25**, 702 (1982).
8. A. M. Belyantsev, L. K. Orlov, Yu. A. Romanov, and V. I. Shashkin, in *Multilayer Semiconductor Structures and Superlattices*, Ed. by A. M. Belyantsev and Yu. A. Romanov (Gor'kiĭ, 1984), p. 185.
9. Ju. Yu. Romanova and Yu. A. Romanov, in *Proceedings of the 7th International Symposium "Nanostructures": Physics and Technology, St. Petersburg, 1999*, p. 390.
10. K. N. Alekseev, E. H. Cannon, J. C. McKinney, *et al.*, Phys. Rev. Lett. **80**, 2669 (1998); K. N. Alekseev, G. P. Berman, D. K. Campbell, *et al.*, Phys. Rev. B **54**, 10625 (1996).
11. T. Ya. Banis, I. V. Parshelyunas, and Yu. K. Pozhela, Fiz. Tekh. Poluprovodn. (Leningrad) **5**, 1990 (1971) [Sov. Phys. Semicond. **5**, 1727 (1971)].

Translated by A. Kazantsev

Semiconductors, Vol. 35, No. 2, 2001, pp. 209–211. Translated from Fizika i Tekhnika Poluprovodnikov, Vol. 35, No. 2, 2001, pp. 216–218.
Original Russian Text Copyright © 2001 by Kurbanov, Bilalov, Nurmagomedov, Safaraliev.

SEMICONDUCTOR STRUCTURES, INTERFACES, AND SURFACES

Investigation of the $SiC/(SiC)_{1-x}(AlN)_x$ Heterostructures by the Method of Capacitance–Voltage Characteristics

M. K. Kurbanov, B. A. Bilalov, Sh. A. Nurmagomedov, and G. K. Safaraliev

Dagestan State University, Makhachkala, Dagestan, 327025 Russia

Submitted July 31, 2000; accepted for publication August 2, 2000

Abstract—Using the method of measuring and analyzing the capacitance–voltage characteristics, it is found that the n-6H-SiC/p-$(SiC)_{1-x}(AlN)_x$ heterostructures obtained by sublimation epitaxy of the $(SiC)_{1-x}(AlN)_x$ layers on the 6H-SiC substrates have abrupt heterojunctions ~10^{-4} cm thick. The basic properties of heterostructures, which depend on the epilayer composition and temperature, were determined from the capacitance–voltage characteristics. *© 2001 MAIK "Nauka/Interperiodica".*

INTRODUCTION

Among the systems with SiC-based solid solutions, the $(SiC)_{1-x}(AlN)_x$ solid solution has been investigated in most detail. This solid solution forms a continuous series of compounds with a gradual variation of the band gap and unit cell parameters. Corresponding values of these quantities are 3.35 eV, a = 3.076 Å, c = 5.048 Å for x = 0 and 6.2 eV, a = 3.114 Å, c = 4.986 Å for x = 1. An indirect gap structure transforms to a direct gap structure at $x > 0.6$ [1]. The problem of controlling the composition and conduction type has already been solved for a sublimation epitaxy of these solid solutions [2]. Due to their high thermal conductivity, as well as their mechanical, chemical and radiation resistance, these solid solutions are promising materials for device structures. The unit cell parameters and thermal expansion coefficients for SiC are close to those for $(SiC)_{1-x}(AlN)_x$, and the synthesis technologies are identical. This permits one to obtain the $SiC/(SiC)_{1-x}(AlN)_x$ heterostructures with a low concentration of defects at the heterointerface.

There is a lack of published data on the electrostatic parameters for the $(SiC)_{1-x}(AlN)_x$-based p–n structures. This paper is devoted to investigating the properties of the n-SiC/p-$(SiC)_{1-x}(AlN)_x$ heterostructures using the method of capacitance–voltage (C–V) characteristics.

SAMPLES AND EXPERIMENTAL TECHNIQUE

Single-crystal epilayers of the p-$(SiC)_{1-x}(AlN)_x$ solid solutions were grown on 6H-SiC substrates by sublimation epitaxy in the temperature range of 2300–2550 K at the pressure of the N_2 + Ar mixture from 2×10^4 to 8×10^4 Pa. The sources were hot-compacted SiC–AlN pellets [3]. The substrates were of n-type conduction with $N_d - N_a = 6 \times 10^{17}$–$3 \times 10^{18}$ cm^{-3}. The epilayers were 10–30 μm thick, and the substrates were 400 μm thick.

The C–V characteristics for the n-SiC/p-$(SiC)_{1-x}(AlN)_x$ heterostructures were measured using the setup based on an E7-8 automated digital meter. The measurement procedure was based on a bridge method with phase-sensitive detectors of balancing. The bridge was powered by a GZ-49a external wide-band oscillator. The amplitude of the sinusoidal signal was no larger than 300 mV. The measurements were carried out using a parallel equivalent circuit, and the error of the capacitance measurement was no larger than 1%. The C–V characteristics were measured on the mesas formed by ion-plasma etching with an Al mask fabricated by high-vacuum thermal evaporation from tungsten wire. After annealing, this mask was used as the nonrectifying contact to the $(SiC)_{1-x}(AlN)_x$ epilayer. The contacts to the base layer (6H-SiC substrate) were formed by the fusion of In subsequent to spark treatment of the surface. Checking the metal contacts confirmed that they were adequately nonrectifying. The mesas under study were installed in a two-probe cell.

To study the C–V characteristics, we selected the p–n structures with a capacitance independent of frequency up to 50 kHz. Corresponding C–V curves plotted in the C^{-2}–U coordinates were linear in the voltage range from –10 to 0 V. The leakage current of the structures was no larger than 10^{-5} A in the above voltage range.

RESULTS AND DISCUSSION

The C–V characteristics for two heterostructures with a different AlN content in the epilayer, which were measured at room temperature (293 K), are shown in Fig. 1. The deviation from a straight line observed for some experimental points is apparently related to a certain nonuniformity of dopant distribution in the $(SiC)_{1-x}(AlN)_x$ epilayer. For the n-6H-SiC/p-$(SiC)_{0.87}(AlN)_{0.13}$ and

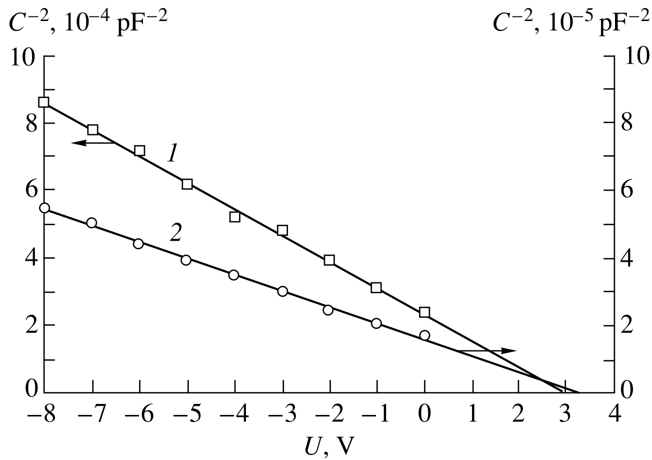

Fig. 1. Capacitance–voltage characteristics for two n-6H-SiC/p-$(SiC)_{1-x}(AlN)_x$ heterostructures at room temperature with the AlN content of x = (*1*) 0.13 and (*2*) 0.56.

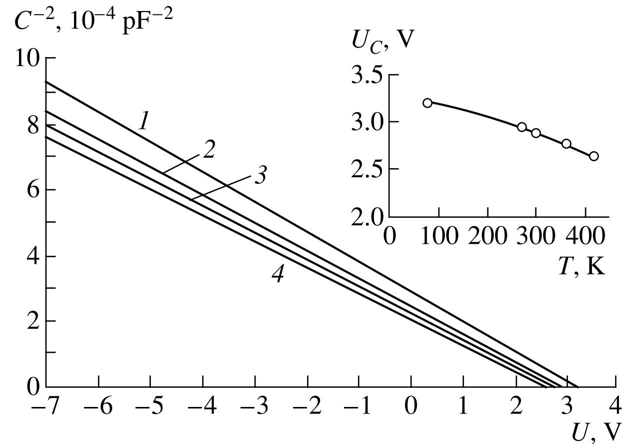

Fig. 2. Capacitance–voltage characteristics for the n-6H-SiC/p-$(SiC)_{0.85}(AlN)_{0.15}$ heterostructures at T = (*1*) 77, (*2*) 273, (*3*) 361, and (*4*) 418 K. The temperature dependence of the capacitance cutoff voltage U_C for this heterostructure is shown in the inset.

n-6H-SiC/p-$(SiC)_{0.44}(AlN)_{0.56}$ heterostructures, the straight lines extrapolated to $C^{-2} = 0$ intersect the voltage axis at 2.95 and 3.5 V, respectively. These voltages correspond to diffusion contact voltages U_d for the above-mentioned structures. For comparison, the value of U_d for the p–n homojunctions based on SiC, which was determined from the C–V and current–voltage characteristics, was about 2.7 V [4, 5]. It seems likely that an increase observed in U_d with increasing AlN content in the $(SiC)_{1-x}(AlN)_x$ epilayer is related to an increase in the epilayer band gap.

Using the values of U_d obtained from C–V characteristics and the expression

$$\Phi_2 = qU_d + \Phi_1,$$

we can determine the work function Φ_2 for the $(SiC)_{1-x}(AlN)_x$ layers with various AlN contents. The work function Φ_1 for the (0001) face of 6H-SiC is 4.5 eV at 300 K [6]. The Φ_2 value increases with increasing AlN content in the epilayer. Thus, for example, for p-$(SiC)_{0.87}(AlN)_{0.13}$ and p-$(SiC)_{0.44}(AlN)_{0.56}$, Φ_2 = 7.45 and 7.85 eV, respectively.

We determined the impurity concentrations in the $(SiC)_{1-x}(AlN)_x$ epilayer from the slope of the C–$V(U)$ characteristic in the C^{-2}–U coordinates, using the known formula [7]

$$\frac{\partial C^{-2}}{\partial U} = \frac{2(\varepsilon_1 N_{d_1} + \varepsilon_2 N_{a_2})}{S^2 q N_{d_1} N_{a_2} \varepsilon_1 \varepsilon_2}.$$

The concentration of N impurity in the 6H-SiC substrate for heterostructures shown in Fig. 1 was ~9 × 10^{17} cm^{-3}. This concentration was preliminarily determined from the value of $N_d - N_a$ obtained from the C–V characteristics for the Schottky barriers. The low-frequency relative permittivity ε_1 of 6H-SiC for $E \parallel c$ and T = 300 K is equal to 10.03 [6]. The relative permittivities ε_2 for the $(SiC)_{1-x}(AlN)_x$ solid solutions were determined from photoelectric measurements for the metal–semiconductor (the $(SiC)_{1-x}(AlN)_x$ solid solution) contact. For $0.1 < x < 0.6$, $\varepsilon_2 \simeq 9.4$–9.8. In our calculations, we used the average value $\varepsilon_2 = 9.6$. The area S for p–n junctions was 2×10^{-2} cm^2. The N_{a_2} concentration determined from the slope of the C–V curves was 9.02×10^{17} cm^{-3} and 7.98×10^{16} cm^{-3} for the $(SiC)_{0.87}(AlN)_{0.13}$ and $(SiC)_{0.44}(AlN)_{0.56}$ epilayers, respectively. Along with other results, this demonstrates that the impurity concentration N_a in the $(SiC)_{1-x}(AlN)_x$ layers decreases with increasing x. This conclusion was also confirmed by the fact that the capacitance dependence on voltage was weakened at high values of AlN content in the epilayer (Fig. 1). This indicates that the epilayer grown has high resistivity, and the depletion region is located mainly in its bulk.

The temperature dependences of the C–$V(U)$ characteristics for n-6H-SiC/p-$(SiC)_{0.85}(AlN)_{0.15}$, measured in the range of 77–418 K, are shown in Fig. 2. The capacitance cutoff voltage U_C, which was found by extrapolating the straight lines to the voltage axis, was 3.2 V at 77 K (curve *1*). With increasing temperature, the cutoff voltage initially decreases nonlinearly and then almost linearly to 2.65 V at 418 K (curve *4*). For the linear portion, $U_C(T) = U_{C0} - \alpha_C T$ (Fig. 2, inset), where U_{C0} is the voltage obtained by extrapolating $U_C(T)$ to T = 0 K, and α_C is the temperature coefficient of the capacitance cutoff voltage. For the structure under study, U = 3.46 V and $\alpha = 2.1 \times 10^{-3}$ V/K. Unfortunately, there is a lack of published data on the temperature dependence of the E_g band gap for the $(SiC)_{1-x}(AlN)_x$ solid solutions. For this reason, the

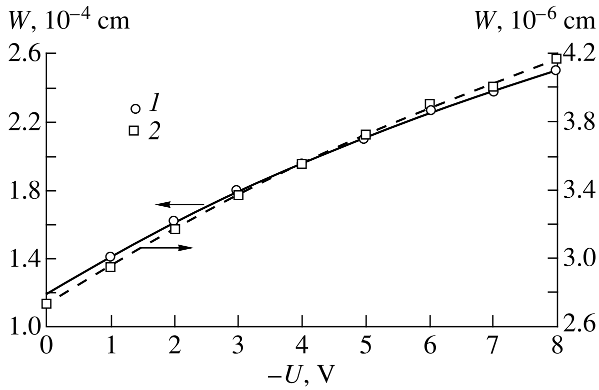

Fig. 3. Thickness W of the space charge region for the n-6H-SiC/p-$(SiC)_{0.87}(AlN)_{0.13}$ heterostructures as a function of the voltage applied to the structure: (*1*) experimental and (*2*) calculated.

nature of the U_C temperature dependence observed and, consequently, the U_d quantity cannot be determined unambiguously. However, knowing that the $U_d(T)$ dependence is more strongly pronounced than $E_g(T)$ for the 6H-SiC based structures [8], we may assume that the $U_C(T)$ dependence is caused mainly by the temperature dependence of the chemical potential in the n- and p-regions. The temperature dependence of the band gap for the components of the SiC–$(SiC)_{1-x}(AlN)_x$ heterocombination also introduces a certain contribution.

Investigation of the C–V characteristics for heterostructures enables the transition-region thickness W to be determined. The dependence $W = f(U)$ for the n-6H-SiC/p-$(SiC)_{0.87}(AlN)_{0.13}$ heterostructure is shown in Fig. 3. The p–n junction thickness determined from the capacitance value at zero bias was 1.2×10^{-4} cm. The thicknesses calculated were compared with those evaluated from the C–$V(U)$ characteristics (Fig. 3). The comparison demonstrated that the experimental values were larger than those calculated. This is apparently related to the effect of mobile charge carriers within the p–n junction and charged states at the interface on the experimental capacitance values.

To clarify the mechanism of electrical breakdown for heterostructures, which was observed at reverse biases larger than 25 V, we calculated the largest values of the electrical field $E_M(U)$ from the C–V characteristics according to the procedure reported elsewhere [9]. The value of $E_M(U)$ in n-6H-SiC/p-$(SiC)_{0.44}(AlN)_{0.56}$ heterostructure is about 5×10^4 V/cm at the prebreakdown voltage. Such an electric-field strength is inadequate to ionize the impurity via tunneling. For this reason, we assumed that the mechanism of the electrical breakdown for the structures under study is impact ionization.

CONCLUSION

Using the method of the capacitance–voltage characteristics, we found that abrupt heterojunctions were formed in the heterostructures fabricated by sublimation epitaxy of the p-$(SiC)_{1-x}(AlN)_x$ layers on the n-6H-SiC substrates. The space charge region was $0.5-2 \times 10^{-4}$ cm thick. The capacitance cutoff voltage U_C exceeded 2.9 V and increased with increasing AlN content in the epilayers. The temperature coefficient α_C of the U_C quantity is equal to $(1–3) \times 10^{-3}$ V/K.

The capacitance measurements demonstrated that the concentration of noncompensated impurities N_a in the epilayers of $(SiC)_{1-x}(AlN)_x$ solid solutions decreases with increasing AlN content. The largest values of the electric field E_M for the prebreakdown region were calculated for the n-SiC/p-$(SiC)_{1-x}(AlN)_x$ heterostructures from the capacitance–voltage characteristics. The values $E_M(U) \simeq 10^4$ V/cm obtained indicate that the mechanism of the electrical breakdown of heterostructures is an impact ionization in the space-charge region.

REFERENCES

1. A. P. Dmitriev, N. V. Evlakhov, and A. S. Furman, Fiz. Tekh. Poluprovodn. (St. Petersburg) **30** (1), 106 (1996) [Semiconductors **30**, 60 (1996)].
2. G. K. Safaraliev, M. K. Kurbanov, N. V. Ofitserova, and Yu. M. Tairov, Izv. Ross. Akad. Nauk, Neorg. Mater., No. 6 (1995).
3. Sh. A. Nurmagomedov, A. N. Pikhtin, V. N. Rezbegaev, *et al.*, Pis'ma Zh. Tekh. Fiz. **12** (17), 1043 (1986) [Sov. Tech. Phys. Lett. **12**, 431 (1986)].
4. A. A. Lebedev, D. V. Davydov, and K. I. Ignat'ev, Fiz. Tekh. Poluprovodn. (St. Petersburg) **30** (10), 1865 (1996) [Semiconductors **30**, 975 (1996)].
5. M. M. Anikin, A. A. Lebedev, I. V. Popov, *et al.*, Fiz. Tekh. Poluprovodn. (Leningrad) **22** (1), 133 (1988) [Sov. Phys. Semicond. **22**, 80 (1988)].
6. *Electrotechnical Materials: A Reference Book*, Ed. by Yu. V. Koritskiĭ, V. V. Pasynkov, and B. M. Tareev (Énergoatomizdat, Leningrad, 1988), Vol. 3.
7. A. G. Milnes and D. L. Feucht, *Heterojunctions and Metal–Semiconductor Junctions* (Academic, New York, 1972; Mir, Moscow, 1975).
8. A. N. Pikhtin and D. A. Yas'kov, Fiz. Tekh. Poluprovodn. (Leningrad) **12** (6), 1047 (1978) [Sov. Phys. Semicond. **12**, 622 (1978)].
9. L. S. Berman, *Capacitance Methods for Studying Semiconductors* (Leningrad, 1972).

Translated by N. Korovin

Semiconductors, Vol. 35, No. 2, 2001, pp. 212–219. Translated from Fizika i Tekhnika Poluprovodnikov, Vol. 35, No. 2, 2001, pp. 219–226.
Original Russian Text Copyright © 2001 by Dmitriev, Suris.

Electron Localization and Bloch Oscillations in Quantum-Dot Superlattices under a Constant Electric Field

I. A. Dmitriev* and R. A. Suris**

* *St. Petersburg State Technical University, ul. Politekhnicheskaya 29, St. Petersburg, 195251 Russia*

e-mail: dmitriev@theory.ioffe.rssi.ru

** *Ioffe Physicotechnical Institute, Russian Academy of Sciences, ul. Politekhnicheskaya 26, St. Petersburg, 194021 Russia*

Submitted June 30, 2000; accepted for publication June 30, 2000

Abstract—It is demonstrated that the electron spectrum in ideal two-dimensional and three-dimensional quantum-dot superlattices (SLs) under a constant electric field can be either discrete or continuous depending on the field orientation with respect to the SL crystallographic axes. In the latter case, the width of the resulting transverse miniband depends exponentially on the crystallographic index corresponding to the direction of the field. The electron localization area undergoes dramatic variations with the field orientation in the vicinity of the directions corresponding to the continuous energy spectrum. The Bloch oscillations in this kind of SL are considered. It is established that the scattering of oscillating electrons can be strongly suppressed by an appropriate choice of the field strength and direction. © *2001 MAIK "Nauka/Interperiodica".*

1. INTRODUCTION

Techniques for growing large ordered arrays of quantum dots (QDs) came into existence several years ago and continue to be actively developed [1]. It can be expected that, in the near future, progress in this technology will result in the fabrication of sufficiently perfect regular QD structures. However, to our knowledge, the properties of two-dimensional (2D) and three-dimensional (3D) QD superlattices (SLs) in a constant electric field remain virtually unexplored. Moreover, interesting effects related to the strong dependence of the electron spectrum and localization region on the field orientation should be observed in these structures.

In the absence of an electric field, the SL electron and hole spectra consist of a set of minibands, which appear due to an extra periodic potential that modulates the bottom of the conduction band and the top of the valence band in the SL material [2]. We assume that the electric field is so weak and the resonance overlap integrals between the QDs are so small that the single-miniband approximation can be used; i.e., we assume that there is only one quantum-confinement level in an isolated QD.

In the first part of this paper, a formal solution to the single-electron Schrödinger equation for an ideal QD SL of arbitrary symmetry and dimensionality under a constant electric field is derived. In this solution, all resonance overlap integrals between the QDs are accounted for.

In the second part, the solution obtained is analyzed. Given that the overlap integrals are small, it is possible that, due to the 3D nature of the QD SL potential, an electron in a perfectly periodic lattice becomes localized in the direction normal to the field orientation. This takes place if there are no crystallographic vectors of the QD SL normal to the field. In the opposite case, one-dimensional (1D) or 2D arrays of QDs under the same electric potential appear in the planes perpendicular to the field direction, and a transverse miniband is formed. The miniband width falls off exponentially with increasing distance between the QDs in such an array, i.e., with an increase in the crystallographic index corresponding to the field direction. Thus, despite the fact that the overlap integrals decrease exponentially with increasing distance between the respective QDs, in an ideal QD SL, any of them, under the appropriate electric-field orientation, can become responsible for a significant reshaping of the spectrum and carrier localization region. The physical adequacy of these results and the modifications to this pattern arising from the QD SL imperfections are discussed (in the context of the single-electron model).

The 3D nature of the QD SL potential has an immediate impact on the specific features of the Bloch oscillations, which are considered in the third part of this paper. In contrast to 1D SLs, oscillations are characterized by two or three fundamental frequencies (for 2D and 3D QD SLs, respectively) and their higher harmonics (which are present with exponentially small amplitudes). Fundamental frequencies can be independently tuned by changing the electric field strength and direction [3].

It is known that, in 1D SLs, the main factor that hinders the observation and practical application of Bloch

oscillations is their fast damping caused by impurity and phonon scattering (here, we restrict our consideration to intraminiband scattering processes). In the final part of this paper, it is demonstrated that, in contrast to 1D SLs, intraminiband scattering in QD SLs can be strongly suppressed by an appropriate choice of electric field strength and direction.

2. A FORMAL SOLUTION TO THE SCHRÖDINGER EQUATION FOR A QD SL IN A CONSTANT ELECTRIC FIELD

To determine the electron states in a QD SL under an electric field, we use, in a modified form, a technique developed in [4] for 1D SLs. Since the electrons in a QD SL under an applied electric field are localized, it is convenient to use a basis formed by the Wannier functions of the corresponding miniband, which in the tight-binding case are close to the isolated-QD wave functions. The Wannier functions are defined as follows [5]:

$$|\boldsymbol{\rho}\rangle = \frac{1}{\sqrt{N}}\sum_{\mathbf{k}} e^{i\mathbf{k}(\mathbf{r}-\boldsymbol{\rho})}u_{\mathbf{k}}(\mathbf{r}), \qquad (1)$$

where N is the total number of the QD SL sites, $\boldsymbol{\rho} = \sum_i n_i \mathbf{a}_i$ are the eigenvectors of the QD SL, $\mathbf{a}_i$ are the QD SL basis vectors $\mathbf{k}$, and $e^{i\mathbf{kr}}u_{\mathbf{k}}(\mathbf{r})$ are the Bloch eigenfunctions of the QD SL Hamiltonian $\hat{H}_0$ in the absence of an electric field; the summation is performed over the allowed $\mathbf{k}$ wave vectors in the QD SL first Brillouin zone. It should be noted here that, when a single miniband is considered, it is always possible to choose real-valued Wannier functions; then, the matrices of any physical quantities calculated in the basis of Wannier functions will be symmetric.

Matrix elements of $\hat{H}_0$ in the basis of Wannier functions are related to the electron spectrum by the following equation [5]:

$$\varepsilon(\mathbf{k}) = \frac{1}{N}\sum_{\boldsymbol{\rho}_1-\boldsymbol{\rho}_2} e^{i\mathbf{k}(\boldsymbol{\rho}_1-\boldsymbol{\rho}_2)}\langle\boldsymbol{\rho}_1|\hat{H}_0|\boldsymbol{\rho}_2\rangle. \qquad (2)$$

Let us express the $\hat{H}_0$ matrix as a sum of diagonal and nondiagonal parts:

$$\langle\boldsymbol{\rho}_1|\hat{H}_0|\boldsymbol{\rho}_2\rangle = \varepsilon_0\delta_{\boldsymbol{\rho}_1,\boldsymbol{\rho}_1} + I_{\boldsymbol{\rho}_1-\boldsymbol{\rho}_2}(1-\delta_{\boldsymbol{\rho}_1,\boldsymbol{\rho}_2}) \qquad (3)$$

(here, we have taken into account that, due to translational symmetry, the matrix element of $\hat{H}_0$ can only depend on the difference $\boldsymbol{\rho}_1 - \boldsymbol{\rho}_2$). Substituting (3) into (2), we can easily verify that ε_0 is the miniband energy averaged over $\mathbf{k}$ (in the following, we take this as the zero energy, $\varepsilon_0 = 0$), while $I(\mathbf{k}) = \sum e^{i\mathbf{k}\boldsymbol{\rho}}I_{\boldsymbol{\rho}}$ governs the electron dispersion law in the miniband. Using the orthogonality of the Wannier functions and their translational properties, the coordinate matrix can be expressed as

$$\langle\boldsymbol{\rho}_1|\mathbf{r}|\boldsymbol{\rho}_2\rangle = (\boldsymbol{\rho}_1+\mathbf{X}_0)\delta_{\boldsymbol{\rho}_1,\boldsymbol{\rho}_2} + \mathbf{X}_{\boldsymbol{\rho}_1-\boldsymbol{\rho}_2}(1-\delta_{\boldsymbol{\rho}_1,\boldsymbol{\rho}_2}). \qquad (4)$$

Vectors $\mathbf{X}_0$ and $\mathbf{X}_{\boldsymbol{\rho}_1-\boldsymbol{\rho}_2}$ do not vanish if the QD SL is invariant under the coordinate inversion ($\mathbf{r} \longrightarrow -\mathbf{r}$). The first of these vectors can be reduced to zero by a shift of the coordinate origin; the others, as will be shown below, determine the correction to the overlap integrals $I_{\boldsymbol{\rho}}$ that are proportional to the field strength. In the case of weak coupling between the QDs, $\mathbf{X}_{\boldsymbol{\rho}}$ and $I_{\boldsymbol{\rho}}$ are small quantities on the order of overlap between the Wannier functions corresponding to the QD SL lattice sites separated by vector $\boldsymbol{\rho}$ (i.e., they decrease exponentially with $|\boldsymbol{\rho}|$). We next consider the Schrödinger equation for an electron in a constant electric field

$$\hat{H}_F\Psi = (\hat{H}_0 + e\mathbf{Fr})\Psi = E\Psi. \qquad (5)$$

Substituting the wave function expanded in terms of Wannier functions, $\Psi = \sum C_{\boldsymbol{\rho}}|\boldsymbol{\rho}\rangle$, we obtain the following equation for the amplitudes $C_{\boldsymbol{\rho}}$:

$$(E - e\mathbf{F}\boldsymbol{\rho})C_{\boldsymbol{\rho}} - \sum_{\boldsymbol{\rho}_1}\Delta_{\boldsymbol{\rho}-\boldsymbol{\rho}_1}C_{\boldsymbol{\rho}_1} = 0. \qquad (6)$$

Here, $\Delta_{\boldsymbol{\rho}} = I_{\boldsymbol{\rho}} + e\mathbf{F}\mathbf{X}_{\boldsymbol{\rho}}$ are the field-modified overlap integrals. In the representation $C(\mathbf{k}) = \sum e^{i\mathbf{k}\boldsymbol{\rho}}C_{\boldsymbol{\rho}}$, we have

$$[E - \Delta(\mathbf{k})]C(\mathbf{k}) + ie\mathbf{F}\nabla_{\mathbf{k}}C(\mathbf{k}) = 0. \qquad (7)$$

Integrating this equation, we obtain

$$C(\mathbf{k}) = g(k_\perp)\exp\left(i\mathbf{k}\beta - \sum_{\boldsymbol{\rho}\not\perp\mathbf{F}}\frac{\Delta_{\boldsymbol{\rho}}}{e\mathbf{F}\boldsymbol{\rho}}e^{i\mathbf{k}\boldsymbol{\rho}}\right), \qquad (8)$$

where $\beta_\parallel = (1/eF)(E - \sum_{\boldsymbol{\rho}\perp\mathbf{F}}\Delta_{\boldsymbol{\rho}}e^{i\mathbf{k}\boldsymbol{\rho}})$, $g(\mathbf{k}_\perp)$ and $\beta_\perp(\mathbf{k}_\perp)$ are unknown functions, and the subscripts $\parallel$ and $\perp$ designate the components of the corresponding vectors in the directions parallel and perpendicular to the field, respectively ($k_\perp$ and $\beta_\perp$ are vectors for a 3D QD SL and scalars for a 2D configuration).

Since coefficients $C_{\boldsymbol{\rho}}$ are defined on a discrete set of QD SL sites, $C(\mathbf{k})$ should be periodic:

$$C(\mathbf{k}+\mathbf{K}) = C(\mathbf{k}). \qquad (9)$$

Here, $\mathbf{K} = \sum m_i\mathbf{b}_i$ and $\mathbf{b}_i$ are the basis vectors of the reciprocal QD SL lattice.

To satisfy this condition, $\boldsymbol{\beta}$ in (8) must be a direct-lattice vector $\mathbf{R} = \sum n_i \mathbf{a}_i$. Consequently, the electron spectrum is given by

$$\varepsilon_{\mathbf{R}}(k_\perp) = -e\mathbf{FR} + \sum_{\boldsymbol{\rho}\perp\mathbf{F}} \Delta_{\boldsymbol{\rho}} \cos\mathbf{k}\boldsymbol{\rho}. \quad (10)$$

The summation in (10) is performed over the SL vectors normal to the field. Such vectors exist for some orientations of the field, and do not exist for others. Thus, depending on the field direction, the spectrum can be either discrete or continuous; correspondingly, the electron can be either localized or delocalized in the direction perpendicular to the field.

2.1. Irrational Field Direction[1]

Let us refer to a particular field direction as irrational if $\mathbf{F}\mathbf{a}_i/\mathbf{F}\mathbf{a}_k$ is an irrational quantity for any $i \neq k$. For such field orientations, there are no SL vectors normal to the field (any equipotential plane can only pass through a single QD) the spectrum is discrete and forms a 2D or 3D Wannier–Stark ladder (for the case of 2D or 3D QDSL, respectively):

$$\varepsilon_{\mathbf{R}} = -e\mathbf{FR} = -\sum e n_i \mathbf{F}\mathbf{a}_i. \quad (11)$$

To determine the eigenfunctions, we just need to find the function $g(k_\perp)$. It follows from (9) that it should be periodic:

$$g(k_\perp + b_{i\perp}) = g(k_\perp). \quad (12)$$

However, for an irrational field direction, $b_{i\perp}/b_{k\perp}$ are irrational quantities for $i \neq k$, and, consequently, $g(k_\perp)$ is a periodic function with two or three incommensurable periods, which means that $g(k_\perp)$ can only be a constant.

Thus, the energy eigenvalues and corresponding eigenfunctions for the electron in a constant electric field oriented along an irrational direction are represented by the following expressions:

$$\hat{H}_F|\mathbf{R}\rangle = \hat{H}_F \sum_{\boldsymbol{\rho}} C_{\boldsymbol{\rho}}^{\mathbf{R}} |\boldsymbol{\rho}\rangle = \varepsilon_{\mathbf{R}}|\mathbf{R}\rangle,$$

$$\varepsilon_{\mathbf{R}} = -e\mathbf{FR},$$

$$C_{\boldsymbol{\rho}}^{\mathbf{R}} = \int \frac{d\mathbf{k}}{V_B} \exp\left(i\mathbf{k}(\boldsymbol{\rho} - \mathbf{R}) + \sum_{\boldsymbol{\rho}_1} \frac{\Delta_{\boldsymbol{\rho}_1}}{e\mathbf{F}\boldsymbol{\rho}_1} e^{i\mathbf{k}\boldsymbol{\rho}_1} \right), \quad (13)$$

where $|\boldsymbol{\rho}\rangle$ are the Wannier functions defined by (1).

To avoid confusion, it should be pointed out that, throughout the paper, Wannier functions are designated by small Greek letters $|\boldsymbol{\rho}\rangle$, and Stark eigenstates, by capital Latin letters $|\mathbf{R}\rangle$. We note also that vector $\mathbf{R}$ is simultaneously the quantum number and the average electron coordinate in the state $|\mathbf{R}\rangle$: $\langle\mathbf{R}|\mathbf{r}|\mathbf{R}\rangle = \mathbf{R}$.

2.2. Rational Field Direction

Next, we consider the case where the field is oriented along a rational direction, i.e., $\mathbf{F}\mathbf{a}_i/\mathbf{F}\mathbf{a}_k$ is a rational quantity for, at least, one pair of indices $i \neq k$. Then, in the planes perpendicular to the field direction, the 1D or 2D arrays of QDs appearing under the same potential are formed. In other words, this means that there are SL vectors normal to the field. Since, in this case, $k_\perp$ is a quantum number (see (10)), $g(k_\perp)$ is determined from the normalization condition. Taking this into account, we find for the case of rational field direction that

$$\varepsilon_{\mathbf{R}}(k_\perp) = \sum_{\boldsymbol{\rho}\perp\mathbf{F}} \Delta_{\boldsymbol{\rho}} \cos(\mathbf{k}_\perp\boldsymbol{\rho}) - e\mathbf{FR},$$
$$C_{\boldsymbol{\rho}}^{\mathbf{R}}(k_\perp) = l_{\text{norm}} \int dk_\parallel \exp\left(i\mathbf{k}(\boldsymbol{\rho} - \mathbf{R}) + \sum_{\boldsymbol{\rho}_1 \not\perp \mathbf{F}} \frac{\Delta_{\boldsymbol{\rho}_1}}{e\mathbf{F}\boldsymbol{\rho}_1} e^{i\mathbf{k}\boldsymbol{\rho}_1} \right), \quad (14)$$

where l_{norm} is the normalization factor.

3. ELECTRON SPECTRUM AND LOCALIZATION REGION IN AN ELECTRIC FIELD

Let us now analyze the results obtained. It was mentioned already that, in the case of tight binding, overlap integrals become exponentially small with increasing distance between the QDs. Seemingly, it is possible to take into account only a limited number and neglect others, which can be commonly done for 1D SLs. However, as follows from (13), the shape of the spectrum and localization regin of the electron can be dramatically affected by any of the overlap integrals (however small) for an appropriate rational direction of the field.

We illustrate this by the example of a 2D square QD SL. Let us designate the distance between the nearest QDs by a and the corresponding overlap integral, by Δ. If all other overlap integrals are neglected (the nearest neighbor approximation), the following two cases are possible [see (12), (13)].

3.1. The Nearest Neighbor Approximation

(a) If the field is oriented along a basis vector of the SL, a miniband of width 4Δ is formed in the direction perpendicular to the field; the electron is localized only in the field direction:

$$\varepsilon_N(k_\perp) = 2\Delta\cos(k_\perp a) + eNFa,$$
$$C_{n_\parallel, n_\perp}^N(k_\perp) = e^{i\mathbf{k}_\perp n_\perp a} J_{n_\parallel - N}(2\Delta/eFa). \quad (15)$$

In weak fields, where the argument of the Bessel function $\lambda = 2\Delta/eFa \gg 1$, the localization length in the field

[1] The correctness of the treatment that distinguishes between rational and irrational field directions is discussed in the next part of the paper. Here, we just mention that, in a spatially confined SL, the number of rational directions is finite, and that such a treatment is physically meaningful.

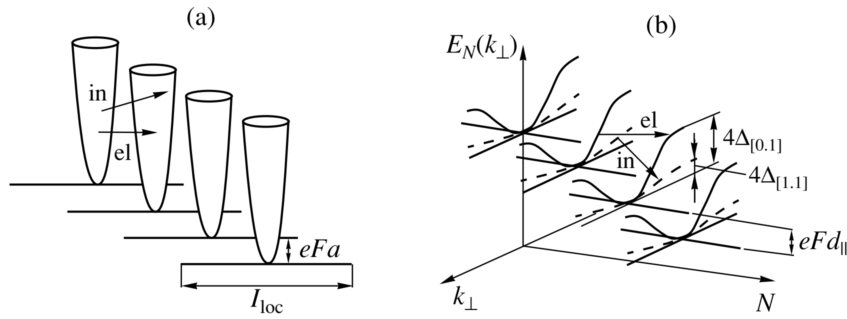

Fig. 1. (a) The spectrum of a quantum-well SL under an electric field; due to the wide transverse spectrum, elastic (el) and inelastic (in) transitions between the Stark-ladder states are allowed at any field strength. (b) The spectrum of a quantum-dot SL under an electric field oriented in a rational direction; with increasing field strength or direction index, elastic and then inelastic phonon processes become forbidden.

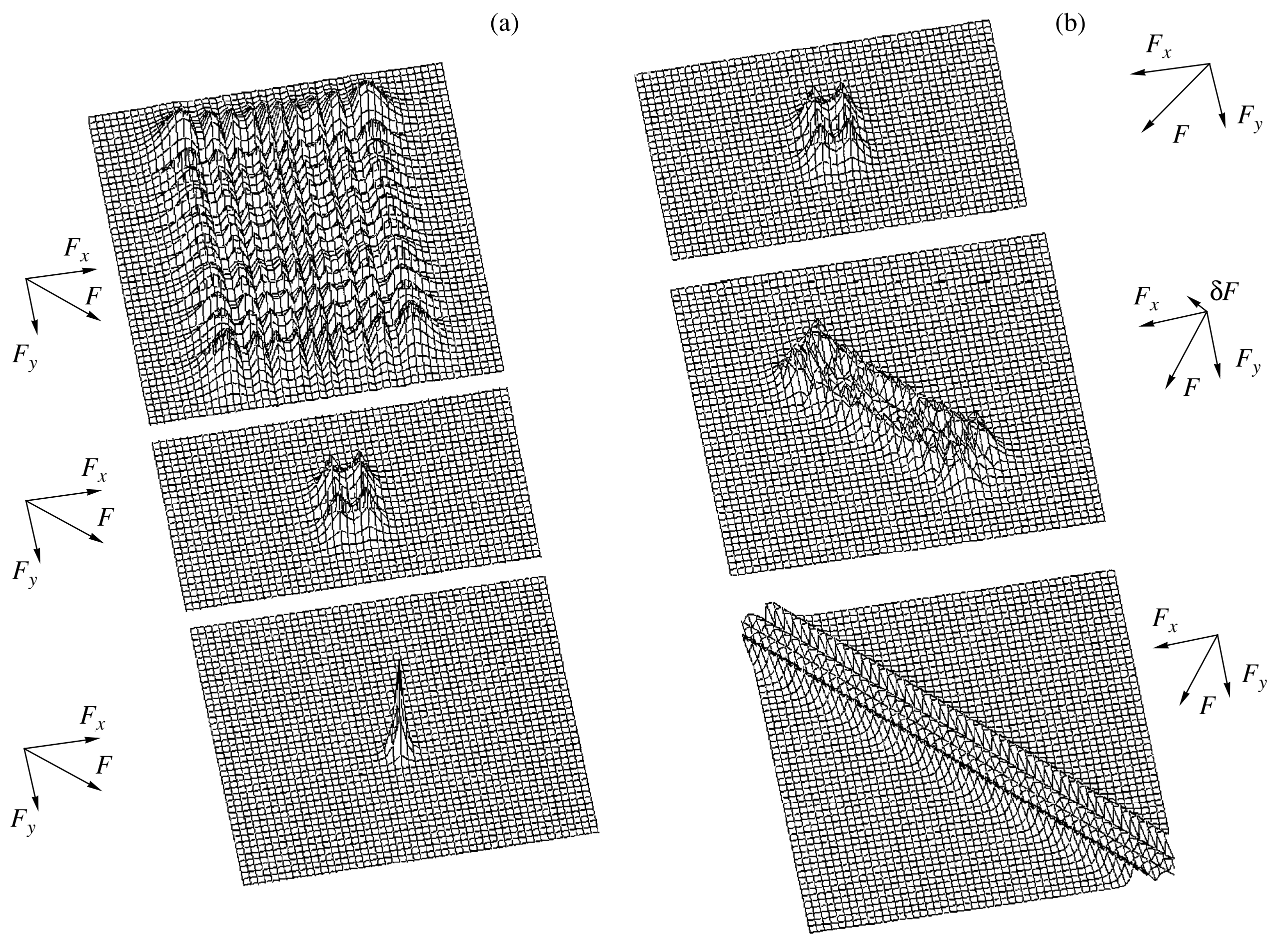

Fig. 2. (a) Dependence of the electron localization area on the field strength for irrational field orientation $F_x/F_y = 2/\pi$, from top to bottom: eFa/Δ = 1/6, 2/3, 5. (b) Dependence of the localization area on the field orientation with respect to the unit-cell diagonal, from top to bottom: far from resonance, $F_x/F_y = 2/\pi$; very close to resonance, $F_x/F_y = 0.99$; exactly at resonance.

direction can be estimated at $2\lambda a$. In the opposite limiting case of a strong field ($\lambda \ll 1$), the electron is mainly localized in a single QD chain with $n_\parallel = N$, while the amplitudes in the adjacent chains are equal to λ. The small width of transverse minibands distinguishes the QD SLs from SLs composed of quantum

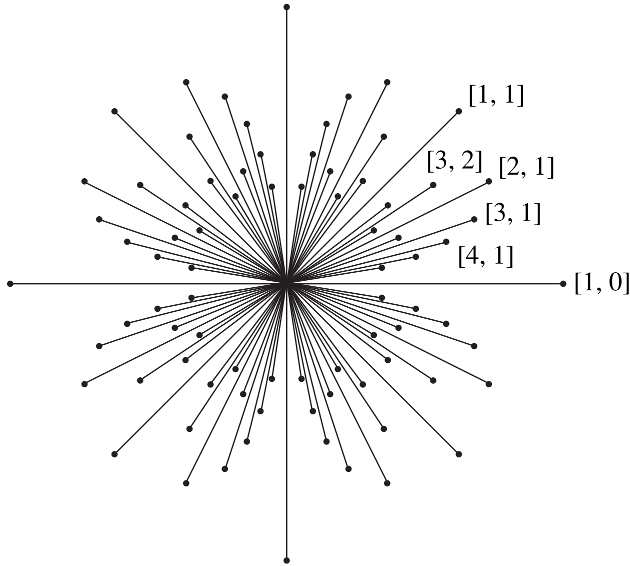

Fig. 3. Dependence of the transverse miniband width on the rational field direction index (logarithmic scale).

wells. In a 1D SL, the states belonging to different levels of a Stark ladder are degenerate at any electric field strength, while, in a QD SL the degeneracy is absent even in rather weak $F \geq 4\Delta/ea$ fields (see Fig. 1).

(b) When the field is oriented at an angle to the SL basis vectors, the spectrum is discrete in the nearest neighbor approximation, and the electron is localized in all directions:

$$\begin{aligned} \varepsilon_{N_x, N_y} &= ea(N_x F_x + N_y F_y), \\ C^{N_x, N_y}_{n_x, n_y} &= J_{n_x - N_x}(2\Delta/eF_x a) J_{n_y - N_y}(2\Delta/eF_y a) \end{aligned} \tag{16}$$

(coordinate axes are oriented along $\mathbf{a}_1$, $\mathbf{a}_2$). The localization region is defined by the quantities $\lambda_x = 2\Delta/eF_x a$, $\lambda_y = 2\Delta/eF_y a$ (Fig. 2a).

3.2. The Effect of Other Overlap Integrals

We now consider the case where an electric field is applied along the diagonal of the SL unit cell. Then, in the nearest neighbor approximation, all the levels in the Stark ladder become multiply degenerate (see (13)). If the finiteness of the overlap integral across the unit-cell diagonal Δ_D is taken into account, this degeneracy is removed, and a transverse miniband of width $4\Delta_D$ appears:

$$\begin{aligned} \varepsilon_N(k_\perp) &= 2\Delta_D \cos(k_\perp d) + eFNd, \\ C^N_{n_\perp, n_\parallel}(k_\perp) &= e^{i\mathbf{k}_\perp n_\perp d} J_{n_\parallel - N}\left(\frac{4\Delta}{eFd}\cos(k_\perp d/2)\right). \end{aligned} \tag{17}$$

Here, $d = \sqrt{2}a$ is the length of the QD SL unit-cell diagonal. For an infinitesimal misorientation of the field from the diagonal direction in an infinite ideal SL, the spectrum becomes discrete. In a narrow range $\delta\varphi = \Delta_D/\Delta$ of field orientations close to the diagonal direction, the localization length in the transverse direction is still determined by the diagonal overlap integral, and localization length in the field direction, by the nearest neighbor overlap integral. With increasing field misorientation, the nearest neighbor approximation becomes valid again (Fig. 2b).

Similar reshaping of the spectrum and localization region takes place in the vicinity of other rational directions. Together with the overlap integral in a QD chain forming in the transverse direction, the width of the appearing miniband depends exponentially on the index $[n, m]$ corresponding to the field direction (Fig. 3):

$$\Delta_{[n, m]} \propto \exp(-\alpha\sqrt{n^2 + m^2}). \tag{18}$$

For the field oriented normally to a high-index direction in a QD SL, the wave function has an interesting feature, which is illustrated in Fig. 4 for the case of field orientation along the [1, 5] direction. Due to the reduced symmetry, a QD chain is coupled to the neighboring chains by different overlap integrals. Chain 0 appears to be coupled to chain 5 more strongly than to chains 2, 3, and 4, despite larger interchain spacing in the latter case. This is manifested most clearly in strong fields, when the electron is almost completely localized in a single chain.

We may conclude that the correct treatment of a 2D QD SL requires that, in addition to the coupling between the nearest neighbors, at least one more overlap integral should be taken into account, namely, the one describing coupling between QDs that are close to a resonance for a given orientation of the field. In a 3D QD SL, there are two types of rational field orientations: the field can be perpendicular to the chains or planes of QDs. Correspondingly, the maximum number of overlap integrals that are significant at a given field orientation increases.

The pattern discussed seems to be physically unrealistic, since an infinitely small variation in the field orientation results in carrier localization or delocalization. However, a physically meaningful pattern results from the consideration of the evolution of the system: with infinitely weak coupling in a chain of resonant QDs, delocalization occurs in an infinite time. In addition, in a finite QD SL, the number of rational field directions is also finite.

Up to now, only ideal QD SLs were considered. However, a certain spread of parameters is inevitable in such a technologically complex structure with many heterointerfaces, which results in the spread in quantum-confinement energies and overlap integrals. In addition, actual structures always have finite size. The problem of an imperfect QD SL is very complicated and can hardly be solved analytically, even if the carrier interaction is neglected. However, it seems possible to outline a general pattern based on the known solution to

the problem of a chain of periodically arranged random scatterers [6]. It was shown [6] that, for a weak diagonal disorder in a chain described by the tight-binding approximation, an electron is localized at a length $l_{\rm loc} = d4\Delta^2/\langle\delta\varepsilon^2\rangle$, where d is the chain period and $\langle\delta\varepsilon^2\rangle$ is the MnS variance of the quantum-confinement energy level in a QD. Consider a finite QD SL whose linear dimension in the direction transverse to the field is L. Evidently, the transverse motion spectrum will be continuous only under the condition of $l_{\rm loc} \gg L \gg d$. For $l_{\rm loc} < d$, complete localization in the transverse direction occurs, and the corresponding overlap integrals may be neglected. In the intermediate case $d < l_{\rm loc} < L$, the localization length in the transverse direction is determined by the energy spread of the quantum-confinement levels. Obviously, in any case we consider the field to be strong enough, so that the spread in quantum-confinement energies is much smaller than the energy spacing between the Stark ladder levels and does not influence localization in the field direction. Thus, it can be stated that, in actual QD SLs, delocalization does not occur for any rational field directions except for several principal ones, and, in sufficiently strong fields, the nearest neighbor approximation can be used. If QDs are arranged in a plane (rather than a chain) normal to the field direction (which can take place in a 3D QD SL), strong localization does not occur in the case of sufficiently small variance. In this situation, the manifestation of weak localization effects is possible.

4. BLOCH OSCILLATIONS

The phenomenon of Bloch oscillations was first described by Bloch in 1928 [7]. It can be understood most simply in the context of the quasi-classical model. Let us consider an electron residing in a crystal and occupying the state with quasi-momentum $\mathbf{k}_0$. If a constant electric field is abruptly switched on, then, in the absence of scattering, the electron starts to accelerate at a constant rate in the quasi-momentum space, experiencing Bragg reflection each time it approaches a Brillouin zone boundary. In real space, this kind of motion corresponds to oscillations with period $eFd/\hbar$ (where d is the lattice constant in the direction of the field). However, in a bulk semiconductor, the electron undergoes scattering before it can reach the zone boundary; thus, Bloch oscillations were experimentally observed only in the beginning of the 1990s in very pure SLs with nearly perfect structures [8]. These studies led to a renewed interest in Bloch oscillations: a number of devices utilizing this phenomenon were proposed, numerous experimental techniques were developed, and different scattering mechanisms resulting in oscillation damping were investigated [9]. Issues related to the lifetime of Bloch oscillations are discussed in the next section. Here, we consider the case of negligibly small scattering.

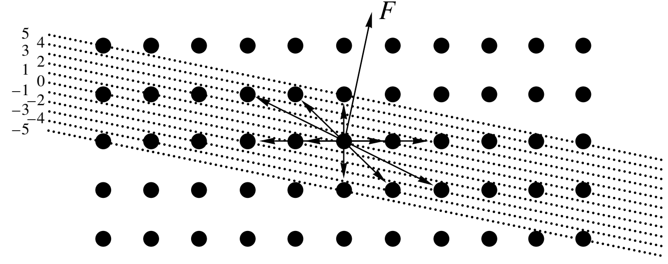

Fig. 4. The electron localization area for the field oriented along the [1, 5] crystallographic direction in the QD SL. Chains 0 and 5, 0 and 1 are coupled by the nearest neighbor overlap integral; coupling between chain 0 and chains 2, 3, and 4 is exponentially weaker.

The electron dynamics in the absence of scattering can be easily traced for different initial conditions using the solution to the time-independent Schrödinger equation, derived above. Similar to the case of 1D SLs, electron Bloch oscillations will take place; however, they exhibit more complex, multimode behavior.

Consider an electron in an initial state specified in the QD SL Wannier function representation by $\Psi(t=0) = \sum a^0_{\boldsymbol{\rho}}|\boldsymbol{\rho}\rangle$. Let us now use the representation of Stark eigenfunctions (11), whose time dependence is known:

$$|R(t)\rangle = e^{-i\Omega_{\mathbf{R}}t}|R(0)\rangle, \tag{19}$$

where $\Omega_{\mathbf{R}} = e\mathbf{FR}/\hbar$ are the QD SL Stark frequencies. Then, the solution to the time-dependent Schrödinger equation can be written as

$$\Psi(t) = \sum a_{\boldsymbol{\rho}}(t)|\boldsymbol{\rho}\rangle = \sum_{\boldsymbol{\rho}_1,\,\boldsymbol{\rho}} a^0_{\boldsymbol{\rho}_1} d^{\boldsymbol{\rho}_1}_{\boldsymbol{\rho}}(r)|\boldsymbol{\rho}\rangle,$$
$$d^{\boldsymbol{\rho}_1}_{\boldsymbol{\rho}}(t) = \sum_R C^R_{\boldsymbol{\rho}_1} e^{-i\Omega_{\mathbf{R}}t} C^R_{\boldsymbol{\rho}}. \tag{20}$$

Electron oscillations are accompanied by oscillations of the current between the QDs:

$$(\mathbf{j}_{\boldsymbol{\rho}})_i = \sum_{(\boldsymbol{\rho}_1)_i < 0} \frac{2e\Delta_{\boldsymbol{\rho}-\boldsymbol{\rho}_1}(\boldsymbol{\rho}-\boldsymbol{\rho}_1)_i}{\hbar} \mathrm{Im}\{a^*_{\boldsymbol{\rho}}(t) a_{\boldsymbol{\rho}_1}(t)\},$$
$$t = x, y, z. \tag{21}$$

The summation is carried out over the transitions from all QDs in the half-space $(\boldsymbol{\rho}_1)_i < 0$ to the QD $\boldsymbol{\rho}$ (in which the current is calculated). This formula represents a generalization to the expression for the current in a 1D SL: $j_n = 2e\Delta a\hbar^{-1}\Psi^*_n\Psi_{n-1}$, where Ψ_n is the wave function amplitude in the nth layer, Δ is the overlap integral between the adjacent SL layers, and a is the SL period.

Characteristics of Bloch oscillations depend significantly on the way in which the field is switched on. Here, we consider two possibilities: (i) the field can be instantly switched on from zero, while the electrons are initially distributed over the SL Bloch states; (ii) the field can be instantly reduced from such a large value that an electron is initially completely localized in a single QD

$$\Delta_{\boldsymbol{\rho}}/e\mathbf{F}\boldsymbol{\rho} \ll 1.$$

4.1. Instant Switching-on of the Field

A Bloch state is described in the Wannier representation by $a^0_{\boldsymbol{\rho}} = N^{-1/2}e^{i\mathbf{k}\boldsymbol{\rho}}$. In this case, the summation in the expression (21) for a single-electron current with the subsequent averaging over the initial quasi-momenta yields the following simple result:

$$\mathbf{j} = \sum_{\boldsymbol{\rho}} \frac{2en_e\Delta_{\boldsymbol{\rho}}\boldsymbol{\rho}}{\hbar}\langle \cos\mathbf{k}\boldsymbol{\rho}\rangle \sin(\Omega_{\boldsymbol{\rho}}t). \quad (22)$$

Amplitudes of different harmonics are independent of electric field strength. The same expression can be derived in the quasi-classical approximation in the absence of scattering. For the sake of clarity, we present the expression for the component of the current in the field direction for the specific case of square 2D QD SL:

$$\frac{\hbar F j_F(t)}{2n\Delta_{[1,0]}\langle\cos(k_xa)\rangle} = \Omega_x\sin(\Omega_xt) + \Omega_y\sin(\Omega_yt)$$

$$+ \frac{\Delta_{[1,1]}\langle\cos[(k_x+k_y)]a\rangle}{\Delta_{[1,0]}\langle\cos(k_xa)\rangle}\{(\Omega_x+\Omega_y) \quad (23)$$

$$\times\sin[(\Omega_x+\Omega_y)t] + (\Omega_x-\Omega_y)\sin[(\Omega_x-\Omega_y)t] + \dots .$$

It can be seen that there are two main oscillation components with frequencies $\Omega_x = eF_xa/\hbar$ and $\Omega_y = eF_ya/\hbar$; other components (whose amplitudes are decreased exponentially due to the reduction of the corresponding overlap integrals) are characterized by different combinations of the fundamental frequencies. Ω_x and Ω_y can be tuned independently by variation of the field strength and direction [4]. For a rational field direction, the electron density centroid moves along a closed orbit within the localization area, and the motion is periodic with period $T = 2\pi/\min\{\Omega_{\boldsymbol{\rho}}\}$. For an irrational direction, the motion is quasi-periodic, since rational directions can be found as close to a given one as is wished; the trajectory of the electron density centroid gradually fills the entire localization area.

4.2. Instant Reduction of the Field

We now consider the case where an electron is initially localized at the SL site $\boldsymbol{\rho} = 0$: $a^0_{\boldsymbol{\rho}} = \delta_{\boldsymbol{\rho},0}$. Then, the so-called "breathing mode" is excited. The current distribution is antisymmetric ($j_{\boldsymbol{\rho}} = -j_{-\boldsymbol{\rho}}$), the electron density centroid remains at $\boldsymbol{\rho} = 0$, and the dipole moment equals zero. For rational field directions, the motion is periodic: after "spreading" over the entire localization area, the electron "collects" again at $\boldsymbol{\rho} = 0$ after the time period $T = 2\pi/\min\{\Omega_{\boldsymbol{\rho}}\}$. For irrational field directions, the electron never returns to the initial state, but remains close to it for the reasons explained above.

5. BLOCH OSCILLATIONS LIFETIME

To make observations and practical applications of Bloch oscillations possible, it is necessary to ensure that their lifetime is much longer than their period. This cannot be attained in 1D SLs: due to the wide spectrum of the transverse motion, strong intraminiband scattering occurs for any electric field strength. Because of the energy overlap between the states belonging to different levels of the Stark ladder, both elastic scattering and inelastic scattering involving phonons is possible (see Fig. 1).

In QD SLs, it is possible to vary the width of the transverse miniband varying the field direction, thus eliminating elastic scattering and greatly suppressing phonon scattering.

Actually, if the transverse-miniband width is smaller than the optical phonon energy and the spacing between the levels of the Stark ladder, and the frequency of the optical phonons is not a multiple of the Stark frequency, then elastic scattering and optical-phonon scattering is completely suppressed (see Fig. 1).

Intraminiband acoustic-phonon scattering is possible only for the electrons whose velocity exceeds the speed of sound; consequently, this scattering is not allowed in sufficiently narrow transverse minibands.

Interminiband scattering in quantizing fields can take place only with the participation of acoustic phonons with wavelengths much smaller than the QD size. Evidently, the interaction of electrons with such short-wavelength phonons would be very weak.

Finally, when the field is so strong that the Stark frequency exceeds the optical-phonon frequency, all single-phonon scattering processes are forbidden.

Thus, in contrast to 1D SLs, main intraminiband scattering channels in QDSLs can be eliminated, with only multiphonon processes remaining.

ACKNOWLEDGMENTS

This study was supported by the Russian Foundation for Basic Research (project nos. 99-02-16796 and 00-15-96812) and the State Interdisciplinary Program

"Physics of the Solid-State Nanostructures" (project no. 97-1035).

REFERENCES

1. R. Notzel, Semicond. Sci. Technol. **11**, 1359 (1996).
2. L. V. Keldysh, Fiz. Tverd. Tela (Leningrad) **4**, 2265 (1962) [Sov. Phys. Solid State **4**, 1658 (1962)].
3. R. F. Kazarinov and R. A. Suris, Fiz. Tekh. Poluprovodn. (Leningrad) **6**, 148 (1972) [Sov. Phys. Semicond. **6**, 120 (1972)].
4. R. A. Suris, NATO Adv. Study Inst. Ser., Ser. E **323**, 197 (1996).
5. G. H. Wannier, Phys. Rev. **52**, 191 (1937).
6. A. P. Dmitriev, Zh. Éksp. Teor. Fiz. **95**, 234 (1989) [Sov. Phys. JETP **68**, 132 (1989)].
7. F. Bloch, Z. Phys. **52**, 555 (1928).
8. K. Leo, Semicond. Sci. Technol. **13**, 249 (1998).
9. F. Rossi, Semicond. Sci. Technol. **13**, 147 (1998).

Translated by M. Skorikov

Semiconductors, Vol. 35, No. 2, 2001, pp. 220–225. Translated from Fizika i Tekhnika Poluprovodnikov, Vol. 35, No. 2, 2001, pp. 227–232.
Original Russian Text Copyright © 2001 by Ivanov-Omskiĭ, Tolmatchev, Yastrebov.

AMORPHOUS, VITREOUS, AND POROUS SEMICONDUCTORS

Optical Properties of Amorphous Carbon Films Deposited by Magnetron Sputtering of Graphite

V. I. Ivanov-Omskiĭ, A. V. Tolmatchev, and S. G. Yastrebov

Ioffe Physicotechnical Institute, Russian Academy of Sciences, Politekhnicheskaya ul. 26, St. Petersburg, 194021 Russia

Submitted May 31, 2000; accepted for publication June 1, 2000

Abstract—The thermal stability of amorphous carbon (*a*-C and *a*-C:H) has been studied by ellipsometry and spectrophotometry in the visible and near-UV range (1.5–5.6 eV). The dielectric function of amorphous carbon has been derived and analyzed using the Kramers–Kronig technique. The conventional analytical approach is shown to be insufficient for the analysis of thermally treated samples. The fundamental absorption edge is analyzed with respect to collective effects in nanoscale fragments of the graphite-like component of the amorphous carbon structure. Two types of graphite-like clusters contributing to the spectral dependence of the fundamental absorption edge and modified by thermal treatment are revealed. © *2001 MAIK "Nauka/Interperiodica".*

1. INTRODUCTION

Thin-film amorphous carbon coatings offer broad prospects for technical applications due to their high hardness and chemical and frictional stability [1–3]. According to the synthesis conditions, amorphous carbon is classified by its hydrogen content. The material fabricated with the use of hydrogen is usually designated as *a*-C:H, and that obtained without hydrogen, as *a*-C. Owing to its remarkable properties, amorphous carbon finds numerous technical applications, including some in electronics. The structure of carbon is determined by its unique ability to form different allotropic forms or modifications. As is known, the structure and properties of amorphous carbon films are determined by the fabrication technique [1–3]. Optical spectroscopy of amorphous carbon films allows one to relate the microstructure of the material to specific features of its optical spectra and to study the influence of fabrication conditions and thermal treatment on the microstructure [4–8].

The optical properties of amorphous carbon films fabricated by magnetron sputtering of graphite were discussed earlier [8, 9]; however, many concepts of their structure have been considerably modified since. Lately, a quantum-dimensional approach to the description of the relative contributions of different structural elements to the electronic structure and, consequently, to the optical properties of amorphous carbon has been developed [4, 7, 9, 10]. According to these concepts, the material is based on nanometer-size structural elements containing carbon in sp^2- and sp^3-hybrid states—graphite- and diamond-like fragments (clusters). These fragments were first directly observed in [10] by means of transmission electron microscopy. The shape and position of the optical absorption edge are determined by graphite-like nanoclusters. We note that, while the semimetallic electron spectrum of well-oriented graphite is determined by the practically infinite size of graphene planes, in the case of limited-size graphite-like nanoclusters in *a*-C:H and *a*-C, the material is a typical amorphous semiconductor.

Therefore, it should be mentioned that due to ambiguity the models, describing the optical absorption edge in amorphous substances and underlying optical diagnostics of the material, require substantial supplementation. For the majority of amorphous materials, the optical diagnostics commonly relate the frequency dependence of the absorption coefficient to the Tauc relation [11, 12], with the energy parameter named the Tauc edge or optical gap E_g evaluated. Several other extrapolation formulas are also employed to analyze optical spectra [5, 12]. As a result of extensive work in this direction, a vast body of experimental data has been accumulated concerning the correlation between the microscopic structure of amorphous carbon and the E_g values [3, 6, 8, 10, 13]. Nevertheless, it is important to remark that all the cited works assumed that the absorption edge is formed only by interband transitions—HOMO–LUMO type transitions—in nanoscale structural elements of amorphous carbon with sp^2-bonds. As shown below, this approach is insufficient for the case of amorphous carbon, especially that treated thermally. It will be shown that a substantial contribution to the light absorption by amorphous carbon is made by collective electronic effects occurring in nanoscale structure fragments containing sp^2-hybridized carbon atoms.

The ratio of two allotropic carbon modifications (sp^2- and sp^3-hybridized carbon) in *a*-C and *a*-C:H is determined by fabrication conditions and, in particular, by the hydrogen content in the film. The behavior of hydrogen in the annealing of *a*-C:H films was studied

1063-7826/01/3502-0220$21.00 © 2001 MAIK "Nauka/Interperiodica"

in [14,15] by IR spectroscopy and UV resonance Raman scattering. It was shown that annealing causes modification of the hydrogen covalently bound to tetrahedral carbon, namely, a reversible transition from a bound to quasi-free state. The activation energy of this process was estimated to be 0.5 ± 0.3 eV. It is natural to assume that a transition between the two states of hydrogen may be accompanied by the reconstruction of the electronic structure in the abandoned graphite-like cluster, causing the generation or loss of one or several π-electrons in it. Thus, it is natural to assume that the loss of hydrogen can modify the fundamental absorption edge of the amorphous carbon. This assumption is supported by the data of [16, 17], where a study of the dependence of optical spectra on the annealing temperature demonstrated a decrease in E_g, starting from some critical temperature. The critical temperatures are different for films obtained under different fabrication conditions, lying in the interval T_a = 300–450°C. In the present work, the dependence of the number of π-electrons on the annealing temperature is obtained from an analysis of optical data, and an activation-type temperature dependence of this parameter is demonstrated. Two types of dependences are compared for samples obtained by ion-plasma sputtering of graphite in argon plasma (*a*-C) and in argon-hydrogen plasma (*a*-C:H). The comparison of the experimental results with published data reveals the role of hydrogen and the mechanism of its influence on the formation of the optical absorption edge.

2. EXPERIMENTAL

Amorphous carbon layers were deposited onto fused silica substrates by dc magnetron sputtering of a graphite target. As a working gas we used an argon–hydrogen (1 : 4) mixture for obtaining *a*-C:H films, and pure argon for *a*-C films. The substrate temperature during growth was 200°C, the gas pressure in the chamber was 8–9 mTorr, and the magnetron power was maintained at 0.36 kW. The growth time for *a*-C and *a*-C:H films was chosen to be 40 and 30 min, respectively, which provided layers 770 and 740 Å thick.

Light transmission for films deposited onto fused silica was studied in the wavelength range λ = 200–850 nm on a "Hitachi U-3410" double-beam spectrophotometer. The light spot on the sample was 0.5 × 0.5 cm^2. Ellipsometry was performed in the reflection geometry on a LEF-3M ellipsometer with photon energy $\hbar\omega$ = 1.96 eV. The grown films were subjected to a series of sequential isochronous (1 h) annealings (under a residual pressure of 1mTorr) at T_a = 260–475°C. The spectral and ellipsometric studies were performed in air, immediately after each annealing. According to the ellipsometric data, the parameters of the annealed films did not change after a month of storage in air.

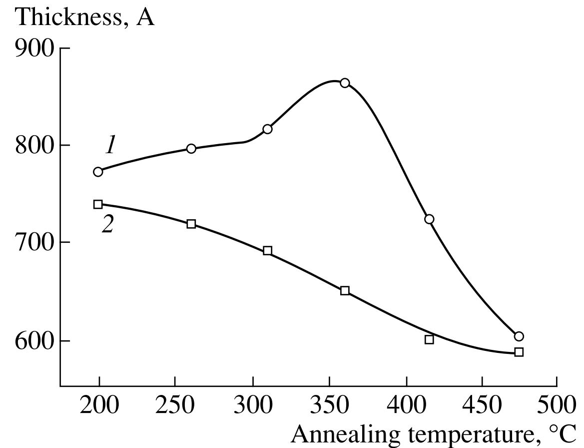

Fig. 1. Thickness of *a*-C (*1*) and *a*-C:H (*2*) samples vs. the annealing temperature.

3. RESULTS AND DISCUSSION

Figure 1 shows the film thickness obtained from ellipsometric data versus the annealing temperature [18]. The dependence of *a*-C film thickness has a peak at around T_a = 360°C, while the *a*-C:H film thickness decreases steadily with increasing annealing temperature. We suppose that two processes are responsible for this temperature dependence: thermal relaxation of internal stresses in the film and thermally activated transition from the sp^3- to the sp^2-phase. As known [1], the presence of hydrogen relieves internal stresses, and, therefore, the first process must evidently exert a considerably weaker effect in *a*-C:H compared with that in *a*-C films. As to the second process, it is evidently independent of the hydrogen content in the film. The fact that the curves in Fig. 1 converge at high temperature indicates that the effect of hydrogen on both processes is insignificant in this temperature range, since the bound state of hydrogen in *a*-C:H practically disappears [15] and the internal strains in *a*-C:H film totally relax. We note also that the refractive index and the extinction coefficient grow steadily with increasing annealing temperature for both *a*-C and *a*-C:H films.

To analyze the influence of annealing on the amorphous carbon film structure in more detail, let us consider the dispersion of the film dielectric constant. The dispersion curves for the dielectric functions were derived from the film transmission spectra using ellipsometric data, as described in [7]. In this approach, the transmission coefficient averaged over the interference extrema, $\langle T\rangle$, can be written as:

$$\langle T\rangle = n_3\frac{|t_{12}|^2|t_{23}|^2x}{1-|r_{12}|^2|t_{23}|^2x^2}, \tag{1}$$

where $x = \exp(-4\pi kd/\lambda)$, t_{12}, r_{12} are the Fresnel coefficients for transmission and reflection at the air–film interface; t_{23}, r_{23} are the Fresnel coefficients at the film–

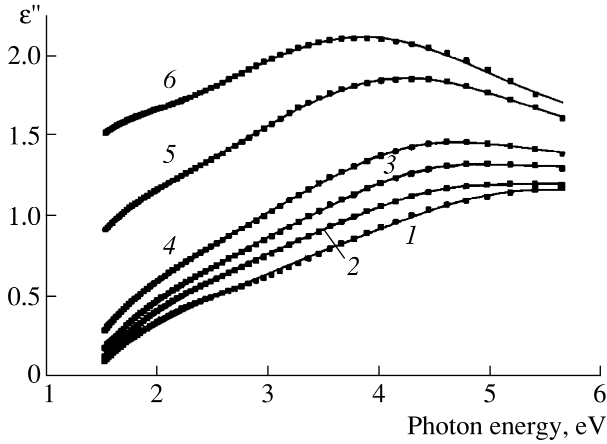

Fig. 2. Spectral dependences of the imaginary part of dielectric function ε'' for *a*-C:H film. (*1*) Unannealed film; annealing temperatures T_a: (*2*) 260, (*3*) 310, (*4*) 360, (*5*) 415, and (*6*) 475°C. Points, experimental data; curves, fitting with relation (3).

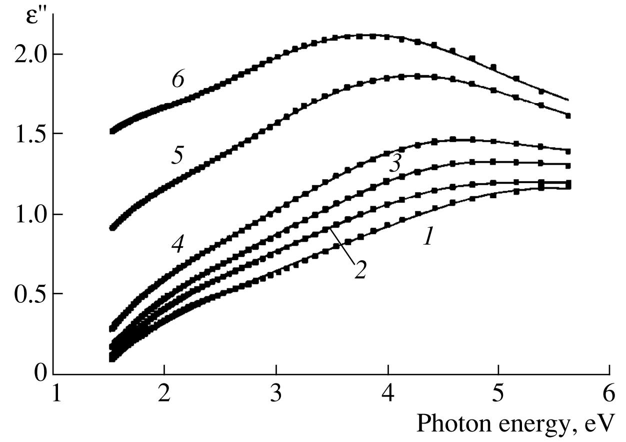

Fig. 3. Spectral dependences of the imaginary part of dielectric function ε'' for *a*-C film. (*1*) Unannealed film; annealing temperatures T_a: (*2*) 260, (*3*) 310, (*4*) 360, (*5*) 415, and (*6*) 475°C. Points, experimental data; curves, fitting with relation (3).

substrate interface; λ is the wavelength; k is the extinction coefficient of the film; d is the film thickness; and n_3 is the refractive index of the substrate. The wavelength dependence of the extinction coefficient was obtained from expression (1) using the ellipsometric data for film thicknesses and the refractive indices and extinction coefficients at the helium-neon laser wavelength. We note that interference can be neglected in processing the spectral data, because the film thickness is small [18]. The wavelength dependence of the refractive index was obtained using the Kramers–Kronig relation [19]. Figures 2 and 3 present spectral dependences of the imaginary part of the dielectric constant, ε''($\hbar\omega$), obtained from spectral dependences of the refractive index and extinction coefficient. As seen from Fig. 2 for *a*-C:H film, at low annealing temperatures the imaginary part of the dielectric constant depends monotonically on the energy $\hbar\omega$. As the annealing temperature becomes higher, a feature appears in the spectrum that becomes more prominent and shifts to lower energies with further increase in the annealing temperature. The dependence for *a*-C is similar (Fig. 3).

Now we analyze the frequency dependence of the imaginary part of the dielectric constant. It is known that the main parameter characterizing the optical properties of amorphous materials is the optical absorption edge E_g [11, 12] described by the Tauc relation [11]:

$$(\hbar\omega\alpha)^{1/2} = G(\hbar\omega - E_g), \tag{2}$$

where $\hbar\omega$ is the photon energy, E_g is the optical gap, α is the absorption coefficient, and G is a constant. This relation is usually applied to amorphous materials, because the experimental dependence is generally monotonic in a wide spectral range [12]. In our case, with a feature appearing in the spectral dependence of the imaginary part of the dielectric constant, this approach is insufficient, and various absorption mechanisms affecting the formation of the optical spectrum are to be taken into account. In this situation some researchers apply the Tauc relation in a narrower spectral range. In the present work we use the additivity of the dielectric function to describe the dielectric constant of amorphous carbon films in a wide spectral range; we propose to describe the imaginary part of the dielectric function, ε''(ω), by the sum of two components:

$$\varepsilon^*(\omega) = \varepsilon^*_{\text{opt}}(\omega) + \varepsilon^*_L(\omega). \tag{3}$$

The first component is related to an interband optical absorption edge of the Tauc type, and can be represented as (2) rewritten in terms of the dielectric constant:

$$\varepsilon''_{\text{opt}}(\omega) = G_1[(\hbar\omega - E^*_g)/\hbar\omega]^2. \tag{4}$$

The second term is related to light absorption by collective electron oscillations in graphite-like fragments. It can be represented as a Lorentz oscillator:

$$\varepsilon''_L(\omega) = \frac{\omega_p^2}{\omega_0^2 - \omega^2 + i\omega/\tau}, \tag{5}$$

where ω_0 is the natural frequency of the oscillator, τ is the relaxation time, and ω_p is the plasma frequency. Earlier, the Lorentz oscillator has been applied to describe the electron resonance in nanoscale copper clusters [7]. This approach has allowed an adequate description of the frequency dependence of the dielectric function for copper-modified *a*-C:H. Evidently, the agreement between the experiment and the simple oscillator model is associated with the collective

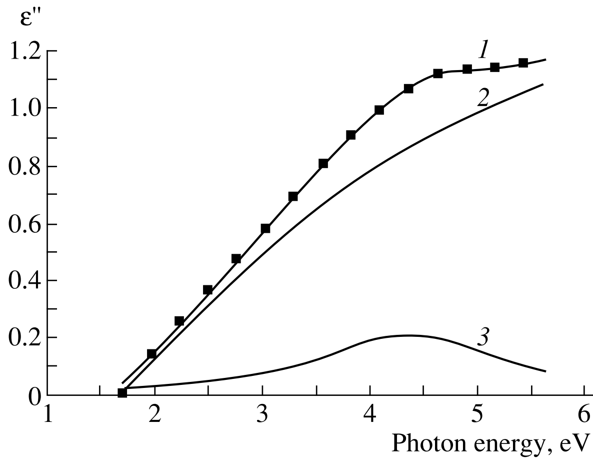

Fig. 4. Deconvolution of the spectral dependence of the imaginary part of the dielectric function ε" for *a*-C:H film annealed at 360°C (*1*) into two components associated with the optical absorption edge ε''_{opt} (*2*) and the Lorentz oscillator ε''_L (*3*).

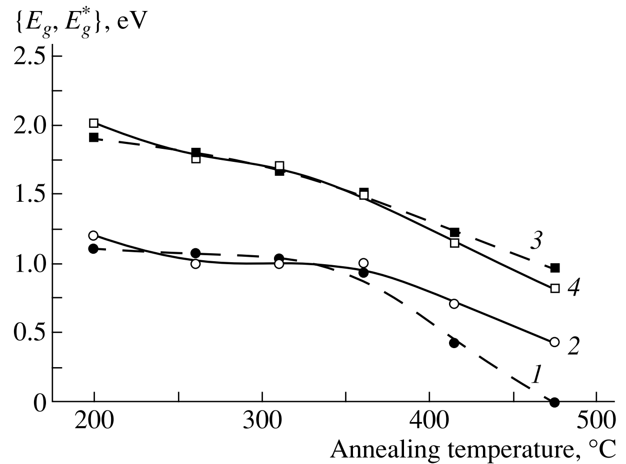

Fig. 5. Optical gap E_g vs. annealing temperature for *a*-C (*1*, *2*) and *a*-C:H (*3*, *4*). (*1*, *3*) E_g found from the Tauc relation (2); (*2*, *4*) E_g^* from relation (4).

motion of electrons in the centrosymmetric field of a graphite-like cluster.

The analytical function (3) was fitted to experimental data by varying the parameters E_g^*, G, ω_0, ω_p, and τ. The E_g^* and G values obtained by applying relation (2) in a limited spectral range, where the experimental dependence corresponds to (1), were chosen as the initial approximation. The ω_0 value was determined from the Lorentzian peak position, and $\omega_p = \omega_0$ and $\tau = 1/\omega_0$ were taken as initial values of the remaining parameters.

This model describes well all the obtained experimental dependences for *a*-C and *a*-C:H films. Figure 4 shows an example of calculation using relation (3). The calculated curve agrees well with the experimental data. Using the proposed method, we performed a best-fit procedure by equation (3) with experimental data on the dielectric constant for all the samples and annealing temperatures. Figures 2 and 3 demonstrate a good agreement between the model and the experiment. The parameters obtained for different annealing temperatures are presented in the table. For comparison, the E_g values calculated by the Tauc relation from the low-energy part of the spectrum are also given.

Parameters E_g^*, $\hbar\omega_0$, $\hbar/\tau$, $\hbar\omega_p$, and G_1 in relation (3) for different annealing temperatures T_a and E_g values obtained from the Tauc relation (2)

Sample	T_a, °C	E_g^*, eV	E_g, eV	$\hbar\omega_0$, eV	$\hbar/\tau$, eV	$\hbar\omega_p$, eV	G_1
a-C:H		2.1	1.92	5.71	2.97	2.24	1.13
	260	1.75	1.8	5.27	2.95	1.77	1.49
	310	1.7	1.66	4.86	2.11	1.19	1.83
	360	1.5	1.51	4.51	2.10	1.39	2.02
	415	1.25	1.22	4.48	4.07	3.18	1.82
	475	0.94	0.96	4.43	5.33	5.25	1.52
a-C		1.2	1.1	5.41	3.40	2.45	1.32
	260	1.0	1.1	4.59	2.06	1.19	1.74
	310	1.0	1.0	4.58	2.48	1.66	1.78
	360	1.0	0.9	4.56	3.01	2.29	1.70
	415	0.7	0.4	4.53	3.91	3.63	1.33
	475	0.43	0	4.34	4.18	3.95	1.20

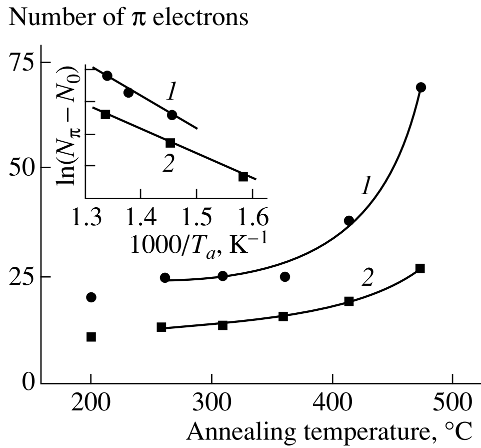

Fig. 6. Average number of π-electrons vs. annealing temperature for type-1 graphite-like fragments in *a*-C (*1*) and *a*-C:H (*2*) films. The inset illustrates the activated behavior of the number of π-electrons with the annealing temperature T_a.

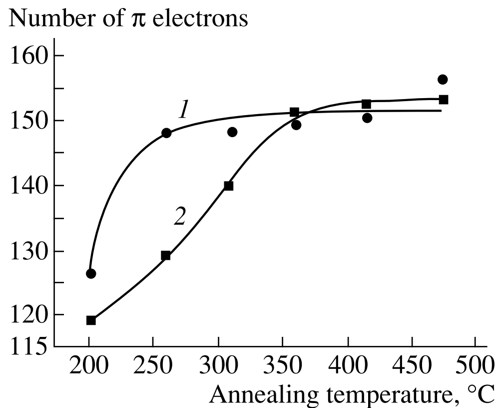

Fig. 7. Average number of π-electrons vs. annealing temperature for type-2 graphite-like fragments in *a*-C (*1*) and *a*-C:H (*2*) films.

Figure 5 presents the dependences of optical absorption edge energies E_g and E_g^* on the annealing temperature, determined using relations (2) and (3), respectively. As seen, the Tauc edge values determined from (2) and (3) differ significantly at high annealing temperatures. It is seen also that the optical gap becomes narrower as the annealing temperature is raised. Usually, the shift of the amorphous carbon absorption edge to lower energy upon annealing is ascribed to a structural rearrangement resulting in a higher number of π-electrons in graphite-like fragments [4, 6, 17]. The average number N_π of π-electrons in graphite-like fragments can be determined using the expression relating the fundamental absorption edge to the number of π-electrons [20]:

$$E_g^* = 2\beta(M)^{-0.75}, \tag{6}$$

where $\beta = 2.66$ is constant, M is the number of sixfold rings in an average graphite-like cluster, and the number of π-electrons N_π is related to M by the Hückel relation [21]:

$$N_\pi = 2(2M+1). \tag{7}$$

Figure 6 shows the obtained dependence of the average number of π-electrons on the annealing temperature. This dependence was analyzed in terms of the model assuming an activated rise in the number of π-electrons in amorphous carbon films with increasing annealing temperature. In this case, by analogy with [14], the expression for the activation dependence can be written as:

$$N_\pi(T) = N_0\left[1 + C\exp\left(-\frac{\Delta E}{k_B T}\right)\right], \tag{8}$$

where ΔE is the activation energy, T is absolute temperature, k_B is the Boltzmann constant, and C is a constant corresponding to the initial concentration of π-electrons in a cluster. Application of this relation to experimental data yields activation energies of 0.69 and 0.87 eV for *a*-C:H and *a*-C, respectively. The value for *a*-C:H matches within the accuracy limit the activation energy of the thermal transition of hydrogen from bound to a quasi-free state [14].

Let us now consider the physical model of the Lorentz oscillator—the second term in (3). As seen from the table, the position of the Lorentz oscillator peak shifts steadily to lower frequencies with increasing annealing temperature. This behavior can be explained by the increasing amplitude of electron oscillations in the centrosymmetric field of a graphite-like cluster, which may be due to increasing cluster size. In the model of a harmonic oscillator, its size can be roughly estimated by the expression

$$D = 2\sqrt{2\hbar/\omega_0 m}, \tag{9}$$

where ω_0 is the natural frequency of the oscillator, $\hbar$ is the Planck constant, $m = 0.2m_0$ is the electron effective mass [22].

The number of carbon rings in such a graphite fragment can be evaluated by the number of hexagons inscribed in a circle of diameter D. In this approximation, the number of carbon rings of size $a = 2.8$ Å in a bulk cluster of size D is determined as $M = 2\pi D^2/\sqrt{3}\,a^2$. The number of π-electrons in such clusters can be evaluated using relation (7). Figure 7 presents the obtained dependence of the average number of π-electrons in a sp^2-cluster on the annealing temperature. The saturation of the curves indicates kinetic limitations on further increase in the cluster size. Comparison of Figs. 6 and 7 reveals the presence of two types of graphite fragments responsible for the fundamental optical absorption edge in *a*-C:H and *a*-C. Clusters with a small number of π-electrons form the fundamental absorption edge itself, and those with a higher number of π-elec-

trons contribute to the spectral feature in the range 4.5–5.5 eV.

4. CONCLUSIONS

(1) When a feature appears in the absorption spectrum of amorphous carbon, the standard approach determining the optical absorption edge by the Tauc relation is inadequate, and the contribution of collective electronic phenomena in graphite-like clusters should be taken into account.

(2) The *a*-C and *a*-C:H film thicknesses behave differently with annealing, presumably due to relaxation of internal strains arising during film growth.

(3) Two types of graphite-like clusters exist, contributing to the spectral dependence of the fundamental absorption edge. A relatively small number—from several to a few tens—of π-electrons is typical of clusters of type 1; clusters of type 2 contain 120–150 π-electrons.

(4) The number of π-electrons in type-1 clusters exhibits temperature-activated behavior.

(5) The dependence of the number of π-electrons in type-2 clusters on the annealing temperature levels off at higher temperatures, indicating kinetic limitations on cluster growth.

ACKNOWLEDGMENT

This study was supported by the Russian Foundation for Basic Research (project no. 00-02-17004).

REFERENCES

1. J. C. Angus, P. Koidl, and S. Domitz, in *Plasma Deposited Thin Films*, Ed. by J. Mort and F. Jancen (CRC Press, Boca Raton, 1986), Chap. 4.
2. J. C. Angus and C. C. Hayman, Science **241**, 913 (1988).
3. H.-C. Tsai and D. B. Body, J. Vac. Sci. Technol. A **5**, 3287 (1987).
4. J. Robertson and E. P. O'Reilly, Phys. Rev. B **35**, 2946 (1987).
5. D. Dasgupta, F. Demichelis, C. F. Pirri, and A. Tagliaferro, Phys. Rev. B **43** (3), 2131 (1991).
6. F. W. Smith, J. Appl. Phys. **55**, 764 (1984).
7. V. I. Ivanov-Omskiĭ, A. V. Tolmatchev, and S. G. Yastrebov, Philos. Mag. B **73**, 715 (1996).
8. V. I. Ivanov-Omskii, V. I. Siklitsky, A. A. Sitnikova, *et al.*, Philos. Mag. B **76**, 973 (1997).
9. D. R. McKenzie, R. C. McPhedran, N. Savvides, and D. J. H. Cocayne, Thin Solid Films **108**, 247 (1983).
10. V. I. Ivanov-Omskii, A. B. Lodygin, A. A. Sitnikova, *et al.*, J. Chem. Vap. Deposition **5** (3), 198 (1997).
11. J. Tauc, R. Grigorovici, and A. Vancu, Phys. Status Solidi **15**, 627 (1966).
12. N. F. Mott and E. A. Davis, *Electronic Processes in Non-Crystalline Materials* (Clarendon Press, Oxford, 1979; Mir, Moscow, 1982).
13. F. W. Smith, Mater. Sci. Forum **52–53**, 323 (1989).
14. V. I. Ivanov-Omskiĭ, G. S. Frolova, and S. G. Yastrebov, Pis'ma Zh. Tekh. Fiz. **23** (7), 1 (1997) [Tech. Phys. Lett. **23**, 251 (1997)].
15. V. I. Ivanov-Omskii, M. P. Korobkov, B. R. Namozov, *et al.*, J. Non-Cryst. Solids **227–230**, 627 (1998).
16. I. Watanabe and T. Okumura, Jpn. J. Appl. Phys. **25**, 1851 (1986).
17. B. Dischler, A. Budenze, and P. Koidl, Solid State Commun. **48**, 105 (1983).
18. V. L. Aver'yanov, V. A. Fedorov, and S. G. Yastrebov, Zh. Tekh. Fiz. **64** (1), 103 (1994) [Tech. Phys. **39**, 57 (1994)].
19. T. S. Moss, *Optical Properties of Semiconductors* (Butterworths, London, 1959; Inostrannaya Literatura, Moscow, 1961).
20. S. G. Yastrebov, V. I. Ivanov-Omskii, V. I. Siklitsky, and A. A. Sitnikova, J. Non-Cryst. Solids **227–230**, 622 (1998).
21. M. Dewar, *The Molecular Theory of Organic Chemistry* (McGraw-Hill, New York, 1969; Mir, Moscow, 1972).
22. H. Zabel and S. A. Solin, *Graphite Intercalation Compounds II (Transport and Electronic Properties)* (Springer-Verlag, Berlin, 1992).

Translated by D. Mashovets

Semiconductors, Vol. 35, No. 2, 2001, pp. 226–229. Translated from Fizika i Tekhnika Poluprovodnikov, Vol. 35, No. 2, 2001, pp. 233–236.
Original Russian Text Copyright © 2001 by Kaliteevskaya, Seĭsyan.

AMORPHOUS, VITREOUS, AND POROUS SEMICONDUCTORS

Contrast Enhancement in Image Transfer via Interaction of UV Radiation with Inorganic Photoresist Films

N. A. Kaliteevskaya and R. P. Seĭsyan

Ioffe Physicotechnical Institute, Russian Academy of Sciences, Politekhnicheskaya ul. 26, St. Petersburg, 194021 Russia

Submitted June 22, 2000; accepted for publication June 22, 2000

Abstract—Photochemical transformations occurring in thin films of inorganic photoresists under UV irradiation from an excimer laser are analyzed theoretically. It is shown that the optimization of the light intensity and irradiation dose can make the transition region between the exposed and unexposed parts of a film narrower, thereby improving the image quality in photolithography. © *2001 MAIK "Nauka/Interperiodica".*

To create high-quality integrated circuits, it is necessary to achieve such a relief structure in photoresist film that the edges of all pattern features are exactly at their assigned positions and that the sidewalls are vertical. The ideal case would be a stepwise profile of the photoresist exposure. However, the light intensity profile at a desired pattern feature boundary is a "smooth function" [1], occasionally nonmonotonic, which is associated with the wave properties of light (Fig. 1). The quantitative measure of this effect is the slope of the light intensity profile in the transition region between light and dark features of the image—edge gradient dI/dx. Blurring of the exposure intensity distribution, statistical fluctuations in the photon distribution, and inhomogeneities arising in the course of chemical etching may result in the edge of a pattern element lying in a certain interval Δx around the prescribed value, which impairs the image quality [1, 2]. Studies of photochemical transformations in films of glassy semiconductors, such as AsSe and As_2Se_3, under irradiation from an excimer laser operating at 193 nm demonstrated that the irradiation dose necessary for photoresist exposure depends on light intensity [3], i.e., the process is "nonlinear." In addition, it has been established that images with a resolution comparable to the wavelength of light can be obtained [4].

The aim of this work was to study the effect of this nonlinearity on pattern formation in photolithography.

A study of the photodarkening of AsSe films under irradiation from an ArF excimer laser made it possible to develop a model quantitatively describing the process of photochemical transformations [5]. In accordance with the results obtained in [5], we assume that under the action of light the film material is transformed from the initial state I into the final state II. These states are characterized by different physical (e.g., light absorption coefficients at the wavelength of the excimer laser inducing photochemical transformations, α_1 and α_2, respectively) and chemical (e.g., solubility in a certain solvent) properties of the material. In the course of irradiation, the film material is a mixture of materials I and II. Let us denote the relative concentrations of materials I and II by, respectively, ρ_1 and ρ_2, so that $\rho_1 + \rho_2 = 1$ and the absorption coefficient of the irradiated material is expressed by

$$\alpha = \alpha_1\rho_1 + \alpha_2\rho_2 = \alpha_2 + (\alpha_1 - \alpha_2)\rho_1. \quad (1a)$$

The absorption in a layer (along the z axis) follows the Bouguer–Lambert–Beer law, so that

$$\frac{\partial I(z, t)}{\partial z} = -\alpha(z, t)I(z, t), \quad (1b)$$

where $I(z, t)$ is the local intensity and t is time.

The change in the concentration of the original material under the action of light is described by

$$\frac{\partial \rho_1}{\partial t} = -C\alpha(z, t)I(z, t)F(I)\rho_1, \quad (1c)$$

where C is the sensitivity having the dimensionality [volume] [energy]$^{-1}$. The physical meaning of the constant C is the volume of material that can be transformed from state I into state II upon absorption of unit energy. The dimensionless intensity-dependent multiplier $F(I)$ reflects the fact that the irradiation dose necessary for material exposure depends on the intensity of incident light.

Equations (1a)–(1c) constitute, together with the initial condition $\rho_1|_{t=0} = 1$ and boundary condition $I(t)|_{z=0} = I_0(t)$, where $I_0(t)$ is the incident light intensity), a system describing the photochemical transformations in films. Since the dependence of the rate of photochemical transformations on light intensity has a

1063-7826/01/3502-0226$21.00 © 2001 MAIK "Nauka/Interperiodica"

threshold, we approximate the function $F(I)$, as was done in [4], by the expression

$$F(I) = \frac{1}{2}\left[1 + \tanh\left(\frac{I - I_{th}}{\delta}\right)\right], \quad (2)$$

where the parameter δ characterizes the blurring of the intensity threshold. A modeling of photodarkening in AsSe films under irradiation from an ArF excimer laser operating at 193 nm allowed us to determine that the sensitivity $C = 3 \times 10^{-3}$ cm^3/J, threshold intensity I_{th} = 1.7×10^4 J/(cm^2 s), and blurring parameter δ = 8.5×10^3 J/(cm^2 s). The absorption coefficients at the excimer laser wavelength in states I and II $\alpha_1 = 0.1 \times 10^5$ cm^{-1} and $\alpha_2 = 1.2 \times 10^5$ cm^{-1}.

Upon exposure, a certain profile of the component concentrations, $\rho_1(z)$ and $\rho_2(z)$, is established in the bulk of the resist film, with the dissolution rate strongly depending on the concentration. When the development conditions (chemical composition of etchant, temperature and duration of development) are set, we can determine the threshold concentration $\rho_{1S}(z)$ separating the exposed (dissolving) and unexposed (nondissolving under the given development conditions) parts of the resist film. The material dissolves if $\rho_1(z) < \rho_{1S}(z)$, and otherwise does not. We denote the boundary position by z_S.

To calculate the concentration profile established in the photoresist bulk upon exposure, it is necessary to solve numerically the system of equations (1). However, preliminary optimization of the irradiation process parameters can be done analytically for such parameters as the concentration profile gradient at the threshold value and the slope of the isoline of threshold concentration near the sample surface.

Introducing the designation $\gamma = (\alpha_1 - \alpha_2)/\alpha_2$, we can rewrite Eq. (1c) for the surface layer of the film (z =0) by separating the variables to obtain

$$\frac{d\rho_1}{(1+\gamma\rho_1)\rho_1} = -\alpha_2 CIF(I)dt. \quad (3)$$

Integrating Eq. (3) and taking into account that $\rho_1 = 1$ at the initial instant of time, we have

$$\rho_1 = \left\{(1+\gamma)\exp\left[\alpha_2 C\int_0^T IF(I)dt\right] - \gamma\right\}^{-1}, \quad (4)$$

where T is the duration of irradiation. In the case of a rectangular pulse of duration T_P and intensity I_P, the following concentration is established at the surface:

$$\rho_1 = \{(1+\gamma)\exp[\alpha_2 CT_P I_P F(I_P)] - \gamma\}^{-1}. \quad (5)$$

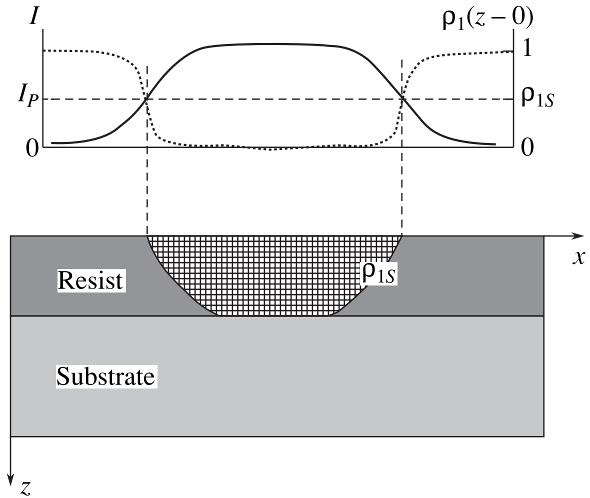

Fig. 1. Photoresist layer on substrate and light intensity profile. The line of constant threshold concentration ρ_{1S} separates the exposed and unexposed parts in the photoresist bulk. The solid line represents the spatial profile of the incident light intensity, and the dashed line, the concentration profile established at the resist surface in the course of irradiation.

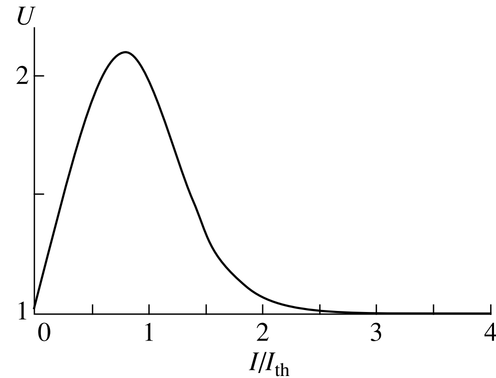

Fig. 2. Image transfer contrast enhancement as a function of light intensity.

Thus, the dose $H_P = T_P I_P$ and intensity I_P ensuring that the threshold concentration ρ_{1S} is reached at the sample surface are related by

$$\ln\left(\frac{1/\rho_{1S} + \gamma}{1+\gamma}\right) = \alpha_2 CI_P F(I_P)T_P. \quad (6)$$

To create as sharp a boundary as possible, it is necessary that $d\rho_1/dx$ be highest around the threshold concentration ρ_{1S}. Let b be the relative edge intensity gradient (see Fig. 1)

$$b = \frac{1}{I_P}\frac{\partial I_P}{\partial x}. \quad (7)$$

Differentiating Eq. (5) with respect to the coordinate x, and using relation (7), we see that the concentration

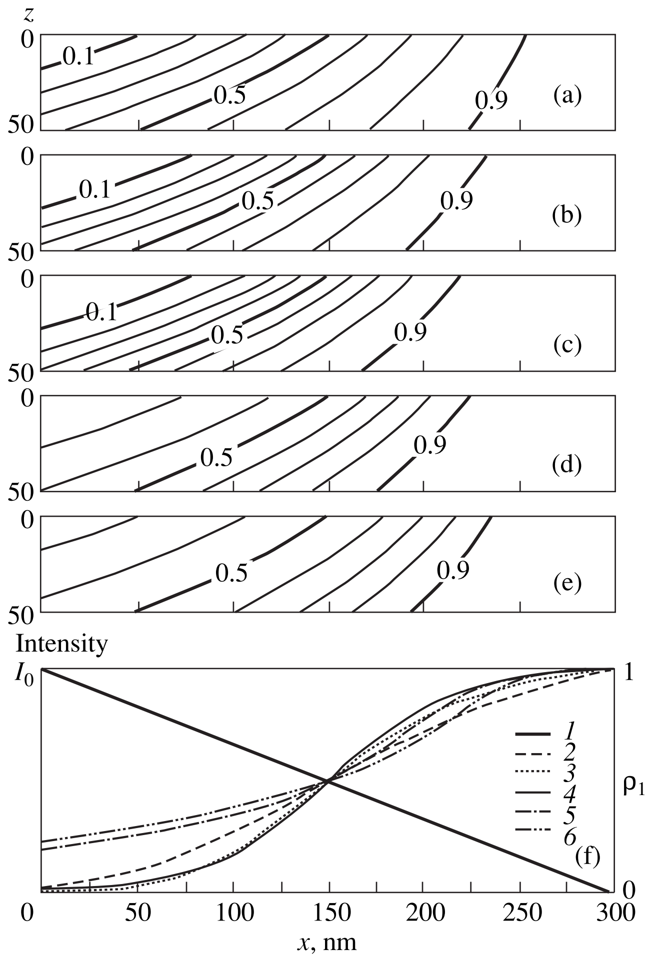

Fig. 3. (a–e) Lines of constant concentration representing concentration profiles in the photoresist bulk upon irradiation; the irradiation dose was selected in such a way that a concentration $\rho_1 = 0.5$ was established upon irradiation at the point $x = 150$ nm on the film surface; the light intensity at the point $x = 150$ nm at the film surface $I_P = I_0/2 = 0.25I_{th}$ (a), $0.5I_{th}$ (b), $0.803I_{th}$ (c), $1.5I_{th}$ (d), and $2I_{th}$ (e). (f) Spatial light intensity profile (*1*) and the dependence of the concentration ρ_1 on the sample surface at $I_P = I_0/2 = 0.25I_{th}$ (*2*), $0.5I_{th}$ (*3*), $0.803I_{th}$ (*4*), $1.5I_{th}$ (*5*), and $2I_{th}$ (*6*).

gradient is proportional to the relative edge intensity gradient with an intensity-dependent proportionality factor:

$$d\rho_1/dx = b(1+\gamma)\alpha_2 CT_P I_P \exp[\alpha_2 CT_P I_P F(I_P)] \times [F(I_P) + I_P(\partial F(I_P)/dI_P)]/\{(1+\gamma) \times \exp[\alpha_2 CT_P I_P F(I_P)] - \gamma\}^2. \quad (8)$$

Introducing the quantity

$$U = \left.\frac{(\partial\rho_1/\partial x)}{b}\right|_{\rho = \rho_{1S}},$$

characterizing the "image transfer contrast enhancement" at the surface and using relation (6), we have

$$U = U_{0\rho}(\rho_{1S}, \gamma)U_1(I_P) = (1+\rho_{1S}\gamma)\rho_{1S} \times \ln\left[\frac{1/\rho_{1S}+\gamma}{1+\gamma}\right]\left[1 + \frac{I_P}{F(I_P)}\frac{\partial F(I_P)}{\partial I_P}\right]. \quad (9)$$

For a function of the type (2), the following equation can be obtained

$$\frac{1}{F(x)}\frac{\partial F(x)}{\partial x} = \frac{2}{\exp(2x)+1}, \quad (10)$$

where $x = (I - I_{th})/\delta$.

Differentiating the right-hand part of Eq. (9) and using expression (10), we see that the concentration gradient grows to the maximum extent at an incident light intensity I_P satisfying the relation

$$\exp\left[2\frac{I_P - I_{th}}{\delta}\right]\left[1 - \frac{2I_P}{\delta}\right] + 1 = 0. \quad (11)$$

Thus, the best quality of pattern transfer can be achieved at the parameters specified by relations (6) and (11).

Figure 2 shows the intensity dependence of the pattern transfer contrast enhancement. In accordance with Eq. (11), the dependence shows a maximum at $I_P = 0.803I_{th}$. By selecting an appropriate light intensity, one can raise the concentration gradient at the boundary by more than a factor of 2.

Figure 3 presents calculated concentration profiles established in the film upon irradiation at varied light intensities. The spatial profile of the incident radiation is shown in Fig. 3f by curve *1*. In the region considered, corresponding to the boundary between the illuminated and unilluminated parts of the film, the intensity falls from the maximum value to 0. The irradiation dose was chosen for each case so that a concentration $\rho_1 = 0.5$ was established at the point $x = 150$ nm (in the middle of the region in question) upon irradiation.

Figure 3c corresponds to the optimal intensity $I_P = 0.803I_{th}$. Figures 3a and 3b correspond to intensities lower than optimal, and Figs. 3d and 3e, to those higher than the optimal value. It can be seen that the transition region separating the exposed and unexposed parts of the film is narrowest when the intensity I_P corresponds to the optimal value $0.803I_{th}$.

In addition to the intensity profile, Fig. 3f shows the dependence of the concentration ρ_1 at the surface upon the coordinate x, demonstrating a pronounced increase in the concentration gradient at the boundary compared with the edge gradient of the incident radiation at optimized light intensity and irradiation dose.

It should be noted that if the pulse pattern is other than rectangular the parameters ensuring the best image quality also change somewhat, but can be determined by numerically solving the system of equations (1).

To conclude, in the case of nonlinear photoresists, in which the rate of photochemical transformation is not directly proportional to the incident light intensity, appropriate choice of the incident light intensity and irradiation dose can make narrower the transition region between the exposed and unexposed parts, thereby improving the quality of image transfer in photolithography.

REFERENCES

1. G. N. Berezin, A. V. Nikitin, and R. A. Suris, *Optical Foundations of Contact Lithography* (Radio i Svyaz', Moscow, 1982).
2. H. I. Smith, J. Vac. Sci. Technol. B **6** (1), 346 (1988).
3. E. G. Barash, A. Yu. Kabin, V. M. Lyubin, and R. P. Seĭsyan, Zh. Tekh. Fiz. **62** (3), 106 (1992) [Sov. Phys. Tech. Phys. **37**, 292 (1992)].
4. L. G. Gladysheva, N. A. Kaliteevskaya, R. P. Seĭsyan, and D. V. Smirnov, Pis'ma Zh. Tekh. Fiz. **22** (15), 91 (1996) [Tech. Phys. Lett. **22**, 640 (1996)].
5. N. A. Kaliteevskaya and R. P. Seĭsyan, Fiz. Tekh. Poluprovodn. (St. Petersburg) **34** (7), 857 (2000) [Semiconductors **34**, 825 (2000)].

Translated by M. Tagirdzhanov

Semiconductors, Vol. 35, No. 2, 2001, pp. 230–234. Translated from Fizika i Tekhnika Poluprovodnikov, Vol. 35, No. 2, 2001, pp. 237–241.
Original Russian Text Copyright © 2001 by Zvonareva, Ivanov-Omskiĭ, Yastrebov, Golubok, Gorbenko, Rozanov.

Investigation of Surface Morphology of Copper-Modified Amorphous Carbon Films

T. K. Zvonareva*, V. I. Ivanov-Omskiĭ*, S. G. Yastrebov*, A. O. Golubok, O. M. Gorbenko**, and V. V. Rozanov****

** Ioffe Physicotechnical Institute, Russian Academy of Sciences, Politekhnicheskaya ul. 26, St. Petersburg, 194021 Russia*

*** Institute for Analytical Instrumentation, Russian Academy of Sciences, St. Petersburg, 198103 Russia*

Submitted June 27, 2000; accepted for publication June 30, 2000

Abstract—A study of the surface morphology of copper-modified amorphous hydrogenated carbon films *a*-C:H(Cu) by scanning tunnel microscopy (STM) is reported. An algorithm is presented for the digital analysis of STM images to obtain the size distribution function for the longitudinal component of the surface relief. *a*-C:H(Cu) films were deposited by magnetron co-sputtering of graphite and copper onto two types of substrates: (100) *n*-Si with a heavily doped surface layer, and Si covered with a chromium layer. A mesoscopic surface structure of crystalline silicon, a chromium layer, and *a*-C:H(Cu) film has been revealed. A correlation between the structural elements of the film and the substrate is considered and a conclusion is made that inherent grains with characteristic size of 6–8 nm are formed in the film. © *2001 MAIK "Nauka/Interperiodica"*.

1. INTRODUCTION

Amorphous hydrogenated carbon (*a*-C:H) films have a smooth chemically inert surface and exhibit high hardness, a low friction coefficient [1–3], and a low electron emission threshold [4]. Owing to these features, they can be used as coatings for various technological purposes and show promise in creating cold cathodes for field-emission displays. The attention given to studies of metal-modified *a*-C:H films is due to the possibility of a wide range of control over their physical properties. In addition, investigations of formation processes and local electronic properties of metal-modified *a*-C:H films arouse interest in the context of their possible application in nanoelectronics [5].

Nanometer-size objects are formed in a *a*-C:H(Cu) matrix as a result of the material modification with copper, and their properties affect the physical characteristics of the obtained material as a whole [5]. So, a nanometer-scale study of the surface morphology of these materials is important. Earlier [5, 6], we have presented preliminary results of the surface morphology investigations for *a*-C:H and *a*-C:H(Cu). In the present paper, an emphasis is made on the study of the distribution function for the longitudinal component of the surface relief in modification of *a*-C:H films with copper. Further, we intend to establish a correlation between this distribution function, on the one hand, and the substrate properties and film thickness, on the other. The distribution function for the longitudinal component of the surface relief is obtained using the algorithm for digital analysis of images, described in detail in [7], and briefly, in Section 3 of this paper.

2. EXPERIMENTAL

a-C:H(Cu) films were deposited onto two types of substrates: (1) ~1.5-μm-thick KEF-1 (100) *n*-Si wafers with a heavily doped n^{++}-Si surface layer with carrier concentration $n \approx 10^{21}$ cm^{-3} (doping was performed from a surface source at 950°C for 1 hour in air [8]), referred to further as Si substrates; and (2) chemically polished KDB-20 (100) *p*-Si wafers, with ~200 nm thick Cr layer deposited by rf ion-plasma sputtering—Cr/Si substrates. *a*-C:H(Cu) films were deposited by magnetron co-sputtering of graphite and copper targets in argon–hydrogen plasma (80% Ar + 20% H_2). Copper concentration determined from Rutherford backscattering data was 18 at. %. The sputtering chamber was pre-evacuated to 10^{-6} Torr. Films were deposited in a working gas flow at $P = 10^{-2}$ Torr onto substrates heated to 200°C. The ion current density was 10^{-1} A/cm^2 at 5-V negative self-bias on the substrate. Under these conditions, the growth rate of *a*-C:H(Cu) films was 5–6 nm/min. The film thickness was monitored with an LEF-3M ellipsometer in the reflection geometry, with an He–Ne laser as the radiation source.

A scanning tunnel microscope with an Ir probe was used in the topography mode. It was assumed that the observed STM surface image is determined by the relief morphology, rather than by sample conductivity fluctuations. STM measurements were done under atmo-

spheric pressure. The scanned area was 200×200 nm^2, and the corresponding surface image contained 250×250 pixels, with a linear size of one pixel equal to 0.8 nm. For some of the substrates and a-C:H(Cu) films studied, the surface image was distorted by noise in the form of current surges appearing as bright points on the image. To suppress this effect, 3×3 pixel median filtration was used in the image processing. We assume that the relief is not distorted by the median filtration, and, moreover, that the size of the longitudinal relief component elements is not affected substantially.

3. IMAGE PROCESSING METHOD

To analyze structural elements constituting the nanometer-scale surface relief, the image background was smoothed. For this purpose, a surface with a shape reproducing the large-scale substrate relief is constructed. Further, this surface is subtracted from the initial image. As a result, the structure elements are arranged in the same plane. Figure 1 shows a typical surface relief image for a-C:H(Cu) film deposited on a type-1 substrate.

To obtain the information on the size distribution of elements, the STM image has been analyzed in terms of the model of a disordered two-dimensional (2D) field with disk-shaped elements of random radii a_i. The disks centers are situated at points r_i. Statistical independence of the random values a_i and r_i, and also of separate disk positions, is assumed. In this case, the light scattering indicatrix $I_p(\theta)$ can be described by the relation [9, 10]:

$$I_p(\theta) = I_0\theta^{-2}\int_0^\infty w(\rho)\rho^2 J_1^2(\rho\theta)d\rho, \quad (1)$$

where I_0 is the light beam intensity in the absence of scattering, θ is the scattering angle, $\rho = 2\pi a/\lambda$, λ is the incident light wavelength, $w(\rho)$ is the distribution density of the normalized disk radii, and J_1 is the Bessel function of the first kind.

Simple transformations of (1) give an expression relating the spectral density $G(f)$ of the image to the size distribution density of the image elements (disks), $w(a)$

$$G(f) = Cf^{-2}\int_0^\infty w(a)a^2 J_1^2(fa)da, \quad (2)$$

where f is the spatial frequency, $f = \sqrt{f_x^2 + f_y^2}$, and C is a constant.

The solution of the inverse problem is based on generalized integral transformations. In this case, we obtain for the size distribution density:

$$w(a) = -\frac{C_1}{a}\int_0^\infty fJ_1(fa)N_1(fa)\frac{d}{df}[f^3G(f)]df, \quad (3)$$

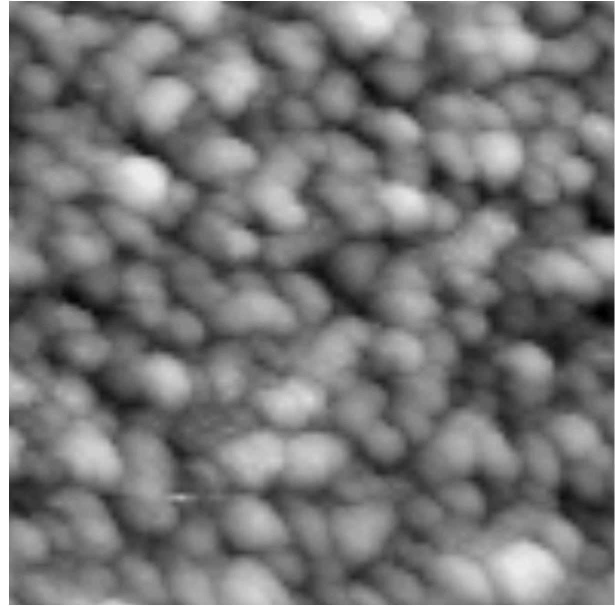

Fig. 1. STM image of a-C:H(Cu) film surface (type-1 substrate). Scanned area 200×200 nm^2.

where C_1 is a constant, and N_1 is the Neumann function of the first kind.

Expression (3) allows one to calculate the radius distribution density of random elements of the 2D field from its spectral density. The difficulty of the numerical determination of $w(a)$ from relation (3) is due to the fact that we have a derivative of the experimental dependence $P(f) = f^3G(f)$ under the integration sign. This poses the problem of smoothing the experimental spectral density $G(f)$ and obtaining a smooth derivative reflecting the character of the $f^3G(f)$ dependence, unrelated to random deviations of the spectral components. It is proposed to perform smoothing in three stages. In the first stage, the 2D spectral density of the image is smoothed using a 2D spectral window $W(f_x, f_y)$, for example, the Bartlett window:

$$G'(f_x, f_y) = G(f_x, f_y)**W(f_x, f_y),$$

where ** is the convolution operation.

Since the above relations have been obtained for the field model with randomly distributed round disks, all the directions in the image are equivalent, and the 2D spectral density can be averaged over several sections. Accordingly, in the second stage we calculate

$$G''(f) = \frac{1}{n}\sum_{i=1}^{n} G_i'(f),$$

where $G_i'(f)$ is the ith section of the $G'(f_x, f_y)$ function, $f = \sqrt{f_x^2 + f_y^2}$.

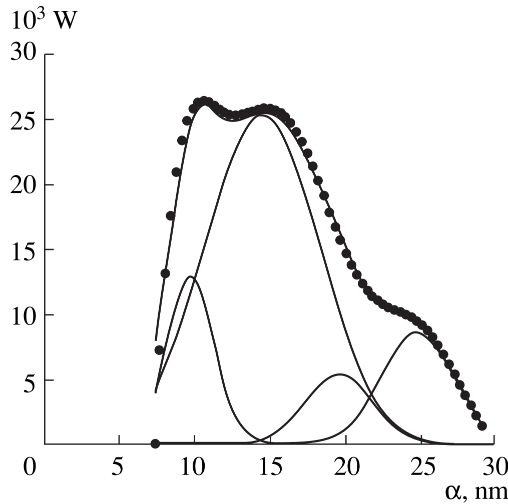

Fig. 2. Distribution function for Si (type-1) substrate (points), and its decomposition into Gaussian profiles. Solid line passing through the experimental points corresponds to the sum of the Gaussian profiles.

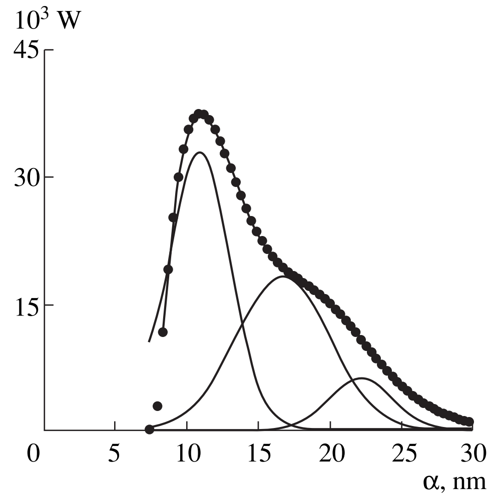

Fig. 3. Distribution function for Cr/Si (type-2) substrate (points), and its decomposition into Gaussian profiles. Solid line passing through the experimental points corresponds to the sum of the Gaussian profiles.

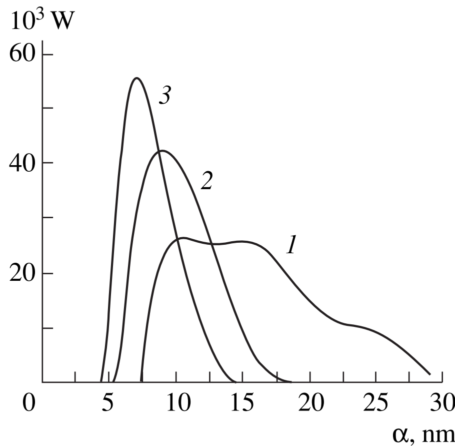

Fig. 4. Size distribution of structural elements: (*1*) Si (type-1) substrate, (*2*) 45-nm-thick *a*-C:H(Cu) film on Si, and (*3*) 83-nm-thick *a*-C:H(Cu) film on Si.

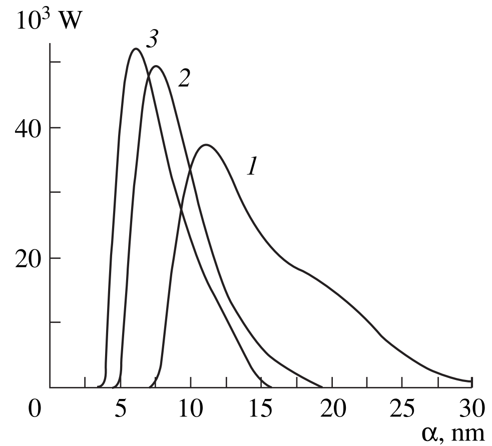

Fig. 5. Size distribution of structural elements for *a*-C:H(Cu) on Cr/Si (type-2) substrate: (*1*) Cr/Si (type-2) substrate, (*2*) 35-nm-thick *a*-C:H(Cu) film on Cr/Si, and (*3*) 80-nm-thick *a*-C:H(Cu) film on Cr/Si.

In the third stage, it is proposed to do the smoothing of the $G''(f)$ curve with the use of splines.

When a smooth enough spectral density function is constructed, the derivative $P(f_k) = f_k^3 G(f_k)$, $k = 1, \ldots, n$ is to be calculated approximately. This is done using the first-order difference operator

$$\frac{dP(f_k)}{df_k} = \frac{P(f_{k+1}) - P(f_k)}{f_{k+1} - f_k}, \qquad k = 2, \ldots, n.$$

Thus, the density of the radius distribution density of the image elements can be determined by approximate calculation of the integral (3) for a given set of radii a_i, $i = 1, \ldots, m$:

$$w(a_i) = -\Delta f \frac{C_1}{a_i} \sum_{k=1}^{n} f_k J_1(f_k a_i) N_1(f_k a_i) \frac{dP(f_k)}{f_k},$$

where Δf is the interval between the adjacent spectral components of the function $G''(f_k)$.

4. EXPERIMENTAL RESULTS AND DISCUSSION

Using the image processing method described above, we have obtained the size distribution functions

W of surface elements for both types of substrates (Figs. 2, 3) and for *a*-C:H(Cu) films on these substrates (Figs. 4, 5). In these figures, the abscissa is the surface structure element radius, and the ordinate represents the probability of finding elements of a given radius on the image. The shape and position of the distribution function peaks suggest that in all cases the surface relief is formed by several groups of structural elements. For *a*-C:H(Cu), the element size changes with increasing film thickness, as follows from Figs. 4 and 5.

To determine the parameters of these element groups, we use the formalism involving decomposition of the experimental distribution function into Gaussian profiles, assuming a random distribution of elements within each group. The results of this procedure are presented as examples in Figs. 2 and 3 and, in full, in the table, where the following parameters of the resulting Gaussian profiles are given: peak position; relative area S bounded by a profile; and dispersion, or the profile half-width. For the type-1 substrate, the best agreement between the calculation and the experimental data is achieved using four Gaussian profiles in the decomposition of $W(a)$ (Fig. 2), while for the type-2 substrate only three specific sizes of structure elements can be distinguished (Fig. 3). For the type-1 substrates, the observed structure elements may reflect the structure of point-defect clusters in the heavily doped silicon surface layer. The characteristic sizes of elements are 10, 15, 20, and 25 nm (see the table). The most probable size of elements in the main group (60% of the total area) is 15 nm, with 4.4 nm variance.

As seen from Fig. 3 and the table, the characteristic sizes of elements for the type-2 substrate are 11, 17, and 22 nm, differing from those for the type-1 substrate within the variance. Narrow peaks of 11 and 17 nm are predominant and have well-defined sizes.

Figures 4 and 5 show distribution functions of the surface structural elements (granules) for *a*-C:H(Cu) films on type-1 and type-2 substrates, respectively. As a result of *a*-C:H(Cu) film deposition, smaller granule sizes start to dominate, with the granule sizes decreasing with increasing film thickness.

Thus, the heating of *a*-C:H(Cu) layer modifies the mesoscopic surface structure, and the correlation between the specific features of the layer and the substrate is lost. With increasing film thickness, granules ~6–8 nm in size appear and become dominant. Within the dispersion, larger granules on the *a*-C:H(Cu) surface correspond, to within the variance, to minor granules on the surface of type-1 and type-2 substrates. Consequently, we can assume that the minimal size of granules on the *a*-C:H(Cu) surface corresponds to the specific intrinsic structure of the film. In connection to this, we note that the size of copper nanoclusters in *a*-C:H(Cu), determined from optical and electron microscopic data [11], coincides with the minimal size of granules obtained in this work.

Gaussian profile characteristics for the size distribution functions of structural elements

Sample	*a*-C:H(Cu) film thickness, nm	Peak position, nm	S, %	Variance, nm
Si substrate	–	10	16	1.8
		15	60	4.4
		20	9	2.5
		25	15	2.5
Cr/Si substrate	–	11	49	2.7
		17	43	3.8
		22	8	2.7
a-C:H(Cu) film on Si substrate	45	9	60	2.2
		12	40	2.5
	83	8	65	1.5
		9	21	1.5
		11	14	1.5
a-C:H(Cu) film on Cr/Si substrate	35	7	55	1.8
		11	38	2.4
		15	7	2.8
	80	6	50	1.8
		9	50	3.3

We note also that all the considered $W(a)$ curves steeply tend to zero on the side of small granule sizes. This effect is usually attributed to the kinetics of processes accompanying the granule formation and growth [12].

The formation of granules on the scale on the order of hundreds of nanometers in thick *a*-C:H(Cu) films (~1 μm) has been discussed earlier [13]. It was demonstrated that the granules grow in size with increasing film thickness, in good agreement with theory [12]. As seen from Figs. 4 and 5 and the table, an opposite tendency exists in the present case of thin films; evidently, this fact must stimulate further progress in the theory of inhomogeneity formation in films.

5. CONCLUSION

The structure of the crystal silicon surface, presumably associated with the regular structure of point defect clusters, has been determined by tunnel microscopy combined with mathematical image processing. The structure of the chromium layer surface is more uniform, with finer structural elements dominating. For *a*-C:H(Cu) films deposited onto substrates of silicon or silicon coated with chromium, the surface profile partially inherits the surface structure of the substrate; nevertheless, with increasing *a*-C:H(Cu) film thickness, the correlation between the longitudinal components of the substrate surface relief and the layer relief weakens,

and the contribution from the film structure elements becomes prominent.

ACKNOWLEDGMENTS

We are grateful to L.V. Sharonova for performing the ellipsometric measurements, and to S.A. Masalov for many helpful discussions on the experimental methods.

This study was performed using the equipment of the St. Petersburg Joint Research Center, with partial support from the Russian Foundation for Basic Research (project no. 00-02-17004) and the Ministry of Science of the Russian Federation, Program “Physics of solid-state nanostructures” (project no. 98-3010).

REFERENCES

1. J. C. Angus, P. Koidl, and S. Domitz, in *Plasma Deposited Thin Films*, Ed. by J. Mort and F. Jansen (CRC Press, Boca Raton, 1986), Chap. 4.
2. J. C. Angus and C. C. Hayman, Science **241**, 913 (1988).
3. H. Tsai and D. B. Bogy, J. Vac. Sci. Technol. A **5**, 3287 (1987).
4. G. A. J. Amaratunga and S. R. P. Silva, Appl. Phys. Lett. **68**, 2529 (1996).
5. A. O. Golubok, O. M. Gorbenko, T. K. Zvonareva, *et al.*, Fiz. Tekh. Poluprovodn. (St. Petersburg) **34** (2), 223 (2000) [Semiconductors **34**, 217 (2000)].
6. V. I. Ivanov-Omskiĭ, S. G. Yastrebov, A. O. Golubok, *et al.*, Pis’ma Zh. Tekh. Fiz. **24** (20), 28 (1998) [Tech. Phys. Lett. **24**, 800 (1998)].
7. O. M. Gorbenko, S. A. Masalov, P. A. Fridman, *et al.*, Nauchn. Priborostr. **10** (1), 83 (2000).
8. Z. Yu. Gotra, *Technology of Microelectronic Devices* (Radio i Svyaz', Moscow, 1991).
9. S. A. Akhmanov, Yu. E. D’yakov, and A. S. Chirkin, *Introduction to Statistical Radio Physics and Optics* (Nauka, Moscow, 1981).
10. L. P. Baĭvel’ and A. S. Lagunov, *Measuring and Control of Particle Dispersion by Light Diffusion Method of Small Angles* (Énergiya, Moscow, 1977).
11. M. V. Baidakova, V. I. Ivaniov-Omskii, V. I. Siklitsky, *et al.*, in *Proceedings of the International Symposium on Nanostructures and Technology, St. Petersburg, 1997*, p. 383.
12. S. A. Kukushkin and V. V. Slezov, *Disperse Systems on Solid Surface* (Nauka, St. Petersburg, 1996).
13. T. K. Zvonareva, V. I. Ivanov-Omskiĭ, A. V. Nashchekin, and L. V. Sharonova, Fiz. Tekh. Poluprovodn. (St. Petersburg) **34** (1), 96 (2000) [Semiconductors **34**, 98 (2000)].

Translated by D. Mashovets

Semiconductors, Vol. 35, No. 2, 2001, pp. 235–237. Translated from Fizika i Tekhnika Poluprovodnikov, Vol. 35, No. 2, 2001, pp. 242–244.
Original Russian Text Copyright © 2001 by Vinokurov, Kapitonov, Nikolaev, Sokolova, Tarasov.

Optical Study of InP Quantum Dots

D. A. Vinokurov, V. A. Kapitonov, D. N. Nikolaev, Z. N. Sokolova, and I. S. Tarasov

Ioffe Physicotechnical Institute, Russian Academy of Sciences, Politekhnicheskaya ul. 26, St. Petersburg, 194021 Russia

Submitted July 18, 2000; accepted for publication July 26, 2000

Abstract—Results of photoluminescence (PL) studies of self-organized nanoscale InP islands (quantum dots, QDs) in the $In_{0.49}Ga_{0.51}P$ matrix, grown on a GaAs substrate by metalorganic vapor phase epitaxy (MOVPE), are presented. Dependences of the PL efficiency on temperature in the range 77–300 K and on excitation level at pumping power densities of 0.01–5 kW/cm^2 have been obtained. The PL spectra are a superposition of emission peaks from QDs and the wetting layer. Their intensity ratio depends on the pumping power and temperature, and the emission wavelength varies in the range 0.65–0.73 μm. At 77 K and low excitation level, InP QDs exhibit high temperature stability of the emission wavelength and high quantum efficiency. *© 2001 MAIK "Nauka/Interperiodica".*

Recently, the fundamental physical properties of zero-dimensional objects have been studied intensively. To such objects belong, in particular, quantum dots (QDs)—nanoscale structures arising in heteroepitaxial growth of semiconductors with large crystal lattice mismatch [1]. In(Ga)As QDs in the GaAs matrix have been used to fabricate efficient photodetectors [2] and heterolasers [3, 4] with threshold current density on the order of 35 A/cm^2 [4]. Of particular practical interest are nanostructures with InP QDs, which can be used to fabricate the shortest-wavelength laser structures emitting in the red spectral range. The main technology employed to obtain QDs is molecular beam epitaxy (MBE), encountering, however, severe difficulties when operating with phosphorus. InP QDs can be reproducibly grown only by metalorganic vapor phase epitaxy (MOVPE), even though fabrication of InP QD lasers by MBE has also been reported [5]. These lasers operate only in pulsed generation mode at temperatures not exceeding 90 K.

This communication presents the results obtained in photoluminescence (PL) studies of heterostructures with InP QDs grown in the $In_{0.49}Ga_{0.51}P$ matrix on GaAs substrates. Measurements were done in a wide temperature range (77–300 K) at various pumping levels. Arrays of strained QDs were obtained by MOVPE [6, 7] in anisotype heterostructures at 700°C. The layer with QDs was confined between a 0.35-μm-thick $In_{0.49}Ga_{0.51}P$ buffer layer, lattice-matched to the (100) GaAs substrate, and 0.04-μm-thick wide-bandgap $In_{0.49}Ga_{0.51}P$ top layer. The thickness of the layer with InP QDs varied between 0.5 and 12 monolayers (ML). The structures were grown in the Stranski-Krastanow mode characteristic of systems with large lattice mismatch ($\Delta a/a$ = 3.7% at the $In_{0.49}Ga_{0.51}P$/InP interface, where a is the lattice constant). In this mode, the so-called wetting layer (WL) (1–3 ML of InP) first grows layer-by-layer on the surface of the wide-bandgap $In_{0.49}Ga_{0.51}P$ matrix, and then three-dimensional QDs start to form.

The PL from the samples under study was excited by an Ar$^+$ laser with wavelength of 0.514 μm. The exciting radiation density was varied in the range 0.01–5 kW/cm^2. The signal from a heterostructure was recorded with a photomultiplier with maximum sensitivity in the wavelength range 0.35–0.9 μm.

The obtained PL spectra exhibited a strong peak associated with the emission from InP QDs. At 77 K and pumping power density of 50 W/cm^2, this peak is located at 1.72 eV, has a half-width of 50 meV, and exceeds in intensity by two orders of magnitude the emission from the matrix. Previous investigations [7] demonstrated that the obtained InP QDs are uniform and coherent (dislocation-free) nanoscale objects, since the QD PL peak energy remains practically unchanged in deposition of 2–7 ML of InP. The highest external quantum efficiency of PL is 30% at 77 K in structures with a nominal thickness of 6 ML of InP.

Figure 1 presents experimental temperature dependences of the PL peak energy for QDs with a nominal thickness of 5 ML and an InGaP matrix at a low excitation level (50 W/cm^2), together with a calculated temperature dependence of the energy of main transitions in a strongly strained 6-ML-thick (1 ML = 2.9 Å) InP quantum well (QW). The temperature dependence of the matrix emission wavelength follows the temperature narrowing of the energy gap in InGaP. The weakest temperature dependence of the emission wavelength in the temperature range 77–300 K is observed for InP QDs.

Figure 2 shows PL spectra for structures with InP QD at the nominal thickness of the deposited InP layer of 3 (solid lines) and 5 ML (dashed lines) at 77 K and varied excitation levels in the range 0.01–3.5 kW/cm^2. These peaks are a superposition of two emission peaks related to QDs and the wetting layer. At low excitation

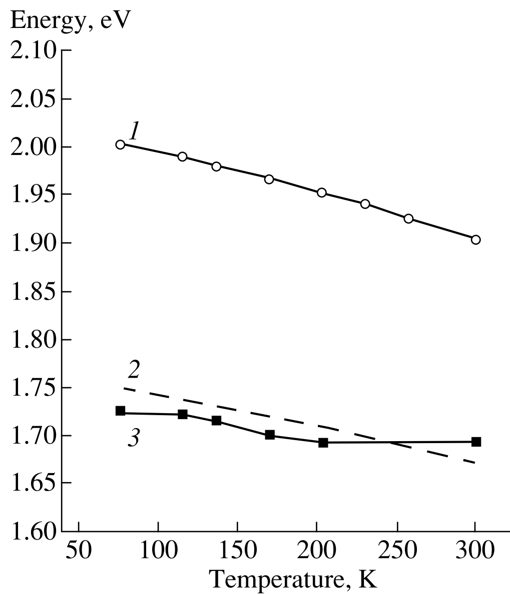

Fig. 1. Experimental temperature dependences of the PL peak energy at excitation level of 50 W/cm^2: (*1*) $In_{0.49}Ga_{0.51}P$ matrix and (*3*) InP QDs (nominal deposited layer thickness of 5 ML); (*2*) calculated values for strongly strained InP QW 6 ML thick.

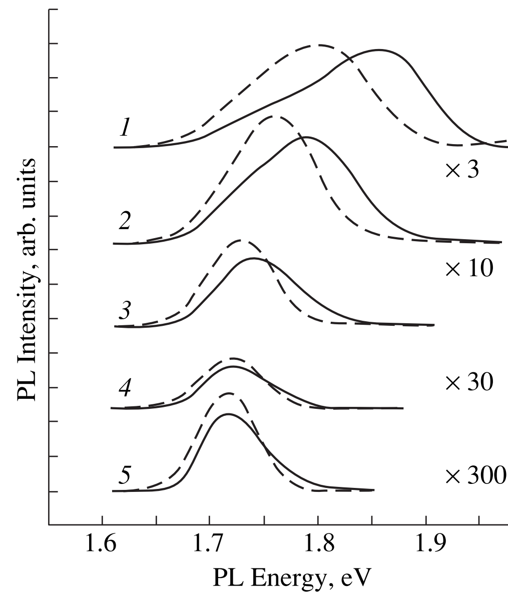

Fig. 2. PL at 77 K from structures with InP QDs at nominal deposited layer thickness of 3 (solid lines) and 5 ML (dashed lines) at varied excitation level: (*1*) 3.5, (*2*) 1.0, (*3*) 0.15, (*4*) 0.04, and (*5*) 0.01 kW/cm^2.

levels (10 and 40 W/cm^2) the spectra contain only the QD emission line, and the PL peak positions of these two structures coincide. At pumping power densities exceeding 100 W/cm^2, the spectra are shifted to shorter wavelengths, which is due to the appearance and further growth in intensity of a short-wavelength peak associated with the WL and to the saturation of the QD emission with increasing pumping power. The WL emission peak energy is around 1.9 eV [7], which corresponds, according to our estimates, to a WL thickness of approximately 2.5 ML (7.3 Å). Calculations show that, in a strongly strained InP WL, the QW for holes is 1.3 times deeper than that for electrons. The QWs contain one size-quantization level each. The binding energy of electrons is less than 6 meV, and that of holes is on the order of 100 meV. At the same time, the hole binding energy in InP QDs is 120 meV [8]. Even at low pumping levels (10 W/cm^2), the wetting layer and QDs are "filled" with electrons, whereas the Fermi level for holes lies 90 meV below the top of the QW in the WL; the hole level in the QD is filled, and that in QDs is empty. The filling of the hole level in the WL starts only at pumping power densities on the order of 150 W/cm^2, just when the spectra in Fig. 2 are shifted to shorter wavelengths. It should be noted that with increasing pumping power the intensity of emission from the wetting layer grows, while that from the QDs remains unchanged because of the saturation occurring already at low excitation levels. However, the fraction of QD emission in the PL spectrum of the structure with 5 ML exceeds that for the structure with 3 ML, which is due to the higher density of QDs in the former (the highest QD PL intensity is observed for structures with 6 ML of InP [7]). As a result, the spectral shift in Fig. 2 is weaker in structures with 5 ML of InP, compared with those comprising 3 ML.

The PL spectra of the heterostructure with 3 ML of InP, taken at high pumping levels (5 kW/cm^2) at different temperatures, are shown in Fig. 3. At 110 K, the intensity of emission from the WL exceeds that from InP QDs. With increasing temperature, the total emission intensity decreases, with the fraction of the PL from the wetting layer markedly decreasing compared with the emission from QDs, which is presumably due to a pronounced leakage of electrons from the WL into the InGaP matrix. Thus, the quantum efficiency of the PL from WL falls with increasing temperature much faster than the efficiency of QD PL at 50 W/cm^2, given in Fig. 4 for a structure with nominally deposited 5 ML of InP. At 77 K, this structure shows 30% external quantum efficiency. Such a behavior points to the existence of intense nonradiative channels, strongly enhanced by increasing temperature. A similar dependence was observed in [8].

Optical studies of InGaP/InP heterostructures grown by MOVPE in the Stranski–Krastanow mode revealed specific features of the luminescence from these structures. At 77 K and low excitation levels, the energy of the QD emission shows higher temperature stability compared to the emission from the InGaP matrix and strained InP QW. Measurements of the quantum efficiency of emission from these structures in

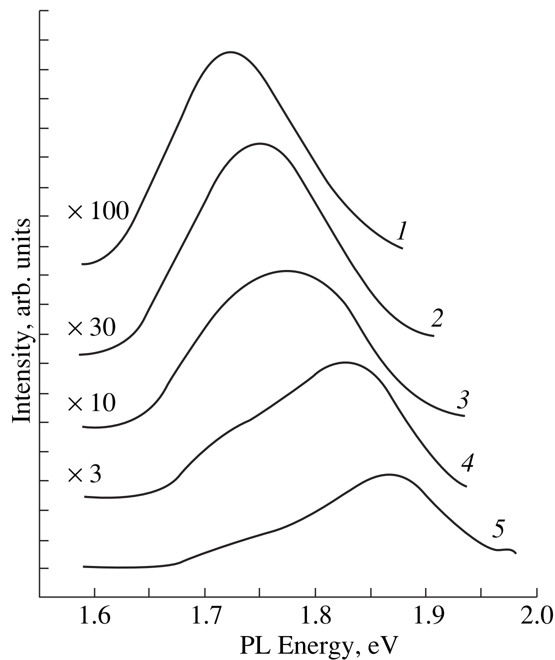

Fig. 3. PL from structures with InP QDs at nominal deposited layer thickness of 3 ML at pumping power density of 5 kW/cm^2 and varied temperature: (*1*) 230, (*2*) 200, (*3*) 170, (*4*) 135, and (*5*) 110 K.

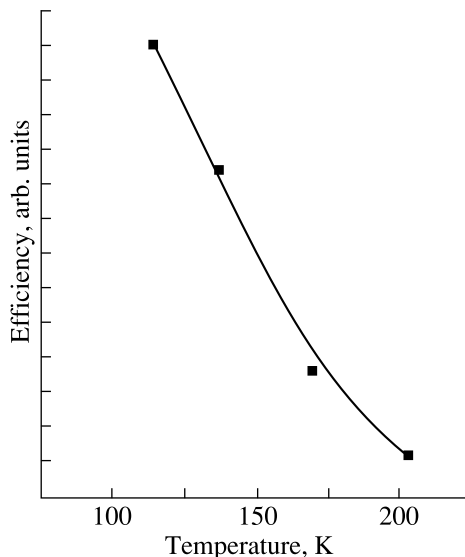

Fig. 4. Temperature dependence of the InP QD luminescence efficiency at nominal deposited layer thickness of 5 ML and excitation level of 50 W/cm^2.

relation to temperature (77–300 K) and excitation level (0.01–5 kW/cm^2) demonstrated that the PL spectra are, as a rule, a superposition of emissions from QDs and WL. The intensity ratio of these two kinds of emissions depends on the pumping power and temperature, with the wavelength varying within 0.65–0.73 μm. The emission from only QDs can be obtained either at low excitation levels and temperatures or at the highest (of those studied) values of these parameters. Thus, the obtained nanoscale heterostructures can be used to create radiation sources readily tunable in the energy range 1.69–1.92 eV by varying the pumping power or temperature.

ACKNOWLEDGMENTS

The work was supported by the Russian Foundation for Basic Research (project no. 98-02-18266) and the Ministry of Science of the Russian Federation, Program “Physics of Solid-State Nanostructures” (identification code “Kvint”).

REFERENCES

1. F. Houzay, C. Guille, J. M. Moison, *et al.*, J. Cryst. Growth **81**, 67 (1987).
2. J. L. Jimenez, L. R. C. Fonseca, D. J. Brady, *et al.*, Appl. Phys. Lett. **71**, 3558 (1997).
3. A. E. Zhukov, A. R. Kovsh, V. M. Ustinov, *et al.*, IEEE Photonics Technol. Lett. **11**, 1345 (1999).
4. O. B. Shchekin, G. Park, D. L. Huffaker, and D. G. Deppe, Appl. Phys. Lett. **77**, 466 (2000).
5. M. K. Zundel, N. Y. Jin-Phillipp, F. Phillipp, *et al.*, Appl. Phys. Lett. **73**, 1784 (1998).
6. O. V. Kovalenkov, D. A. Vinokurov, D. A. Livshits, *et al.*, in *Proceedings of the 23rd International Symposium on Compound Semiconductors, St. Petersburg, 1996*; Inst. Phys. Conf. Ser., No. 155 (3), 271 (1996).
7. D. A. Vinokurov, V. A. Kapitonov, O. V. Kovalenkov, *et al.*, Fiz. Tekh. Poluprovodn. (St. Petersburg) **33**, 858 (1999) [Semiconductors **33**, 788 (1999)].
8. V. Zwiller, M.-E. Pistol, M. A. Odnoblyudov, and L. Samuelson, in *Abstracts of the International Symposium “Nanostructures: Physics and Technology”, St. Petersburg, 1999*, p. 28.

Translated by M. Tagirdzhanov

Semiconductors, Vol. 35, No. 2, 2001, pp. 238–241. Translated from Fizika i Tekhnika Poluprovodnikov, Vol. 35, No. 2, 2001, pp. 245–248.
Original Russian Text Copyright © 2001 by Volokobinskiĭ, Komarov, Matyukhina, Reshetnikov, Rush, Falina, Yastrebov.

PHYSICS OF SEMICONDUCTOR DEVICES

High-Power High-Voltage Bipolar Transistors Based on Complex Semiconductor Structures

M. Yu. Volokobinskiĭ*, I. N. Komarov, T. V. Matyukhina, V. I. Reshetnikov, A. A. Rush, I. V. Falina, and A. S. Yastrebov

Bonch-Bruevich St. Petersburg State University of Telecommunications, ul. Moika 61, St. Petersburg, 191168 Russia

**e-mail: volokobin@hotmail.com*

Submitted July 3, 2000; accepted for publication July 4, 2000

Abstract—Physical processes in transistors in which a new structural element (an array of bulk inclusions in the collector region) is introduced were studied. This array gives rise to a decrease in the electric field at the metallurgical boundary of the collector p–n junction and inhibits the development of the secondary breakdown.
© 2001 MAIK "Nauka/Interperiodica".

1. INTRODUCTION

When designing the transistors used in switching circuits with inductive load, it is necessary to account that the energy $W = \tilde{L}I^2/2$ stored in the inductance $\tilde{L}$ owing to the current flow I before the switch-off should be released in the blocked transistor or in other dedicated components. If pinching of the current occurs during the transistor switch-off, and the energy W is released in a small volume, the semiconducting material becomes overheated, and the device is damaged.

The design tools related to modifying the emitter structure [1] are used to prevent current pinching and increase the secondary-breakdown voltage.

We consider one of the feasible methods for controlling current pinching and increasing the operating voltage of transistors in the common-emitter configuration. This method is based on introduction of a planar array of spheroidal inclusions into the collector region; these inclusions are doped with impurities that convert the conductivity type of the semiconductor to the conductivity-type of the base.

2. ELECTRIC FIELD IN THE COLLECTOR p–n JUNCTION OF TRANSISTORS WITH AN ARRAY OF VOLUME INCLUSIONS IN THE COLLECTOR REGION

In order to prevent current pinching and increase the breakdown voltage of switching transistors in the common-emitter configuration, an array of heavily doped oval inclusions, whose shape is almost spherical, is formed in the collector region at the distance H from the metallurgical boundary of the p–n junction (Fig. 1).

The p^+ inclusions are formed in n–p–n transistors; the designation p^+ is used for the array in the n–p–n–(p^+)–n transistor structure. If an array with p^+ inclusions located in the collector region at the boundary between the lightly doped n^- layer and the buffer n layer is used in an n–p–n^-–n–n^+ transistor, the designation n–p–n^-–(p^+)–n–n^+ is used for the transistors.

The n^+-inclusion array is used in p–n–p– or p–n–p^-–p–p^+ transistors, so that p–n–p–(n^+)–p or p–n–p^-–(n^+)–p–p^+ transistor structures are formed.

If zero or low voltage is applied to the collector p–n junction, the thickness of the space-charge layer of the collector p–n junction is small and the isolated inclusions may be located outside this layer. In this case, each p^+ inclusion is surrounded by a double spherical layer of the space charge (negative charge inside the inclusion and positive charge in the adjoining layer outside the inclusion).

Thicknesses of the layers and the distribution of the electric-field strength in these layers can be calculated [2]. The net charge of the double layer is equal to zero. The volume inclusion does not affect the electric-field distribution in the collector region outside the related spherical layer of the space charge.

As the blocking voltage U_{cb} is increased, the thickness d of the space-charge layer near an abrupt p^+–n junction increases: $d = [2\varepsilon(U_{cb} + U_c)/\rho]^{0.5}$, where $\varepsilon = \varepsilon_0\varepsilon_r$ is the absolute permittivity, ε_0 is the permittivity of free space, ε_r is the relative permittivity, U_c is the contact potential difference between the collector and the base, $\rho = qN_D$ is the space-charge density in the collector region, q is the elementary charge, and N_D is the donor concentration [3].

For a certain value of the blocking voltage, the space-charge layer at the collector p–n junction reaches the inclusion. The p–n junction enveloping the inclusion sphere on the side closer to the base becomes conducting, and the inclusion becomes charged; as a result, the electric-field distribution in the collector region changes.

Calculation of the electric-field potential ϕ in the space-charge layer near the collector p–n junction with an array of inclusions in the n–p–n–(p^+)–n transistors is related to solving Poisson's equation $\Delta\phi = -\rho/\varepsilon$.

We consider first the case where there is only a single spherical p^+ inclusion with a radius R.

We render the origin of the spherical-coordinate system coincident with the inclusion center, and we direct the Z-axis from the metallurgical boundary to the depth of the collector region (Fig. 2). The problem is axially symmetric, and Poisson's equation $\Delta\phi(\rho, \vartheta) = -\rho/\varepsilon$ in the spherical coordinate system is written as

$$\frac{1}{r^2}\left(r^2\frac{\partial^2\phi}{\partial r^2} + 2r\frac{\partial\phi}{\partial r} + \frac{\partial^2\phi}{\partial\vartheta^2} + \frac{\cos\vartheta}{\sin\vartheta}\frac{\partial\phi}{\partial\vartheta}\right) = -\rho/\varepsilon, \quad (1)$$

where r and ϑ are the radial and angular coordinates.

For the thickness of the space-charge layer $d = H + h$ exceeding the inclusion size and for $H \gg R$ and $h \gg R$, the following solution [4] satisfies Eq. (1) and the boundary conditions (a constant value of ϕ at the inclusion surface and the zero value of the electric-field component $E_r(r, \vartheta)$ normal to the sphere surface at the point $r = R$ and $\vartheta = \pi$):

$$\phi = (\rho/\varepsilon)[hr\cos\vartheta - (r^2\cos^2\vartheta)/2 - (1+\chi)R^3/3r - (hR^3\cos\vartheta)/r^2 + R^5(3\cos^2\vartheta - 1)/6r^3]. \quad (2)$$

Here, $\chi = (9h + 5R)/R$.

The first two terms in expression (2) account for contribution of the space charge, and the other three terms account for the impact of the sphere that acquires the following charge under the effect of the electric field in the collector p–n junction:

$$Q_0 = -(4\pi/3)R^3\rho\chi. \quad (3)$$

In the n–p–n–(p^+)–n transistors, the p^+ inclusions are negatively charged, owing to transition of holes from these inclusions to the base; in the p–n–p–(n^+)–p transistors, the n^+ inclusions are positively charged as a result of drift of electrons to the base.

Using formula (2), we can derive the following expression for the radial component of the electric-field strength:

$$E_r(r, \vartheta) = -(\rho/\varepsilon)[h\cos\vartheta - r\cos^2\vartheta + (1+\chi)R^3/3r^2 + (2hR^3\cos\vartheta)/r^3 - R^5(3\cos^2\vartheta - 1)/2r^4]. \quad (4)$$

Distributions of magnitude of the electric-field strength $|E|$ in the p–n junction along the Z-axis are shown in Fig. 2 for the cases of (*1*) the p–n junction without inclusions and (*2*) the collector junction that contains only a single inclusion (the Z-axis passes through the inclusion center).

In the absence of inclusions, the electric-field strength $|E|$ varies linearly over the width of the space-charge layer, attains a maximum $|E_{max}| = \rho d/\varepsilon = 2(U_{cb} + U_c)/d \approx 2U_{cb}/d$ at the boundary of the base, and vanishes at the boundary of the space-charge layer in the collector.

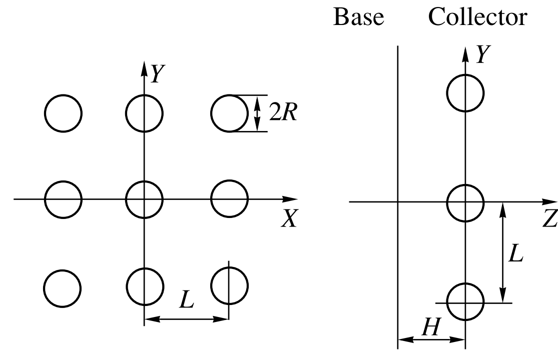

Fig. 1. An array of inclusions in the collector region of a transistor: the array viewed in the device plane (on the left) and in section (on the right).

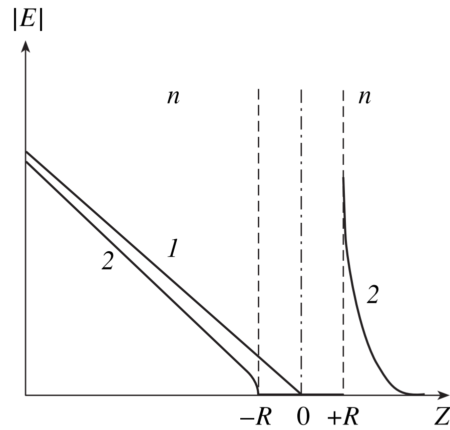

Fig. 2. Distribution of magnitude of the electric-field strength in the space-charge layer of the collector p–n junction that (*1*) contains no inclusions and (*2*) contains a single inclusion with a radius R along the Z-axis going through the inclusion center.

In a p–n junction with an inclusion, the field strength at the metallurgical boundary to the base decreases as a result of the charge redistribution; at the same time, the field strength increases at the inclusion on the junction side remote from the base (where this strength was initially low). The field strength $E(R, 0)$ at the sphere surface at the point with $r = R$ and $\vartheta = 0$ exceeds by a factor of 6 the mean field strength $|E_0| = \rho h/\varepsilon$ that takes place at the point corresponding to the sphere center in the absence of inclusion in the plane $Z = 0$.

In order to avoid large values of $E(R, 0)$, the inclusions are arranged at a fairly large distance from the base; for $h/d = 1/6$, the field strength $E(R, 0)$ does not exceed that ($|E_{max}|$) at the boundary of the base in the absence of an inclusion; consequently, formation of an

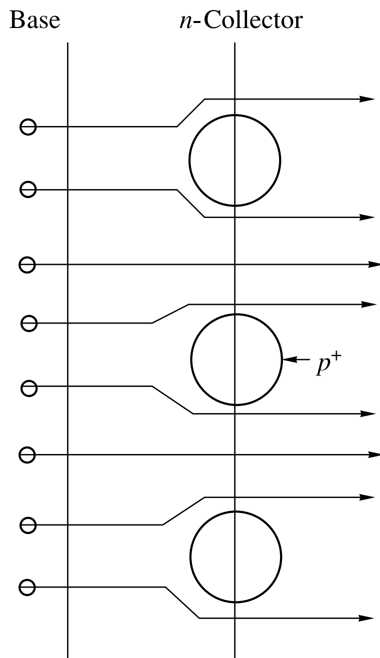

Fig. 3. A representation of the collector region having the n-type conduction and containing an array of p^+-inclusions; the paths of motion of electrons bypassing the negatively charged p^+ inclusions are also shown.

inclusion does give rise to regions where the field strength is higher than $|E_{max}|$.

The influence of a spherical inclusion on the electric-field distribution is important only at small distances from the inclusion that do not exceed several values of R. Therefore, in order to obtain a more uniform distribution of electric field over the entire area of the collector p–n junction, we have to form an array of inclusions.

For $H \gg L > R > L/6$ and $h \gg R$, and for a fixed thickness of the space-charge layer $d = H + h$ in transistors with an array of inclusions in the collector region, the highest electric-field strength at the metallurgical boundary of the base decreases to about $E_G = \rho H/\varepsilon$, which is lower than the highest field strength $|E_{max}| = \rho d/\varepsilon$ in a transistor without inclusions. To the right of the array (Fig. 1), the electric-field strengths along the lines parallel to the Z-axis and equidistant from two neighboring inclusions or from four neighboring inclusions do not exceed the electric-field strength at the same points in the absence of the inclusion array.

For a fixed value of the blocking voltage U_{cb}, the distribution of the electric-field strength to the left of the array is approximately the same as in the preceding case where a constant value of d was specified. For a fixed value of U_{cb}, the thickness of the space-charge layer d in the transistor with an inclusion array is larger than in that without this array. An array arranged at a distance of H from the base leads to an increase in h and to redistribution of the electric field in the collector region; as a result, the electric-field strength decreases to the left of the inclusion array and increases to the right of the array.

3. BREAKDOWN OF TRANSISTORS WITH AN ARRAY OF INCLUSIONS

The process of the formation of an electron avalanche in the collector p–n junction and the breakdown voltage depend heavily on the bipolar-transistor structure and on the breakdown test for this transistor.

For high voltages at the collector p–n junction, the inclusions are charged relative to the surrounding collector region in such a way that the sign of charge at the inclusions coincides with the charge sign of the majority charge carriers in the collector and emitter. This gives rise to two effects.

First, the charge carriers, when coming to the collector from the emitter via the base, bypass the inclusions in the collector region (Fig. 3). Thus, the inclusions prevent the pinching of current from the entire collector area to a single current filament and the development of the secondary breakdown.

Second, geometric dimensions of the inclusion array and physical parameters of materials forming the transistor structure are specified in such a way that the breakdown voltage U_{cb0} of the collector–base junction in the common-base and open-emitter modes virtually does not change, whereas the collector–emitter breakdown voltage U_{ce0} increases significantly when the transistor is connected in the common-emitter and open-base mode and approaches the value of U_{cb0}.

An increase in U_{ce0} to the value of U_{cb0} is caused by the fact that the inclusion array gives rise to redistribution of the electric field.

In a transistor with an array of inclusions, if a voltage applied to the collector p–n junction is increased, an increase in the electric-field strength at the technological base–collector boundary is stopped, so that the electric-field strength remains lower than the maximal electric-field strength in the absence of inclusions and is insufficient for formation of an avalanche. Electrons that come from the emitter pass through the base and penetrate into the collector, bypassing the negatively charged spheres, do not enter the strong-field region to the right of inclusions, do not induce ionization, and are not involved in formation of an avalanche; this does not lead to a decrease in U_{ce0}. Thus, in transistors with an inclusion array, the cause of difference between the values of U_{ce0} and U_{cb0} (as was mentioned by Miller [5]) in the transistors with conventional structure is eliminated.

This can be verified by comparing the current–voltage characteristics $I(U)$ of the p–n–p^-–(n^+)–p^-–p–p^+ and p–n–p^-–p–p^+ transistors or the n–p–n^-–(p^+)–n–n^+

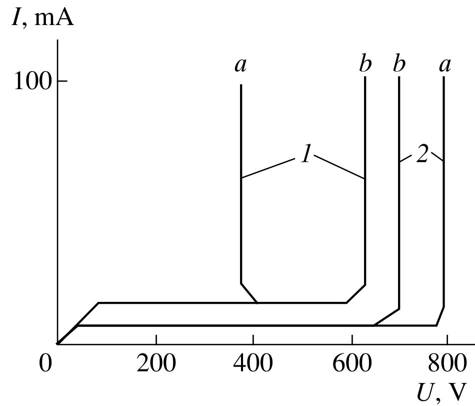

Fig. 4. The current–voltage characteristics of (*a*) n–p–n^-–n–n^+ transistors and (*b*) p–n–p^-–p–p^+ transistors with an array of inclusions. Curves *1* correspond to the common-emitter circuit with disconnected base, and curves *2* correspond to the common-base circuit with disconnected emitter.

and n–p–n^-–n–n^+ transistors (Fig. 4). The voltages U_{ce0} and U_{cb0} have almost the same average values in the transistors with an array of inclusions. The breakdown voltage U_{ce0} is lower than U_{cb0} in transistors without an array of inclusions.

Theoretical analysis shows (and experimental studies of the new-type transistors verify) that good results are obtained only if the sizes and arrangement of inclusions are chosen properly. Sparsely located inclusions do not affect the distribution of the electric-field strength away from these inclusions and, therefore, cannot be conducive to an increase in the breakdown voltage U_{ce0} or U_{cb0}.

If the sizes and arrangement of inclusions are chosen nonoptimally (the inclusions are located too close to the base), the electric-field strength increases appreciably near the inclusions, and the transistors that include an array of inclusions have a lower value of U_{cb0} than similar devices without such an array.

The outlined theoretical concepts were used in the development of the structure and production technology for transistors that include an array of inclusions in the collector region; specific features of such transistors will be described in the succeeding publication.

REFERENCES

1. A. Blicher, *Field-Effect and Bipolar Power Transistor Physics* (Academic, New York, 1981; Énergoatomizdat, Leningad, 1986).
2. T. P. Lee and S. M. Sze, Solid-State Electron. **10**, 1105 (1967).
3. S. Sze, *Physics of Semiconductor Devices* (Wiley, New York, 1981; Mir, Moscow, 1984).
4. M. Yu. Volokobinskiĭ and A. S. Yastrebov, Dokl. Akad. Nauk **362**, 323 (1998) [Dokl. Phys. **43**, 552 (1998)].
5. S. L. Miller, Phys. Rev. **99**, 1234 (1955).

Translated by A. Spitsyn